

See discussions, stats, and author profiles for this publication at: <https://www.researchgate.net/publication/283722259>

Digital Processing of SAR Data and Image Analysis Techniques

Chapter · January 2015

DOI: 10.1007/978-94-017-9813-6_14

CITATIONS

0

READS

128

1 author:



Saied Pirasteh

University of Waterloo

106 PUBLICATIONS 857 CITATIONS

SEE PROFILE

Some of the authors of this publication are also working on these related projects:



Workshop on Geomatics Development and Point clouds processing of LiDAR and UAV for 3D mapping

[View project](#)



Mapping of groundwater potentials in Western Cameroon Highlands: contribution of Remote Sensing (optical and radar), Geographic Information Systems and Neural Networks [View project](#)

Springer Remote Sensing/Photogrammetry

Jonathan Li
Xiaojun Yang *Editors*

Monitoring and Modeling of Global Changes: A Geomatics Perspective

 Springer

Springer Remote Sensing/Photogrammetry

More information about this series at <http://www.springer.com/series/10182>

Jonathan Li • Xiaojun Yang
Editors

Monitoring and Modeling of Global Changes: A Geomatics Perspective

 Springer

Editors

Jonathan Li
Department of Geography
and Environmental Management
University of Waterloo
Waterloo, ON, Canada

Xiaojun Yang
Department of Geography
Florida State University
Tallahassee, FL, USA

ISSN 2198-0721 ISSN 2198-073X (electronic)
Springer Remote Sensing/Photogrammetry
ISBN 978-94-017-9812-9 ISBN 978-94-017-9813-6 (eBook)
DOI 10.1007/978-94-017-9813-6

Library of Congress Control Number: 2015946987

Springer Dordrecht Heidelberg New York London
© Springer Science+Business Media Dordrecht 2015

This work is subject to copyright. All rights are reserved by the Publisher, whether the whole or part of the material is concerned, specifically the rights of translation, reprinting, reuse of illustrations, recitation, broadcasting, reproduction on microfilms or in any other physical way, and transmission or information storage and retrieval, electronic adaptation, computer software, or by similar or dissimilar methodology now known or hereafter developed.

The use of general descriptive names, registered names, trademarks, service marks, etc. in this publication does not imply, even in the absence of a specific statement, that such names are exempt from the relevant protective laws and regulations and therefore free for general use.

The publisher, the authors and the editors are safe to assume that the advice and information in this book are believed to be true and accurate at the date of publication. Neither the publisher nor the authors or the editors give a warranty, express or implied, with respect to the material contained herein or for any errors or omissions that may have been made.

Printed on acid-free paper

Springer Science+Business Media B.V. Dordrecht is part of Springer Science+Business Media (www.springer.com)

Preface

Global change studies are growingly considered a vital source of information to understand the Earth environment, especially in the framework of human-induced climate change and land use transformation. Earth observing systems and geomatics technologies provide a unique tool to monitor and model those changes, respectively. While the range of applications and innovative techniques is constantly increasing, this book provides a summary of key study cases where the Earth observation data offers critical information to understand both the causes and consequences of global change and the geomatics technologies provide powerful tools to model and analyze the effects of those global environmental changes, toward minimizing their negative impacts.

This book focuses on the monitoring and modeling aspects in global changes and provides the state of the art in geomatics technologies for detecting and modeling global landscape dynamics.

This volume includes 15 chapters, which are organized in five topics:

- Monitoring and Modeling of Land Use Changes (Chaps. 1 and 2)
- Monitoring and Analyzing of Urban Dynamics (Chaps. 3, 4, and 5)
- Monitoring and Mapping Environmental Changes (Chaps. 6, 7, and 8)
- Environmental Modeling and Risk Assessment (Chaps. 9, 10, 11, and 12)
- Earth Observation Data Processing (Chaps. 13, 14, and 15)

Chapters are written by leading scholars and researchers from a variety of fields, including remote sensing, geoinformatics, geography, and environmental science, with case studies predominately drawn from North America, Europe, and Asia.

This volume will be of greatest interest to graduates and undergraduates studying geography, geosciences, and environmental sciences and to researchers and professionals working in the fields of remote sensing, geographic information sciences, climate change studies, environmental modeling, and risk assessment.

We would like to thank all the authors and reviewers for their contribution to this book. Thanks also go to Hermine Vloemans for her generous support to this book.

Waterloo, ON, Canada
Tallahassee, FL, USA

Jonathan Li
Xiaojun Yang

Contents

Part I Monitoring and Modeling of Land Use Changes		
1	Land Change Modeling: Status and Challenges	3
	Ting Liu and Xiaojun Yang	
2	Modeling the Effects of Land Use Change and Climate Change on Stream Flow Using GIS and a Hydrological Model	17
	Maochuan Hu, Bin He, Pingping Luo, Kaoru Takara, and Weili Duan	
Part II Monitoring and Analyzing of Urban Dynamics		
3	Combining Different Data Sources for City Growth Analysis and Architectural Heritage Mapping	37
	Karel Pavelka and Eva Matoušková	
4	Long-Term Change Dynamics Using Landsat Archive for the Region of Waterloo in Ontario, Canada	63
	Anqi Fu, Jonathan Li, and Saied Pirasteh	
5	Influence of Political Regime Change to Land Use Development in Urban Areas in the Czech Republic	87
	Lena Halounová and Vladimír Holubec	
Part III Monitoring and Mapping Environmental Changes		
6	Mapping Sea Ice from Satellite SAR Imagery	113
	Linlin Xu and Jonathan Li	
7	Landscape Ecological Mapping for Biodiversity Evaluation Using Airborne Laser Scanning Data	137
	Mamoru Koarai	

8	Grassland Productivity Simulation: Integrating Remote Sensing and an Ecosystem Process Model	155
	Yuhong He, Zhangbao Ma, and Xulin Guo	
Part IV Environmental Modeling and Risk Assessment		
9	Glaciological Studies at Pasterze Glacier (Austria) Based on Aerial Photographs	173
	Viktor Kaufmann, Andreas Kellerer-Pirklbauer, Gerhard Karl Lieb, Heinz Slupetzky, and Michael Avian	
10	Mapping Coastal Erosion Risk in the Southern Red River Delta, Vietnam	199
	Mizue Murooka, Yasuhiro Kuwahara, and Shigeiko Haruyama	
11	Modelling Shallow Landslide Risk Using GIS and a Distributed Hydro-geotechnical Model	221
	Pingping Luo, Apip, Bin He, Kaoru Takara, Weili Duan, Mochuan Hu, and Daniel Nover	
12	An Integrated Model for Assessing Carbon Dioxide Emissions Considering Climate Change Mitigation and Flood Risk Adaptation Interaction	241
	Kumiko Nakamichi, Yoshiki Yamagata, and Hajime Seya	
Part V Earth Observation Data Processing		
13	Support Vector Machines for Land Cover Mapping from Remote Sensor Imagery	265
	Dee Shi and Xiaojun Yang	
14	Digital Processing of SAR Data and Image Analysis Techniques	281
	Saied Pirasteh, Hojjat O. Safari, and Somayeh Mollaei	
15	Development of a New Wetness Index Based on RADARSAT-1 ScanSAR Data	301
	Quazi K. Hassan and Charles P.-A. Bourque	
	Index	315

List of Contributors

Apip Research Centre for Limnology, Indonesian Institute of Sciences (LIPI), Cibinong, Indonesia

Michael Avian Institute of Earth Sciences, University of Graz, Graz, Austria

Charles P.-A. Bourque Faculty of Forestry and Environmental Management, University of New Brunswick, Fredericton, NB, Canada

Weili Duan CAS Key Laboratory of Watershed Geographic Sciences, Chinese Academy of Sciences, Nanjing Institute of Geography and Limnology, Nanjing, China

Anqi Fu Department of Geography and Environmental Management, University of Waterloo, Waterloo, ON, Canada

Xulin Guo Department of Geography and Planning, University of Saskatchewan, Saskatoon, SK, Canada

Lena Halounová Faculty of Civil Engineering, Czech Technical University in Prague, Prague, Czech Republic

Shigeko Haruyama Graduate School of Bioresources, Mie University, Tsu City, Mie Prefecture, Japan

Quazi K. Hassan Department of Geomatics Engineering, Schulich School of Engineering, University of Calgary, Calgary, AB, Canada

Bin He CAS Key Laboratory of Watershed Geographic Sciences, Chinese Academy of Sciences, Nanjing Institute of Geography and Limnology, Nanjing, China

Yuhong He Department of Geography, University of Toronto Mississauga, Mississauga, ON, Canada

Vladimír Holubec Faculty of Civil Engineering, Czech Technical University in Prague, Prague, Czech Republic

Maochuan Hu Department of Civil and Earth Resources Engineering, Graduate School of Engineering, Kyoto University, Nishikyo-ku, Kyoto, Japan

Viktor Kaufmann Institute of Remote Sensing and Photogrammetry, Graz University of Technology, Graz, Austria

Andreas Kellerer-Pirklbauer Department of Geography and Regional Science, University of Graz, Graz, Austria

Mamoru Koarai Survey Department, College of Land, Infrastructure, Transport and Tourism (MLIT), Kodaira, Tokyo, Japan

Yasuhiro Kuwahara Abashiri Fisheries Research Institute, Abashiri, Hokkaido, Japan

Jonathan Li Department of Geography and Environmental Management, University of Waterloo, Waterloo, ON, Canada

Gerhard Karl Lieb Department of Geography and Regional Science, University of Graz, Graz, Austria

Ting Liu Department of Geography and Environmental Studies, Northeastern Illinois University, Chicago, IL, USA

Pingping Luo Institute for the Advanced Study of Sustainability (UNU-IAS), United Nations University, Shibuya, Tokyo, Japan

Disaster Prevention Research Institute (DPRI), Kyoto University, Uji, Kyoto, Japan

Zhangbao Ma Department of Geography and Planning, University of Saskatchewan, Saskatoon, SK, Canada

Eva Matoušková Department of Geomatics, Faculty of Civil Engineering, Czech Technical University in Prague, Prague, Czech Republic

Somayeh Mollaee Department of Geography and Environmental Management, University of Waterloo, Waterloo, ON, Canada

Mizue Murooka Abashiri Fisheries Research Institute, Abashiri, Hokkaido, Japan

Kumiko Nakamichi Center for Global Environmental Research (CGER), National Institute for Environmental Studies (NIES), Tsukuba City, Ibaraki, Japan
Graduate School of Science and Engineering, Tokyo Institute of Technology, Meguro-ku, Tokyo, Japan

Daniel Nover Global Change Research Program, U.S. Environmental Protection Agency, Washington, DC, USA

Karel Pavelka Department of Geomatics, Faculty of Civil Engineering, Czech Technical University in Prague, Prague, Czech Republic

Saied Pirasteh Department of Geography and Environmental Management, University of Waterloo, Waterloo, ON, Canada

Hojjat O. Safari Department of Geology, Golestan University, Gorgan, Iran

Hajime Seya Center for Global Environmental Research (CGER), National Institute for Environmental Studies (NIES), Tsukuba City, Ibaraki, Japan

Graduate School for International Development and Cooperation, Hiroshima University, Higashi-hiroshima, Hiroshima, Japan

Dee Shi Department of Geography, Florida State University, Tallahassee, FL, USA

Heinz Slupetzky Department of Geography and Geology, University of Salzburg, Bergheim, Austria

Kaoru Takara Disaster Prevention Research Institute (DPRI), Kyoto University, Uji, Kyoto, Japan

Linlin Xu Department of Geography and Environmental Management, University of Waterloo, Waterloo, ON, Canada

Yoshiki Yamagata Center for Global Environmental Research (CGER), National Institute for Environmental Studies (NIES), Tsukuba City, Ibaraki, Japan

Xiaojun Yang Department of Geography, Florida State University, Tallahassee, FL, USA

Part I
Monitoring and Modeling of Land Use
Changes

Chapter 1

Land Change Modeling: Status and Challenges

Ting Liu and Xiaojun Yang

Abstract Over the past years, land change science has emerged as a fundamental component of global environmental change and sustainability research, and modeling of land change has been recognized as a premier research area in land change science. Various land change modeling approaches have been developed to explore the functioning of land changes at aggregated and individual levels, across various spatiotemporal scales, as well as in human, natural, or the coupled systems. This chapter will review a collection of land change modeling approaches including statistical regression models, artificial neural networks, Markov chain models, cellular automata, economic models, and agent-based models. For each approach, the theoretical and methodological basics and major characteristics will be examined. Moreover, several important issues challenging the successful implementation of land change modeling will be discussed, which include coupling human and environmental systems, scale dependency and multilevel interactions, and temporal dynamics and complexity. Finally, a review on the progress of integrating land change models with other environmental modeling techniques for global environmental change research will be provided.

Keywords Land change modeling • Land change science • Global change • Land use and land cover change • Coupled human-environmental systems

1.1 Introduction

The process of global change is altering the earth system and its capacity to sustain life (U.S. Global Change Research Program 2014). Rapid human population growth, along with their increasing demand for food, water, energy, and other

T. Liu (✉)

Department of Geography and Environmental Studies, Northeastern Illinois University,
Chicago, IL 60625, USA

e-mail: tliu1@neu.edu

X. Yang

Department of Geography, Florida State University, Tallahassee, FL 32306, USA

e-mail: xyang@fsu.edu

© Springer Science+Business Media Dordrecht 2015

J. Li, X. Yang (eds.), *Monitoring and Modeling of Global Changes: A Geomatics Perspective*, Springer Remote Sensing/Photogrammetry,
DOI 10.1007/978-94-017-9813-6_1

3

benefits, has become the main drivers of global change, especially since the second half of twentieth century (Turner et al. 2007). Well-documented global changes include concentrations of carbon dioxide in the atmosphere; alterations in the biochemistry of the global nitrogen cycle; and on-going land use and land cover change (Vitousek 1994). Land use and land cover change is a pervasive factor of global importance not only because it represents a major component of global change but also it strongly interacts with other components of global environmental change. To date, as much as 50 % of the earth's ice-free land has been transformed or degraded (Haberl et al. 2007). Only between 2000 and 2010, approximately 13 million hectares of land area (about the area of Greece) were converted each year to other land cover types (FAO 2010). Moreover, land changes have far-reaching influences on the structure and function of the earth's ecosystems, with equally significant implications for the human society (Steffen et al. 2004). On the one hand, land changes affect the ecosystems in several ways, such as reducing native habitat and species, accelerating soil decomposition, disrupting freshwater resources and quality, as well as leading to additional greenhouse gas release (Turner et al. 1993; Camill 2010). For example, deforestation is thought to contribute to nearly 20 % of the global carbon dioxide release (1.5–2 billion tons of carbon) (Camill 2010). On the other hand, rapid urbanization and the concentration of human populations into large metropolises have altered the city's cultures, politics, and economics, which are just beginning to be fully recognized as a significant global problem.

Over the past years, land change science has emerged as a fundamental component of global environmental change and sustainability research (Turner et al. 2007). This interdisciplinary field seeks to understand land use and land cover dynamics through integrating the human, environmental, and geographical information-remote sensing sciences. Challenges lie in the complexity of land change processes, in which human and environmental systems interact over space and time to reshape the earth's surface. Research in land change science has been dedicated to enhance our understanding of land changes through: (i) monitoring land changes at different spatiotemporal scales, (ii) exploring the driving forces (both human and environmental) and feedbacks underlying land changes, (iii) spatially explicit modeling of land changes, and (iv) assessing system outcomes (Turner et al. 2007). Land change modeling is a promising research area which can support an integrated earth system science enterprise. Models allow us to link human behaviors with landscape patterns for simulating the processes of land changes in the past and present, for forecasting future landscape dynamics under different scenarios, and for informing decision-making towards sustainable land and resource management.

This chapter examines a collection of land change models (LCM) for global environmental change research. To a large degree, modeling is a way of thinking more than a technology. Over the past several decades, various modeling approaches have been developed, which provide insights into the functioning of land changes at aggregated and individual levels, across various spatiotemporal scales, as well as in human, natural, and the coupled systems. Meanwhile, there are numerous theoretical and technological challenges for the modeling of land

changes given the complexity of the coupled human-environmental systems (Rindfuss et al. 2004). Advances in geospatial theories, technologies and data provide great opportunities for addressing various challenges and for developing the next generation of LCMs. In the following sections, we first discuss the theoretical foundations and major characteristics of various modeling approaches. We then identify some outstanding issues for the LCM communities. Finally, we describe several examples to illustrate how land change modeling can be coupled with other ecological modeling techniques for integrated global environmental change research.

1.2 Land Change Modeling Approaches

This section discusses several frequently used land change modeling approaches, including statistical regression models, artificial neural networks, Markov chain models, cellular automata, economic models, and agent-based models. The above modeling approaches were identified based on the authors' knowledge and a personal archive of relevant publications, and a search on Web of Science using the Keywords: (Topic = "land change" or "land use change" or "land cover change" or "land use and land cover change" or "urbanization" or "urban growth" or "urbanization" or "deforestation" or "farmland") AND (Topic = model or simulation). In the following subsections, we will briefly present the theoretical and methodological basics and the relative strengths and weaknesses of each modeling approach with selected examples.

1.2.1 Statistical Regression Models

The basic structure of statistical regression models is based upon empirical analyses that link between land use and land cover changes (i.e., dependent variable) and a set of environmental and socio-economic explanatory variables. The derived relationships are usually used to generate maps of land transitional probability to predict potential land changes in the future. Some frequently used statistical methods for land change modeling include logistic regression (Hu and Lo 2007), generalized linear models (Aspinall 2004), generalized additive models (Brown et al. 2002), and Bayesian statistics (Agarwal et al. 2005). A popular example is the CLUE-S (Conversion of Land Use and its Effects at Small regional extent) model developed by Verburg et al. (2002). The CLUE-S model consists of a non-spatial demand module and a spatially explicit allocation module. The non-spatial module estimates the aggregate demand of land changes, and the spatial module allocates the land demands at various locations on a raster space based on stepwise logistic regression. Logistic regression is a form of multivariate models when the dependent variable has a categorical output, e.g., change or no-change of land use. Logistic

regression can be binomial or multinomial. It takes the logit transformation of the categorical dependent variable to ensure that the dependent variable of the regression is continuous.

Given the less demand of computational resources and easy operability, statistical regression models have become one of the most popular approaches for land change research communities. Statistical methods provide valuable information on key factors of land changes but are relatively deterministic compared to more advanced forms of model. It can also contribute to theory building and testing (Lesschen et al. 2005). However, it has very limited capability to represent the complex interactions and the temporal dynamics within the coupled human-environmental systems.

1.2.2 Artificial Neural Networks

Artificial neural networks (ANN) are developed based on machine learning algorithms (e.g., Li and Yeh 2002; Liu and Seto 2008). The functioning of ANN is relating to regression models in that they both seek to associate land change and its potential drivers. ANN is characterized by its ‘learning’ ability which can be used to detect non-linear relationships through the incorporation of a hidden layer. The algorithms of ANN calculate weights for input layers, hidden layers, and output layers by introducing the input in a feed-forward manner. For example, Liu and Seto (2008) presented an ART-MMAP neural network model for urban growth prediction from historical data. A set of proximity, neighborhood, and physical factors were included. This paper also applied a multi-resolution analysis to test the model’s performance. In general, spatial aggregation results in higher accuracies. By comparing with a null model, two random models and a naive model, neural network outperforms other models at finer resolution.

The strength of neural networks lies in their flexibility and non-linearity (Lesschen et al. 2005) in predicting future changes. However, it provides little interpretability because the relationships between variables remain invisible, criticized as a “black box”. ANN is commonly used for predicting future land cover/use changes based on the ‘knowledge’ learned from the patterns and behaviors observed from historical data. The assumption here is that past and present trend will continue into the future (i.e., stationarity), which tends to oversimplify the temporal complexity of land change processes.

1.2.3 Markov Chain Modeling

The Markov chain modeling approach employs a discrete stochastic process to determine the transition probability of land conversion. There is a set of discrete states in the modeling structure. In the context of land change modeling, each state

usually represents different types of land cover/use. The model moves from one state (e.g., land cover/use type) to the other with some transition probability depending on the current state but not the previous ones (often called a process without memory). Transition probabilities are computed based on the observed land change data which represent the probability that the land cover/use type within a cell (i.e. spatial unit) will convert (or, move) to another land type within the same period of time in the future. For example, Muller and Middleton (1994) applied Markovian analysis to time series data to quantify land use changes over a human-dominated landscape. Markovian analysis can represent all the multi-directional land use changes between land use categories. Sequential time series data were used to simulate land use change over a longer time period.

Markov models usually do not account for specific drivers of land changes, which assume that collective forces functioning to produce the observed patterns in the past will continue to do so in the future. In other words, Markov models are used to project future land changes based on the assumption of stationarity. Markov model can be dynamic by changing the transition probabilities in some sort of regular patterns over time (Howard et al. 1995). Given the capability of automatically computing land transition probability with time series data, Markov chain models are often integrated with more complex forms of models such as cellular automata and agent-based model that will be discussed shortly.

1.2.4 Cellular Automata

A conventional modeling framework describes systems in equilibrium or as moving between equilibriums. However, the evolution of land changes usually does not reach a stable equilibrium but exhibits features of complexity (e.g., edge of chaos, emergence, and non-linearity). The concept of complexity emphasizes on the interdependence among constituent parts. Therefore, complex adaptive system (CAS) is a system composed of interconnected parts that as a whole exhibits one or more properties that are not obvious from the individual parts. Cellular automata (CA) models are built upon static cell-based environment where each cell has a state and can transfer to others based on the current state and the interactions with its neighborhoods using a set of transition rules (Batty and Xie 1994; Clarke et al. 1997; Miller and Page 2007). The four major components of CA therefore are state, landscape/space, neighborhoods and transition rules. For each of the four components, their structures vary from simple to more complex forms (e.g., Stevens and Dragicevic 2007). The transition rules are usually set to represent spatial and temporal constraints (Sante et al. 2010). One of the well tested CA models is the SLEUTH (Slope, Land use, Exclusion, Urban extent, Transportation, Hillshade) model developed by Clarke et al. (1997) for simulating urbanization. This model defines complex rules representing control parameters that allow the model to self-modify under the circumstances it generates. More applications of this model are

found in Clarke and Gaydos (1998), Yang and Lo (2003), Jantz et al. (2004), Mahiny and Clarke (2012), and Akin et al. (2014).

As a dynamic modeling tool, CA model has gained great popularity among all modeling approaches. Although offering a framework for studying complex systems, CA modeling does not explicitly incorporate drivers of change except for the neighborhood interactions and transition rules. In addition, CA does not explicitly account for human decision makings in their modeling structures as the cells cannot move and their transition in states mainly represent the physical processes of land conversion.

1.2.5 Economic Models

Economic models generate land use patterns as aggregate outcomes from the underlying microeconomic behavior that determines demand and supply relationships. These models explicitly involve human choices and economic behaviors and thus address the human dimension of land changes, mainly focused on land uses. The basic idea of economic models of land changes is based on market equilibrium (e.g., market clear with zero excess demand and zero excess supply). Economic models can operate at aggregate scale (e.g., sector-based models) and disaggregate scale (e.g., spatially disaggregate models). Sector-based models represent the global economy and the interactions between different sectors (i.e., general equilibrium models) or only some specific sectors as a closed system (i.e., partial equilibrium models). Therefore, sector-based models describe the amount of land allocated to different uses by demand-supply structures (Sohngen et al. 1999). Spatially disaggregate models simulate the optimal land use decision based on profits or utility maximization or cost minimization (Bockstael 1996; Wu et al. 2004). These models explicitly represent individual decision-making at the micro level that will lead to land change outcomes at the aggregate level.

Economic models explicitly represent human land use decisions based on market and price mechanism compared with most statistical, machine learning and cellular models. The spatially disaggregate models are promising in accounting for the market feedbacks and dynamics within the land change systems. These models are often used in the agent-based framework to simulate the decision-making processes of human agents. Economic models are useful for non-marginal land change simulation and prediction. However, given the complexity of human choices and data scarcity, it is quite challenging for economic models to build the underlying assumptions.

1.2.6 Agent-Based Models

Agent-based models (ABM), or the multi-agent system models (MAS), are developed based upon the assumption that “agent” is the major driver of a system (e.g., Parker et al. 2003; Batty 2005; Torrens and Benenson 2005; Xie et al. 2007). ABMs are similar to CA models which are both spatial transition models built on a bottom-up perspective for the simulation of emergent properties of complex adaptive systems (Couclelis 2001). The three primary components of an ABM are the agents, landscape and their interactions. Within the modeling structure, the agents can interact with each other as well as the environment across multiple scales. Agents could employ high degree of rationality and information-processing ability in decision making which will influence the behavior of the systems (Miller and Page 2007). A number of ABMs apply the utility function to represent agents’ decision-making on location choices (e.g., Brown and Robinson 2006; Xie et al. 2007; Ligmann-Zielinska 2009). Usually, an agent will select a location that can maximize the utility or profit. Although traditional ABM is built on the bottom-up perspective, researchers in geographic and ecological modeling have proposed that ABM should not be restricted to the bottom-up simulation (Xie et al. 2007). In the paper by Xie et al. (2007), the author considers both macro level and micro level spatiotemporal urban dynamics. The macro level model is based on a stepwise regression model to project the aggregated rate of change at township level. The micro level model is to allocate the changes at the cellular level. The interaction among the two levels is also modeled through incorporating township competition in the utility function.

The structure of ABM is promising for land change research in that it explicitly represents human-nature interactions and feedbacks which are essential components for simulating land changes as coupled human-environmental systems. However, given its complexity in model design and implementation, much effort needs to be done to examine its operability for simulating real world processes and to fully realize the potential of ABM. Moreover, the advancement of ABM is challenged by the lack of detailed data to represent and validate complex human decision-making processes and interactions among agents at the micro level.

1.3 Major Issues in Land Change Modeling

The usefulness and complexity of land change modeling lie in the necessity to treat land changes as coupled human-environmental systems with complex interactions and feedbacks at multiple spatiotemporal scales (Turner et al. 2007). This section discusses several important theoretical and methodological issues in land change modeling: (i) coupling of human decision-making and environmental conditions, (ii) scale dependency and multilevel interactions, and (iii) temporal dynamics and complexity. These proposed issues are important for developing a comprehensive

understanding of land changes in an integrated framework for global environmental change.

1.3.1 Coupling Human and Environmental Systems

Land changes are both causes and consequences of earth system changes, including the biophysical and the socioeconomic processes. Models taking specific drivers into considerations have tried to include factors from both subsystems. One major challenge arises from the integration of data and processes representing biophysical conditions and human decision making. Difficulty lies in the different levels of aggregation and spatial unit of observation (Rindfuss et al. 2004). In social-demographic analysis, data are usually collected at some levels of aggregation, whereas direct measurements and remote sensing techniques have been more commonly used in extracting biophysical variables (Jensen 1983). As a result, research of the coupled human-environmental systems has to deal with the problem of (i) integrating different types of data (e.g., raster and vector), (ii) integrating spatial data at different scales, (iii) integrating spatial data from different dimensions (e.g., point, line, polygon), and (iv) integrating data acquired at different locations (Gotway and Young 2002). These four types of spatial data integration problems are often intertwined, which leads to even more challenges.

The issue of coupling human and environmental systems is also related to the scale issues in that statistical modeling and machine learning are designed at the scale of the coupled system as a whole while cell-based models can represent multilevel dynamics in both dimensions. Moreover, it is quite challenging to fully represent the processes in the human subsystems due to the lack of specific data on human decision-making and a high level of uncertainty. Towards a comprehensive understanding of the coupled system, the potential interactions and feedbacks within the land change system need to be incorporated in the models. In this sense, the structures of agent-based models and integrated models seem promising for integrating human behaviors and biophysical feedbacks. Its capability in representing temporal dynamics further facilitates the realization of simulating system feedbacks in land change processes.

1.3.2 Scale Dependency and Multilevel Interactions

Research on the coupled human-environmental systems is further complicated by the issue of scale dependency and the multilevel interactions within the system. One of the early steps in spatially explicit modeling is to identify an appropriate scale (e.g., extent and resolution) for analyzing the spatial phenomena, such as land changes. This is known as the Modifiable Areal Unit Problem (MAUP) in geospatial science, that is, the correlation between variables may change with scales

(Openshaw and Taylor 1979). The common approach to deal with the MAUP issue is to apply a multi-scale analysis to examine how the relationships among variables change with varying levels of aggregation and different ways of zoning (e.g., Veldkamp and Fresco 1997; Walsh et al. 2001; Evans and Kelley 2004; Hu and Lo 2007). Multilevel statistical modeling has also been used for analyzing land change driving factors at nested hierarchical levels (Hoshino 2001).

Land change modeling is further complicated by the potential interactions and feedbacks among different levels of processes (Verburg 2006). In simulating the multilevel interactions, the modeling frameworks of cellular automata and agent-based model allow for the representation and incorporation of processes at multiple levels. The current land use models focus on two types of cross-scale dynamics: top-down and bottom-up simulation. The top-down control is represented by the government policies and global interactions affecting land demand and growth suitability. From the bottom-up perspective, human makes decisions on land allocation which produces the aggregate land use patterns. Further exploration on their capabilities is needed given the challenges in theoretical development and data availability, as well as the high computing demand of agent-based modeling.

1.3.3 Temporal Dynamics and Complexity

Simulating temporal dynamics is another critical issue for land change modeling, which brings about the need to handle time lags and feedback responses in the temporal dimension of land change processes (Agarwal et al. 2002). Under the assumption of stationarity, statistical modeling and machine learning have very limited capability to represent temporal dynamics and complexity of the land change processes. They often assume the factors leading to the observed patterns and processes in the past will continue to do so in the future. This assumption is problematic as it is very likely the factors will alter their future behaviors given changes in the landscape or some exogenous conditions. To the contrary, the framework of cellular automata and agent-based models allows for the temporal dynamics to be considered as the behaviors at individual level may alter in response to landscape changes or incorporated external variables at each simulation time step.

The ecological and socioeconomic responses within the coupled human-environmental systems may not be immediately observable or predictable because the existence of time lags between the human-nature interactions and the appearance of ecological and socioeconomic consequences. To address this issue, a temporally lagged variable can usually be included in some models such as the statistical regression models. More complex models have the flexibility to represent time lags in land use decisions. For example, Irwin and Bockstael (2002) treat the interactions among neighboring agents making a residential conversion decisions as a temporally lagged process to better represent the real world decision-making processes.

1.4 Land Change Modeling for Global Environmental Changes

The use and integration of models will lead to a comprehensive understanding of the complexity of the coupled human-environmental systems (i.e., synthesis and assessment issues). In the context of global environmental change and sustainability science, increasing concerns are given to research on sustainability that can inform practice and decision making in planning and management domains. The development of the next generation of LCMs needs to take these concerns into consideration towards an integrated research framework for land change and earth system studies. In this section, we review four research articles that illustrate the progress of coupling land change modeling with other environmental analysis and modeling techniques for studying the interactions between land change and other components of global environmental changes, such as climate change, hydrological processes, soil degradation, and biodiversity loss.

Kerr et al. (2003) described an integrated process-based modeling approach that couples ecological modeling of Carbon dynamics with economic modeling of land use for the prediction of land use and Carbon storage. This integrated model contains three components to simulate the interactions and feedbacks between ecosystems and human land-use activities. The ecological model and economic model were coupled through the land manager's choice of land use at each time step. The complex interactions were then realized through the exchange of individual model outputs as endogenous variables that will affect the next step of simulation. For example, the ecological model provides inputs to the land use choice model through estimates of biomass productivity. The key outputs from the integrated model include both land use and Carbon stocks.

Lin et al. (2007) developed an approach for modeling the impacts of future land use and climate changes on hydrological process through integrating the CLUE-S model (Verburg et al. 2002) and the generalized watershed loading functions model (Haith and Shoemaker 1987). The structure of the CLUE-S model was described earlier in Sect. 1.2.1. The hydrological model is a combined distributed/lumped parameter watershed model that simulates runoff, sediment, and nutrient loadings in a watershed using variable sized source areas of different land use/cover types. The simulated land use/cover types have different coefficient values that are used to determine the evapotranspiration in the hydrological model. Moreover, climate change scenarios generated from general circulation models (GCM) simulations have also been included to examine the impacts of climate change on the hydrological cycle.

Van Rompaey et al. (2002) loosely coupled land use change model with soil erosion model to predict future soil degradation and its on-site and off-site consequences. They firstly applied stochastic simulations to simulate future land changes based on the calculated afforestation and deforestation probabilities from historical land use maps. Then a spatially distributed soil erosion/sediment delivery model, SEDEM, was used to quantify the effects of afforestation or deforestation on soil

erosion and sediment delivery. Land use classes are not directly involved in calculating the soil erosion component of SEDEM. But the probability of land conversion and soil erosion rate are both affected by the same factor of slope gradient. The simulated future land use patterns were used as input for the sediment transport component in SEDEM, with a transporting capacity coefficient estimated for each land use class.

Reidsma et al. (2006) assessed the relationship between land use intensity and related biodiversity in agricultural landscapes. For land use simulation, an integrated model was applied to quantify the area changes in agricultural land use and the CLUE model was used for land use allocation. Biodiversity in this study was measured using the ecosystem quality, which is expressed as the mean abundance of species originally present in the natural ecosystems relative to their abundance in undisturbed situations. Following the land use scenarios, the ecosystem quality of agricultural landscapes can be calculated as conditioned by land use. Then the impact of agricultural land use changes on overall biodiversity was assessed by comparing the relative size of nature area and the average ecosystem quality of natural ecosystems.

1.5 Conclusions

Land changes are processes in which human and natural systems interact over space and time to reshape the earth's surface. They are both causes and consequences of global change that interacts with other components of the earth system. Land change science has recently emerged as a fundamental component of global environmental change and sustainability science. However, the complexity of land systems leads to many challenges for the research communities. Among the research components in land change science, land change modeling appears to be promising in improving our understanding of land use and land cover change as a coupled human-environmental system.

A wide variety of modeling approaches has been developed to simulate the processes of land changes. This chapter has reviewed some commonly used approaches, including statistical regression models, artificial neural networks (ANN), Markov chain modeling, cellular automata, economic models, and agent-based models (ABM). These different approaches are built upon various theoretical and methodological foundations. The order of these approaches generally represents the theoretical transition of land change modeling from aggregate to individual modeling frameworks. The best model to use depends on specific applications given their unique strengths and weaknesses.

The complexity for land change modeling is owing to their need to represent the spatiotemporal dynamics of the coupled human-environment systems. For coupling the factors from human and environmental systems, development of data integration techniques can help address the differences in spatial data. However, more comprehensive understanding and representation of the integrated processes within

the coupled system is one of the major challenges for land change modeling. To deal with the influences of spatial dependency, multi-scale analysis is necessary to address the Modifiable Areal Unit Problem (MAUP). Another important issue is to model the interactions and feedbacks among multiple scales in the land change processes. New models need to take into consideration of the multilevel processes and to integrate alternative perspectives into the existing modeling framework. In modeling land change processes, a temporally dynamic modeling framework is critical to capture the necessary behavior changes during the modeling time periods. Moreover, the factor of time lags needs to be considered to avoid biased simulation.

The advances in land change modeling offer great opportunities to study global environmental change in an integrated framework. The examples reviewed in this chapter should shed light on the progress of coupling land change modeling with other ecological modeling and analysis techniques for analyzing the interactions between land changes and other components of global environmental change. Many of the integrated frameworks are based on the use of simulated land use patterns or other land use/cover derived variables as input to the ecological models. More complex examples make use of the process-based models that integrate land change models and ecological models through individual decision-making using outputs from each model.

Acknowledgments The authors like to thank the Florida State University for the time release in conducting this work. The research was partially supported by the Florida State University Council on Research and Creativity, CAS/SAFEA International Partnership Program for Creative Research Teams of “Ecosystem Processes and Services”, the Natural Science Foundation of China through the grant “A Study on Environmental Impacts of Urban Landscape Changes and Optimized Ecological Modeling” (ID 41230633).

References

- Agarwal C, Green GM, Grove JM, Evans TP, Schweik CM (2002) A review and assessment of land-use change models: dynamics of space, time, and human choice. GTR NE-297. U.S.D.A. Forest Service, Northeastern Research Station, Newton Square
- Agarwal DK, Silander JA, Gelfand AE, Dewar RE, Mickelson JG (2005) Tropical deforestation in Madagascar: analysis using hierarchical spatially explicit, Bayesian regression models. *Ecol Model* 185(1):105–131
- Akin A, Clarke KC, Berberoglu S (2014) The impact of historical exclusion on the calibration of the SLEUTH urban growth model. *Int J Appl Earth Obs Geoinf* 27:156–168
- Aspinall R (2004) Modelling land use change with generalized linear models - a multi-model analysis of change between 1860 and 2000 in Gallatin Valley, Montana. *J Environ Manag* 72(1–2):91–103
- Batty M (2005) Agents, cells, and cities: new representational models for simulating multiscale urban dynamics. *Environ Plan A* 37(8):1373–1394
- Batty M, Xie Y (1994) From cells to cities. *Environ Plan B Plan Des* 21:31–38
- Bockstael NE (1996) Modeling economics and ecology: the importance of a spatial perspective. *Am J Agric Econ* 78(5):1168–1180

- Brown DG, Robinson DT (2006) Effects of heterogeneity in residential preferences on an agent-based model of urban sprawl. *Ecol Soc* 11(1):46
- Brown DG, Goovaerts P, Burnicki A, Li MY (2002) Stochastic simulation of land-cover change using geostatistics and generalized additive models. *Photogramm Eng Remote Sens* 68(10):1051–1061
- Camill P (2010) Global change. *Nat Educ Knowl* 3(10):49
- Clarke KC, Gaydos LJ (1998) Loose-coupling a cellular automaton model and GIS: long-term urban growth prediction for San Francisco and Washington/Baltimore. *Int J Geogr Inf Sci* 12(7):699–714
- Clarke KC, Hoppen S, Gaydos L (1997) A self-modifying cellular automaton model of historical urbanization in the San Francisco Bay area. *Environ Plan B Plan Des* 24(2):247–261
- Couclelis H (2001) Modeling frameworks, paradigms, and approaches. In: Clarke KC, Parks BO, Crane MP (eds) *Geographic information systems and environmental modeling*. Prentice Hall, Upper Saddle River, pp 36–50
- Evans TP, Kelley H (2004) Multi-scale analysis of a household level agent-based model of landcover change. *J Environ Manag* 72(1–2):57–72
- FAO (2010) *Global forest resources assessment*. Food and Agriculture Organization of the United Nations, Rome
- Gotway CA, Young LJ (2002) Combining incompatible spatial data. *J Am Stat Assoc* 97(458):632–648
- Haberl H, Erb KH, Krausmann F, Gaube V, Bondeau A, Plutzer C, Gingrich S, Lucht W, Fischer-Kowalski M (2007) Quantifying and mapping the human appropriation of net primary production in earth's terrestrial ecosystems. *Proc Natl Acad Sci U S A* 104(31):12942–12945
- Haith DA, Shoemaker LL (1987) Generalized watershed loading functions for stream-flow nutrients. *Water Resour Bull* 23(3):471–478
- Hoshino S (2001) Multilevel modeling on farmland distribution in Japan. *Land Use Policy* 18(1):75–90
- Howard DM, Howard PJA, Howard DC (1995) A Markov model projection of soil organic-carbon stores following land-use changes. *J Environ Manag* 45(3):287–302
- Hu ZY, Lo CP (2007) Modeling urban growth in Atlanta using logistic regression. *Comput Environ Urban Syst* 31(6):667–688
- Irwin EG, Bockstael NE (2002) Interacting agents, spatial externalities and the evolution of residential land use patterns. *J Econ Geogr* 2(1):31–54
- Jantz CA, Goetz SJ, Shelley MK (2004) Using the SLEUTH urban growth model to simulate the impacts of future policy scenarios on urban land use in the Baltimore-Washington metropolitan area. *Environ Plan B Plan Des* 31(2):251–271
- Jensen JR (1983) Biophysical remote-sensing. *Ann Assoc Am Geogr* 73(1):111–132
- Kerr S, Liu SG, Pfaff ASP, Hughes RF (2003) Carbon dynamics and land-use choices: building a regional-scale multidisciplinary model. *J Environ Manag* 69(1):25–37
- Lesschen JP, Verburg PH, Staal SJ (2005) *Statistical methods for analysing the spatial dimension of changes in land use and farming systems*. Lucc report series no. 7. International Livestock Research Institute/Lucc Focus 3 Office, Nairobi/Wageningen
- Li X, Yeh AG (2002) Neural-network-based cellular automata for simulating multiple land use changes using GIS. *Int J Geogr Inf Sci* 16(4):323–343
- Ligmann-Zielinska A (2009) The impact of risk-taking attitudes on a land use pattern: an agent-based model of residential development. *J Land Use Sci* 4(4):215–232
- Lin YP, Hong NM, Wu PJ, Lin CJ (2007) Modeling and assessing land-use and hydrological processes to future land-use and climate change scenarios in watershed land-use planning. *Environ Geol* 53(3):623–634
- Liu WG, Seto KC (2008) Using the ART-MMAP neural network to model and predict urban growth: a spatiotemporal data mining approach. *Environ Plan B Plan Des* 35(2):296–317

- Mahiny AS, Clarke KC (2012) Guiding SLEUTH land-use/land-cover change modeling using multicriteria evaluation: towards dynamic sustainable land-use planning. *Environ Plan B Plan Des* 39(5):925–944
- Miller JH, Page SE (2007) *Complex adaptive systems: an introduction to computational models of social life*. Princeton University Press, Princeton
- Muller MR, Middleton J (1994) A Markov model of land-use change dynamics in the Niagara region, Ontario, Canada. *Landsc Ecol* 9(2):151–157
- Openshaw S, Taylor PJ (1979) A million or so correlation coefficients: three experiments on the modifiable areal unit problem. In: Wrigley N (ed) *Statistical applications in the spatial sciences*. Pion, London, pp 127–144
- Parker DC, Manson SM, Janssen MA, Hoffmann MJ, Deadman P (2003) Multi-agent systems for the simulation of land-use and land-cover change: a review. *Ann Assoc Am Geogr* 93(2):314–337
- Reidsma P, Tekelenburg T, van den Berg M, Alkemade R (2006) Impacts of land-use change on biodiversity: an assessment of agricultural biodiversity in the European Union. *Agric Ecosyst Environ* 114(1):86–102
- Rindfuss RR, Walsh SJ, Turner BL, Fox J, Mishra V (2004) Developing a science of land change: challenges and methodological issues. *Proc Natl Acad Sci U S A* 101(39):13976–13981
- Sante I, Garcia AM, Miranda D, Crecente R (2010) Cellular automata models for the simulation of real-world urban processes: a review and analysis. *Landsc Urban Plan* 96(2):108–122
- Sohngen B, Mendelsohn R, Sedjo R (1999) Forest management, conservation, and global timber markets. *Am J Agric Econ* 81(1):1–13
- Steffen W, Sanderson A, Tyson P, Jager J, Matson P, Moore B III, Oldfield F, Richardson K, Schellnhuber H-J, Turner BL, Wasson R (2004) *Global change and the earth system: a planet under pressure*. Springer, London
- Stevens D, Dragicevic S (2007) A GIS-based irregular cellular automata model of land-use change. *Environ Plan B Plan Des* 34(4):708–724
- Torrens PM, Benenson I (2005) Geographic automata systems. *Int J Geogr Inf Sci* 19(4):385–412
- Turner BL, Moss RH, Skole DL (1993) Relating land use and global land-cover change: a proposal for an IGBP-HDP core project, IGBP-HDP report no 5. IGBP, Stockholm
- Turner BL, Lambin EF, Reenberg A (2007) The emergence of land change science for global environmental change and sustainability. *Proc Natl Acad Sci U S A* 104(52):20666–20671
- U.S. Global Change Research Program (2014). <http://globalchange.gov>. Accessed 21 June 2014
- Van Rompaey AJJ, Govers G, Puttemans C (2002) Modelling land use changes and their impact on soil erosion and sediment supply to rivers. *Earth Surf Process Landf* 27(5):481–494
- Veldkamp A, Fresco LO (1997) Reconstructing land use drivers and their spatial scale dependence for Costa Rica (1973 and 1984). *Agric Syst* 55(1):19–43
- Verburg PH (2006) Simulating feedbacks in land use and land cover change models. *Landsc Ecol* 21(8):1171–1183
- Verburg PH, Soepboer W, Veldkamp A, Limpiada R, Espaldon V, Mastura SSA (2002) Modeling the spatial dynamics of regional land use: the CLUE-S model. *Environ Manag* 30(3):391–405
- Vitousek PM (1994) Beyond global warming – ecology and global change. *Ecology* 75(7):1861–1876
- Walsh SJ, Crawford TW, Welsh WF, Crews-Meyer KA (2001) A multiscale analysis of LULC and NDVI variation in Nang Rong district, northeast Thailand. *Agric Ecosyst Environ* 85(1–3):47–64
- Wu JJ, Adams RM, Kling CL, Tanaka K (2004) From microlevel decisions to landscape changes: an assessment of agricultural conservation policies. *Am J Agric Econ* 86(1):26–41
- Xie YC, Batty M, Zhao K (2007) Simulating emergent urban form using agent-based modeling: Desakota in the suzhou-wuxian region in china. *Ann Assoc Am Geogr* 97(3):477–495
- Yang XJ, Lo CP (2003) Modelling urban growth and landscape changes in the Atlanta metropolitan area. *Int J Geogr Inf Sci* 17(5):463–488

Chapter 2

Modeling the Effects of Land Use Change and Climate Change on Stream Flow Using GIS and a Hydrological Model

Maochuan Hu, Bin He, Pingping Luo, Kaoru Takara, and Weili Duan

Abstract This paper reports our research effort aiming to investigate the applicability of integrating a hydrological model and the Hydrological Predictions for the Environment (HYPE) model with a geographic information system (GIS) to examine the effect of land use change and climate change on stream-flows with the Kamo River basin (KRB) located in the central Honshu island, Japan as a case study. The goal of this study was to provide important information for understanding water discharge variations as a basis to guide water resource managers in environmental change decisions in this river basin. This goal was accomplished by two steps (i) comparing HYPE-generated hydrographs for various meteorological data from history to present at current land use (S1 and S2); and (ii) comparing HYPE-generated hydrographs for historical and current land use scenarios at current climate (S3 and S4). The calibration and validation results suggest that HYPE performs well in the case study site for daily simulations. The results of S1–S2 indicate that with the impact of climate change, the trend of annual and seasonal stream flows at the Kamo River Basin outlet would decrease. However, there is no evidence to indicate that the flood risk would be decreasing. The results of S3–S4

M. Hu (✉)

Department of Civil and Earth Resources Engineering, Graduate School of Engineering, Kyoto University, Kyoto daigaku-Kastura, Nishikyo-ku, Kyoto 615-8530, Japan
e-mail: hu-maochuan@163.com

B. He • W. Duan

CAS Key Laboratory of Watershed Geographic Sciences, Chinese Academy of Sciences, Nanjing Institute of Geography and Limnology, Nanjing, China
e-mail: hebin@niglas.ac.cn; wlduan@niglas.ac.cn

P. Luo (✉)

Institute for the Advanced Study of Sustainability (UNU-IAS), United Nations University, Shibuya, Tokyo, Japan

Disaster Prevention Research Institute (DPRI), Kyoto University, Uji, Kyoto, Japan
e-mail: luoping198121@gmail.com

K. Takara

Disaster Prevention Research Institute (DPRI), Kyoto University, Uji, Kyoto, Japan
e-mail: kaoru.takara@gmail.com

© Springer Science+Business Media Dordrecht 2015

J. Li, X. Yang (eds.), *Monitoring and Modeling of Global Changes: A Geomatics Perspective*, Springer Remote Sensing/Photogrammetry, DOI 10.1007/978-94-017-9813-6_2

17

show that the conversion of forest, grass and agriculture (FGA) into urban area would induce high peak flows, a reduction in annual evaporation and an increase in annual surface runoff.

Keywords Land use change • Climate change • Hydrologic modeling • HYPE • GIS • Kamo River basin

2.1 Introduction

In the last decades, the relentless usage of fossil fuel, growth of population, migration to urban areas and consequent global climate change, land use transition not only induce hydrological cycle variation and increase the risk of water-related disasters also bring challenges to the current water management and planning efforts. Water authorities in many places have paid special attention to water management in order to mitigate the disaster risk. Understanding hydrological processes, especially in the context of climate change and land use change is necessary for water resources sustainable management.

A number of studies have been conducted on the impact of climate and land cover variations on water resources balance at catchments (Cuo et al. 2013; Cornelissen et al. 2013; Öztürk et al. 2013; Arheimer et al. 2012; Chu et al. 2012; Zhang et al. 2012; Delpla et al. 2009). Cuo et al. (2013) found that the upper Yellow River Basin hydrological regimes had undergone changes over the past decades as reflected by a decrease in wet and warm season stream flow, and annual stream flow due to climate change and human activity. Öztürk et al. (2013) showed the water budget was most sensitive to variations in precipitation and conversion between forest and agricultural lands but was less sensitive to the type of forest stands in the Bartın spring watershed, Turkey. However, hydrological responses to climate and land-use changes are different from place to place. It is necessary to conduct a study of hydrological variation under climate and land-use changes on the regions with few previous studies to provide valuable information for water management.

The basin of interest in this study, Kamo River basin (KRB), is the political and socioeconomic center of Japan in history and also a famous tourist attraction with about 1.5 million residents nowadays. The riverbank of Kamo River is popular with tourists and residents for many activities such as sightseeing during Sakura blooms (cherry blossoms), fishing and walking. These activities are sensitive to stream flow changes. To date, there has been limited research on discharge variation in this basin. Luo et al. (2014a) took a palaeoflood simulation in KRB and found that lower discharge and earlier peak discharge time were exhibited under historical land use. However, to what degree water discharge has been altered under climate and land use changes certainly merits further investigation.

Rainfall-runoff dynamics are a complex process affected by various factors: rainfall, temperature, vegetation etc. Many methods have been used to quantify hydrological variations to all kinds of driving factors in river basins (Swank and Crossley 1988; Singh and Gosain 2011; Beskow et al. 2012; Dixon and Earls 2012;

Dechmi et al. 2012; Koch et al. 2013). Swank and Crossley (1988) studied hydrological responses of deforestation and forestation from an early age using comparative tests method. Dixon and Earls (2012) examined the effects of land use change on a stream flow with a hydrological model. Hao et al. (2008) reports the variations of surface runoff under climate change and human activities in the Tarim River Basin by trend analysis of meteorological, socioeconomic and hydrological data. Among them, hydrological simulation is the most widely used method and modelling can be looked upon as an objective and repeatable method with which to interpolate and extrapolate knowledge in time and space between observations (Strömqvist et al. 2012). Also, the modelled data can be widely used by water authorities where measured data are not available for expert judgments.

This study, by applying a rigorously calibrated and validated process-based, integrated semi-distributed hydrology model over the KRB aims to identify the variations of stream flow at the outlet of the basin and to estimate the effects of climate change and land use transition on stream flow changes. The ultimate goal of this study is to provide important information for understanding water discharge variation, and guide water resource managers in environmental change decisions in the KRB.

2.2 Methodology

2.2.1 Study Area

The KRB is in the central part of the island of Honshu, Japan. The length of the river is about 31 km, flowing into Katsura River. The area of the basin is 210 km², ranging in elevation from 25 to 882 m, with average slope angles of about 25.7°. There is no weather station in the basin and the nearest station is Kyoto station (shown in Fig. 2.1). The annual precipitation from 1978 to 2008 at the Kyoto station is 1,491 mm and 84.3 % of precipitation is concentrated from March to October. The daily temperature ranges from -3.2 to 32.8 °C and annual mean temperature from 1978 to 2008 is about 16 °C.

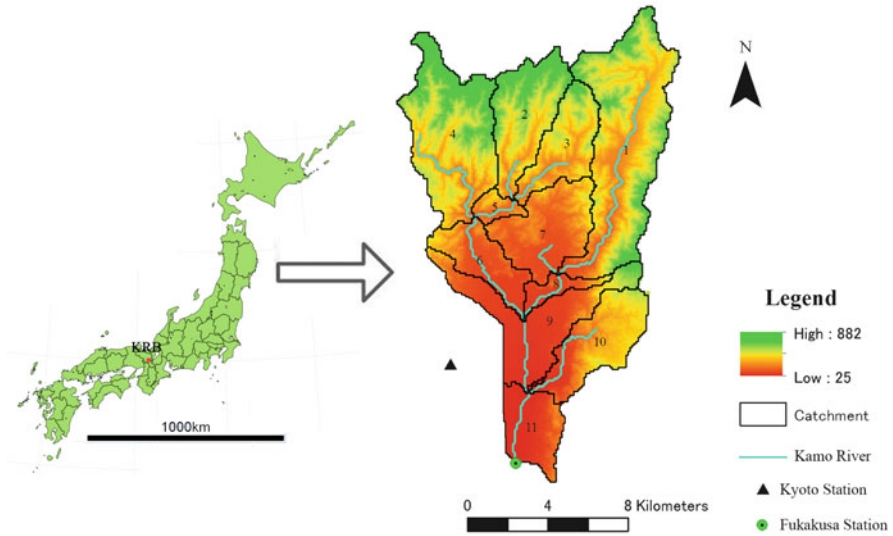


Fig. 2.1 Location of the study site: The Kamo River Basin (KRB) and a digital elevation model (DEM)

2.2.2 Model Description

The Hydrological Prediction for the Environment model (HYPE) was employed to investigate and understand the influences of climate and land use changes on KRB hydrology. HYPE is a process-based, temporally continuous, semi-distributed hydrology model, which integrates landscape elements and hydrological components along the flow paths (Lindstrom et al. 2010; Strömqvist et al. 2012). It has been applied in some regions of the world in a range of climate conditions and resolutions and existing studies have shown that it performed well in simulating stream flow (Strömqvist et al. 2009, 2012; Lindstrom et al. 2010; Arheimer et al. 2012; Jiang et al. 2013; Jomaa et al. 2013; Donnelly et al. 2014).

HYPE shares some similarities to the HBV (Bergström 1976), VIC (Liang et al. 1994) and SWAT (Arnold et al. 1998). The model partitions a basin into multiple sub-basins, which are further subdivided into a set of hydrological response units (HRUs) (Flügel 1995). HRU is determined by land use and soil type or other landscape characteristics such as elevation and slope. In this study HRUs are the combinations of land use and soils. Flows generated from each HRU in a sub-watershed are summed and routed through channels. HYPE model is based on the water balance in the soil profile and the simulating processes mainly include snowmelt, infiltration, surface flow, evapotranspiration, percolation, tile drainage, macro-pore flow and groundwater flow. The detailed calculation methods of each model component can be found in literature (Lindstrom et al. 2010).

2.2.3 Data Preparing and Model Setup

The meteorological data at Kyoto station is obtained from Japan Meteorological Agency and the daily data from 1979 to 2008 is used as input data to the model. The 100 m DEM of KRB and 100 m mesh land use data sheet of 2006 are from the Nation and Regional Planning Bureau of MLIT. The 1927 land use stems from the research of Luo et al. (2014b) (Shown in Table 2.2). The soil map of the KRB (from MLIT) is presented in Fig. 2.2a and there are six types and the percentage

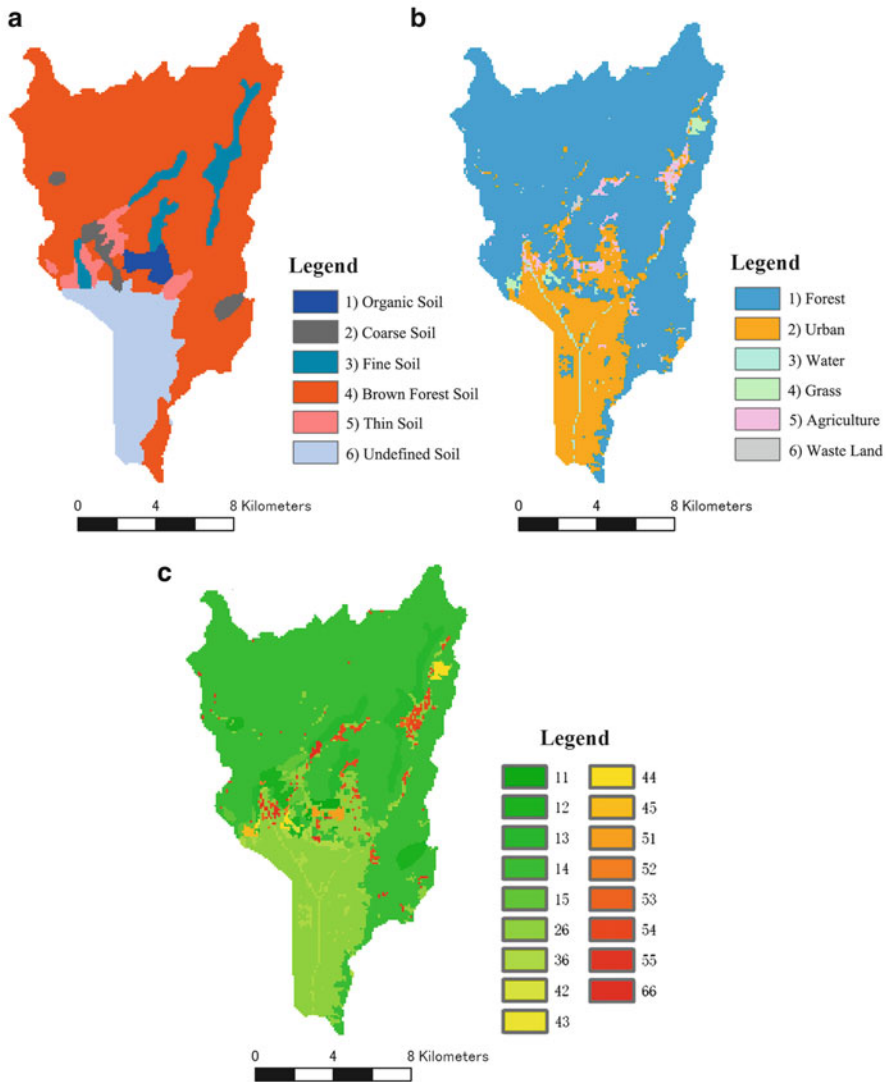


Fig. 2.2 (a) Soil type map (b) Land use map of 2006 (c) Hydrological response units (HRUs) map of 2006

distribution is: (1) Organic Soil (1.7 %), (2) Coarse Soil (2.4 %), (3) Fine Soil (5.4 %), (4) Brown Forest Soil (72.1 %), (5) Thin Soil (3.2 %), and (6) Undefined Soil (15.2 %). At the outlet of the basin, there is a monitoring station called Fukakusa station, which has discharge data of several years from 1991 to 1995 and from 2002 to 2005. The observed discharge data are used to calibrate and validate the model.

The DEM, land use and soil type data were processed in ArcGIS. Based on the DEM data and hydrological analysis tools of ArcGIS, the basin was divided into 11 sub-basins (Fig. 2.1). Hydrological response units were created by the combination land use and soil type maps using the tool of raster calculation. Figure 2.2c shows the distribution of HRUs in 2006. There are 18 HRUs in KRB. Each HRU is named with double-digit. The first digit means land use type and the second digit means the soil type.

After pre-processing in ArcGIS, the database files were prepared including meteorological, geographical, hydrological data, etc. And some parameters without observed data were set manually in general agreement with hydrological knowledge and literature values in the process of calibration and a HYPE project was built.

2.2.4 Model Calibration

The initial conditions used for the hydrologic models strongly influence the values of the parameters and predicted outcome (Flügel 1995; Dixon and Earls. 2012). In order to reduce the uncertainties over initial conditions, the beginning date of the simulation in the model is 1978.1.1 under calibration, validation and all scenarios. The model is calibrated and validated by comparing the simulated stream flow and observed stream flow on a daily basis for two different 3-year periods. The calibration period is from 2003.1.1 to 2005.12.31 and the validation period is from 1993.1.1 to 1995.12.31. Calibration of the model was carried out automatically with an aim of obtaining a good calibration results fit, but with the constraint that parameters should be in general agreement with hydrological knowledge and literature values. In these processes, Monte Carlo simulation method is used. The performance of the calibrated parameters was evaluated by Nash-Sutcliff efficiency (NSE). The NSE is commonly used in hydrological modeling. It measures the efficiency of a model by relating the errors to the variance in the observations. A perfect fit corresponds to $NSE = 1$, whereas a naive model that uses the mean value results in $NSE = 0$. The NSE efficiency is usually evaluated over a certain time period (n time steps) for one basin at a time. The equation for NSE is as follows:

$$NSE = 1 - \frac{\sum_{i=1}^n (O - S)^2}{\sum_{i=1}^n (O - \bar{O})^2} \quad (2.1)$$

where O and S are the observed and simulated data, respectively, and n is the total number of data records.

Monte Carlo simulation is a broad class of computational algorithms that rely on repeated random sampling to obtain numerical results; typically one runs simulations many times over in order to obtain the distribution of an unknown probabilistic entity. In the structure of HYPE, there is a module of Monte Carlo simulation. The work of modelers is to assign the intervals and tolerance values of calibrated parameters. Then the parameters are automatic calibrated in the model with the task of Monte Carlo simulation.

2.2.5 Climate Trends Analysis

The Mann Kendall test (MKT) was applied in this study to analyze the monotonic trend of annual and monthly precipitation and mean temperature from Kyoto station. MKT is a non-parametric statistical procedure used to test for trends in time series data (Yu et al. 1993). The null hypothesis in the Mann-Kendall test is that the data are independent and randomly ordered, i.e. there is no trend or serial correlation structure in the time-series (Hamed and Rao 1998). For independent and randomly ordered data in a time-series x_i $\{x_i, i = 1, 2, \dots, n\}$, the null hypothesis H_0 is tested on the observations x_i against the alternative hypothesis H_1 , where there is an increasing or decreasing monotonic trend (Yu et al. 1993). According to the condition of $n \geq 10$, the S variance is described according to Eq. 2.2 below:

$$\text{Var}(S) = \frac{n(n-1)(2n+5) - \sum_{i=1}^e (t_i-1)(2t_i+5)}{18} \quad (2.2)$$

where e is the number of tied groups and t_i is the number of data values in the i_{th} group.

The statistical S test is given as follows:

$$S = \sum_{e=1}^{n-1} \sum_{i=e+1}^n \text{sgn}(x_i - x_e) \quad (2.3)$$

where

$$\text{sgn}(\varphi) = \begin{cases} 1 & \varphi > 0 \\ 0 & \varphi = 0 \\ -1 & \varphi < 0 \end{cases} \quad (2.4)$$

The normal approximation Z test by using the statistical value S and the variance value $\text{Var}(S)$ is written in the following form:

$$Z = \begin{cases} \frac{S - 1}{\sqrt{\text{Var}(S)}} & \text{if } S > 0 \\ 0 & \text{if } S = 0 \\ \frac{S + 1}{\sqrt{\text{Var}(S)}} & \text{if } S < 0 \end{cases} \quad (2.5)$$

For the normal approximation Z test and the cumulative standard normal distribution ϕ , if $|Z| \leq Z_{\alpha/2}$ and $\phi(Z_{\alpha/2}) = \alpha/2$, then the H_0 hypothesis is adopted. Where α is the probability level of rejecting the null hypothesis H_0 when it is true? The value of Z shows the statistical trend. If $Z < 0$, it indicates a decreasing trend and if $Z > 0$ it indicates an increasing trend (Luo et al., 2011).

2.2.6 Impact Assessment of Meteorological Variation

To evaluate the effects of climate change, the meteorological data from 1979.1.1 to 2008.12.31 was selected. Coupling the meteorological data and land use map of 2006, two scenarios were established (as follows). The influences of climate variations were quantified by the trend analysis of the simulation results from 1979 to 2008 and comparing the simulation results of two scenarios.

S1: 1979–1988 climate and 2006 land use

S2: 1999–2008 climate and 2006 land use

2.2.7 Impact Assessment of Land Use Variation

To evaluate the effects of land use change, the meteorological data from 2003.1.1 to 2005.12.31 was selected. Coupling the meteorological data and land use maps of 2006 and 1926, two scenarios were established (as follows). The influences of land use changes were quantified by comparing the simulation results of the two scenarios.

S3: 1927 land use and 2003–2005 climate

S4: 2006 land use and 2003–2005 climate

Table 2.1 Trend analysis for precipitation and temperature

Item	Period	Mann-Kendall	
		Z	P
Precipitation	Annual	-0.91	N
	Dry seasonal	0.61	N
	Flood seasonal	-1.2	N
Temperature	Annual	3.35	Y
	Dry seasonal	1.75	Y
	Flood seasonal	3.25	Y

Z is statistics of MKT; Y means significant at the level of $P = 0.05$

2.3 Results

2.3.1 Variations of Precipitation and Temperature

The trend analysis was carried out for the annual, flood (from March to October) and dry (from November to next February) seasonal rainfall and mean temperature. The annual and seasonal results were shown in Table 2.1. The annual and flood seasonal rainfall trended to decrease and dry seasonal rainfall trended to increase during 1979–2008. However, the trend is statistically insignificant. Whereas annual and seasonal mean temperature increased significantly.

2.3.2 Land Use Changes

Table 2.2 exhibited the land use types of KRB in 2006 and 1927. From 1927 to 2006, the trend is forestland, grassland and farmland converted into urban areas. The city sprawled twice larger (from 10.7 % of total area to 21.3 %). Rising rate is almost up to 100 %. The decreased areas of forest, grassland and farmland are 4.3 km², 5.56 km² and 9.09 km², respectively. However, since the proportions of grass and agriculture field in KRB are small, there are 80.6 % of grass and 69.1 % of agriculture field disappeared.

2.3.3 Calibration and Validation of the HYPE Model

The HYPE model was calibrated for a 3-year period from 2003 to 2005 using the land use of 2006 and the resulting parameters were kept constant for the validation step for a different period from 1993 to 1995. Figure 2.3 provides observed and HYPE simulated daily stream flow at the KRB outlet for calibrated and validated periods. Simulations during the calibration period captured the observed evolution well for daily time scales and in general, the observed peak flow was higher than the modelled peak flow. Deficiencies in HYPE simulations included mismatched peak flows for some days of extreme rainfall and underestimation of base flow, which

Table 2.2 Classification and the area for each land use type for 2006 and 1927

ID	Name	Land use area (km ²)		Changed area from 1927 to 2006 (%)	Rising rate from 1927 to 2006 (%)
		1927	2006		
1	Forest	138.21	133.91	-2.4	-3.1
2	Urban	19.3	38.35	10.6	98.7
3	Water	1.67	1.911	0.1	14.4
4	Grass	6.9	1.34	-3.1	-80.6
5	Agriculture field	13.16	4.07	-5	-69.1
6	Waste Land	1.12	0.78	-0.2	-30.4

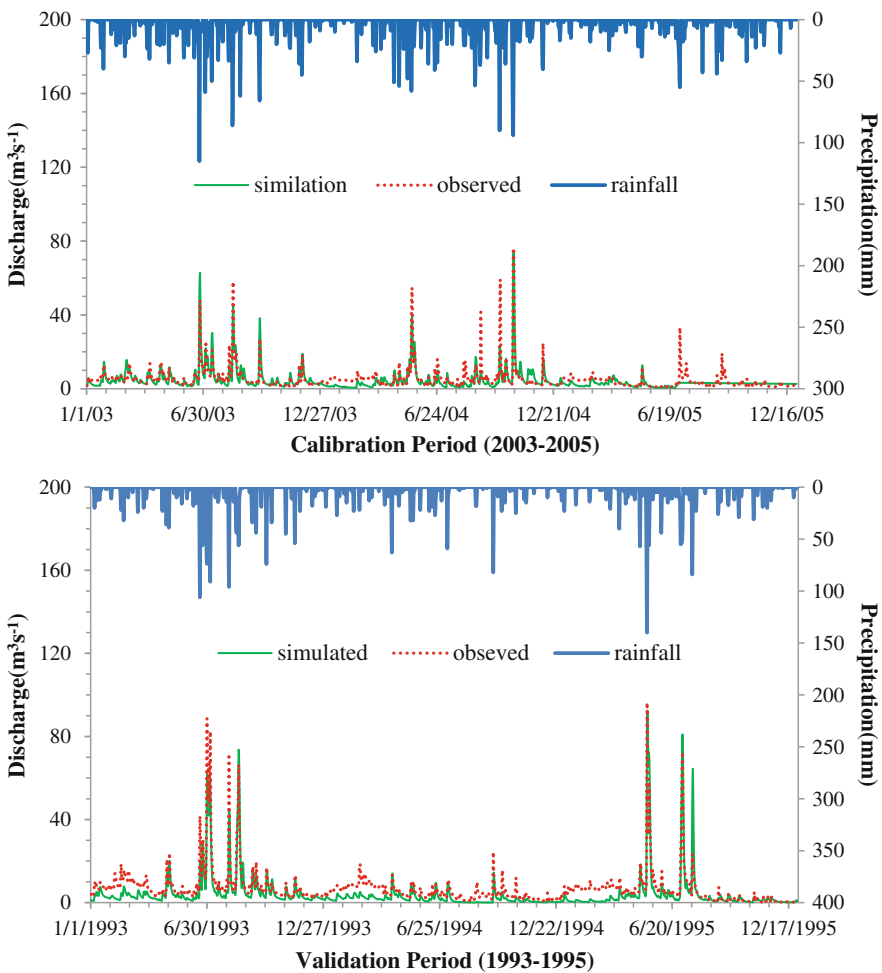


Fig. 2.3 Observed and simulated daily streamflows at the outlet of the KRB and rainfall data over the calibration and validation periods

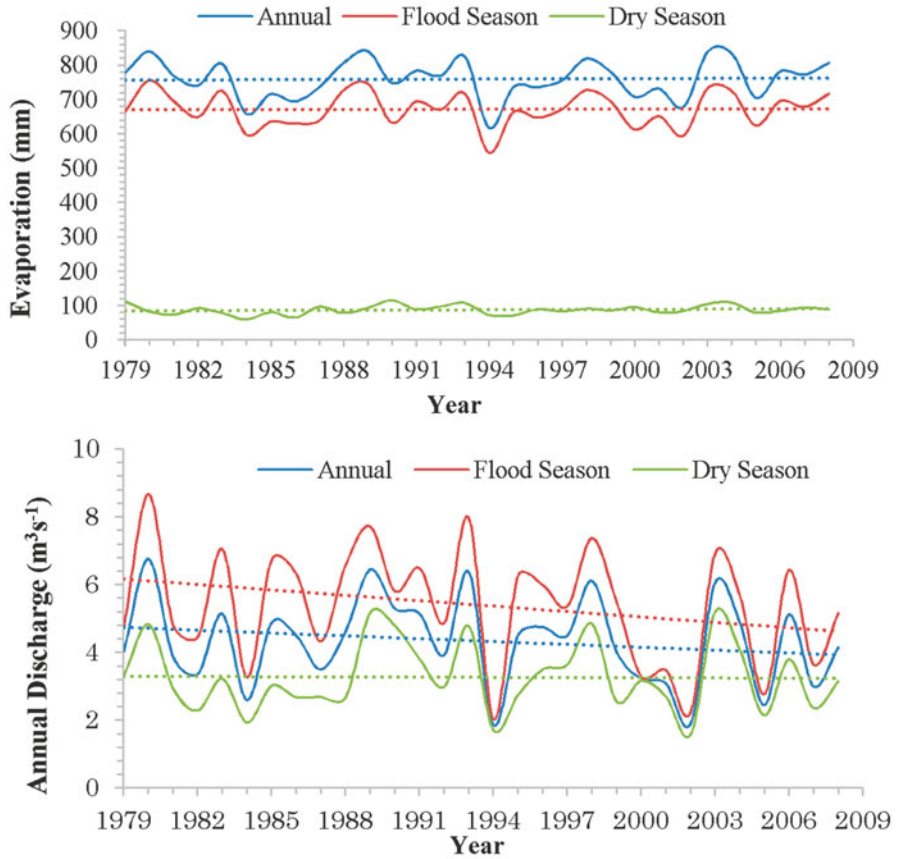


Fig. 2.4 Simulated annual and seasonal evaporation and outlet stream flows in the KRB

was most due to errors in rough soil data. There is no initial soil observed data (field capacity, wilting point, etc.). During the calibration period, correlation coefficients and NSE were 0.87 % and 0.72, respectively.

During the validation period, simulated daily stream flow at the outlet of the KRB also captured the observed evolution well. Peak flow simulations improved in comparison to the calibration period. However, base flow still was underestimated. Correlation coefficients and NSE were 0.83 % and 0.69, respectively.

2.3.4 Climate Change Impact

Figure 2.4 displays simulated annual and seasonal evaporation and outlet stream flow at the KRB. The figure illustrates that linear trends occurred in evaporation and

Table 2.3 Differences of mete-hydrology between S1 and S2 in the KRB

		Precipitation	Temperature	Surface runoff	Evaporation
S1	Annual	1,519.2	15.3	361	754.3
	Flood season	1,320.8	19.6	327.7	672.2
	Dry season	198.4	6.5	33.4	82.1
S2	Annual	1,388.1	16.2	314.8	763.4
	Flood season	1,142	20.6	261.2	672.9
	Dry season	246.1	7.4	53.7	90.7
S2–S1	Annual	−131.1	0.9	−46.2	9.1
	Flood season	−178.8	1	−66.5	0.7
	Dry season	47.7	0.9	20.3	8.6

Table 2.4 Simulated daily stream flow at the outlet of KRB for two scenarios

Stream flow	S1	S2
AAMD (m^3s^{-1})	69.7	54.8
MD (m^3s^{-1})	102.2	104.5

stream flow. Annual and flood seasonal stream flows trended to decrease from 1979 to 2008, whereas dry seasonal stream flow had rising trends. Annual and seasonal evaporation seemed to increase. In addition, stream flow and evaporation have same trends as precipitation and temperature (Table 2.1 and Fig. 2.4), respectively.

Table 2.3 shows average annual precipitation, mean temperature, stream flow, surface runoff and evaporation in two scenarios of S1 and S2. It reveals that annual and flood seasonal rainfall and surface runoff of S2 decreased 131.1 mm and 46.2 mm respectively in comparison to S1. Evaporation rose 9.1 mm and 0.7 mm, respectively. In arid season, however, rainfall, surface runoff and evaporation all increased.

In addition, the comparison of average annual maximum daily (AAMD) stream flows and maximum daily (MD) stream flows of S1 and S2 demonstrates that AAMD stream flow of S1 was higher, while MD stream flow of S2 was larger (Table 2.4).

2.3.5 Land Use Change Impact

Computed daily stream flows of scenarios 3 and 4 are shown in Fig. 2.5. There are large differences on peak flows. The peak flows of S4 are much higher than the ones of S3. It can be concluded that the conversion of forest, grass and agriculture (FGA) into urbanization would lead to high peak flow.

Furthermore, annual and monthly differences of surface runoff and evaporation between S3 and S4 were estimated (shown in Figs. 2.6 and 2.7). With respect to evaporation, the conversion of FGA into urbanization would result in a reduction of about 35 mm, 36 mm and 31 mm for the years of 2003, 2004 and 2005. Greatest

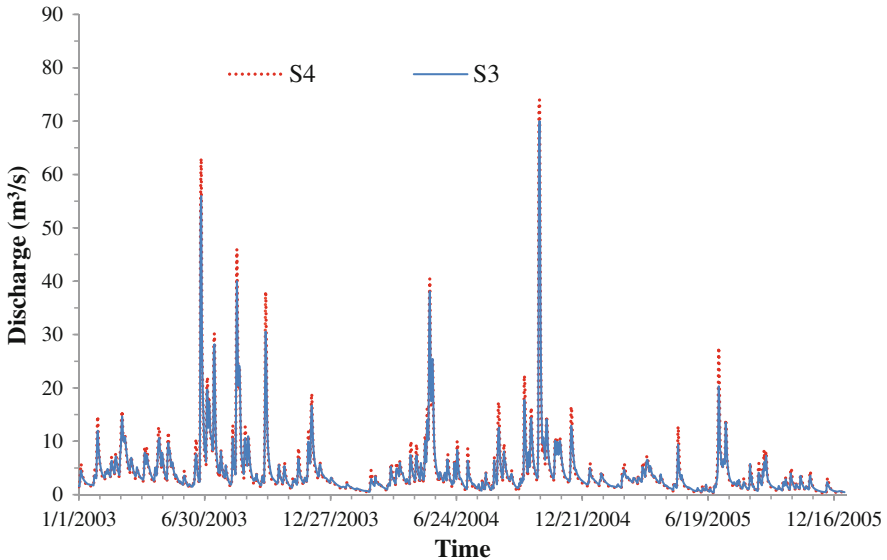


Fig. 2.5 Simulated daily stream flows at KRB outlet according to S3 and S4

differences were presented in summer. On the contrary, the surface runoff increased about 39 mm, 35 mm and 23 mm for the years of 2003, 2004 and 2005 under the conversion of FGA into urbanization.

2.4 Discussion

2.4.1 Model Uncertainty

Model uncertainties are resulted from uncertainties in input data, model dynamics and physics and parameter values. To reduce uncertainties of the HYPE model and examine the suitability of HYPE for impact studies in the KRB, the model was calibrated and validated at the gauge of the basin outlet. The calibration and validation results showed that HYPE simulations matched observations well in various periods. Although this ensures that HYPE is applicable in this basin, it is recognized that HYPE displayed relatively large biases in terms of base flows that were most likely due to lack of soil hydrology data (field capacity, wilting point, etc.). These biases, however, should not compromise our analysis results since the analysis was based on the comparison of different simulated scenarios and was not focused on base flow.

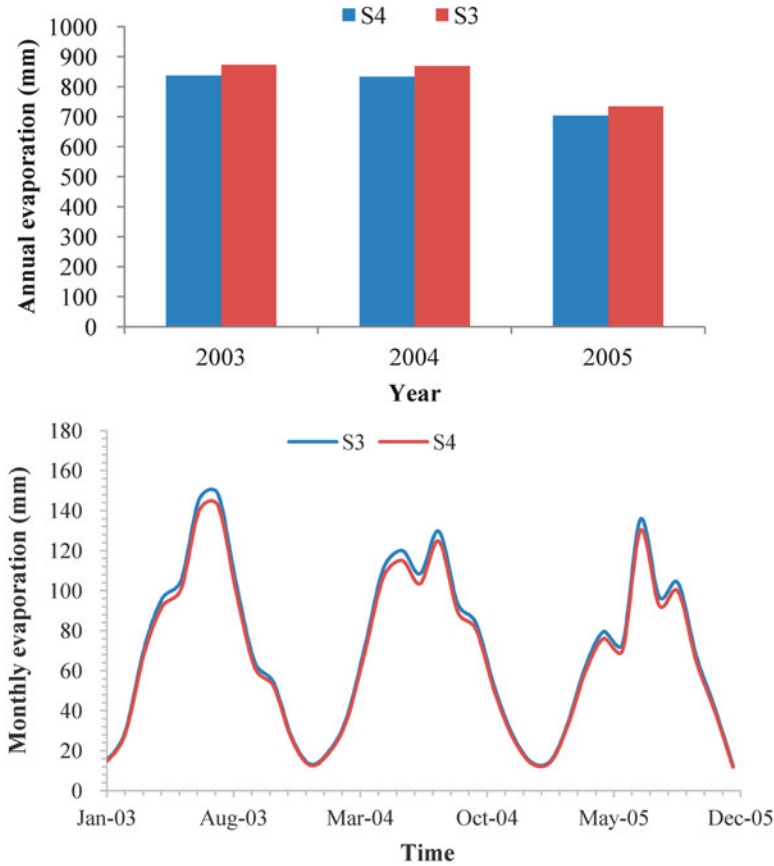


Fig. 2.6 Annual and monthly evaporation of S3 and S4 in the KRB

2.4.2 Results Discussion

As we know, runoff has positive correlation with rainfall and negative relation with evaporation. The simulated results of annual and flood seasonal stream flows demonstrate the relationships. In arid season, rainfall, evaporation and surface runoff had the same rising trends revealing that the contributions of rainfall to runoff were larger than these of evaporation to runoff. Similar results had been reported in some regions suffered homogeneous climate changes (Hao et al. 2008; Zhang et al. 2012). But, there is no evidence to prove the flood risk decreasing in the KRB since there is no decreasing trend in the MD stream flow in the two different periods, though AAMD stream flow decreased from S1 to S2 and annual stream flows seemed to reduce.

The results of stream flow variations under land use changes indicate that the conversion of FGA into urban area resulted in high peak flow, a reduction in annual

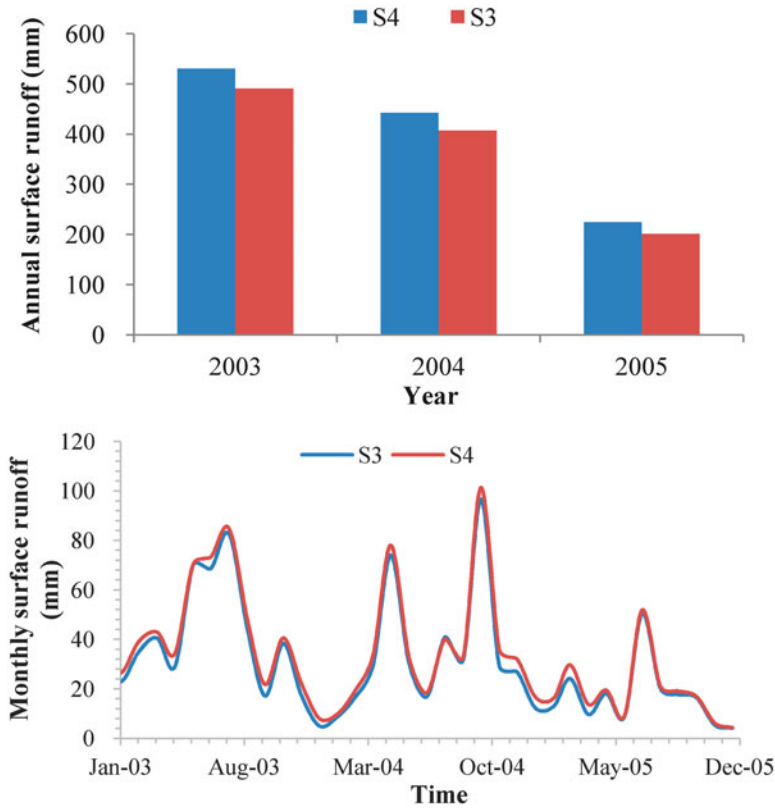


Fig. 2.7 Annual and monthly surface runoff of S3 and S4 in the KRB

evaporation and an increase in annual surface runoff. This phenomenon might be explained by different hydrological processes in different land-use types. With contrast to FGA area, infiltration in urban area is much smaller as most of urban areas are covered by impervious surface, which leads to quick runoff and reduce infiltration. Luo et al. (2014a) took a Palaeoflood research in KRB and found similar results that higher and earlier peak discharge was driven by urbanization. In addition, the conversion of FGA into urban area presented a greater effect on evaporation in summer. This phenomenon can be explained by the research of Tucci (2003) that precipitation distribution over the year allowed identification (if it exists) of water availability for evapotranspiration. As the temperature and precipitation in these months are the highest in a year in the KRB, there is water availability in the soil during periods with the greatest potential evapotranspiration. Beskow et al. (2012) reported the similar behavior that stream flows presented the greatest differences among different scenarios of land use in the wettest and hottest months like December, January, February, March, and April in Brazil. There are no apparent characteristics with respect to monthly surface runoff differences of S3

and S4, which are inconsistent with monthly evaporation changes. These might be due to the rainfall density and extreme rainfall and it requires more research.

2.5 Summary and Conclusion

In this study, the influences of climate and land use changes on stream flow in the KRB were estimated by an application of the HYPE model. The simulated stream flow and its components were shown to vary among different scenarios of climate and land use. Comparing the results of climate scenarios revealed that annual and flood seasonal stream flows had a decrease trend from 1979 to 2008, whereas dry seasonal stream flow trended to rise. However, there is no evidence to prove the flood risk decreased. The differences of simulated outputs between land use scenarios exhibited the conversion of FGA into urban area induced high peak flow, a reduction in annual evaporation and an increase in annual surface runoff. In general, the results of this study provide important information for understanding hydrology variation, and guide water resource managers to plan decisions associated with water environmental change.

Acknowledgments The authors thank the supports from the “One Hundred Talents Program” of Chinese Academy of Sciences and National Natural Science Foundation of China (No. 41471460). The first author would like to thank China Scholarship Council (CSC) for his PhD scholarships.

References

- Arheimer B, Dahne J, Donnelly C (2012) Climate change impact on riverine nutrient load and land-based remedial measures of the Baltic sea action plan. *Ambio* 41(6):600–612
- Arnold JG, Srinivasan R, Muttiah RS, Williams JR (1998) Large area hydrologic modeling and assessment part I: model development. *J Am Water Resour Assoc* 34(1):74–89
- Bergström S (1976) Development and application of a conceptual runoff model for Scandinavian catchments. Ph.D. thesis, SMHI reports RHO no. 7, Norrköping
- Beskow S, Norton LD, Mello CR (2012) Hydrological prediction in a tropical watershed dominated by oxisols using a distributed hydrological model. *Water Resour Manag* 27(2):341–363
- Chu JG, Zhang C, Wang YL, Zhou HC, Shoemaker CA (2012) A watershed rainfall data recovery approach with application to distributed hydrological models. *Hydrol Process* 26(13):1937–1948
- Cornelissen T, Diekkrüger B, Giertz S (2013) A comparison of hydrological models for assessing the impact of land use and climate change on discharge in a tropical catchment. *J Hydrol* 498:221–236
- Cuo L, Zhang Y, Gao Y, Hao Z, Cairang L (2013) The impacts of climate change and land cover/use transition on the hydrology in the upper Yellow River Basin, China. *J Hydrol* 502:37–52
- Dechmi F, Burguete J, Skhiri A (2012) SWAT application in intensive irrigation systems: model modification, calibration and validation. *J Hydrol* 470:227–238
- Delpla I, Jung AV, Baures E, Clement M, Thomas O (2009) Impacts of climate change on surface water quality in relation to drinking water production. *Environ Int* 35(8):1225–1233

- Dixon B, Earls J (2012) Effects of urbanization on streamflow using SWAT with real and simulated meteorological data. *Appl Geogr* 35(1–2):174–190
- Donnelly C, Yang W, Dahne J (2014) River discharge to the Baltic Sea in a future climate. *Clim Chang* 122(1–2):157–170
- Flügel W (1995) Delineating hydrological response units by geographical information-system analyses for regional hydrological modeling using PRMS/MMS in the drainagebasin of the River Brol, Germany. *Hydrol Process* 9:423–436
- Hamed KH, Rao AR (1998) A modified Mann-Kendall trend test for autocorrelated data. *J Hydrol* 204(1–4):182–196
- Hao XM, Chen YN, Xu CC, Li WH (2008) Impacts of climate change and human activities on the surface runoff in the Tarim River basin over the last fifty years. *Water Resour Manag* 22(9):1159–1171
- Jiang S, Jomaa S, Rode M (2013) Identification and uncertainty analysis of a hydrological water quality model with varying input data information content. EGU General Assembly Conference Abstracts
- Jomaa S, Jiang S, Rode M (2013) Effect of increased bioenergy crop production on hydrological response and nutrient emission in central Germany. EGU General Assembly Conference Abstracts
- Koch S, Bauwe A, Lennartz B (2013) Application of the SWAT model for a tile-drained lowland catchment in North-Eastern Germany on subbasin scale. *Water Resour Manag* 27(3):791–805
- Liang X, Lettenmaier DP, Wood EF, Burges SJ (1994) A simple hydrologically based model of land surface water and energy fluxes for general circulation models. *J Geophys Res Atmos* (1984–2012) 99(D7):14415–14428
- Lindstrom G, Pers C, Rosberg J, Stromqvist J, Arheimer B (2010) Development and testing of the HYPE (Hydrological Predictions for the Environment) water quality model for different spatial scales. *Hydrol Res* 41(3–4):295–319
- Luo P, He B, Takara K et al (2011) Spatiotemporal trend analysis of recent river water quality conditions in Japan. *J Environ Monit* 13:2819–2829
- Luo P, Takara K, Apip, He B, Nover D (2014a) Palaeoflood simulation of the Kamo River basin using a grid-cell distributed rainfall run-off model. *J Flood Risk Manag* 7(2):182–192
- Luo P, Takara K, Apip, He B, Nover D (2014b) Reconstruction assessment of historical land use: a case study in the Kamo River basin, Kyoto, Japan. *Comput Geosci* 63:106–115
- Öztiürk M, Copty NK, Saysel AK (2013) Modeling the impact of land use change on the hydrology of a rural watershed. *J Hydrol* 497:97–109
- Singh A, Gosain AK (2011) Climate-change impact assessment using GIS-based hydrological modelling. *Water Int* 36(3):386–397
- Strömqvist J, Dahne J, Donnelly C, Lindström G, Rosberg J, Pers C, Yang W, Arheimer B (2009) Using recently developed global data sets for hydrological predictions. *IAHS Publ.* 333
- Strömqvist J, Arheimer B, Dahné J, Donnelly C, Lindström G (2012) Water and nutrient predictions in ungauged basins: set-up and evaluation of a model at the national scale. *Hydrol Sci J* 57(2):229–247
- Swank WT, Crossley DA (1988) *Forest hydrology and ecology at Coweta*. Springer, New York
- Tucci CEM (2003) Processos hidrológicos e os impactos do uso do solo. In: Tucci CEM, Braga B (eds) *Climae recursos hídricos no Brasil*. ABRH, Porto Alegre, pp 31–76
- Yu YS, Zou SM, Whittemore D (1993) Nonparametric trend analysis of water-quality data of rivers in Kansas. *J Hydrol* 150(1):61–80
- Zhang A, Zhang C, Fu G, Wang B, Bao Z, Zheng H (2012) Assessments of impacts of climate change and human activities on runoff with SWAT for the Huifa River Basin, Northeast China. *Water Resour Manag* 26(8):2199–2217

Part II
Monitoring and Analyzing of Urban
Dynamics

Chapter 3

Combining Different Data Sources for City Growth Analysis and Architectural Heritage Mapping

Karel Pavelka and Eva Matoušková

Abstract This chapter discusses our research effort on city growth documentation and architectural heritage mapping through the combined use of maps and sketches, declassified satellite data, aerial photographs and modern satellite imagery. For analyzing city growth, an extended time frame is preferred. We selected the City of Erbil in northern Iraq as a case study site due to its extensive expansion and the lack of information documenting this process. The area of Iraqi Kurdistan has been inhabited for at least 6,000 years and the sandy dry landscape has retained many monuments there. The centre of Kurdistan is the rapidly growing City of Erbil. Shortly after World War II the city had about 40,000 inhabitants, but now the number is close to two million. This area has become the commercial, cultural, agricultural and administrative centre of the region. The world-renowned historical monument known as the Citadel Al-Qala is located at Erbil's historic center. This project has focused upon the mapping of the Al-Qala citadel using satellite images and aerial photographs. After creating a vector-based planimetric map, we have further produced a virtual three-dimensional model covering the valuable parts of the Citadel with textures, along with a citadel information system. Our work has demonstrated the utility of combining various sources of data for temporal analysis of city growth and for heritage mapping.

Keywords Erbil • 3D documentation • Land use change • City growth • Satellite images • Aerial photos • Maps • Sketches

K. Pavelka (✉) • E. Matoušková

Department of Geomatics, Faculty of Civil Engineering, Czech Technical University in Prague, Thákurova 7, 166 09 Prague 6, Czech Republic
e-mail: pavelka@fsv.cvut.cz; eva.matouskova@fsv.cvut.cz

© Springer Science+Business Media Dordrecht 2015

J. Li, X. Yang (eds.), *Monitoring and Modeling of Global Changes: A Geomatics Perspective*, Springer Remote Sensing/Photogrammetry, DOI 10.1007/978-94-017-9813-6_3

37

3.1 Introduction

3.1.1 Data and Techniques

Civilian satellite data have become available for more than four decades. There is a possibility to use declassified satellite images from the US Corona system (and other orbital systems) for city growth documentation, particularly for the period when civilian satellite data were not available. Before civilian satellites were launched, we relied upon only on maps and sketches. It can be helpful not only for documenting the past of a city, but also for sustainable urban development, especially in developing countries, where the growth of cities is at a very rapid pace and there aren't precise urban plans, maps or documentation. The use of historical and on-going satellite images can partially solve this problem.

3.1.2 Land Use Change and Urbanization

Monitoring urban development generally includes the use of evolving documentation techniques for built up areas (Pavelka and Svatušková 2008). Monitoring the artificial environment components associated with human economic activities began in the 1970s of the twentieth century (Tayyebi et al. 2014). It has become necessary due to an attempt to monitor particular irreversible changes of Earth's surface, which are mostly unsustainable. The development of contactless data collection methods such as remote sensing and photogrammetry has made possible for rapid, inexpensive and reproducible analyses of the area of interest. At first, the monitoring of vegetation based on multispectral satellite data had been enforced. Nowadays, there is more than 40 years of civilian satellite multispectral images ready to be used. This data can be employed to analyze the change in the past.

A number of multinational projects has been conducted because environmental problems are not bounded by state borders. For example, the Black Triangle includes the devastated area across the boundaries of the Czech Republic, Germany and Poland (www.gisat.cz). Other projects were focused on the vegetation monitoring in connection to scientific research or for agricultural purposes (e.g., MARS, Monitoring Agriculture with Remote Sensing). Many of these projects were supported by the CEO (The Centre for Earth Observation, Ispra, Italy).

In addition to the built environment monitoring, some general projects dealing with the global development or the condition of Earth's surface have been conducted (e.g., Tayyebi and Pijanowski 2014). In the last 20 years, projects aiming to monitor urban development with the use of geoinformation system have also emerged (Tayyebi et al. 2013a, b). This enables better decision-making for planning future development (Antonson et al. 2010). In particular, the airborne laser scanning method is a relatively new area, offering the possibility to monitor complex urban areas.

3.1.3 Land Cover

The most famous European project for global land cover monitoring is the CORINE Land Cover (CLC) program (Kopecká et al. 2014). It was created as a project under the EU Phare Topic Link on Land Cover in the early 1990s and is well known as a unique map composition based on satellite image interpretation. It is a homogeneous database firstly covering the European Union countries and later (in the late 1990s) the entire Europe.

The image outputs were prepared in the form of topographic map sheets at the scale of 1:100,000. These map sheets were created by using georectified Landsat Thematic Mapper (TM) data acquired between 1990 and 1993. Individual types of Earth's surface by the interpretative key of the CORINE program were performed by hand drawing on transparent foils and fitted with a three-digit identification code. Five basic classes were created, including artificial surfaces, agricultural areas, forest and semi natural areas, wetlands, and water bodies, which were further sub-divided up to the third level. All interpreted areas had been defined as a closed polygon with a minimum area of 25 ha and in case of linear elements with minimum width of 100 m. Transparency with interpretations were scanned and vectorised secondarily into GIS vector layers, where polygon codes were converted into the attribute form. For the attributes colours were assigned and entire layer had been printed as a thematic map with legend, where the colour code characterized land cover type that had been classified on the earth's surface. Given the success of the primary mapping, it was decided to extend the interpretation into the time scale. The aim of this study was to define temporal changes in the Corine Land Cover database and to explain the reason of the alteration.

3.1.4 Large City Dynamics Monitoring

Data from the CORINE Land Cover can be used to assess the expansion of large European cities. For smaller cities the information from this data source at the scale of 1:100,000 is insufficient. Also the geometric accuracy of the employed satellites (namely Landsat and SPOT) may not be sufficient for detailed mapping of smaller cities. Satellite data were not available before 1972, with an exception of some declassified spying satellite images whose information potential has not been fully appreciated. Another option is, of course, to include contemporary maps or aerial photographs. Historical aerial photographs as well as declassified spying satellite images vary in quality, and usually it is difficult to find technical and photogrammetric parameters for these images. Unlike the maps, however, these photographs can be very useful to examine the recent past with details.

3.1.5 Monitoring Urban Dynamics

In 1998 the project called “Monitoring Urban Dynamics” was launched by the Centre of Earth Research, Ispra, Italy (CEO, The Centre for Earth Observation). The aim was to compare four periods of city growth with satellite images or aerial photographs. The project was based on photogrammetric method to produce orthophotos with subsequent manual processing of image content under interpretative key of CORINE Land Cover program, with an enlargement in the first class, i.e. urban areas. The goal was to find information potential of archive black and white aerial photographs, as well as opportunities and challenges of the thematic content processing.

As already mentioned, the manual interpretation technology had to be used because automatic procedures cannot be employed due to a high number of classification classes and their specifications. For example, it would be extremely difficult to separate simply parks, cemeteries, orchards and small vegetation or various kinds of industrial areas through an automatic approach. But this can be done with the combined use of the experience of an interpreter and auxiliary information such as maps and logical relations for the analysis. In general, automatic classification of historic black and white images is not quite capable (Halounová 2004a, b, c).

3.1.6 Photogrammetry and 3D Modeling

Photogrammetry encompasses image measurement and interpretation methods to derive the object shape and location from one or more photographs (Remondino and El-Hakim 2006). It is a non-contact measurement technique. A primary purpose of photogrammetry is to construct a three dimensional model of an object in digital or paper formats (Apollonio et al. 2013). The photograph or image represents a store of information, which can be re-accessed at any time.

The photogrammetric process can be a source of 3D data of an object (e.g. building), and 3D visualization methods can generate a photo realistic representation of the data (Grussenmeyer et al. 2008). These models have many practical applications, in addition to the purely aesthetic effect. In close-range photogrammetry, the main focus of 3D visualization is the representation of photogrammetrically reconstructed real objects (Hanzalová and Pavelka 2013). In general, 3D graphics or CAD programs are used here to provide additional elements and graphical editing of the 3D data (Gruen 2008).

3.2 The Study Area

3.2.1 *Iraq*

The area of today's Iraq is the location where the first important civilizations formed (Ur 2000). Due to its long history, Iraq is very rich in valuable historical monuments. Large numbers of monuments are unfortunately in very bad condition. An urgent need for the preservation of the most important architectural monuments arose in connection with the post-war reconstruction of the Iraqi culture. Architectural monuments were often damaged by the war and today even simple preservation is impossible. Most of the architectural monuments suffered from a lack of interest from state authorities under Saddam Hussein's Republic and their condition, even before the latest conflict ended, can be described as critical in most cases. Now, after the fall of Saddam Hussein's regime, the situation, unfortunately, isn't any better; many areas are affected with civil or religious unrest. Research, restoration of monuments and their protection is often very dangerous and, together with the lack of finance and experts, impossible. In the last decade, many Czech expeditions aimed for archaeological prospection and monuments restoration were carried out in the northern part of Iraq, in the Kurdish autonomous region. Iraqi Kurdistan has its own regional government in Erbil, which is the largest city in the north, after Mosul.

3.2.2 *Erbil*

Erbil is an ancient, originally Sumerian and Assyrian city located in the foothills of the eastern Iraqi mountains. Historically, the centre of Erbil (ancient Urbilum, Arbela, Arbil or Irbil) belongs to the towns with the longest settlement continuity in the world. The city began to gain importance during the Neo-Assyrian period (tenth to seventh centuries BC). The city was a religious centre of the cult of Istar of Arbela (Porter 2004) and a royal residence of King Assurbanipal (669–627 BC). Nearby was also a legendary battle in which Alexander the Great defeated the Persians and opened the way to Babylon; the headquarters of Persian King Dareios was directly in Erbil (the Battle of Arbela or Gaugamela, 331 BC).

Erbil (also written as Arbil or Irbil and known as Hewler) is the capital city of the Erbil (Kurdish Hewler) province and is located in the northeastern part of Iraq, 77 km east of Mosul. Thanks to its location, it is the big Kurdish commercial, cultural, agricultural and administrative centre of the region, with a main railway station and the intersection of roads leading to Turkey, Syria and Iran. Erbil is the fourth largest city in Iraq after Baghdad, Basra and Mosul. In the historic centre of Erbil, there are two world-renowned historical monuments: the minaret Choli and the Al-Qala Citadel (Morris 1979) The Al-Qala Citadel in Erbil is one of the oldest continuously inhabited urban settlements in the world. According to ICOMOS data,

8,000 years of inhabitation are proven in this unique urban concentration, making it the longest inhabited place on the Earth. This has been made possible by rich water sources, still available today, which have never dried out in recorded history. Before World War II water was 2–5 m below the surface, but today it is pumped from a depth of 40 m and its quantity is not enough. Erbil is dependent on other sources. Before World War II, Erbil had approximately 40,000 residents, whereas now there are about 1.5 million, mostly Kurdish Muslims and a minority of Christians.

The historic city centre, the Citadel of Erbil (Al-Qala Citadel), is formed by a vast complex of buildings and narrow streets enclosed by town walls (Sahid 2004). The fortified Citadel itself is situated on an artificial elevation of 28–32 m high above the surrounding countryside, which is now the city of Erbil. Well-known records and archaeological finds proved layers of Assyrian, Akkadian, Babylonian, Persian and Greek Pre-Arabic settlements. Fortifications were primarily built in the twelfth century.

The Citadel is spread out over more than 10 ha of land. Among more than 800 buildings, traditional one to two-story residential houses with internal atriums, brick walling and clay roofs on joists prevail. Only some of them have a basement. About half of them are privately owned, while the rest are owned by regional and central governments. Slightly more than 20 of the residential houses are, according to the ICOMOS (International Council on Monuments and Sites) data, in an acceptable and well-kept condition. The rest are in urgent need of restoration. Many important buildings have rich interior decorations with painted niches and ornaments, carved doors and arcades supported by timber or marble columns. The biggest houses have their own historic fountains in the central atria. The Citadel has two mosques and one public bath. Important parts of the fortification are three gates – two of them, the new and old gate, allow entrance of vehicles, and one is for pedestrians. The construction of two access roads (and also one pedestrian path) has caused progressive changes in the tell topography. New access roads were created, so the state of hillsides has been changed. Slope tells hillsides are strongly affected by erosion, which is mainly caused by poor Citadel drainage (Justa and Houska 2006).

Before Iraq became a totalitarian state, the citadel was the traditional centre of the city and the province. It was a place where prominent families, representing the intellectual elite of Erbil, lived. The citadel was divided into a few quarters formed by palaces and burgess brownstone houses. They were concentrated around the public bath and two mosques.

During the totalitarian era, almost all palaces were bulldozed and the main gate of the fortress was torn down (in the 1980s a new, modern, main portal was built in a retro style). The medieval bath and the mosques were concreted. The original inhabitants were expelled and the citadel was settled by refugees from mountain villages that were destroyed by the regime. Seven thousand provincial refugees changed the rich fortress to a slum (Justa 2005). The last known renovation took place in the year 1982, when the State Board for Antiquities and Heritage renovated seven houses.

Since 2007, the number of inhabitants in the historic city centre was still very high (5,000–5,500). Vehicular access was permitted to the Citadel. The construction of an access road and two pedestrian paths caused progressive erosion of the western slope of the elevation. Water for households is pumped to steel tanks on the roofs and water is distributed by gravity. Electrical wiring is situated on the posts and the houses elevations. There is no sanitation in the Citadel, and the remaining inhabitants use dry toilets, which have all the expected health and hygiene hazards. The regional government of Kurdistan is looking for opportunities to revitalize and preserve this unique complex for the future when a significant rise in tourism is expected. For this reason, almost all residents were evicted in 2009. At the moment, the number of inhabitants of the historic city centre is negligible. Unfortunately, the state of the citadel began degrading, rapidly causing the deterioration of buildings. The Al-Qala Citadel in Erbil is one of the world's most endangered historic sites (based on UNESCO's data). In 2014 Al-Qala Citadel was added to the UNESCO's World Heritages List.¹

The practical work is part of an international project of the post-war reconstruction and regeneration of Iraq. It is made in connection with the Cultural Heritage Regeneration Assistance Program of the Iraqi Republic, approved by the Government of the Czech Republic. The content of the project is the comprehensive assistance in the preservation and revitalization of the historic city centre and assistance in the preservation and renovation of the architectural monuments of Erbil city.

The Czech Republic was part of the project represented by the Gema Art Group, Czech Technical University in Prague (Musílek et al. 2001), University of West Bohemia in Pilsen and University of Pardubice. The Iraqi partners were the Ministry of Culture of the Republic of Iraq, official representatives of the region and the city, religious leaders of the region, and Salahaddin University in Erbil (Nováček et al. 2008). Between the years 2006 and 2010, many Czech expeditions to Erbil had been conducted to document the basic monuments, investigate the archaeological conditions, and find appropriate technology for objects restoration (Rezníček et al. 2013). In the frame of the previous project of post-war reconstruction, the Czech firm GemaArt realized together with other specialists the photogrammetric and geodetic measurement of Al-Qala Citadel. Inside the citadel was reconstructed one building used as a Czech cultural centre (located near the French centre).

In Erbil, the next valuable historic object after Al-Qala citadel is the Choli minaret (Nováček 2011). It is from fourteenth century and it is a last part of the oldest Kurdish mosque. It is ranked among the most significant Kurdish monuments and its condition is alarming because of the tilting of the upper part of the minaret. The lower seven-angle part of the minaret is ca 12 m high. The circular part of the minaret is about 24 m high and shelters a double spiral staircase. As stated by the

¹ Erbil citadel has been inscribed on the World Heritage List on June 21, 2014. <http://whc.unesco.org/en/news/1155>.

owner, the thickness of wall is around 36 cm. The minaret lost its upper part a long time ago. Since then, it has been opened for weathering and particularly for rainwater leakage. A large extent of precious historic fragments of renderings and embossments were identified on the lower part of the object. A particularly large-scale discovery of stucco decoration was found in niches of the tower. All fragments of stucco decorations were seriously affected by weathering and mechanical damage. The Choli minaret was in detail documented using photogrammetry and other geodetic methods (Pavelka et al. 2007; Králová 2008) and after this was successfully restored by the Czech firm GemaArt (Justa 2005).

Other expeditions were focused on the northern part of Kurdistan, Dalal Bridge in Zakho (Pavelka 2009) and on archaeological research in Amadíja or on lost cities on the Turkish border (Nováček and Šůvová 2011).

3.3 Methods

3.3.1 Data Sources

Many sites have been irretrievably destroyed due to the Erbil growth and a proper study of the historical information may revive it again. There are old sketches, maps, aerial and satellite images for this purpose (Ioannides et al. 2012).

3.3.1.1 Old Maps and Sketches

Only very few of older maps and sketches were available. Processing of these old materials are difficult, although they have mostly historical values (Fig. 3.1a). Some information is of course important for our aim.

3.3.1.2 Aerial and Terrestrial Photographs

In Iraq, there are no modern photogrammetric aerial photographs at disposal. A few interesting old photos have been preserved, like photo in Fig.3.1b – it shows the original south gate, which was destroyed during Saddam Husain's regime and a bridge over a deep wadi that no longer exists today (Verhoeven et al. 2012). On Fig. 3.2a the best-preserved aerial photo with a lot of details is shown; aerial camera parameters are unknown (Wilson 2000). This photo is one from the only preserved stereo-pairs, taken during the Royal Air Force mission in January 1951. This stereo-pair is archived in the John Bradford papers in the Pitt Rivers Museum, University of Oxford, no.1998.296.67 and 68. A collection of oblique aerial images gives some added details. As example oblique's aerial images from 1973 (Fig.3.2b) and from 1933 (Fig. 3.3) have been found (Wilkinson 2008).

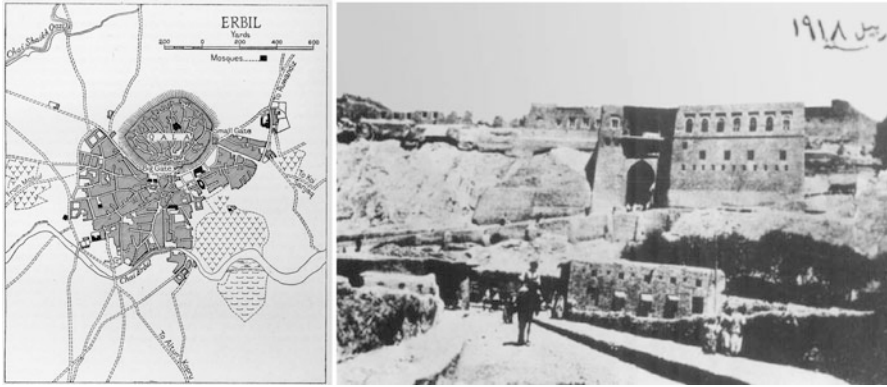


Fig. 3.1 (a) (left) – a map of Erbil (1944); (b) (right) – South gate of the Al-Qala citadel in Erbil on a photo taken in 1918 by an unknown author



Fig. 3.2 (a) (left) – an aerial photo of Bradford (1951); (b) (right) – an oblique aerial photo of the Al-Qala Citadel; major changes can be seen on this photo (destruction of the central part of Citadel and main entry; 1973)

3.3.1.3 Military Satellite Images

Although civilian satellite data became available since early 1970s, better data in terms of image resolution from some improved sensors, such as Landsat Thematic Mapper (TM) and SPOT High Resolution Visible (HRV), have become available for a much shorter period of time. These data may not be sufficient for some studies that need to look backwards for a long period, such as urban growth since the World War II. Given these limitations, the declassified satellite images from 1960s to 1970s can provide a very good information source to look into the past. For areas where there are no other historical image data, it is important to include geo-data sources. Note that military satellite data with 1–3 m spatial resolution acquired in 1960s are at our disposal. Since later 1990s, satellite images with 1 m resolution



Fig. 3.3 An oblique aerial photo of the Citadel in 1933 (Erbil archive)

have become available. However, the quality of scanned declassified analogue image data is not very high for some early-date images, such as the Multispectral Scanner (MSS) images from the first Landsat (see Fig. 3.4).

Satellite images from 1968, 1973, 1975 and 1980 were used (see Figs. 3.4 and 3.5). These declassified satellite images are freely available from <http://edcns17.cr.usgs.gov/EarthExplorer/>). The Corona satellite system (KeyHole-4B) represents many types of satellites and cameras. The image from 1968 was taken on 16.8. using AFT 70 mm stereo high-resolution camera on black and white film and its quality is very good. Images from other years (1980-07-07, 1975-06-19, 1973-12-23) were taken using KeyHole-9 on 9 × 18 in. black and white film with theoretical resolution of about 6–9 m and they quality is worse.

For our work, it was necessary to search through hundreds of images on the USGS server and find suitable data. From selected images it was necessary to create cuts within a relevant area of the Erbil city. The next step was to logically enhance the images (filtration, interpolating, etc.); the quality of scanned analogue film data was in many cases not very high. After this, cuts were transformed to control points and processed to the vector data.



Fig. 3.4 (a) (left) – Corona satellite system (KH-4B); 16.8.1968; (b) (right) – details of the citadel – geometrical resolution approximately 3 m; very good quality (Source: USGS)



Fig. 3.5 Erbil on declassified satellite images (Source: USGS). (a) (left) – 1973-12-23; (b) (middle) – 1975-06-16; (c) (right) – 1980-07-07

3.3.1.4 Scientific Satellites

A new type of satellite data for non-military use became available after 1972 (Landsat 1, spatial resolution 80 m) but a spatial resolution of approximately 1 m was achieved at the end of the 21st century. However, Landsat images do not provide sufficient spatial resolution for detailed mapping and monitoring. The new generation of commercial satellites such as IKONOS, QuickBird, WorldView or GeoEye provides images with excellent quality and sufficient resolution for detailed mapping of small cities. In this study, satellite images were used for the Citadel base plain map creation. The processed image was geometrically rectified with 16 ground control points and converted into a vector map using single photogrammetrical method. Landsat 7 (2000-06-19), IKONOS (2005-05-12) and QuickBird (2005-08-23) data were used (Pavelka and Svatušková 2008).

3.3.2 *Methods Used for Documenting City Growth*

At the beginning of the analysis digital editing of aerial and satellite images (*Geomatica*, *PhotoShop* software) and image data transformation using the *Topol* software was conducted. Automatic classification may not be suitable for black and white aerial or satellite images, and this is especially true when a poor quality image is employed. Based on the extension of textural signatures the classification has been improved, but this technology seems not to be able to provide a fine classification. A primary visual interpretation using the *Topol* software was done. It runs in two steps – vectorisation and interpretation. Homogenous areas were manually vectorised. For the interpretation a simplified and modified classification key from the Corine Land Cover was elected. In this case it is primarily a demonstration of research possibilities of urban growth (Muhmmad 2004).

The method of single-image photogrammetry with collinear transformation was used (Pavelka 2001). When more than four control points were found and implemented, the adjustment at individual point deviations from the ideal state was found. Achieved deviations varied between 15 and 20 m on the ground control points for the declassified satellite images from a relatively flat area (theoretical geometrical resolution depends on the quality and satellite system; it can be 10 m or better for high quality and resolution images). Better results cannot be achieved without image orthogonalization. Due to the character of this project the absolute accuracy is not the main factor. The main objective was to evaluate the content of images on a case project that demonstrates the potential of this technology.

The main challenge was the image quality, which varies greatly. Images from the 1970s have been worse from a radiometric point of view even after digital image processing. In terms of evaluating the condition and type of vegetation unambiguously these images are not suitable for such work because panchromatic range does not give a good alternative to separate classes using classification and the number of classes is very hard to recognize. Either additional information about the landscape (e.g. archive maps) or multispectral images should be used. Unfortunately these images are not available for older data. The classification of high quality black and white aerial photographs into core classes (various types of built-up areas, roads, fields, low vegetation outside the agricultural fields, forests of different ages, isolated trees, water) achieved an accuracy of 86–93 % class depended. Experiments were made using recognition software based on object-oriented classification with help of newly calculated channels (Halounová 2004a, b, c).

Theoretically, it would be logical to start from the oldest images and to expand the vector database to rectify based on visible changes. The procedure was necessary to reverse because the latest images are of the best quality. There is a sufficient amount of additional material and the possibility of multispectral images for the new images. It is also possible to assume that the character of some essential parts hasn't changed fundamentally. The final task was to choose a suitable interpretive key from the Corine Land Cover.

Content of the photographs were interpreted as closed polygons which formed each area. Those were assigned an attribute that categorized all areas as a type of code. As in the Corine project the smallest interpreted elements of about 1 ha or linear elements with a width of 20 m were defined (it is necessary to set a generalization limit at this stage). The resulting classification images were not possible to overlay and thus created exact differences between individual years. The problem was the different size of the scanned area. For example, in 1951 an image of the city centre without the outside city parts was the only one available, whereas from the earlier period there were only sketches without the wider neighborhood. Interpreted elements analysis was performed approximately in the area around the city for the elements that clearly belonged to the urban areas (parks, buildings, etc.), i.e. not losses of arable land. A full analysis would require cropping all the interpretations made by the smallest of them and find out a comprehensive acreage for each of the included classification classes. Given the purpose of demonstration analysis selected classes for the entire area of the city were performed.

3.3.3 Creating a Base Map of the Al-Qala Citadel

The Citadel is spread out over more than 10 ha of land (300–350 m in diameter). It is a classic case of adapted hillock – “tell”. The height of hillock averages to about 30 m around flat surroundings. No maps or plans of Citadel were at our disposal – only a copy of a cadastral plan from 1920 was available. Complex documentation of this object during a short expedition was not possible. For this reason, the terrestrial photogrammetry and satellite images were used.

In 2007, the vector plan of the Citadel was created based on aerial photos and satellite data (supplemented and improved in 2010). On the other hand we have processed photogrammetrical images into a virtual 3D model of the Citadel fortification and the valuable objects inside (a big part inside was damaged and the inhabitanancies are provisory – slum). The last part of this project was the creation of an information system for the Citadel, which can be used for all information storage.

In the research and preservation of cultural heritage in Erbil, it is necessary to take consideration of the rapid development and lack of documentation of things such as maps and especially the older city status. As was mentioned above, the city, after World War II, had about 40,000 residents while today the population is more than 1.5 million. These information have been notified us by the governorate of the city of Erbil in 2010 and also by consultation on local cultural heritage authorities. About the postwar Erbil population other publications are written (Justa and Houska 2006; Muhmmad 2004).

After the war in Iraq and the emergence of the Kurdish autonomous region, experienced a markedly accelerated development mainly due to capital inflows from abroad has been achieved. This enormous city growth brings many negatives.

A number of historically valuable sites have been destroyed through quick construction. The majority of finances is intended for economic activity. Planned, responsive and sustainable development of the city is very problematic and hints inter alia on lack of information about the state of the city (actual maps and plans).

3.3.3.1 Photogrammetry

A calibrated digital reflex camera (Canon 20D) with 8 MPix resolution was used for the photogrammetric survey. A wide-range 22 mm lens was employed for terrestrial images and a 17 mm lens was used for aerial photographs. Terrestrial images were taken during several days in different times of the day to avoid the influence of sun and shadows. Approximately 1,000 terrestrial photographs of the Citadel's fortification and interior were acquired. Of course, not all photographs were processed using intersection photogrammetry.

Terrestrial images taken from peripheral communication were not sufficient for 3D model creation, so aerial images had to be acquired. Considering the fact that Iraq is a no-flight zone, it was very hard to perform aerial imaging. Historical photographs do not exist or are not available, so finally a short flight by an American army helicopter was arranged. During this flight more than 80 photographs of the Citadel's fortifications were taken and then used for intersection photogrammetry. Unfortunately no perpendicular images of the interior were acquired, so QuickBird satellite images were used for basic photo plan and vector plan of the Citadel.

In the case of the new mapping of the Al-Qala Citadel, the intersection photogrammetry was used as a base photogrammetric method for the creation of the 3D model. It means that about 150 terrestrial and 80 aerial images (see Figs. 3.6 and 3.7) around the Citadel were selected. Only a part (images with good intersecting axis) from this set was processed in Photomodeler software to the 3D model. Only good visible outside facades and big houses inside were processed in real 3D. Next, parts of the Citadel were constructed from a plain vector map (Höhle 2013).

3.3.3.2 Satellite Images

Unfortunately, no perpendicular images of the interior were acquired during the helicopter flight, so QuickBird satellite images were used for the basic photo plan and vector plan of the Citadel (see Fig. 3.8). Histogram adjustments, filtration methods and resampling to 25 cm pixel size were performed on the satellite image.

3.3.3.3 Geodetic Survey

The interior of the citadel is a set of temporary shelters and building ruins that are connected by winding aisles no more than 1–2 m wide. The axis of the Citadel is a



Fig. 3.6 Details of aerial photos from a helicopter flight (2006) with provisory created control point for photogrammetrical mapping (Photographed by K. Pavelka in 2006)



Fig. 3.7 Settlement tell and citadel (qal'a) of Erbil; an aerial view from southwest (Photographed by K. Pavelka in 2006)



Fig. 3.8 Creating of a virtual model – texturing

main street with width from 5 to 10 m. The only bigger buildings are palace-like and located on the right side of Citadel's new main entrance. Roofs of these buildings were used as survey stations and as ground control points for aerial imaging. A total of 16 survey stations and 600 detailed survey points were measured.

On selected points, a GPS survey was conducted in order to transform the data into geographic coordinates. A Trimble 5,000 total station with self-reflective laser and GPS Trimble instruments were used for measurements. A geodetic point field had been calculated and adjusted with a standard error of position $m_{xy} = 20,32$ mm, with an average standard error of adjusted elevation $m_h = 15,05$ mm. These results are sufficient for photogrammetric work and for following geodetic survey inside the Citadel.

3.3.3.4 Data Evaluation and 3D Model Creation

The evaluation of available data and 3D model creation was performed using intersection photogrammetry methods. Stereoscopy methods could not be used due to the absence of perpendicular stereo pairs of the Citadel's interior. Intersection photogrammetry is more time consuming than stereo photogrammetry because it is necessary to find a single point on two or more oriented images and to ascertain its image coordinates. When dealing with a smaller amount of detailed points and a lower complexity of the objects as in the case of the Citadel's building facades, this work can be done with no difficulties. The only problem was the large number of photographs, so high-performance computer technology had to be used. Before final processing, photographs had to be categorized and only the best ones were

used for the analysis. For a better orientation of the project the fortification had been divided into 18 work packages. The orientation and processing of images had been performed using PhotoModeller Pro software developed by Canadian company Eos Systems Inc.

Relative orientation components were calculated using aerial images completed with closely selected terrestrial images. Twenty-three images covering the entire object had been oriented at the beginning. Photographs with fine resolution and with maximum overlap were preferred. Tie points that connected were selected on fortification facades, building roofs in interior and in surrounding terrain (hillsides, low walls and communication under the Citadel). The relative orientation had been extended by 11 photographs in order to enlarge intersections between images and for better processing of the chosen objects inside the Citadel.

Absolute orientation on previously surveyed and adjusted ground control points followed. Quantity and distribution of ground control points had to be analyzed. Fourteen ground control points were chosen for the absolute orientation computations (see Fig. 3.9). The computed position error oscillated around 10 cm. For accuracy improvement, 19 terrestrial images perpendicular to the facades were added. These images were equally distributed around the Citadel's perimeter. It was found that best results are given when 10–20 connecting tie points are equally distributed around an image. Computation in PhotoModeller had to be closely watched and problems were solved by changing point configuration, deleting points with high residual error, deleting points with small intersection angle, adding new points and image replacements. A total of 53 images were oriented and were the

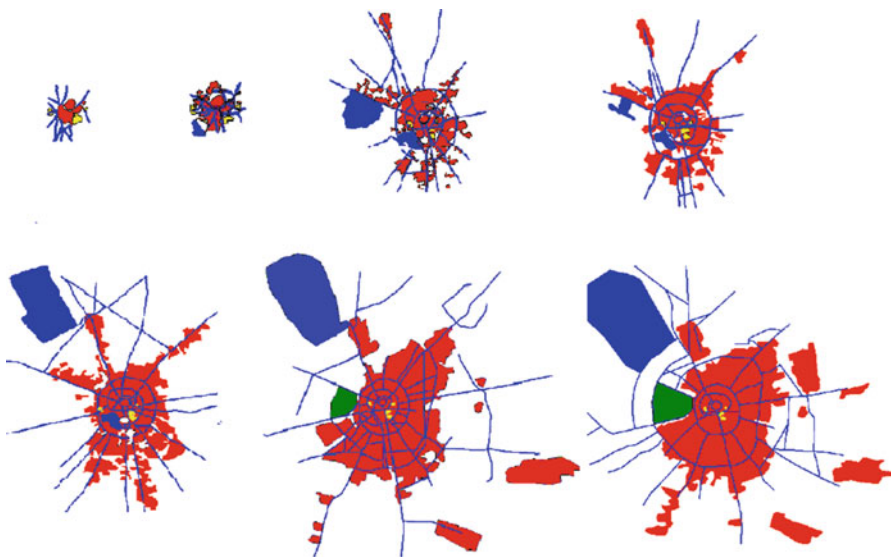


Fig. 3.9 Progress of the city growth (Erbil: 1944, 1951, 1968, 1975, 1980, 2000, 2012). *Red*-urban area; *green*-parks; *yellow*-cemetery; *blue*-streets, train station and airport (new dominant after 1980)

base for detailed point processing. The result is a line 3D model of the fortification. The final point accuracy when using 53 photographs varies from several centimeters' to 0.5 m depending on point position. Lower accuracy occurs on interior points and on points with a small beam intersection angle.

3.3.3.5 Vector Plan Creation

The survey of the entire Citadel interior by classical geodetic measurements is hardly achievable. Part of it had been surveyed from building roofs; other parts were processed from satellite images. No convenient images for vector plan creation were acquired from the army helicopter flight due to its high speed (combat type helicopter) and low flight height. Even if the flight height had been sufficient many details were distorted or hidden. Due to this fact, an archived QuickBird image with four multispectral channels (R, G, B, NIR) and one panchromatic channel had been used. The resolution was 2.4 m in multispectral and 0.65 m in panchromatic channel and the image was acquired on 2005-08-23. Pan sharpening together with filtration methods and resampling to 25 cm pixel size had been performed. The scene quality was excellent and together with geodetic survey and PhotoModeller results these data were used for basic plan of the Citadel (see Fig. 3.10).

The next necessary step was to transform the satellite data to geodetic coordinates using ground control points measured by geodetical survey. Polynomial high-level transformation based on number of ground control points was performed. Due to problems with PhotoModeller data transformation, affine transformation had been used for different type data merging. The deviations vary between 10 and 30 cm, which are sufficient when the resolution of satellite image is taken into account.

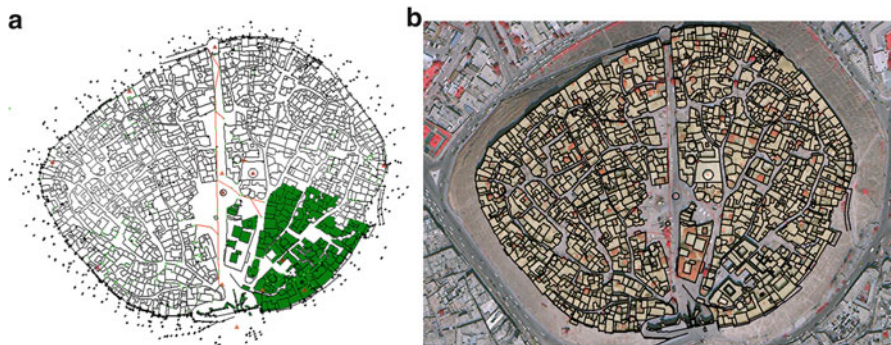


Fig. 3.10 (a) Scheme of control points and measured data: *black* (Photomodeler), *green* (total station), *red* (control and geodetic points), *black lines* (vectorisation of satellite image, 8/2007), *red lines* (electric line); (b) vector processing of the Al Qala Citadel

3.3.4 Citadel Information System

A virtual model of the citadel was created based on image data processing (Meyer et al. 2007). Terrestrial, aerial and satellite data has been used. All 3D constructions were created in Photomodeler software and supplemented and edited in AutoCAD with original textures (see Fig. 3.11). After processing, the model was transferred using an interchanging format to a newly established virtual information system (.dxf to .wrl). The base map of the Al Qala Citadel was made from a QuickBird satellite image which was digitally enhanced.

The information system was also partially developed in Aalborg University, Denmark during an Erasmus internship (Höhle 2013; Králová 2008). It consists of a 3D model of the citadel in Erbil based on the photogrammetric and satellite remote sensing surveying, database of the citadel, according the demands of the archaeologists. It consists of more detailed data about the monument and user interface, which is necessary for comfortable work with graphical data and database content. It is built up separately in various programming languages like HTML (Hypertext Markup Language), PHP (PHP Hypertext Pre-processor), SQL (Structure Query Language), VRML (Virtual Reality Modeling Language), JavaScript and CSS (Cascading Style Sheets). The emphasis is placed on open source software solutions (Králová 2008). Final output is in *wrl* format, which can be investigated using open source browsers like Cortona or BS Contact. The part of this system is accessible on <http://lfgm.fsv.cvut.cz/citadel/>.



Fig. 3.11 A virtual model of the citadel created from a QuickBird imagery

3.4 Results

3.4.1 *Processing of the Image Time Series for Erbil*

In this project, old sketches, historical (declassified) satellite data and new satellite data were used. The aim of the project was to demonstrate the usefulness of combining historical data for city growth documentation. The biggest developments of the city were recorded between 1950 and 1960 and after 2000.

Only a simple classification scheme similar to the one used for the Corine land cover was used. With the use of satellite images, land uses are manually classified into four classes: urban areas (red); parks (green); cemetery (yellow); and streets, railways and airport (blue). The train station and airport are new dominants after 1980. For better classification, complementary data are needed. Although it is a simple classification, it is a very well documentable enormous city growth and outlines the directions of construction expansion. This can help in land use planning and sustainable city development. The next pictures (Fig. 3.11) show the intensive city growth of Erbil based on old plans or sketches and later on from satellite images from the range of 1944–2012 is shown.

3.4.2 *Creating a Base Map of Al-Qala Citadel*

The second part of the project was to map Erbil's historical centre (Al-Qala citadel). The whole Citadel has never been documented with modern methods before. A satellite image from the QuickBird satellite was used for the ground plan of the Citadel (date of image acquisition: 2005-08-23). The satellite image was processed by using Geomatica 10.0, ENVI Classic (pan-sharpening) and Adobe Photoshop 7.0. As mentioned above, the image sharpening, filtration and interpolating to 25 cm pixel were used for image quality improvements. The outputs of this procedure are encouraging and enable the next step to process with better quality. A provisory geodetic network in the Citadel area was built and over 600 object points were geodetically measured. Next, 16 control points were signalized and measured for aerial imaging, mainly on the roofs. The Photomodeler software was used for all photogrammetric image processing (Pavelka and Bílá 2013). Finally the 33 aerial images and 19 terrestrial images were adjusted to the base model. The mathematically least square adjustment and absolute transformation utilizing the control points were sufficiently accurate: the mean co-ordinate's error of control points was approximately 15 cm (mean position error 20 cm). In the 3D model about 1,000 object points were measured and calculated. A comparison of geodetically measured and Photomodeler calculated object points were made; a small systematical and scale error had been found (the model from Photomodeler was a little bit bigger and moved to south; the typical differences were approximately 15–30 cm in comparison to geodetic measurement by total station). These

displacements were solved by affine transformation into the geodetical measurements. Finally, we had geodetically measured object points, points from Photomodeler processing, measured control points and a transformed satellite photo plan (as an under layer photo plan). These data were then used for processing to the base vector plan (see Fig. 3.10).

3.4.3 Citadel in Erbil Information System

After creating a virtual model (see Sect. 3.4), an information system according to the given specifications was created. It consists of a photorealistic, virtual reality 3D model of the monument, a database, and a web-based user interface. Objects of the model have built-in interactive elements that allow the bi-directional connection between the model and the database. The database stores detailed data of interest to the archaeologists (Ardissone et al. 2013). The user interface enables comfortable work with both the graphical data and the database content. The system allows remote access and management of the data in the Internet environment. There are different access rights for system administrators, specialists, and general (anonymous) users. The emphasis is placed on open source software usage.

All outputs were stored as a model of the Citadel. For valuable parts, an interactive information system was created, in which archaeological, architectural, building structural, restoration and next information are stored. Our citadel information system contains:

- Photo-realistic VR 3D model of the monument, database, web-based user interface;
- User-friendly interface, different access rights, remote access;
- Interactive elements, bi-directional connection between model and database; and
- Necessary – ordinary web browser with Java Script and cookies for working with the database, for viewing the three model, one of several freeware plugins is needed.

3.5 Discussion

Knowledge of behavior trends of techno-economic systems and processes is necessary for their further development prediction. Economic phenomena lead to fluctuations in the uniform development. To understand the behavior mechanisms of the area development and their long-term activity, it is necessary to analyze the previous development.

It appears that with some exceptions the development of the area in time series can be made using a relatively simple method based on interpreting aerial and

satellite images. Long-term trends in built-up areas are clearly visible. In the long-term proportions urban areas, roads, housing and industrial estates enlarges. To obtain the most reliable results it would be necessary to ensure the scanned negatives of photos and to determine internal orientation parameters of the used camera together with other supporting data like an approximate image scale, the exact date, etc. If possible, it would be convenient to create orthophotos from either a stereo image pair or from photogrammetric images and sufficiently accurate digital terrain model. Digital terrain models can be obtained from photogrammetric processing or the digitized contour lines from maps can be used; recently airborne laser scanning can be employed. The archived maps are suitable to data set complement. They often describe interpreted components the best and they allow one to obtain appropriate control points. The transformation of historical maps is a separate issue (Cajthaml 2013; Krejčí and Cajthaml 2009). In some cases they are available only in a form of sketches that are low or locally different positional accuracy.

The turn of the twenty-first century brought rapid development in satellite and aerial image technology together with data processing. A number of various innovations had been made. There is the utilization of airborne laser scanning for 3D city model creation. Satellite images with geometrical resolution better than 1 m in panchromatic range and with a resolution of 2–4 m in multispectral range are available. Precise GNSS instruments are at our disposal. This considerably increases accuracy and possibilities available when applying classification methods. Given the tumultuous growth and development of settlements in many places on the world together with accumulation of people in megacities, such data is extremely valuable. If one wants a longer look to the past, a necessary compromise on details and on existing data quality must be made.

In our case study, increasing or decreasing areas of classes, for example in graphs or tables, can be seen (based on differences in the sum of individual classes given by an interpretative key). In many cities the development of industrial areas can be observed with a peak in the 1960s and after the year 2000, always accompanied by a certain kind of housing construction. Transport infrastructure often tends to delay significant changes from occurring in the construction of airports and motorway junctions. On the contrary, the railway did not develop as rapidly as in the last century (only high-speed tracks in Europe, Japan or China). A clear trend is the migration of people to big cities in the 1980s, which still continues. In many cases on the earth, this leads to uncontrolled expansion, which is very hard to handle. This rapid expansion can be only observed or, with certain difficulties, predicted. This allows us to perform timely interventions. However, it is possible to successfully document the development and direction of the city growth through the above-mentioned technology. It is necessary for planning and especially for the sustainable development of the area.

The virtual model of the Al Qala Citadel has been created. The analysis of the model quality assessed the precision of the model and showed ways of precision improvements, which were realized. The field calibration of aerial and terrestrial image sets was very important. It has improved the project precision and, at the

same time, it has supported the theory of Shortis et al. (2006) that digital cameras equipped with zoom lenses may be used in photogrammetry practice with the exception of projects with high precision demands.

For the Al-Qala citadel, there are distinctive benefits:

- A combination of different imagery types for a historic monument modeling;
- A visualization of the model with photo textures using precise methods;
- Model precision analysis;
- Information system creation consisting of a 3D model and a database;
- Information system establishment designed for archaeological data storing and managing, promotion of the monument;
- The first documentation of the Citadel, though it is an important historical monument that was placed on the UNESCO list of endangered historic sites;
- The project can serve as an example of documentation obtained in hard conditions in a developing country. It may show a possibility of development of a commonly usable technology for creating such systems of historical object documentation;
- The project fulfilled the requirements of precision – a point error of 0.5 m (standard deviation). Points in the PhotoModeler project have standard deviation of 14 cm (internal project precision). Taking into account the data from geodetical surveying, the estimated accuracy of point measurement is 45 cm; and
- A way to orient an irregular set of oblique aerial and terrestrial images together with a satellite image was found. To solve such a large project meant to find a solution for a system of equations with thousands of unknowns. Suitable software, such as PhotoModeler, was chosen and special sequences of operations were kept.

3.6 Conclusions

The use of satellite or aerial images provides a low-cost, non-contact and complex overview for city planners and managers from comprehensive areas. This chapter discusses the combined use of maps and sketches, declassified satellite data and new satellite data for city growth documentation. As a case project, the city of Erbil, Iraq was selected. This is an example of the mapping of urban dynamics based on land cover/land use analysis. It can be helpful not only for the documentation of Erbil in the past, but also for sustainable city development, especially in developing countries, where the growth of cities is very rapid and there aren't precise urban plans, maps or documentation. The processing of historical and on-going satellite images can partially solve this problem. The presented project is focused on city growth monitoring based on the processing of historical sketches, old aerial images, military declassified satellite images and new satellite images. In many countries, there are no historical data for long-term area development monitoring at our disposal. For this reason, declassified military satellite images give us the

possibility to preview the past in the same way old maps or sketches would have. The development of many cities and regions in recent years is almost uncontrollable and historical information is often absent. It was shown that it is possible to join different image data sources. From image time series it is possible to extract historical information about cities. In this case project, the final classification based on land use technology is very simple, because we did not have any additional information at our disposal (but they do exist).

The second part deals with the mapping of Erbil's city centre. A new vector map of Al-Qala Citadel was created based on satellite images. Next, an accurate, dynamic, and photorealistic virtual model of the citadel was made. The 3D model of the citadel is based on photogrammetric surveying and vector mapping such as on advanced virtual presentation technology.

Acknowledgement This project was supported with a grant from the Ministry of Education, Youth and Sports (# MSM6840770040), Czech Republic.

References

- Antonson H, Gustafsson M, Angelstam P (2010) Cultural heritage connectivity. A tool for EIA in transportation infrastructure planning. *Transp Res Part D: Transp Environ* 15(8):463–472
- Apollonio FI, Daiani M, Sun Z (2013) 3D modelling and data enrichment in digital reconstruction of architectural heritage. *ISPRS archives*, vol XL-5/W2, pp 43–48
- Ardisson P, Bornaz L, Degattis G, Domaine R (2013) A 3D information system for the documentation of archaeological excavations. *ISPRS archives*, vol XL-5/W2, pp 55–60
- Cajthaml J (2013) Polynomial georeferencing method for old map series. In: 13th international multidisciplinary scientific geoconference, vol. I. STEF92, Sofia, pp 859–866
- Gruen A (2008) Reality-based generation of virtual environments for Digital Earth. *Int J Digit Earth* 1:88–106
- Grussenmeyer P, Landes T, Voegle T, Rongle K (2008) Comparison methods of terrestrial laser scanning, photogrammetry and tachometry data for recording of cultural heritage buildings. *ISPRS archives*, vol. 37(B5) pp 213–218
- Halounová L (2003) Textural classification of B and W aerial photos for the forest classification. In: *EARSEL 03*, vol 1. Millpress Science Publishers, Rotterdam, pp 324–335
- Halounová L (2004a) Automatic classification of B&W aerial orthophotos. In: *Proceedings of the 24th EARSEL symposium and workshop*, vol 1. Millpress Science Publishers, Rotterdam, pp 31–40
- Halounová L (2004b) Automatic classification of forest areas from B&W aerial orthophotos. In: *Remote sensing and geographical information systems for environmental studies – application for forestry*, vol 1. J.D.Sauerländer's Verlag, Frankfurt am Main, pp 176–183
- Halounová L (2004c) The automatic classification of B&W aerial photos. In: *ISPRS proceedings*, vol 1. ISPRS, New York, pp 156–160
- Hanzalová K, Pavelka K (2013) Documentation and virtual reconstruction of historical objects in Peru damaged by an earthquake and climatic events. *Adv Geosci* 2013(35):67–71, Internet: <http://www.adv-geosci.net/35/67/2013/adgeo-35-67-2013.pdf>
- Höhle J (2013) Oblique aerial images and their use in cultural heritage documentation. *ISPRS archives*, vol XL-5/W2, pp 349–354
- Ioannides M, Fritsch D, Leissner J (2012) *Progress in cultural heritage preservation*, vol 7616. Springer. ISBN 978-3-642-34233-2

- Justa P (2005) Choli minaret, preliminary study and proposal for scientific research of the site. GemaArt, Prague
- Justa P, Houska M (2006) Citadel in Erbil, study for reconstruction project proposal. GemaArt, Prague
- Kopecká M, Vateva R, Feranec J, Otahel J, Rosina K (2014) Mapping and analyzing urban dynamics based on remote sensing for spatial planning and management, Bulgaria, 5th international conference on cartography and GIS
- Králová V (2008) Application of digital photogrammetry, modern visualization methods and GIS technology for monument preservation, Doctoral dissertation, CTU in Prague, Faculty of Civil Engineering, 122 p
- Krejčí J, Cajthaml J (2009) Müller's maps of the Czech lands and their analysis. *Acta Geodaetica et Geophysica Hungarica* 44(1):27–38
- Meyer É, Grussenmeyer P, Perrin JP, Durand A, Drap P (2007) A web information system for the management and the dissemination of Cultural Heritage data. *J Cult Herit* 8(4):396–411
- Morris AEJ (1979) A history of urban form: before the industrial revolutions, ISBN-13:978-0-582-30154-2
- Muhammad KI (2004) Erbil Citadel – study of population growth. In: 1st scientific conference for renovation and reconstruction of Erbil Citadel, Erbil, pp 29–33
- Musílek L, Čechák T, Kubelík M, Pavelka K, Pavlík M (2001) The laboratory of quantitative methods in historic monument research at the CTU Prague. *Radiat Phys Chem* 61(3–6):725–727
- Nováček K (2011) Arbil/Hawler: archaeology of the town under the citadel, Subartu. *J Kurdish Assoc Archaeol* 4–5:10–13
- Nováček K, Sůvová Z (2011) Zangi-period architecture in Iraqi Kurdistan: Medrese Qubahan at Amedi (‘Amadiya). *Zeitschrift für Orient-Archäologie* 4:176–210
- Nováček K, Chabrt T, Filipický D, Pavelka K, Šída P (2008) Research of the Arbil Citadel, Iraqi Kurdistan, first season. *Památky archeologické* (in Czech with English abstract), vol 2008, no 1, pp 259–302
- Pavelka K (2001) Complex photogrammetric and architectural analysis of the historic monuments, CIPA international symposium, Potsdam, TU Berlin, 9/2001, Germany, pp 475–479
- Pavelka K (2009) Detailed documentation and 3D model creation of Dalal Bridge using terrestrial photogrammetry in Zakhu, northern Iraqi Kurdistan. In: Proceedings of 22nd CIPA symposium, vol 1. ISPRS, Bangkok, pp 325–331
- Pavelka K, Bílá Z (2013) Use of historical images for object reconstruction. In 13th international multidisciplinary scientific geoconference SGEM 2013, vol I. STEF92, Sofia, pp 719–726
- Pavelka K., Svatušková J, Králová V (2007) Photogrammetric documentation and visualization of Choli Minaret and Great Citadel in Erbil/Iraq. CIPA Symposium, Athens, pp 245–258
- Pavelka K Svatušková J (2008) Using of VHR satellite data and aerial orthophoto for archaeological prospection. In: Proceedings of 29th ACRS, vol 1. URSI, Tokyo, pp 142–149
- Porter BN (2004) Ishtar of Nineveh and her collaborator, Ishtar of Arbela, in the Reign of Assurbanipal. In: *Compte Rendu, 49e Rencontre Assyriologique Internationale, Iraq* 66
- Remondino F, El-Hakim S (2006) Image-based 3D modelling: a review. *Photogramm Rec* 21(115):269–291
- Řezníček J, Pavelka K, Bílá Z (2013) Non-invasive and non-contact prospection of archaeological and historical objects. 13th international multidisciplinary scientific geoconference SGEM 2013, vol I, STEF92, Sofia, pp 647–654
- Sahid M (2004) Antiques buildings in Erbil (Hawler) Citadel. A comparative study of traditional buildings throughout Iraq. 1st scientific conference for renovation and reconstruction of Erbil Citadel. Erbil, pp 6–9
- Shortis MR, Bellman CJ, Robson S, Johnston GJ, Johnson GW (2006) Stability of zoom and fixed lenses used with digital SLR cameras. *ISPRS archives*, vol. 36(5):285–290
- Tayyebi A, Pijanowski BC (2014) Modeling multiple land use changes using ANN, CART and MARS: comparing tradeoffs in goodness of fit and explanatory power of data mining tools. *Int J Appl Earth Obs Geoinf* 28:102–116

- Tayyebi A, Perry PC, Tayyebi AH (2013a) Predicting the expansion of an urban boundary using spatial logistic regression and hybrid raster–vector routines with remote sensing and GIS. *Int J Geogr Inf Sci* (ahead-of-print), 1–21
- Tayyebi A, Pekin BK, Pijanowski BC, Plourde JD, Doucette JS, Braun D (2013b) Hierarchical modeling of urban growth across the conterminous USA: developing meso-scale quantity drivers for the Land Transformation Model. *J Land Use Sci* 8(4):422–442
- Tayyebi AH, Tayyebi A, Khanna N (2014) Assessing uncertainty dimensions in land-use change models: using swap and multiplicative error models for injecting attribute and positional errors in spatial data. *Int J Remote Sens* 35(1):149–170
- Ur JA (2000) Cycles of civilizations in Northern Mesopotamia, 4400–200BC. *J Archaeol Res* 18:387–431
- Verhoeven G, Doneus M, Briese C, Vermeulen F (2012) Mapping by matching: a computer vision-based approach to fast and accurate georeferencing of archaeological aerial photographs. *J Archaeol Sci* 39(7):2060–2070
- Wilkinson TJ (2008) Falling out of an aircraft: aerovisualism and the aerial photography of J.S.P. Bradford. *Vis Anthropol* 21:18–38
- Wilson D (2000) *Air photo interpretation for archaeologists*, 2nd edn. Tempus, Stroud, 256 pp

Chapter 4

Long-Term Change Dynamics Using Landsat Archive for the Region of Waterloo in Ontario, Canada

Anqi Fu, Jonathan Li, and Saied Pirasteh

Abstract Urban land use and land cover classification have always been crucial due to the ability and to link many elements of human and physical environments. Timely, accurate, and detailed knowledge of the urban land cover information derived from remote sensing data is increasingly required among a wide variety of communities. This chapter presents a surge of interest that has predominately driven from the recent innovations in data, theories in urban remote sensing, and technologies. The Region of Waterloo was chosen for land use and land cover classification by applying remote sensing techniques to satellite images from 1984 to 2013.

4.1 Introduction

To date, the entire world is continuously experiencing rapid urbanization (Ridd and Hipple 2006). Urban growth is mainly caused by population growth, economic growth, environmental condition, availability of technologies and frequent human activities such as industrialization and migration from rural to urban area and resettlement (Bhatta 2010; Ridd and Hipple 2006). It is obvious that the aforementioned will inevitably lead to land use changes and landscape pattern alteration at local and regional scale (Yin et al. 2011; Tan et al. 2009; Deng et al. 2009; Sundarakumar et al. 2012). Those changes include losses of agriculture fields, water bodies, forest and other vegetated green spaces and non-vegetated fields (Yang 2002; Sexton et al. 2013a, b; Sundarakumar et al. 2012; Yin et al. 2011). Disturbance of natural environment by urban growth can bring various urban

A. Fu • J. Li (✉) • S. Pirasteh

Department of Geography and Environmental Management, University of Waterloo,
200 University AVE W., Waterloo, ON N2L3G1, Canada
e-mail: a3fu@uwaterloo.ca; junli@uwaterloo.ca; s2pirast@uwaterloo.ca

© Springer Science+Business Media Dordrecht 2015

J. Li, X. Yang (eds.), *Monitoring and Modeling of Global Changes: A Geomatics Perspective*, Springer Remote Sensing/Photogrammetry, DOI 10.1007/978-94-017-9813-6_4

63

environmental issues such as climate change, urban heat island effect, water quality deterioration, vegetation degradation, increased flooding risk, decreased air quality (Bhatta 2010; Sexton et al. 2013a, b; Li et al. 2011; Tan et al. 2009; Sundarakumar et al. 2012; Thapa and Murayama 2009). Therefore, consistent monitoring of land use and land cover (LULC) change at local and regional scale is an urgent need for planners and policy makers to understand change dynamics of an area to make it more appropriate and effective decisions of planning and environmental management in the future.

With recent development of remote sensing technologies and accessibility to remotely sensed data, the study of identifying detailed spatial and temporal changes of urban area and monitoring urban growth have become more cost-effective and successful (Huang et al. 2011; IRS 2013; Jensen 2006; Thapa and Murayama 2009; Patino and Duque 2013; Lunetta et al. 2004). To date, various change detection methods have been explored and developed for detecting LULC change analysis (Singh 1989). Technically, image algebra (i.e. image differencing and image ratioing), principal component analysis (PCA), post-classification change detection (PCCD), direct multi-date classification, and change vector analysis (CVA) are most widely used methods for change detection (Singh 1989; Alumutairi and Warner 2010; Coppin et al. 2004; Jensen 2005). From an application perspective, most of the previous studies on urban growth and LULC change detection were based on bi-temporal and coarsely multi-temporal analyses.

The previous researchers indicated that the bi-temporal and coarsely multi-temporal analyses have their own advantages of providing useful change information. They are unable to observe dynamic change patterns and higher-order complexities, such as acceleration, deceleration of specific LULC change within a long-term time span (Sexton et al. 2013a, b). The dynamic change patterns include spatially and temporally complex changes in water, forest, agriculture, and urban built-up area caused by natural and anthropogenic processes (Sexton et al. 2013a, b). Moreover, the impacts on ecosystems caused by frequent human activities exhibit nonlinearities, time lags, and legacy effects, and the change dynamics is only able to be detected by long-term repeatedly measurements (Sexton et al. 2013a, b).

With the opening of Landsat archive from United States Geological Survey (USGS) in 2009 (Sexton et al. 2013a, b; Wulder et al. 2011), an increased demand of long-term time-serial analysis of urban growth and LULC change dynamics can be met (Sexton et al. 2013a, b; Hansen and Loveland 2012). Therefore, with a free access of Landsat archive, processing dense datasets with high frequency will shift research focus from analyzing static bi-temporal change to comprehending more detailed long-term change dynamics in which planners, policy makers and resource managers are much more interested (Sexton et al. 2013a, b).

In this chapter, the role of satellite data and Landsat archive data for change detection analysis will be introduced. In addition, an overview of change detection methods will be provided. To reveal the superiority of long-term change dynamics analysis using high-dense Landsat images, this chapter focuses on a case study of change detection analysis of the Region of Waterloo. Also, based on a case study

the limitations and uncertainties of the change dynamics analysis method will be discussed. In addition, some recommendations will be considered for future studies.

4.2 Satellite Data and Change Detection Methods

4.2.1 *Satellite Data for Monitoring LULC Change*

The objects on the earth surface and sometimes subsurface can be interpreted from remotely sensed data such as Landsat ETM+, Quick Bird etc. The various techniques can be applied to extract the information from the satellite images. Basically, objects are interpreted based on their reflected or emitted electromagnetic radiation (Patino and Duque 2013; Jensen 2005). Thus land use and land cover, urban morphology, vegetation distribution, and some other biophysical information can be extracted for planners and environmental scientists to analyze the environment disturbance (Patino and Duque 2013). Since the late 1950s, aerial images have been used for LULC change analyses. However, with the launch of several earth-orbiting satellites, the focus of studies has shifted from using aerial images to satellite-based images because of their lower costs, wider area coverage, and frequent image updates (Patino and Duque 2013). Since the earliest satellite Landsat 1 with Multispectral Scanner (MSS) was launched in 1972, many satellites with various sensors in different spectral, spatial and temporal resolutions were launched in the past four decades (Patino and Duque 2013; Jensen 2005). Patino and Duque (2013) reviewed that Earth-orbiting satellite sensors such as Landsat 5 Thematic Mapper (TM), Landsat 7 Enhanced Thematic Mapper Plus (ETM+), SPOT 1–5, QuickBird, IKONOS, NASA Terra Advanced Spaceborne Thermal Emission and Reflection Radiometer (ASTER) and Indian Remote Sensing (IRS-1C) are the most often used earth observation (EO) systems in LULC change detection studies. They also stated that the moderate spatial resolution images are appropriate for detecting LULC change. It is because historical images can be used dating back to 1970s. To illustrate the lengths of the archives of listed remote sensing systems, a time scale figure, showed in Fig. 4.1 was generated by Patino and Duque (2013).

A long-term record of global landscape information has been acquired since the first Landsat satellite launched in 1972 (USGS 2013a, b, c, d, e, f). Landsat project is the oldest satellite project in the United States for land-surface observation (Jensen 2007). Landsat Project which was initiated by National Aeronautics and Space Administration (NASA) and USGS has launched eight satellites to collect data from the earth surface. This provides the resources for people who manage regional development, manage natural resources, and those who do research in various environmental fields throughout the United States and worldwide (USGS 2013a, b, c, d, e, f). Based on Landsat Project Statistics on USGS website (2013) the most primary use of Landsat data is detecting LULC change. To consider establishment of routinely gather earth resource information from space, the Landsat

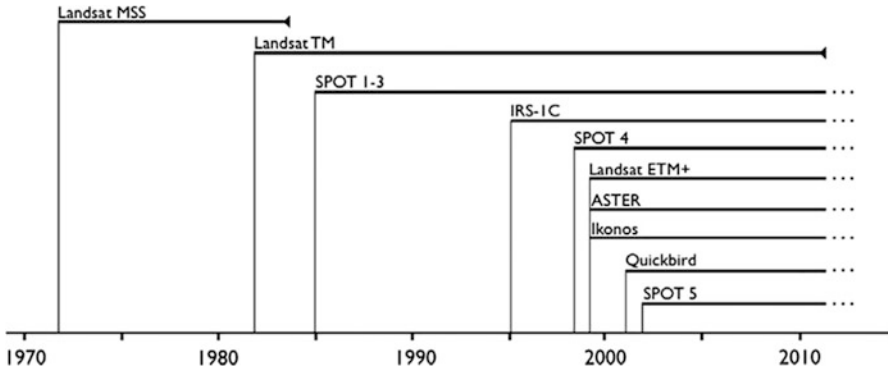


Fig. 4.1 Time scale of several remote sensing systems (Source: Patino and Duque 2013)

satellites have had a very well performance during their missions, expect for Landsat 6 (USGS 2013a, b, c, d, e, f). To continue the mission of Landsat Project of observing land-surface information the Landsat 8 with providing higher quality data was recently launched on February 11, 2013 (USGS 2013a, b, c, d, e, f).

With technologies development, sensors onboard Landsat satellites have been improved as well. Spectral and spatial information retrieved from USGS (2013a, b, c, d, e, f) of each Landsat sensor are specified in Table 4.1. Landsat Multispectral Scanner (MSS) was the primary sensor placed on Landsat 1, 2, and 3. MSS images have four multispectral bands from green to near-infrared (IR) with 80 m resolution and one thermal band with 240 m resolution only onboard Landsat 3. Thematic Mapper (TM) sensors were placed on Landsat 4 and 5 with two added shortwave infrared (SWIR) and one thermal band. Resolutions have been increased to 30 m for visible and infrared bands and to 120 m for thermal band. Enhanced Thematic Mapper Plus (ETM+) onboard Landsat 7 has one more panchromatic band in 15 m resolution; and thermal band increased to 60 m resolution. As for the newly launched Landsat 8, Operational Land Imager (OLI) sensor has eight spectral bands in 30 m resolution. In OLI the following bands have been added (a) one deep blue band and one cirrus band, and (b) one panchromatic band in 15 m resolution. In addition, the Thermal Infrared Sensor (TIRS) has two thermal bands with 100 m resolution (USGS 2013a, b, c, d, e, f).

4.2.2 Change Detection Methods

As Singh (1989) defined, “change detection is the process of identifying differences in the state of an object or phenomenon by observing it at different times”. Changes can be detected because of the radiance values of the objects and also change in LULC alterations (Singh 1989). To monitor landscape changes effectively by using remote sensing techniques, a variety of change detection methods have been

Table 4.1 Band designations for Landsat sensors

Sensor	Spectral bands		Wavelength (µm)	Resolution (m)
	Landsat 1,2,3	Landsat 4,5		
MSS	4 – green	1 – green	0.5–0.6	80
	5 – red	2 – red	0.6–0.7	80
	6 – near-IR	3 – near-IR	0.7–0.8	80
	7 – near-IR	4 – near-IR	0.8–1.1	80
	8 – thermal (Landsat 3)		10.4–12.6	240
TM and ETM+	1 – blue – green		0.45–0.52	30
	2 – green		0.52–0.60	30
	3 – red		0.63–0.69	30
	4 – near-IR		0.76–0.90	30
	5 – SWIR 1		1.55–1.75	30
	6 – thermal		10.40–12.5	120; 60 (ETM+)
	7 – SWIR 2		0.98–2.35	30
	8 – panchromatic (ETM+)		0.52–0.90	15
OLI and TIRS	1 – coastal/aerosol		0.43–0.45	30
	2 – blue		0.45–0.51	30
	3 – green		0.53–0.59	30
	4 – red		0.64–0.67	30
	5 – near IR		0.85–0.88	30
	6 – SWIR 1		1.57–1.65	30
	7 – SWIR 2		2.11–2.29	30
	8 – panchromatic		0.50–0.68	15
	9 – cirrus		1.36–1.38	30
	10 – thermal 1		10.60–11.19	100
	11 – thermal 2		11.50–12.51	100

developed and applied in many studies (Singh 1989; Jensen 2005; Lu and Weng 2004). Four important aspects of monitoring changes were suggested and summarized by Macleod and Congalton (1998). They are (a) determination of whether or not the changes happened, (b) identification of the nature of the changes, (c) detection of the areal extent of the changes, and (d) analysis of the change patterns. It is worth that to know selecting an appropriate change detection method is very critical to obtain reliable results because of different purposes and objectives of applications (Jensen 2005; Lu and Weng 2004). To illustrate and compare the key characteristics, advantages and disadvantages of the most often used change detection methods, Table 4.2 is depicted in terms of some previous review works (Singh 1989; Jensen 2005; Lu and Weng 2004; Coppin et al. 2004; Alphan 2011; Lunetta and Elvidge 1998).

The methods listed in Table 4.2 have been proved to be effective for detecting changes in various applications. Image algebra method can be used in monitoring forest canopy change (Hayes and Sader 2001), monitoring irrigated crops

Table 4.2 Summary of most often used change detection methods

Methods		Characteristics	Advantages	Disadvantages	Key considerations
Write function memory (WFM)		Visual interpretation by inserting three individual bands from multiple dates into Red, Green, and Blue planes to highlight the change area	Quick visual interpretation of the change at two and even three dates	No quantitative information	Determine appropriate bands
			Normally not necessary to have atmospheric correction	No “from-to” change class information	
Image algebra	Image differencing	Subtract one image of one date from another image of second date	Simple and quick method to identify change/no change information	No “from-to” change class information	Determine appropriate bands
			Normally not necessary to have atmospheric correction	Difficult to determine the threshold to distinguish change/no change information	Threshold should be identified carefully
	Image regression	Identify the linear relationship between images from two dates. Subtract the first image from the regressed image	Impacts of atmospheric effect and sun angle effect can be reduced	No “from-to” change class information	Develop regression model
				Need to establish accurate regression model	Determine appropriate bands and threshold
Image ratioing	Calculate the ratio of two images from two dates, band by band	Simple and quick method to identify change/no change information	No “from-to” change class information	Determine appropriate bands	
			Normally not necessary to have atmospheric correction	Difficult to determine the threshold to distinguish change/no change information	Select appropriate threshold
Vegetation index differencing	Calculate vegetation index for two dates before using image differencing method	Difference of spectral features can be enhanced	Reduce impacts of topographic effects	Enhance random noise and coherent noise	Determine appropriate vegetation index
					Select appropriate threshold

(continued)

Table 4.2 (continued)

Methods	Characteristics	Advantages	Disadvantages	Key considerations
Principal component analysis (PCA)	Put bands from two dates into one single dataset. Perform PCA and analyze minor component which represents change information	Data redundancy can be reduced	Difficult to label change classes	Need skills to identify the component which represents the change information
		Change can be visually interpreted from minor component	Threshold is needed to identify change/no change information	Select appropriate threshold
		Normally not necessary to have atmospheric correction		
Multi-date composite classification (MCC)	Put bands from two or more dates into one single dataset. Supervised or unsupervised approach is used to extract change information	Requires only one classification	Data redundancy	Need thorough examination of the images to label the change classes
			Difficult to select training sites because of many change classes	
Change vector analysis (CVA)	Direction and magnitude of change from one date to another date are generated. Direction vector determines the change types. Magnitude vector determines whether the change happens	Have ability to process any number of spectral bands	Difficult to identify change trajectories	Determine direction of change
		Detailed change information can be provided		Identify threshold for magnitude of each change vector
Post classification change detection (PCCD)	Change information is obtained by comparing independently classified thematic maps	No atmospheric correction required	Requires two classifications	Sufficient training sample for classification
		Provides “from-to” information	Accuracy of change information heavily relies on the accuracy of classification results	

Jensen (2005) and Lu and Weng (2004, 2007)

(Manavalan et al. 1995), detecting land cover change (Kleynhans et al. 2011; Kaufmann and Seto 2001), detecting mining process and land use change (Prakash and Gupta; 1998), and monitoring landscape change of coastal area (Alphan 2011). Using PCA method, land cover change (Byrne et al. 1980; Parra et al. 1996), forest conversion (Jha and Unni 1994) can be detected. CVA also can be used in vegetation degradation detection (Lunetta et al. 2004), desertification monitoring (Dawelbait and Morari 2012), and LULC change detection (Song et al. 2012). As for PCCD method, thematic maps and valuable “from-to” change information can be obtained from PCCD (Jensen 2005). Therefore, many applications are focusing on LULC change and urban growth employed PCCD method to identify specific categories of LULC. Thus to explore the change pattern and change effect on surrounding environment (Abd El-Kawy et al. 2011; Yuan et al. 2005; Sundarakumar et al. 2012; Peiman 2011) has been stressed.

To monitor nation-wide LULC change of the U.S. and evaluate and manage the consequences of change, USGS had developed a Land Cover Trends (LCT) project to detect LULC changes at ecoregional scale for the 1972–2000 period using Landsat data (USGS 2013a, b, c, d, e, f). The PCCD method has been employed to obtain specific “from-to” information (which LULC classes are changing, what they are changing to, and how much they change) and monitor LULC change dynamics (Sleeter et al. 2012). The study of Mojave Basin and Range Ecoregion is a typical example of LULC change detection. Since Las Vegas is one of the fastest growing cities in the U.S., significant urban growth in place of grassland has been detected. It showed that the most rapid growth happened during 1986–1992. In 2011, Huang et al. applied PCCD method using the Iterative Self Organizing Data Analysis (ISODATA) classifier to analyze urbanization process and its effect on irrigation districts of the Lower Rio Grande Valley in the south of Texas. Using the same PCCD method, Tan et al. (2009) evaluate the impact of land surface temperature by monitoring urban expansion based on LULC maps which were classified by maximum likelihood classifier (MLC) in Penang Island, Malaysia. For spatial progressive urban growth mapping of Atlanta metropolitan area Yang (2002) and Yang et al. (2003) designed a change detection scheme based on multi-temporal map-by-map comparison. Similarly, Yin et al. (2011) detected urban growth dynamics applying multi-temporal change detection scheme. They evaluated how Shanghai metropolitan area conformed to the “reform and opening-up” policy. In addition, Yin et al. (2011) generated radar graphs to illustrate spatial orientation of LULC change. Moreover, other studies, conducted by Yuan et al. (2005), Sundarakumar et al. (2012), Tang et al. (2008), Afify (2011), and Abd El-Kawy et al. (2011) proved that PCCD is a very useful and popular approach for LULC change detection.

According to previous studies, most of the urban area change detection analyses were conducted based on bi-temporal scheme (Afify 2011) or coarsely multi-temporal scheme (Abd El-Kawy et al. 2011; Yuan et al. 2005; Sundarakumar et al. 2012; Peiman 2011; Tian et al. 2011; Zha et al. 2003; Zhao et al. 2005). With easy accessibility of data availability recently, more and more studies used multi-temporal datasets to detect change dynamics of urban area. However, as

Sexton et al. (2013a, b) mentioned that in order to understand the causes and consequences of urbanization, coarsely multi-temporal datasets are still insufficient. To detect the spatially and temporally complex change of LULC of North Carolina Piedmont from 1984 to 2007, Sexton et al. (2013a, b) derived LULC information from a dense time-serial Landsat dataset using supervised classification approach. The results clearly illustrated the change dynamics, and well depicted the trajectories of each LULC type spanning a long-term period. Such long-term detailed change information has great potential for planners, policy makers, social scientists and ecologists to better understand the complicated urbanization process and human-natural systems (Sexton et al. 2013a, b). Therefore, in this chapter, a case study of long-term change dynamics analysis has been performed on the Region of Waterloo, a prosperous growing region in Ontario, Canada in order to detect the trajectory of LULC long-term change. It subsequently shows the effectiveness and superiority of change dynamics analysis method.

4.3 Research Design

4.3.1 Study Area and Data

The Region of Waterloo is located in the southern Ontario. It comprises of cities of Waterloo, Kitchener, Cambridge along with four rural townships (North Dumfries, Wellesley, Wilmot, and Woolwich). The region of Waterloo is one of the rapidest growing regions in Canada after its formation in 1973 (RGMS 2006a, b; Region of Waterloo 2010). The location of Region of Waterloo is shown in Fig. 4.2. The region is 1,369 km² in size and the Region's population was 507,079 as of the 2011 census (Region of Waterloo 2010). Population of urban area of Waterloo Region has increased by 5.7 % from 2006 to 2011. With such tremendous population growth, urban area of Waterloo Region is now ranked as the fourth largest in Ontario and tenth largest in Canada (Statistics Canada 2011). To detect the LULC change caused by urban growth the study area is determined as the union of the municipal area of the cities and the official-defined urban built-up area, which is depicted in Figs. 4.2. and 4.3.

As an overview, within this study area, urban built-up area is one of the most typical land cover types. They are included of low-density urban use area (e.g. single/multiple family houses, local roads, etc.) and high-density urban use area (e.g. commercial and industrial areas, high-density residential areas, etc.). Another typical land cover type is vegetation such as agriculture area and grassland (e.g. pastures, golf courses, parks, etc.). Forest land, considered as very important land cover type, occupies relatively small area in general. This study area also covers some water bodies, such as part of Grand River and Laurel Creek Reservoir. Moreover, there are small areas of exposed lands, including natural barren land and building sites.

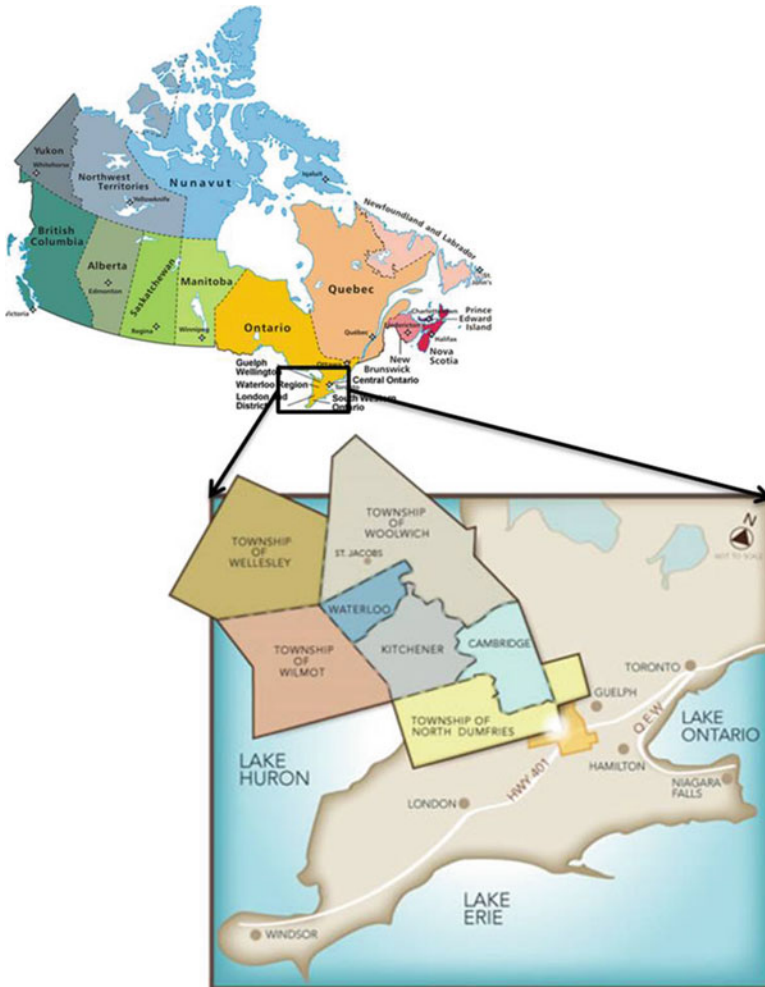


Fig. 4.2 Location of Region of Waterloo

Free access of a long-term Landsat archive data provides opportunity to detecting time-serial change dynamics at regional scale. In this study, Landsat archive data is the core data of extracting urban LULC information. Some other ancillary data are utilized as reference during Landsat data processing and accuracy assessment. Landsat data are listed in Table 4.3.

The entire study area can be covered by the WRS-2 path-18/row-30 scene. Images are projected in Universal Transverse Mercator (UTM) coordinates based on World Geodetic System of 1984 (WGS84) datum. Since the time span of this study is from 1984 to 2013, one scene of each year is needed. To obtain high quality data, images with no cloud and no haze were selected. Data for 1988, 2004, and

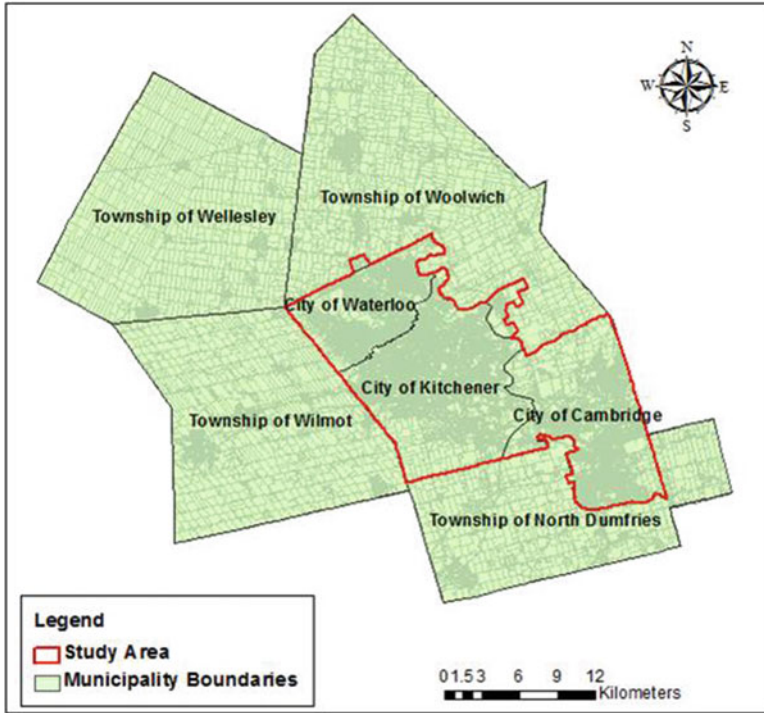


Fig. 4.3 Map of study area

Table 4.3 Landsat images used for classification

Year	Sensor system	Date (mm/dd)	Year	Sensor system	Date (mm/dd)
1984	Landsat 5 TM	06/13	1999	Landsat 7 ETM+	09/03
1985	Landsat 5 TM	09/20	2000	Landsat 5 TM	08/28
1986	Landsat 5 TM	06/03	2001	Landsat 5 TM	08/15
1987	Landsat 5 TM	09/10	2002	Landsat 7 ETM+	08/01
1989	Landsat 5 TM	06/11	2003	Landsat 5 TM	06/02
1990	Landsat 5 TM	09/02	2005	Landsat 5 TM	08/26
1991	Landsat 5 TM	07/19	2006	Landsat 5 TM	08/13
1992	Landsat 5 TM	08/22	2007	Landsat 5 TM	06/29
1993	Landsat 5 TM	08/09	2008	Landsat 5 TM	09/03
1994	Landsat 5 TM	10/15	2009	Landsat 5 TM	05/17
1995	Landsat 5 TM	07/30	2010	Landsat 5 TM	05/20
1996	Landsat 5 TM	05/29	2011	Landsat 5 TM	06/08
1997	Landsat 5 TM	07/19	2013	Landsat 8 OLI and TIRS	09/17
1998	Landsat 5 TM	05/19			

2012 were eliminated due to a large cloud obstructed area. In order to minimize the phenological effect during change detection analysis, data acquired in summer season were preferred. Most of the data are obtained from June to September. All used Landsat data were retrieved from USGS Global Visualization Viewer (GloVis) interface (<http://glovis.usgs.gov/>).

To help select training samples of the supervised classification and reference samples for accuracy assessment, two full-colour digital orthoimages with 12 cm spatial resolution have been acquired from University Geospatial Centre. These two orthoimages cover the entire area of Waterloo Region in 2006 and 2010 respectively. With 12 cm spatial resolution, the orthoimages have been projected in UTM coordinates and they are stored in MrSID image format accompanying with SDW world files. The datum used is the North American Datum of 1983 (NAD83). Another data that can be used for aiding choosing training samples is a land use shapefile of Waterloo Region in 2007. It also has been obtained from the University of Waterloo Geospatial Centre. This shapefile parcels the study area into polygons based on different land use types. Additionally, Google Map is providing high spatial resolution aerial or satellite images of the world. It is an auxiliary source for training samples selection and accuracy assessment. Selecting appropriate training samples is very critical for satisfactory classification results. Even though there is no reference data for every year, the two orthoimages (i.e. the land use shapefile and images from Google Maps) are the effective reference data for understanding the land surface information of this study area.

4.3.2 Classification Scheme

Image classification is the most important process for obtaining accurate LULC information. To generate consistent classification results, an appropriate classification algorithm needs to be determined. For this case study a support vector machine (SVM) was used for the classification process. It is because of its outstanding performance in contrast to traditional classifier such as MLC for LULC classification using remote sensing techniques (Huang et al. 2002; Pal 2005; Frohn and Arellano-Neri 2005; Gislason et al. 2006; Kotsiantis 2007; Benediktsson et al. 2007; Mellor et al. 2013). SVM is based on statistical learning theory and used structural risk minimization method proposed that was by Vapnik to discriminate class members (Nemmour and Chibani 2011; Song et al. 2012). SVM employs optimization algorithms to decide the location of optimal boundaries that can best separate the classes (Huang et al. 2002; Pal and Mather 2005). Thus a minimal generalization error can be obtained by minimizing the probability of misclassification of the unseen data points. The workflow of classification process is shown in Fig. 4.4.

An appropriate classification system and sufficient representative training samples are very critical for a successful classification (Lu and Weng 2007). As referring to the USGS "Land-Use/Land-Cover Classification System for Use with

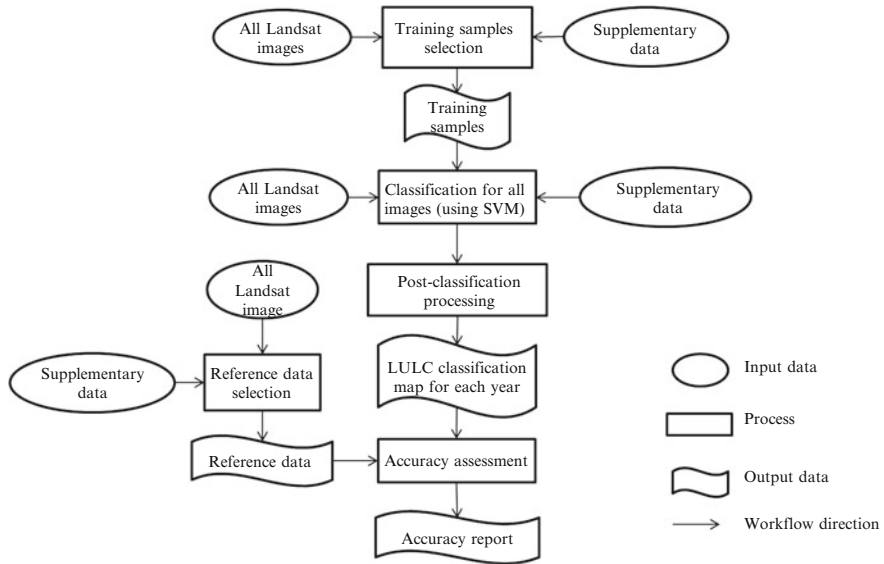


Fig. 4.4 Workflow chart of image classification process

Remote Sensor Data” (Anderson et al. 1976) the classification design in this study has been determined at a mixed USGS Level I/II based on the consideration of spectral and spatial resolution of Landsat image. With visual interpretation and analysis of the satellite images and supplementary data, eight classes were determined. They were water, forest land, agricultural land I (green cropland), agricultural land II (fallow), low-density urban built-up area, high-density urban built-up area, grassland, and barren land. Explanations of the classes and examples of training sites are illustrated in Table 4.4. Examples are displayed in RGB by true color composite (Bands 1, 2, 3) and false color composite (Bands 2, 3, 4) of 2006 image.

One of the key factors of training samples selection is identifying relatively homogeneous pixels of each class from the satellite images. Different classes are distinguished by their different color, shape, textures, tones, and spectral signatures. Training sites are selected by visual observation of Landsat images and higher resolution orthoimages, and distinguishing spectral characteristics of each LULC type. As for the number of samples, a minimum of 10–100n pixels have been selected for each class, where n (is 6 in this study) is the number of spectral bands that is been used for classification. The total number of training samples is approximately 8,000 for each image in this study. Moreover, training samples were distributed dispersedly over the study area to obtain sufficient representative samples.

Table 4.4 Accuracy assessment of multi-temporal classification maps

	1984	1990	1996	2002	2008	2013
Overall accuracy (%)	90.37	92.90	88.67	88.55	92.08	92.84

4.3.3 Accuracy Assessment

Accuracy assessment requires unbiased design, strict sampling procedures, and rigorous analysis of the classification results to make the accuracy itself reliable (Congalton and Green 1999). Some factors and issues need to be considered when performing accuracy assessment, which are reference data selection, sample size, sampling schemes, assessment techniques (confusion error matrix), etc. (Congalton 1991). Reference data were selected on Landsat images based on visual interpretation of the high resolution orthoimages to identify the pixel type. As for the sample size, it has been minimized to reduce the cost and time, and also has a large enough to generate an appropriate error matrix (Congalton and Green 1999). A general guideline is to collect a minimum of 50 samples for each land cover type (Congalton and Green 1999). In this study, a more reliable sample size determination method Thompson (1992) was used. When investigating the accuracy of multi-class classification map, sample size can be calculated by:

$$N = \frac{B\Pi_i(1 - \Pi_i)}{b_i^2} \quad (4.1)$$

where N is the sample size; Π_i is the proportion of the i th class out of all classes that has the proportion closest to 50 %; b_i is the desired precision; B is determined from the chi-squared (χ^2) table that B is the upper $(\alpha/k) \times 100$ th percentile of the χ^2 distribution with one degree of freedom; α is the allowable probability of error; and k is the number of classes. When determine the sample size before performing accuracy assessment, the allowable probability of error α should be determined first (Thompson 1992). $100\%(1-\alpha)$ is called the confidence interval. Confidence interval is a very important parameter of estimating the sample size, because generally it shows the reliability of an estimation (Thompson 1992). In this study, α and b_i was set to be 0.05 and 0.05 respectively. χ^2 value that used to determine B was $1 - 0.99375$. Then B was obtained as 7.568 from the chi-squared table. Since the values of Π_i varied from image to image of different years, 2006 classification map was taken as an example here. The value of Π_i was 39 %. Then sample size can be determined as 720.

Sampling scheme is another important factor that needs to be considered before accuracy assessment. Stratified random sampling scheme was employed in this study to ensure that sufficient samples can be selected for each class. This method considers classes as strata; then certain number of sample points can be selected randomly without bias within each stratum (Thompson 1992).

4.3.4 Change Detection Method

The change detection method that used in this study is post-classification change detection. LULC information of each year was extracted to detect changes. To fully understand the change occurred in recent three decades, multi-temporal (in 6-year interval) and time-serial change analyses were performed. The logic of change detection analysis and some major outputs are illustrated in Fig. 4.5.

In order to minimize the vegetation phenological effect and periodic cultivation cycle of agriculture in suburban and rural area, green cropland, fallow, and grassland were combined into one category, which is called “vegetated area”. Forest land was not combined into the new class because forest is important natural resource that needs to be considered individually. Other classes also remained the same. Then LULC information was extracted for change detection analyses. Analyses were conducted both qualitatively and quantitatively. Multi-temporal analysis has detected changes based on classification maps in 6-year interval, which were 1984, 1990, 1996, 2002, 2008, and 2013 classification maps. Time-serial analysis is used in all images to illustrate the trajectories of each LULC type change dynamics over these three decades. Various graphics and tables have been created to help interpret and analyze the results shown in Fig. 4.5. For example, change maps demonstrating

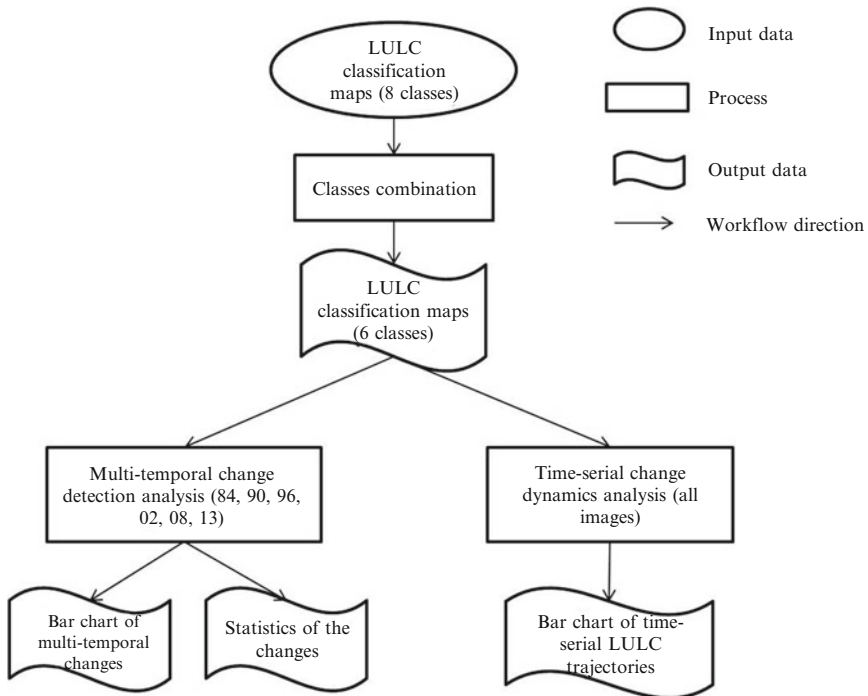


Fig. 4.5 Workflow chart of change detection analysis

significant spatial change of LULC types can be obtained; and confusion matrix showing very detailed statistical “from-to” information of each class can be generated.

4.4 Change Detection Analysis

4.4.1 Multi-temporal Change Detection Analysis

To detect relatively more detailed change processes over the 30-year time period than bi-temporal approach, multi-temporal change detection has been conducted with 6-year interval. The classification maps extracted from the satellite images of the years 1984, 1990, 1996, 2002, 2008, and 2013 have been used for analysis (Fig. 4.6). Overall accuracy of each classification map is shown in Table 4.4. All classification maps have shown a high overall accuracy. The growth process of built-up area are detected roughly by visual interpretation of the maps. It is obvious that both low-density built-up area and high-density built-up area expand outward in general. Low-density area grows surrounding the existing built-up area in Waterloo and Kitchener region, while it grows eastward and southward in Cambridge. As for high-density built-up area, a significant growth has been occurred in the following areas: (a) north of Waterloo, (b) south of Kitchener, and (c) middle of Cambridge. Another emergence of high-density industrial area is detected near the boundary of Kitchener and Cambridge with rapid growth. In addition to outward growth, high-density built-up area also has inward growth pattern which increases



Fig. 4.6 Classification maps of (a) 1984, (b) 1990, (c) 1996, (d) 2002, (e) 2008, and (f) 2013

Table 4.5 Statistics of multi-temporal LULC net change

Time period		Water	Forest land	Vegetated area	Low-density urban area	High-density urban area	Barren land
1984–1990	km ²	-0.848	-1.981	-20.898	10.941	4.694	8.113
	%	-0.27	-0.62	-6.58	3.44	1.48	2.55
1990–1996	km ²	0.321	15.535	-28.716	9.937	5.633	-2.748
	%	0.10	4.89	-9.04	3.13	1.77	-0.87
1996–2002	km ²	-0.543	-4.541	-24.634	24.818	1.912	2.984
	%	-0.17	-1.43	-7.75	7.81	0.60	0.94
2002–2008	km ²	0.761	-6.430	-3.880	8.124	5.609	-4.252
	%	0.24	-2.02	-1.22	2.56	1.77	-1.34
2008–2013	km ²	0.046	-2.355	-3.040	8.756	1.042	-4.174
	%	0.01	-0.74	-0.96	2.76	0.33	-1.31
1984–2013	km ²	-0.263	0.228	-81.168	62.577	18.889	-0.077
	%	-0.08	0.07	-25.54	19.69	5.94	-0.02

built-up density inside urban area. Correspondingly, the coverage of vegetated area shrinks. Some barren lands detected in earlier years and are replaced by built-up area successively. Furthermore, the newly emerged barren lands are mostly located on the fringe of the urban built-up area.

To detect specific change processes quantitatively, the area and percentage of change of each class over each time interval are calculated and summarized in Table 4.5. Looking at the table we can see that only a vegetated area experiences constant shrinkage during each time period with total loss of about 81 km². To the contrary, coverage of both low-density and high-density built-up area keeps increasing and the expanded areas are about 63 km² and 19 km² respectively. As for forest land, it only has gained in coverage during 1990–1996 period; and over other time period, the area decreases slightly and constantly. Comparatively, gain and loss of coverage of water and barren land are erratic. To more intuitively detect the change process of each class over this time span, the area net changes is represented by percentage in municipality area of each class and are shown in Fig. 4.7. Much of the change occurs during time period of 1990–1996 and 1996–2002, while least change occurs during 2008–2013 according to the present research. Gain in urban area is mainly cost by the loss of great amount of vegetated area and small portion of forest land. It is clearly shown that vegetated area experiences constant great loss from 1984 to 2002 with a decrease about 23 % of the entire municipality area. Low-density built-up area increases most rapidly during 1996–2002 time period and the gaining area is about 8 %. During other four time periods, low-density urban area grows at similar rates and they are about 3 % in average. High-density urban area grows relatively slower than low-density urban area. The most rapid growth occurs during 1990–1996 and 2002–2008 time period with increasing area about 2 %. Barren land fluctuates around gain and loss within the 30 years. And water experiences very subtle change that is not easy to detect.

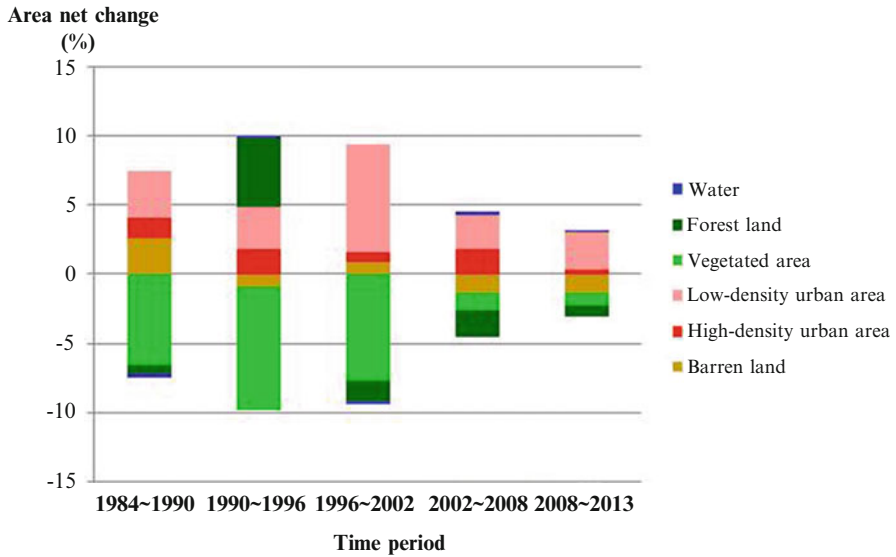


Fig. 4.7 Normalized net change in municipality area by time period for each LULC class

4.4.2 Change Dynamics Analysis

In terms of coarsely multi-temporal change detection method, intermediate LULC classification maps have been generated with given time interval and are used and analyzed to reveal the change processes during the time period. However, to detect more complex dynamics of LULC changes, all classification maps need to be involved to accomplish time-serial analysis. A trajectory of change process of each class is clearly illustrated in Fig. 4.8. It shows a dynamic change of each class too.

Obviously, urban built-up area experiences growth over the 30 years in general. However, based on the statistics recorded in Table 4.6, the overall trend of built-up area has been increased, but the process is torturous. The area increases in 1 year, but falls back slightly in next year and increases again in later years. For example, according to the table total percentage of built-up area is 48.3 % in 2002, but the value decreases to 47.9 % in 2003 and rebounds to 51.3 % in 2005. The situation of vegetated area is similar as built-up area that the coverage decreases over the period but experiences fluctuation. As for forest land and barren land, they have erratic change throughout the years, while water cover keeps relatively stable values around 2 %. Based on the observation of built-up area over the entire time span, the Region of Waterloo has experienced relatively accelerating urbanization process in 1990s and in early 2000s.

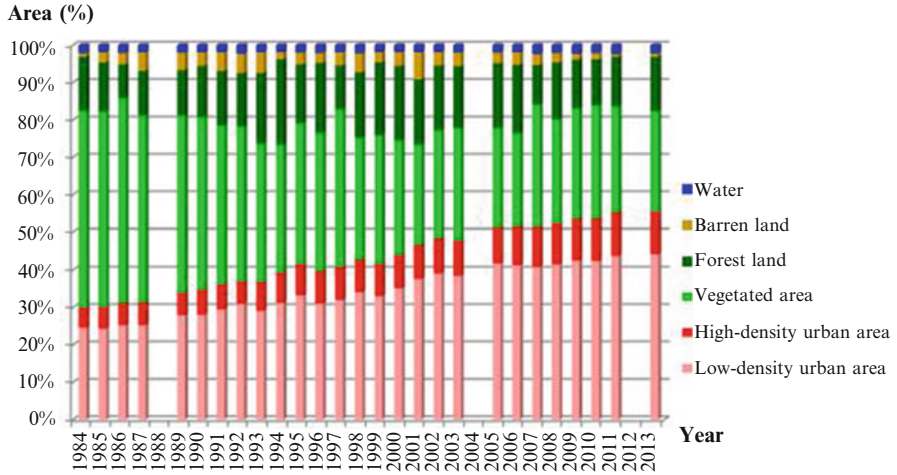


Fig. 4.8 LULC dynamic change from 1984 to 2013

Table 4.6 Percentage of each class in municipality area for each year

Class Year	Water (%)	Forest land (%)	Vegetated area (%)	Low-density urban area (%)	High-density urban area (%)	Barren land (%)
1984	2.14	14.37	52.44	24.71	5.32	1.03
1985	1.75	13.06	52.09	24.42	5.79	2.88
1986	2.09	8.99	54.67	25.31	5.82	3.09
1987	1.84	12.02	49.79	25.35	5.98	5.03
1989	1.97	12.21	47.22	28.01	5.92	4.67
1990	1.89	13.71	45.95	28.09	6.74	3.64
1991	1.83	14.58	42.34	29.59	6.56	5.07
1992	2.22	14.31	41.21	30.97	6.03	5.21
1993	1.83	18.88	36.93	29.20	7.56	5.58
1994	1.78	22.83	33.99	31.26	8.09	2.03
1995	1.93	15.74	37.56	33.27	8.31	3.19
1996	2.03	18.65	36.83	31.11	8.61	2.77
1997	1.92	11.65	42.01	32.09	8.80	3.50
1998	2.18	17.57	32.41	34.17	8.64	5.04
1999	1.74	19.41	34.29	33.07	8.63	2.85
2000	1.79	19.97	30.43	35.21	8.87	3.70
2001	1.82	17.43	26.70	37.71	8.99	7.32
2002	1.82	17.31	28.92	39.14	9.19	3.62
2003	1.99	16.53	29.92	38.49	9.43	3.62
2005	2.01	17.28	26.51	41.83	9.51	2.83
2006	1.90	18.39	24.85	41.39	10.15	3.29
2007	2.35	10.53	32.72	40.91	10.50	2.98
2008	2.09	15.16	27.77	41.49	10.90	2.55
2009	2.25	13.03	29.49	42.55	11.03	1.63
2010	2.06	12.31	30.14	42.48	11.27	1.73
2011	2.32	13.25	28.44	43.89	11.32	0.78
2013	2.19	14.50	26.80	44.37	11.29	0.98

4.5 Discussion

With the free access to Landsat archive data, LULC change dynamics can be completely explored by extracting LULC information from the temporally dense and extensive time-serial classification maps. Complexities of LULC change of urban systems of the Region of Waterloo have been successfully detected. One major finding has been obtained from the time-serial trajectory analysis and it shows that LULC change processes of urban area of the Region of Waterloo are very complex, not simply increasing or decreasing all the way. Taking built-up area as an example, it experienced dramatic growth over the time period, but the coverage still had irregular fluctuation up and down during the process. Water and forest which were not supposed to change too much, also experienced observable fluctuation during this time period.

Apart from the real change, those fluctuations might be resulted from other two aspects. One is the classification error which cannot be completely eliminated because of the medium spatial resolution of Landsat data and atmospheric noise. The other one might be the phenological effects that influence the classification results. Under this circumstance, the use of long-term dense datasets reveals its superiority of reducing the impacts caused by those factors. Time-series trajectory analysis detects the long-term change of complex ecosystems in a macroscopic view and reducing reliance on one single classification map. For example, it can be detected that there was an acceleration of growth of urban built-up area of the Region of Waterloo in 1990s and deceleration in late 2000s. Such valuable information of change complexities are required by environmental researchers and decision makers. However, it cannot be detected by bi-temporal method or coarsely multi-temporal method.

4.6 Limitations and Uncertainties

Based on the case study of the Region of Waterloo there are some limitations and uncertainties of performing change dynamics analysis. From the data perspective, in order to detect long-term dynamic change of urban area the remote sensing data are required for sufficiently dense and extensive in time. With long-term record and free open policy Landsat archive data is the best choice for this study. However, Landsat data with medium spatial resolution (30 m) cannot detect every subtle object on land surface. Therefore, classification errors should be counted in a study since it cannot be eliminated. In addition, in this study a classification was performed on each Landsat image taken from 1984 to 2013 except for 1988, 2004, and 2012. Training samples were selected for each year. In this way, the quality of classification maps can be guaranteed because the training samples are sufficient. However, for high dense dataset selecting training samples for each year was a huge task in this study. The work might become more burdensome when the

study area is large. Additionally, it is hard to control all sets of training samples with the same quality. Therefore, effective image normalization methods should be developed to let training sample selection process much easier. During classification process parameters determination of using SVM is critical for obtaining the best result. Also, it is difficult to determine which combination of the parameter setting is the most superior.

4.7 Recommendations

Based on both the superiorities and limitations of this study, some potential future studies are proposed here. With the global coverage of Landsat data, the time-serial change detection method can also be applied to other cities or metropolitan areas or even global scale to detect the LULC dynamic change. As for urban area analysis by using remote sensing data, an effort can be given into improving the urban area classification result. Since machine learning classifiers can deal with high dimensional dataset, various input features can be integrated together to investigate their effectiveness of improving the classification result. Moreover, the time-serial remote sensing data, GIS data and socio-economic data can be also incorporated to generated more accurate urban growth model. Furthermore, the accessibility of long-term Landsat record also makes it possible to detect time-serial dynamic change of different land cover types, such as dynamic change of forest cover, glacier, watershed and coastline.

4.8 Summary

This chapter gives an introduction of long-term change detection from a different perspective. By using long-term high-dense Landsat dataset, specific detailed LULC change dynamics can be extracted based on per-image classification. Compared to coarsely multi-temporal change detection, long-term trajectory of LULC dynamic change can provide higher-order complexities of LULC change. Information, such as acceleration and deceleration can be analyzed. The detailed long-term change processes are very valuable information for planners and governments to understand the causes and consequences of LULC change to make more appropriate and effective regulations and policies for better planning and environmental management.

References

- Abd El-Kawy OR, Rød JK, Ismail HA, Suliman AS (2011) Land use and land cover change detection in the western Nile delta of Egypt using remote sensing data. *Appl Geogr* 31(2):483–494

- Afify HA (2011) Evaluation of change detection techniques for monitoring land-cover changes: a case study in new Burg El-Arab area. *Alex Eng J* 50(2):187–195
- Alphan H (2011) Comparing the utility of image algebra operations for characterizing landscape changes: the case of the Mediterranean coast. *J Environ Manage* 92(11):2961–2971
- Alumutairi A, Warner TA (2010) Change detection accuracy and image properties: a study using simulated data. *Remote Sens* 2:1508–1529
- Anderson JR, Hardy EE, Roach JT, Witmer RE (1976) A land use and land cover classification system for use with remote sensor data. United States Government Printing Office, Washington
- Benediktsson JA, Chanussot J, Fauvel M (2007) Multiple classifier systems in remote sensing: from basics to recent developments. *MCS 2007. LNCS 4472*:501–512
- Bhatta B (2010) Analysis of urban growth and sprawl from remote sensing data, Elsevier
- Byrne GF, Crapper PF, Mayo KK (1980) Monitoring land-cover change by principal component analysis of multitemporal landsat data. *Remote Sens Environ* 10(3):175–184
- Congalton R (1991) A review of assessing the accuracy of classifications of remotely sensed data. *Remote Sens Environ* 46:35–46
- Congalton RG, Green K (1999) Assessing the accuracy of remotely sensed data: principles and practices. CRC Press, New York. ISBN 0-87371-986-7
- Coppin P, Jonckheere I, Nackaerts K, Muys B, Lambin E (2004) Digital change detection methods in ecosystem monitoring: a review. *Int J Remote Sens* 25(9):1565–1596
- Dawelbait M, Morari F (2012) Monitoring desertification in a Savannah region in Sudan using Landsat images and spectral mixture analysis. *J Arid Environ* 80:45–55
- Deng JS, Wang K, Li J, Deng YH (2009) Urban land use change detection using multisensor satellite images. *Pedosphere* 19(1):96–103
- Frohn R, Arellano-Neri O (2005) Improving artificial neural networks using texture analysis and decision trees for the classification of land cover. *GISci Remote Sens* 42(1):44–65
- Gislason PO, Benediktsson JA, Sveinsson JR (2006) Random forests for land cover classification. *Pattern Recogn Lett* 27(4):294–300
- Hansen MC, Loveland TR (2012) A review of large area monitoring of land cover change using Landsat data. *Remote Sens Environ* 122:66–74
- Hayes DJ, Sader SA (2001) Comparison of change detection techniques for monitoring tropical forest clearing and vegetation regrowth in a time series. *Photogramm Eng Remote Sens* 67(9):1067–1075
- Huang C, Davis LS, Townshend JRG (2002) An assessment of support vector machines for land cover classification. *Int J Remote Sens* 23(4):725–749
- Huang Y, Fipps G, Lacey RE, Thomson SJ (2011) Landsat satellite multi-spectral image classification of land cover and land use changes for GIS-based urbanization analysis in irrigation districts of Lower Rio Grande Valley of Texas. *Appl Remote Sens J* 2(1):27–36
- IRS (2013) ITC's database of satellites and sensors, Faculty of geo-information science and earth observation (ITC). University of Twente. Retrieved from: <http://www.itc.nl/research/products/sensordb/AllSatellites.aspx>
- Jensen JR (2005) Introductory of digital image processing: a remote sensing perspective, 3rd edn. Pearson Education, Hardcover, USA, ISBN 0-13-145361-0
- Jensen JR (2006) Remote sensing of the environment: an earth resource perspective, 2nd edn. Pearson Education, Hardcover, USA, ISBN 0-13-188950-8
- Jha CS, Unni NVM (1994) Digital change detection of forest conversion of a dry tropical Indian forest region. *Int J Remote Sens* 15(13):2543–2552
- Kaufmann RK, Seto KC (2001) Change detection, accuracy, and bias in a sequential analysis of Landsat imagery in the Pearl River Delta, China: econometric techniques. *Agr Ecosyst Environ* 85(1–3):95–105
- Kleynhans W, Olivier JC, Wessels KJ, Salmon BP, van den Bergh F, Steenkamp K (2011) Detecting land cover change using an extended Kalman filter on MODIS NDVI time-series data. *IEEE Geosci Remote Sens Lett* 8(3):507–511

- Kotsiantis SB (2007) Supervised machine learning: a review of classification techniques. *Informatica* 31:249–268
- Lu D, Weng Q (2004) Spectral mixture analysis of the urban landscape in Indianapolis with Landsat ETM+ imagery. *Photogramm Eng Remote Sens* 70(9):1053–1062
- Lu D, Weng Q (2007) A survey of image classification methods and techniques for improving classification performance. *Int J Remote Sens* 28(5):823–870
- Lunetta RS, Elvidge CD (1998) Remote sensing change detection: environmental monitoring methods and applications. Sleeping Bear Press, Ann Arbor. ISBN 1-57504-037-9
- Lunetta RS, Johnson DM, Lyon JG, Crowell J (2004) Impacts of imagery temporal frequency on land-cover change detection monitoring. *Remote Sens Environ* 89:444–454
- Macleod RD, Congalton RG (1998) A quantitative comparison of change-detection algorithms for monitoring eelgrass from remotely sensed data. *Photogramm Eng Remote Sens* 64(3):207–216
- Manavalan P, Kesavasamy K, Adiga S (1995) Irrigated crops monitoring through seasons using digital change detection analysis of IRS-LISS 2 data. *Int J Remote Sens* 16(4):633–640
- Mellor A, Haywood A, Stone C, Jones S (2013) The performance of random forests in an operational setting for large area sclerophyll forest classification. *Remote Sens* 5(6):2838–2856
- Nemmour H, Chibani Y (2011) Support vector machines for automatic multi-class change detection in Algerian Capital using landsat TM imagery. *J Indian Soc Remote Sens* 38(4):585–591
- Pal M (2005) Random forest classifier for remote sensing classification. *Int J Remote Sens* 26(1):217–222
- Pal M, Mather PM (2005) Support vector machines for classification in remote sensing. *Int J Remote Sens* 26(5):1007–1011
- Parra GA, Mouchot MC, Roux C (1996) A multitemporal land-cover change analysis tool using change vector and principal components analysis. *IEEE 0-7803-3068-4/96*, pp 1753–1755
- Patino JE, Duque JC (2013) A review of regional science applications of satellite remote sensing in urban settings. *Comput Environ Urban Syst* 37:1–17
- Peiman R (2011) Pre-classification and post-classification change-detection techniques to monitor land-cover and land-use change using multi-temporal Landsat imagery: a case study on Pisa Province in Italy. *Int J Remote Sens* 32(15):4365–4381
- Prakash A, Gupta RP (1998) Land-use mapping and change detection in a coal mining area — a case study in the Jharia coalfield, India. *Int J Remote Sens* 19(3):391–410
- Region of Waterloo (2006a) Regional Growth Management Strategy (RGMS). Retrieved from: <http://www.regionofwaterloo.ca/en/aboutTheEnvironment/resources/RegionalGrowthManagement.pdf>
- Region of Waterloo (2006b) Regional Growth Management Strategy (RGMS) highlights brochure. Retrieved from: Region of Waterloo (2006) Regional Growth Management Strategy (RGMS) highlights brochure. Retrieved from: <http://www.regionofwaterloo.ca/en/aboutTheEnvironment/resources/FINALRGMSBrochure2006.pdf>
- Region of Waterloo (2010) Regional Official Plan (ROP). Retrieved from: <http://www.regionofwaterloo.ca/en/regionalGovernment/PreviousROP.asp>
- Ridd MK, Hipple JD (2006) Remote sensing of human settlements: manual of remote sensing, 3rd edn. American Society for Photogrammetry and Remote Sensing. ISBN 1-57083-077-0
- Sexton JO, Urban DL, Donohue MJ, Song C (2013a) Long-term land cover dynamics by multi-temporal classification across the Landsat-5 record. *Remote Sens Environ* 128:246–258
- Sexton JO, Song X, Huang C, Channan S (2013b) Urban growth of the Washington, D.C.-Baltimore, MD metropolitan region from 1984 to 2010 by annual, landsat-based estimates of impervious cover. *Remote Sens Environ* 129:42–53
- Singh A (1989) Digital change detection techniques using remotely-sensed data. *Int J Remote Sens* 10(6):989–1003
- Sleeter BM, Wilson TS, Acevedo W (2012) Status and trends of land change in the Western United States – 1973 to 2000: USGS professional paper 1794–A, 324 p. Retrieved from: <http://pubs.usgs.gov/pp/1794/a/>

- Song X, Duan Z, Jiang X (2012) Comparison of artificial neural networks and support vector machine classifiers for land cover classification in Northern China using a SPOT-5 HRG image. *Int J Remote Sens* 33(10):3301–3320
- Statistics Canada (2011) Focus on geography series, 2011 census. Retrieved from: <http://www12.statcan.gc.ca/census-recensement/2011/as-sa/fogs-spg/Facts-pr-eng.cfm?Lang=Eng&GK=PR&GC=35>
- Sundarakumar K, Harika M, Begum SKA, Yamini S, Balakrishna K (2012) Land use and land cover change detection and urban sprawl analysis of Vijayamada city using multitemporal Landsat data. *Int J Eng Sci Technol* 4(01):170–178
- Tan KC, Lim HS, MatJafri MZ, Abdullah K (2009) Landsat data to evaluate urban expansion and determine land use/land cover changes in Penang Island, Malaysia. *Environ Earth Sci* 60(7):1509–1521
- Tang J, Wang L, Yao Z (2008) Analyses of urban landscape dynamics using multi-temporal satellite images: a comparison of two petroleum-oriented cities. *Landsc Urban Plan* 87(4):269–278
- Thapa RB, Murayama Y (2009) Urban mapping, accuracy, & image classification: a comparison of multiple approaches in Tsukuba City, Japan. *Appl Geogr* 29(1):135–144
- Thompson SK (1992) *Sampling*. Wiley, New York. ISBN 0-471-54045-5
- Tian G, Jiang J, Yang Z, Zhang Y (2011) The urban growth, size distribution and spatio-temporal dynamic pattern of the Yangtze River Delta megalopolitan region, China. *Ecol Model* 222(3):865–878
- USGS (2013a) Landsat 8. Fact sheet 2013–3060. Retrieved from: <http://pubs.er.usgs.gov/publication/fs20133060>
- USGS (2013b) Landsat-A global land-imaging mission. Fact sheet 2012-3072. Retrieved from: <http://pubs.usgs.gov/fs/2012/3072/fs2012-3072.pdf>
- USGS (2013c) Landsat 8. Retrieved from: <http://landsat.usgs.gov/landsat8.php>
- USGS (2013d) Landsat project statistics. Retrieved from: http://landsat.usgs.gov/Landsat_Project_Statistics.php
- USGS (2013e) Landsat project description. Retrieved from: http://landsat.usgs.gov/about_project_descriptions.php
- USGS (2013f) Landsat processing details. Retrieved from: http://landsat.usgs.gov/Landsat_Processing_Details.php
- Wulder MA, White JC, Masek JG, Dwyer J, Roy DP (2011) Continuity of Landsat observations: short term considerations. *Remote Sens Environ* 115:747–751
- Yang X (2002) Satellite monitoring of urban spatial growth in the Atlanta Metropolitan area. *Photogramm Eng Remote Sens* 68(7):725–734
- Yang L, Xian G, Klaver JM, Deal B (2003) Urban land-cover change detection through sub-pixel imperviousness mapping using remotely sensed data. *Photogramm Eng Remote Sens* 69(9):1003–1010
- Yin J, Yin Z, Zhong H, Xu S, Hu X, Wang J, Wu J (2011) Monitoring urban expansion and land use/land cover changes of Shanghai metropolitan area during the transitional economy (1979–2009) in China. *Environ Monit Assess* 177(1–4):609–621
- Yuan F, Sawaya KE, Loeffelholz BC, Bauer ME (2005) Land cover classification and change analysis of the Twin Cities (Minnesota) Metropolitan area by multitemporal Landsat remote sensing. *Remote Sens Environ* 98(2–3):317–328
- Zha Y, Gao J, Ni S (2003) Use of normalized difference built-up index in automatically mapping urban areas from TM imagery. *Int J Remote Sens* 24(3):583–594
- Zhao H, Chen X, Area AS (2005) Use of normalized difference bareness index in quickly mapping bare areas from TM/ETM+. *IEEE Trans Geosci Remote Sens* 4(5):1666–1668

Chapter 5

Influence of Political Regime Change to Land Use Development in Urban Areas in the Czech Republic

Lena Halounová and Vladimír Holubec

Abstract This chapter focuses on the development of some selected cities in the Czech Republic during the last 40 years. This time period has two halves. The first one is before 1990 when the country was part of Czechoslovakia, one of the communist countries; the second period covers a democratic regime after 1990. Land use development of dozens of cities was analyzed on the base of basic land use classes. These classes allow in an objective way to compare all the cities. The development is shown through values of 14 attributes for cities grouped into 3 categories – big, medium and small cities. Spatial values show land use development as total areas of land use classes and as ratios of the number of inhabitants and land use areas. All the values are also related to road traffic intensity, as one of the most important indicators of the development of society in the last 40 years. Time development of the values of the indicators, multiple linear regression and correlation for both periods were used to show their dependency on road traffic intensity. The main conclusion from this analysis is that the political change followed by economical change had a strong impact on some of the land use class changes and road traffic intensity.

Keywords Land use • GIS • Multiple linear regression • Road traffic intensity • Correlation coefficient

5.1 Introduction

Stimulating the development of human society is based on production, the exchange and consumption of goods and other products of human activity. Transport routes substantially influence the dynamics in an increase of production and exchange. The main carrier of these economic relations is road transport; which has

L. Halounová (✉) • V. Holubec
Faculty of Civil Engineering, Czech Technical University in Prague, Thákurova 7,
166 29 Prague 6, Czech Republic
e-mail: halounov@gmail.com; vladimir.holubec@fsv.cvut.cz

© Springer Science+Business Media Dordrecht 2015
J. Li, X. Yang (eds.), *Monitoring and Modeling of Global Changes: A Geomatics Perspective*, Springer Remote Sensing/Photogrammetry,
DOI 10.1007/978-94-017-9813-6_5

87

the highest transport volume. The quick growth of cities/towns, the development of urbanization in other words, is closely connected with large investments in traffic infrastructure, mainly roads (Vepřek 2000, 2009).

Urbanization is an important phenomenon of the last 50 years which has occurred in most countries of the world and has resulted in larger cities, even megacities. It is not the case in the Czech Republic. Urbanization is accompanied by many problems in the environment and human life. It is the reason why urban development is analyzed by many authors. One of the most important impacts of the political change in the Czech Republic is the growth of road traffic intensity, which is a source of increasing noise and emissions since other sources of emissions – industry and heating – were substantially lowered by protecting devices and changes in heating sources.

Urbanism is influenced by many indicators. This paper deals with some of them under two different political regimes. The political regimes in the Czech Republic differ in prevailing parts in the socio-economic situation of a high number of the population. Analyses of urban development under different political regimes were not publicized very often. Anthony (2014) took into account political influence and analyzed the 5 largest cities of 123 nations from 1960 to 2005. He focused on political determinants on urban population distributions, tested and evaluated four hypotheses related to the length of capital status as well as colonial, democratic, and communist experiences. The main findings suggest that the length of a nation's largest city's capital status is positively associated with urban primacy. Conversely, nations with longer democratic or communist regimes have lower levels of urban primacy while the results from colonial experience are curvilinear. China is not a country where a sharp political change has occurred, however, economic development is significant. Yen and Wu (2014) show in their study for 1999–2009 period that 286 Chinese prefecture-level cities with higher real estate investment pushed towards higher urbanization. Political influences can be found in Newton and Schuermans (2013) who studied housing, spatial planning and urban development in post-apartheid South Africa and found an important improvement in housing conditions carried out by various bodies. Local political changes since 1960s influencing the relation between transport and urban development in four cities in Switzerland on one side and France on the other side are described in Gallez et al. (2013). They analyzed the contents of master plans, principal technical solutions and projects that have been implemented, and the means of inter-sectorial coordination used. Stead (2001) found that more socio-economic reasons than land-use characteristics had an impact on travel conditions. These were mainly socio-economic conditions which changed in post-communist countries thanks to new political regimes.

Urban development in this paper was analyzed by 13 indicators in relation to road traffic intensity as an important impact of development of urban areas under different political regimes (Halounová and Holubec 2014). Many authors have studied this topic under a given political situation from the transport energy consumption view (Kitamura et al. 1997; Næss and Sandberg 1996; Handy 1992). Litman and Steele (2013) describes the methods for evaluating how transport planning decisions influence land use – and how land use planning decisions

affect transport. He uses 12 factors as a location of development relative to the regional urban centre, which reduces vehicle mileage per capita. The higher number of people or jobs per unit areas reduces vehicle ownership, etc. He mentions that the actual impacts will vary depending on the specific conditions and combinations of applied factors. Similar argumentation about the relation between transportation and land use can be found in (Jacobson 2003) who states that land use type distribution and transportation systems are interdependent. The affects of various land use characteristics on travel activity were analyzed in many other publications (e.g. Barla et al. 2011; Ewing and Cervero 2010; Kuzmyak et al. 2006; Ristimäki and Kalenoja 2011).

The relation between transport and land use has an impact on business analysis, especially access management. Banister (2011a) and Banister et al. (2011) emphasize that transportation infrastructure is one of the crucial phenomena of economic development, which is a typical feature that changed in two different political regimes in the Czech Republic. The increasing trend of road traffic is unsustainable (Banister 2011b) causing high energy consumption. He suggests reducing energy consumption based on a change of travel habits taking in to account to land use and its planning.

Some other authors focus on this topic from the point of view of commuting. Ma and Banister (2007) deal with commuting and its efficiency linked to the urban form. They take into account excess commuting (additional journey-to-work travel represented by the difference between the actual average commute and the smallest possible average commute, given the spatial configuration of workplaces and residential sites). Another type of analysis is of urban expansion by the gradient analysis of multi-temporal data and the influence of road traffic (Fan et al. 2009).

5.2 Cities in the Czech Republic

A city or town is a geographical area with a set of attributes differentiating it from a village. These attributes are the relative size of the area if we compare it with villages, density of population, compactness, and concentration of urban areas. Inhabitants of cities have typical demographic, social and professional structures, as their employment is in services, industry, and business offering managing, educational business and cultural functions for larger surrounding areas.

The history of cities in the Czech Republic is similar to other European countries. Multifunctional centralized places came into being during the early Medieval Ages. Places were more densely occupied and their inhabitants were not employed in agriculture. These places were situated close to castles or bishop's seats, and monasteries in prevailing parts. The other reasons were suitable locations for mercantile travelling, crossing of paths, places near fords or springs. These centers accumulated crafts and markets. This city pattern is formed by centralized areas with many job opportunities and surrounding areas dedicated to residential, productivity and other areas.

There are only a low number of cities in the Czech Republic whose history is different. Ostrava, one of these processed cities, is such an example. It is a city, which is not centralized as other Czech cities even though it is the third largest city in the country as far as number of inhabitants. Ostrava (north-eastern part of the Czech Republic) arose from the small city of Moravian Ostrava and seven neighbouring settlements in the period of opening hard coal mines in the eighteenth century and the development of heavy industry plants – steelworks in the nineteenth century. The city of Ostrava as a unit has existed only since 1924.

There are 593 cities in the Czech Republic. The largest one is Prague with more than 1,290 million inhabitants. According to the present Czech law about municipalities, the lowest number of inhabitants to become a city is 3,000.

One fifth of the inhabitants of the Czech Republic live in its three largest cities – Prague, Brno and Ostrava. Moving people from rural areas to cities is a trend that occurs in the Czech Republic as well as in many parts of the world.

The Czech Republic was a part of Czechoslovakia with the communist political regime before 1990. The regime did not allow its inhabitants to become owners of enterprises, companies, etc. All decisions about land use/land cover were performed by the government, and local, district and regional representatives of the communist party according to a planning system of short or long periods. The change to the political system at the end of 1989 brought substantial development in many spheres. The previous society, where most of the population was practically on one standard of living without important differences, started to differentiate after 1990. This differentiation created a more layered society, which is allowed and able to control and manage the country taking into account also the financial aspects of individual decisions. The impact of this new way of thinking and management can be also found in, for better or worse, land use development.

5.3 Methodology

5.3.1 *Definition of Terms of Urban Areas*

The urban development of Czech cities after 1970 was a reason why parts of their areas have individual names of urban areas classification. The urban changes (highlighted below) were allowed, initiated, and decided by governmental and local authorities.

- Administrative city areas are their entire areas in individual years. They were determined by local, regional and country headquarters of individual cities in individual years using cadaster data of boundaries.
- Core city areas are administrative areas of individual cities at the end of 1970s and early 1980s. The first half of 1980s was the first period when some villages in the neighborhood of cities were amalgamated; the second half of 1980s was the second period. Their land enlarged the original administrative areas of these

cities. Original city areas (before joining) were separated from these villages by agricultural and/or forested areas in many cities. Core areas and amalgamated ones did not have a common historical development and created in fact a set of individual urban areas with a central headquarter, services, etc.

- Associated areas are neighboring cadasters of villages that enlarged the core areas in 1980s.
- Peripheral areas are villages that became self-standing administrative areas. The separations occurred in the Czech Republic after the political change in the country in early 1990s.

Core areas represent compact urban areas with a common historical development – described in Sect. 5.2. – forming thus homogenous units from the point of view of urbanization. It was the reason why the authors analyzed the development within core areas of cities and administrative areas.

5.3.2 *Selected Cities*

To analyze the influence of political regimes on land use development in the Czech Republic, a set of 36 cities of various sizes was processed. These cities had a complete set of indicators of 35 year period from the end of 1970s till 2005. The communist regime covers in this analysis 1970–1989 period and the democratic one 1990–2005.

It was decided to analyze the differences in the developments of urbanization in this time scale and as a function of road traffic intensity. Road traffic intensity expresses significantly economical differentiation among the population and is one of the more important indicators of urban areas. Figure 5.1 shows a distinct break of the number of cars between both periods/regimes in examples of big cities (Brno, Ostrava, Olomouc, Hradec Králové) and small cities (Zlín and Kutná Hora).

Table 5.1 comprises of a list of all the cities which are processed in the chapter. Three groups of cities were used for processing to separate them into groups with relatively common sizes and therefore similar conditions within each group. The groups were created according to the number of inhabitants in the processed cities.

Location of the cities is in Fig. 5.2 and the position of the Czech Republic in Europe is in Fig. 5.3.

5.3.3 *Spatial Data*

Spatial data had two different sources. One of them were data of the Czech Office of Survey, Mapping and Cadastre (COSMOC) that determines administrative boundaries. Administrative areas of individual years were derived from a list of cadasters which formed the given city area in the appropriate year.

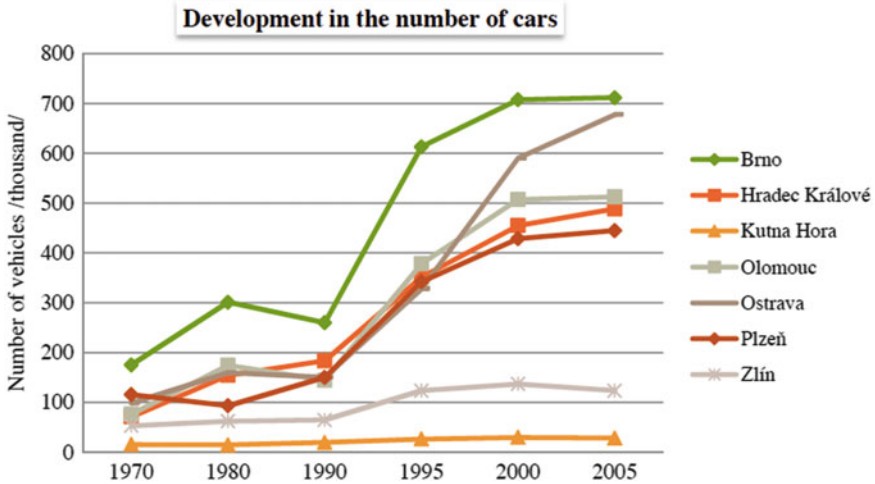


Fig. 5.1 Development of number of cars in some Czech cities since 1970

Table 5.1 List of processed cities ordered according to their number of inhabitants

Small cities number of inhabitants <30,000	Medium cities number of inhabitants ≤30,000 and <70,000	Large cities number of inhabitants ≥70,000
Písek	Kladno	Ostrava
Valašské Meziříčí	Most	Olomouc
Litvínov	Frýdek-Místek	Liberec
Český Těšín	Opava	České Budějovice
Havlíčkův Brod	Děčín	Hradec Králové
Žďár nad Sázavou	Jihlava	Pardubice
Strakonice	Chomutov	
Klatovy	Přerov	
Kutná Hora	Jablonec nad Nisou	
Náchod	Mladá Boleslav	
Mělník	Třebíč	
Česká Třebová	Znojmo	
	Příbram	
	Cheb	
	Kolín	

The second group of spatial data was determined for core areas. The group of spatial data defined land use, however, from the urban architecture point of view. Land use classes, also called functional classes, used in the analyses were residential, production, transport, recreational and other areas. They were processed from image analysis and interpretations in core city areas. These land use areas were derived using city plans (vector data), aerial orthophotos and satellite images (both are raster data). City plans represent the actual state of land use of cities and plans

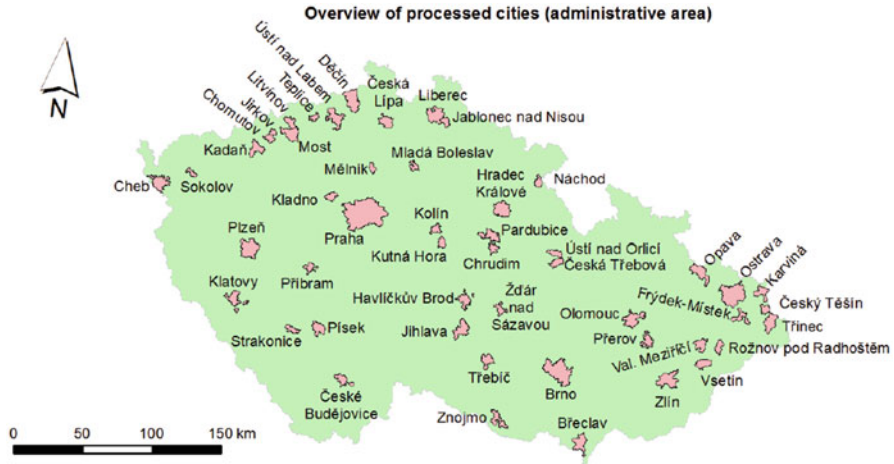


Fig. 5.2 Distribution of administrative areas of processed cities in the map of the Czech Republic



Fig. 5.3 Position of the Czech Republic in Europe

for their future. Two steps were done to determine land use data in individual years. Detailed city map classes of the latest period were simplified and aggregated (see Table 5.2) and thus more general classes were formed. Detailed class polygons were edited according to the real land use state by eliminating areas only planned and merged into the above-mentioned simplified five land use classes and respective polygons.

Table 5.2 Aggregation of detailed city map classes to functional classes

Area type in city plan	Complex type of land use	Functional class
Mixed residential area	Housing	Residential areas
General residential area		
Purely residential area		
Rural residential area		
Public areas		
Central mixed area	Facilities	
Civic facilities		
Areas of work activities	Production and storage	Production areas
Production areas, industry		
Sports areas	Recreation	Recreational areas
Areas of gardening		
Parks and cemeteries	Greenery	
Gardens		
Area close to nature		
Other greenery		
Water features	Water	
Cultivated areas	Agriculture	Other areas
Vineyards		
Agricultural land		
Railway	Transport	Transportation areas
Road class I, II, III		
Local roads		

To determine land use development in individual cities GIS tools were applied. The latest GIS layer created from city maps and remote sensing data was used as the first input data to determine the previous (= older) GIS land use layer. A copy of the “younger” land use layer was edited using historical aerial photos to create the “older” one. It is a method which allows to maintain topology among layers – to avoid slivers of polygons of different years – and to make the interpretation relatively easy and quick. This is because large areas, especially in city centres, have not changed considerably within dozens of years. The mapping of these areas by editing saves time. GIS tools are irreplaceable for this time series processing – both for editing and multilayer vector data quality. Aerial photographs (20–50 pixel size) offer a suitable scale for visual interpretation. Satellite data were applied only in cases where no aerial photographs of a given city in a given year were available.

Orthophoto data were provided by COSMOC (colour orthophotos) and from the military archives (black and white photographs). Satellite Landsat data of the appropriate years were downloaded from <http://glovis.usgs.gov>. GIS vector data of land use classes were a source of spatial data functional classes for indicators in Tables 5.3 and 5.4. The functional class areas can be dated by remote sensing data measurements. Dates of measurements are dates of the data capture of aerial photographs and satellite images. The time difference between the analyzed years

Table 5.3 List of indicators and their trends of cities from Figs. 5.4, 5.5, and 5.6 in two regimes/periods

Name of indicators	Small cities 1970–1990/1990–2005	Medium cities 1970–1990/1990–2005	Big cities 1970–1990/1990–2005
Average number of inhabitants	Growth/decline	Growth/decline	Growth/decline
Average population growth in core areas	Growth/decline	Growth/decline	Growth/decline
Average ratio of number of inhabitants and core areas	Growth/decline	Growth/decline	Growth/stable
Average ratio of number of inhabitants and residential areas	Growth (up to 1995)/decline	Growth (up to 2000)/decline	Growth (up to 1995)/decline
Average ratio of population growth and residential areas	Growth/decline (growth since 2000)	Growth/growth	Decline/growth
Average ratio of number of inhabitants and administrative areas	Growth/growth	Growth/decline	Stable/decline in 2005
Average ratio of number of inhabitants and transportation areas	Growth/decline	Growth/decline	Growth/decline
Average ratio of number of inhabitants and production areas	Growth/decline	Growth/decline	Growth/decline
Development of average transportation areas in core areas	Growth/growth with smaller gradient	Growth/growth with smaller gradient	Growth/growth with smaller gradient
Development of average residential areas in core areas	Growth/growth with smaller gradient	Growth/growth with smaller gradient	Growth/growth with smaller gradient
Development of average other areas in core areas	Decline/decline	Decline/decline	Decline/decline
Development of average recreation areas in core areas	Decline/growth	Growth/growth with higher gradient	Growth/growth
Development of average production areas in core areas	Growth/growth	Growth/growth	Growth/growth

(1970, 1980, 1990, 1995, 2000 and 2005) and the remote sensing data was less than 2 years. Land use polygons of individual years were edited and topologically corrected not only for individual years, but also between years.

The application of remote sensing data and city maps data allowed to use the knowledge of urban architects and to process a reliable and objective land use of urban areas. City maps combined with aerial photographs – show and help to interpret individual land use classes. Aerial photographs are – unlike city maps – accurately dated and it is necessary for additional analyses with other data. GIS analyses are a very good method how to locate trends in the spatial development of features occurring on Earth, in individual countries, or regions. The key point is to decide what spatial/remote sensing data are suitable, especially their scale and thus

Table 5.4 List of indicators used for multiple linear regression analysis

Indicators used in	Small cities	Medium cities	Big cities
Administrative areas	x	x	x
Transportation areas	x	x	
Residential areas	x	x	
Other areas	x	x	
Recreational areas	x	x	
Production areas	x	x	
Number of inhabitants	x	x	
Population growth		x	
Number of inhabitants/traffic areas	x	x	
Number of inhabitants/production areas	x	x	x
Number of inhabitants/residential areas	x	x	x
Number of inhabitants/ administrative areas		x	x

spatial resolution, spectral bands, and temporal resolution, and to choose other data describing the features. As there are various data with similar spatial and spectral characteristics like aerial photographs and VHR data, e.g., temporal resolution, date and price can become the decisive issues.

5.3.4 Non-spatial Data

Non-spatial data were twofold. Statistical data were collected and processed from the Czech Statistical Office (CSO) and are available on their web site <http://www.czso.cz>. They are updated at least once per year. The only statistical indicator from CSO used in this chapter was the number of inhabitants in cities. The rest – 12 – of the indicators were calculated from the statistical and spatial data and are in Table 5.3. The 14th indicator is road traffic intensity.

The average number of inhabitants (see Table 5.3) is calculated for individual years as an average of value of all cities in individual groups – small, medium and big cities from statistical values in the appropriate years. Average population growth and other indicators were calculated in the same way. All these values were used in the following indicators where individual land use areas were determined from spatial data for individual years (1979, 1980. . .). Six indicators show the spatial development of land use areas and core areas in individual city groups and were determined in GIS. Six indicators were calculated as ratios between the average number of inhabitants and individual land use areas (one value for each city) and core areas.

Road traffic intensity data have been collected since 1968 and are archived by the Road and Motorway Directorate. At present this chapter comprises of the evaluations from 1973, 1980, 1990, 2000, and 2005. The Directorate measures the number of all passing vehicles in selected points within 24 h. These points are

defined by their identification numbers and geographical coordinates and are located on important roads of various classes in the entire country – both in, and outside of urban areas. Their number has increased since the first year of the measurement in 1968, however, the original points were preserved in most cases and many new ones were added in all cities.

The intensities were used as two different values – average and maximal road traffic intensities. Average road traffic intensity is a sum of the measured intensities in all points of one city core area divided by the number of the points. This value provides a chance to compare cities with an unequal number of points where road traffic intensities were measured. The number of points varied from 3 to more than 60. Maximum road traffic intensity is a sum of all arriving and departing vehicles to core areas from other directions. It provides an overview of the influences of incoming and outgoing traffic.

5.4 Method of Evaluation and Results

5.4.1 *Interpretation of Graphs of Development of Individual Indicators*

The list of analyzed indicators is in Table 5.3. The first analysis was made from individual graphs for individual indicators and groups of cities (small, medium and big). Graphs in Figs. 5.4, 5.5, and 5.6 are shortly summarized in Table 5.3.

Table 5.3 and Figs. 5.4, 5.5, and 5.6 show great differences between periods – before and after the year of 1990 separating the communist and democratic regimes. The development of the average number of inhabitants (indicator 1) grew in cities of all sizes during the communist regime and went down in cities of all sizes in the democratic regime. One of the main reasons was that the democratic regime opened a large work market and young women replaced/shifted from a “family life period” to an “active work period”. These were economical reasons which had an important social impact on society. Similar behaviour can be found in the number of inhabitants in core areas of all cities. The only difference among them is that the decline of the population in medium cities started in 1995 unlike small and big cities where the break occurred in 1990. It shows that changes appeared in small cities with a substantially lower number of work opportunities and in big cities with a far larger range of economic opportunities directly after the political change.

The positive growth of the number of inhabitants (indicator 2) lasted in all group of cities up to 1995. Trends of five indicators (3, 4, 7, 8, 11) changed in 1990 from growth to decline and/or stable. Transportation, indicator 9, residential, indicator 10, and recreational areas, indicator 12, grew in both periods, however, the gradient was lower after 1990. Production area growth has not shown a significant difference between the periods. Growth of residential, transportation, production and recreational areas was at the expense of other areas.

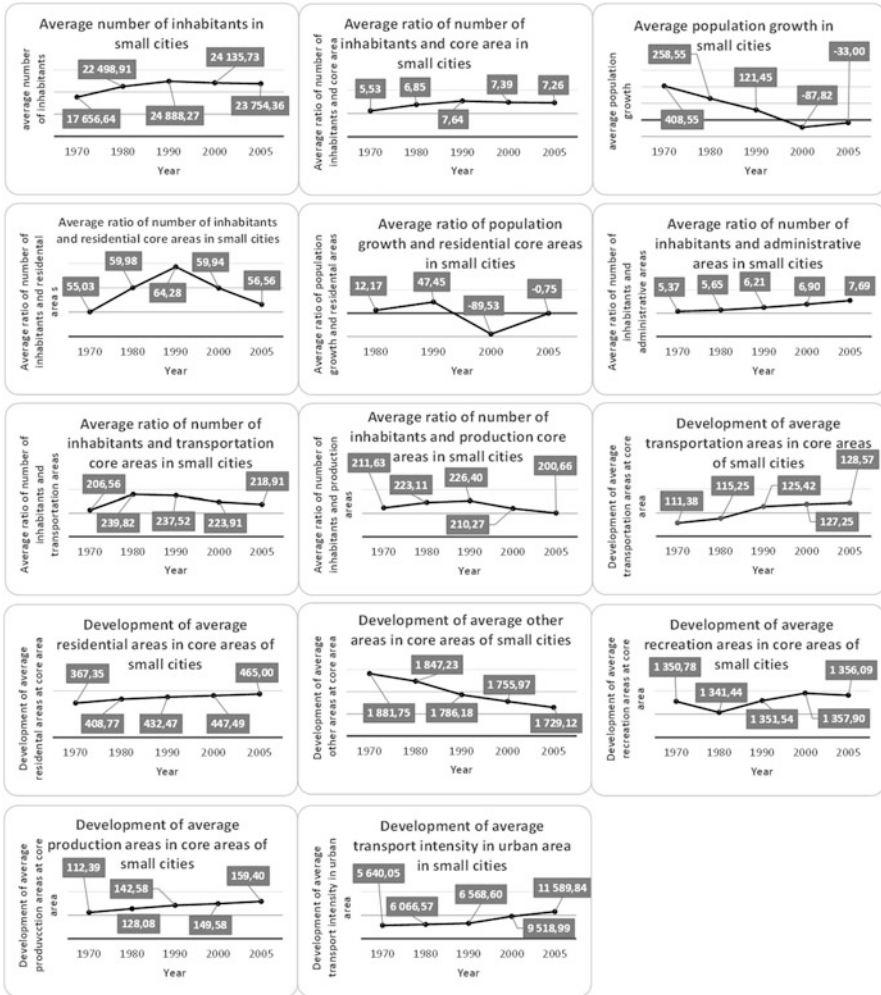


Fig. 5.4 Development of indicators of small cities

It is necessary to realize that individual cities have different values of indicators and the table shows the average values of the whole groups. This simple method shows clearly the substantial differences between the two political periods, which have generally occurred in all city sizes in the country.



Fig. 5.5 Development of indicators of medium cities

5.4.2 Regression Analysis

To analyze mutual relations among indicators, multiple linear regression analysis was chosen. Road traffic intensity is one of the very important indicators of urban areas. There are significant differences between road traffic intensity in the regimes (see Figs. 5.4, 5.5, and 5.6) and therefore road traffic intensity was chosen as one of the indicators that reflects changes between the political periods. This analysis should confirm if there is a dependency between the intensity and indicators of land use areas in different regimes. Both periods show growth of road traffic intensity. However, the intensity of growth in big cities was 25 % during the

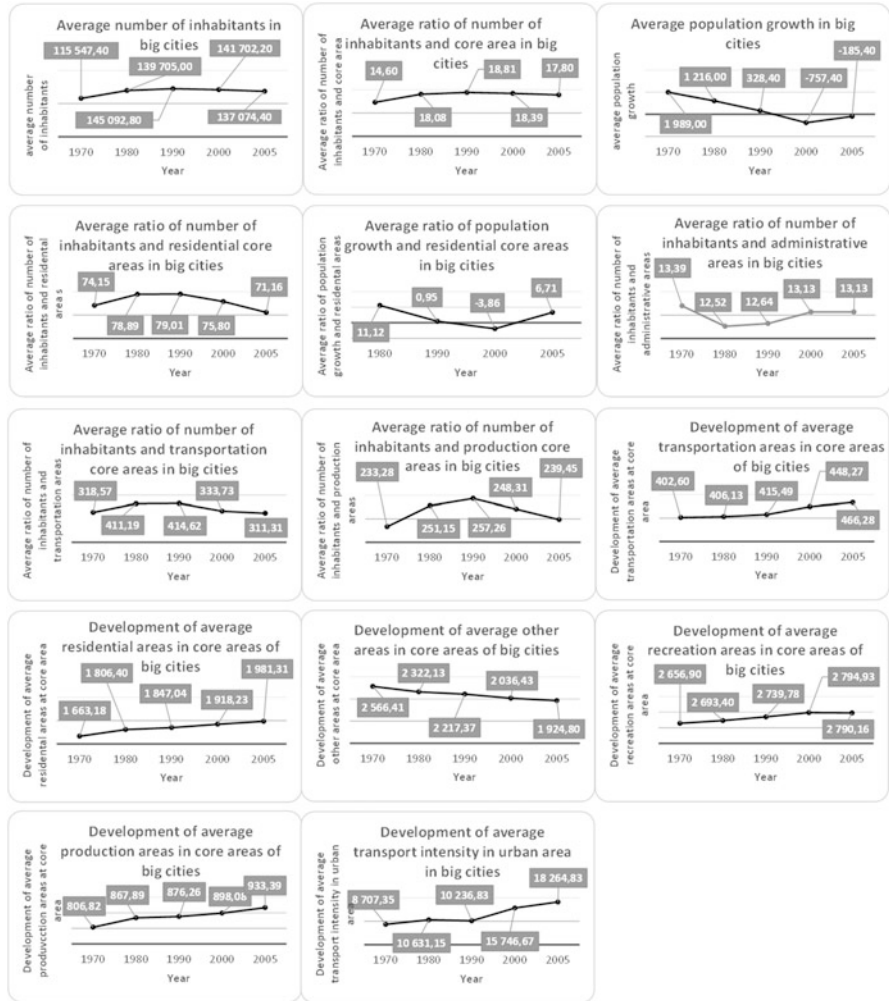


Fig. 5.6 Development of indicators of big cities

communist regime and 80 % in the democratic regime, 19 % and 81 % in medium cities, and 18 % and 44 % in small cities. It was the reason why the analysis of land use dependency on road traffic intensity during different political regimes was processed.

The list of indicators was not the same for all city groups (see Table 5.3). The list of indicators had to be adapted to a number of processed cities in individual groups as the low number of cities allowed for the use of only a lower number of indicators. A group of big cities comprises of only six cities.

Regression analysis is a statistical method whose goal is to find a relation between dependent and independent variables. If we use one independent variable

Table 5.5 Results of multiple linear regression analysis for small cities before and after 1990

Indicator	Std. error	t- stat	P-value
Transport areas 70-90	21.59477837	-2.224422349	0.268961497
90-05	1.822978	-10.5839	0.059972
Residential areas 70-90	12.22371537	0.57080272	0.669801755
90-05	1.047294	14.81925	0.042894
Other areas 70-90	0.475742124	0.10104548	0.93589005
90-05	0.0432	8.582103	0.073847
Recreational areas 70-90	0.448298719	-2.679595562	0.227390043
90-05	0.036784	-26.6697	0.023859
Production areas 70-90	22.2153785	0.961241538	0.512579375
90-05	1.397767	10.05442	0.06311
Number of inhabitants 70-90	0.322577794	1.720817818	0.335129853
90-05	0.023357	7.200552	0.087851
Number of inhabitants/traffic area 70-90	9.1951904	-0.944071454	0.518309718
90-05	0.716079	-10.6351	0.059685
Number of inhabitants/production area 70-90	10.97723256	-0.478570031	0.715840227
90-05	0.796793	-6.45812	0.0978
Number of inhabitants/residential area 70-90	72.33747079	0.007553272	0.995191529
90-05	6.740035	7.310378	0.086547
R ² value 70-90	0.97574884		
R ² value 90-05	0.99980001		

and one dependent (explanatory) variable and if we suppose a linear dependency, we work with a simple linear regression with the following definition:

$$y = b_1 + b_2 \cdot x + E \tag{5.1}$$

where y is dependent variable

b_1 is a constant value for independent variable equal to zero

b_2 is a slope of the line of dependency or a coefficient of the x_2 variable

x is independent/explanatory variable

E is a “noise” factor, which shows an influence of other phenomena, which are not included in independent variables.

Multiple linear regression uses line of dependency and uses more than one independent/explanatory values (x_1, \dots, x_n), as the following equation shows

$$y = b_1 + b_2 \cdot x_1 + b_2 \cdot x_2 + b_3 \cdot x_3 + \dots + b_n \cdot x_n + E \tag{5.2}$$

where y is dependent variable

b_1 is a constant value for independent variable equal to zero

b_2, b_3, \dots, b_n are coefficient of the x_2, x_3, \dots, x_n variables

Table 5.6 Results of multiple linear regression analysis for medium cities before and after 1990

Indicator	Std. error	t-stat	P-value
Transport areas 70-90	4.917899915	-1.430615699	0.38837265
90-05	10.12631679	-2.254593704	0.265768316
Residential areas 70-90	31.09119476	-1.771237807	0.327200782
90-05	41.83472391	3.114846718	0.197765202
Other areas 70-90	0.470168635	-2.204974981	0.271058188
90-05	1.555199034	-0.412508925	0.750926839
Recreational areas 70-90	0.547781888	-3.779889992	0.164650661
90-05	0.628239138	-1.503790647	0.373592857
Production areas 70-90	12.36180238	1.828703984	0.31857109
90-05	37.53990291	2.052132608	0.288665321
Number of inhabitants 70-90	0.514347275	1.807619885	0.321688528
90-05	0.703811916	-2.787696006	0.219265371
Population growth 70-90	3.084603385	-2.25270524	0.265966087
90-05	5.833536804	1.172736585	0.449493778
Number of inhabitants/traffic area 70-90	0.828696907	-3.463182379	0.178957402
90-05	3.34419677	-2.500000411	0.242237847
Number of inhabitants/production area 70-90	16.29315569	1.906977699	0.307467405
90-05	33.8839719	1.578108941	0.359568902
Number of inhabitants/residential area 70-90	237.6857397	-1.755190986	0.329687036
90-05	286.1630563	3.073065201	0.200281138
Number of inhabitants/administrative area 70-90	237.214962	-0.066127463	0.957963152
90-05	228.2258806	-2.326113909	0.258477162
R ² value: 70-90: 0.98585041			
R ² value: 90-05: 0.95922436			

x_2, x_3, x_n are independent/explanatory variables
 E is a “noise” factor.

There were only land use areas, number of inhabitants and ratios of the number of inhabitants and land use areas which were applied in the multi linear regression. The regression was processed separately for individual groups of cities.

Tables 5.5, 5.6, and 5.7 show some of the resulting values of the regression. The values in the regression result tables are:

- R² is a coefficient of determination. It shows what percentage of the dependent variable is explained by the model.
- t-statistic is the ratio of the estimated value of the regression and standard error of the coefficient
- P-value, called also significance level, is the probability of obtaining a test statistic at least as extreme as the one that was actually observed, assuming

Table 5.7 Results of multiple linear regression analysis for big cities before and after 1990

Indicator	Std. error	t- stat	P-value
Number of inhabitants/traffic area 70-90	1.83503145	8.096590597	0.07823194
90-05	5.14758132	1.217860622	0.437664771
Number of inhabitants/production area 70-90	1.700598733	-3.553981472	0.174613907
90-05	4.859125158	-1.14128285	0.458056324
Number of inhabitants/residential area 70-90	13.95538909	-6.973847392	0.09066868
90-05	35.95796002	-2.819766287	0.216961197
R ² value 70 – 90: 0.9876			
R ² value 90 – 05: 0.921			

that the null hypothesis is true. It confirms whether the components of the regression line are statistically significant. P-value < 0,01, < 0,05, or < 0,1 are usually used as significant (Sykes 1992).

The results of the regression analysis show that independent variables = explanatory indicators determine from 92,1 % (big cities in 1990–2005) to 99,98 % (small cities in 1990–2005).

However, all *P-values* (except for two of nine indicators of small cities from all used indicators) are higher than 0,05. In other words they have lower level of significance. All indicators for small cities are smaller than 0,1 for the 1990–2005 period, however none for 1970–1990. It means that nearly none of the dependent variables are statistically significant in all city groups in both periods. P-values for the 1970–1990 period are in most cases even ten times higher (=worse) than in 1990–2005 for small cities. The P-values for small cities in 1990–2005 are the best in the complete set of regimes and periods and vary in single percentage only. Medium cities have some P-values higher in the democratic period and some in the communist regime. P-values in big cities are lower in the 1970–1990 period.

The results of the individual groups of cities are different. As there are only six cities in the group of big cities, the number of used indicators is substantially lower and therefore the results are less representative. The regrouping of cities by adding smaller cities to this group would not be correct as their “character” is different due to their economical state, position in governmental hierarchy, education opportunities, etc.

5.4.3 Correlation Analyses

Another tool was suggested to analyze the dependency of road traffic intensity and land use areas in cities. It was the correlation coefficient. The equation for the correlation coefficient is

Table 5.8 Correlation between average road traffic intensity [number of vehicles/24 h] and land use areas [ha]

	Years	Small cities	Medium cities	Big cities	All cities
Transportation areas	1970	-0.029	-0.074	0.142	0.331
	1980	-0.059	-0.044	-0.267	0.281
	1990	0.389	0.016	0.121	0.41
	2000	0.888	-0.027	0.495	0.545
	2005	0.737	0.044	0.572	0.568
Residential areas	1970	0.057	0.202	0.091	0.383
	1980	0.46	-0.209	-0.08	0.421
	1990	0.512	-0.086	0.366	0.443
	2000	0.742	0.379	0.514	0.575
	2005	0.777	0.4	0.727	0.625
Other areas	1970	0.069	0.214	0.776	0.279
	1980	0.359	0.293	0.121	0.278
	1990	0.474	0.644	-0.81	0.26
	2000	0.615	0.451	0.886	0.404
	2005	0.537	0.239	0.532	0.312
Recreational areas	1970	0.161	-0.013	-0.042	0.211
	1980	0.063	-0.375	-0.403	0.059
	1990	0.088	-0.177	-0.096	0.181
	2000	0.057	0.285	0.73	0.421
	2005	0.118	0.046	0.867	0.343
Production areas	1970	0.481	0.645	0.071	0.335
	1980	0.607	0.245	-0.105	0.314
	1990	0.761	0.377	0.431	0.41
	2000	0.554	0.172	0.388	0.434
	2005	0.773	-0.098	0.575	0.462

$$CC = \frac{\sum (x - \bar{x}) \cdot (y - \bar{y})}{\sqrt{\sum (x - \bar{x})^2 \cdot (y - \bar{y})^2}} \quad (5.3)$$

where x, y are independent and depend data values

\bar{x}, \bar{y} are average values of x, y .

Correlation coefficients were calculated (see Tables 5.8 and 5.9) for individual years and all cities as one group. The correlation coefficients were evaluated twice for two different road traffic intensities. The first one was average road traffic intensity and the second one was maximum road traffic intensity defined in the part of non-spatial data.

The correlation between the average road traffic intensity and land use areas shows the break between the regimes at residential areas (growth after stagnation). It is a result of new residential areas built outside of city centers and in prevailing part without facilities. Therefore inhabitants from these areas were forced to use

Table 5.9 Correlation between maximal road traffic intensity [number of vehicles/24 h] and land use areas [ha]

	Years	Small cities	Medium cities	Big cities	All cities
Transportation areas	1970	-0.264	-0.023	0.98	0.316
	1980	-0.013	0.124	-0.203	0.19
	1990	-0.146	0.042	-0.171	0.176
	2000	0.292	0.018	-0.658	0.248
	2005	0.404	0.064	-0.753	0.264
Residential areas	1970	-0.053	0.633	0.917	0.601
	1980	0.152	0.524	-0.478	0.189
	1990	0.207	0.171	-0.452	0.177
	2000	0.497	0.212	-0.813	0.257
	2005	0.668	0.203	-0.792	0.298
Other areas	1970	0.027	0.674	0.971	0.516
	1980	-0.044	0.813	0.596	0.511
	1990	-0.245	0.591	0.609	0.307
	2000	-0.043	0.228	0.362	0.194
	2005	0.054	0.109	0.147	0.16
Recreational areas	1970	-0.085	0.044	0.834	0.188
	1980	0.177	0.235	-0.036	0.267
	1990	0.034	0.183	0.025	0.234
	2000	0.298	0.269	-0.383	0.331
	2005	0.033	0.212	-0.283	0.284
Production areas	1970	0.361	0.781	0.928	0.757
	1980	0.333	0.86	-0.497	0.124
	1990	0.147	0.685	-0.466	0.135
	2000	0.263	0.576	-0.859	0.114
	2005	0.283	0.327	-0.892	0.089

personal vehicles for commuting and services. Recreational areas suggest a break by higher correlation values in medium and big cities. The break can be found also in production areas in all cities from higher values in 1990 than 2000, however, this decreasing trend changes between 2000 and 2005 to increasing in small and big cities.

The correlation between maximum road traffic intensity and land use areas is negligible. There are only two land use areas showing the dependency. The correlation coefficient grows for transportation areas in small cities and decreases to high negative values in big cities. The negative values trend in big cities occurs also in the correlation coefficient in production areas. The other correlations do not show any changes between the regimes.

5.5 Conclusions

The real political change in 1989 was replaced by 1990 in the analysis since the most important economical changes occurred in 1990. It was a year when a lot of private enterprises and companies came into being. It substantially changed the relation between people and production, and people and the service sector. It was also the starting year of activities of international organizations in Czechoslovakia – previous country of the Czech and Slovak Republics. Higher economical power of a certain part of the society appeared. Impacts of the change in cities were analyzed using land use and other indicators. One of them was even visually detectable – road traffic.

To determine the differences between two political and therefore also economical periods, three approaches were applied. Fourteen attributes were analyzed – land use, number of inhabitants and its growth, ratios calculated from number of inhabitants and land use areas, and road traffic intensity – are processed in this chapter.

The first method shows development of individual indicators in discrete years – in this chapter in 1970, 1980, 1990, 2000 and 2005 for two given periods: 1970–1990 (communist regime) and 1990–2005 (democratic regime). These graphs were processed for selected 14 indicators (each indicator in an individual graph for one city group) show clearly how different the two political regimes are (see Table 5.3). The development of residential areas in all city groups was relatively unchanged. They grew in both periods, however, the growth gradients were different – higher in the democratic regime. The higher growth started shortly after 1990. A similar situation occurred in production areas. Distinctive differences can be found in recreational areas where different behavior suggests in small cities than in medium and big cities.

More distinctive values presented in the graph system were the ratios of the number of inhabitants and individual land use areas. All these ratios had an increasing trend in the first period and a decreasing trend in the second period even though most land use areas increased since 1970s. The values in an objective way describe the differences between the regimes in land use connected to the number of inhabitants. These calculated indicators are more useful for determining differences.

It is a quick evaluation when all necessary data are available. To make the result clearer, the gradient of growth and decline can be calculated. The advantage of the first method is its simplicity, easy visualization, calculation of trends individually for individual indicators. The disadvantage of the method is the missing information on mutual dependencies among indicators. It should be taken into account if we would like to understand the changes in the land use indicators under different political regimes.

Road traffic intensity is an indicator which clearly shows the differences between both regimes. Therefore this indicator was used as a dependent variable to find which indicators of urban areas influence the intensity.

Multiple linear regression was used as the second method. It shows the differences between both political regimes using all the selected urban development indicators in one calculation. The method determines which indicators have/had an important or less important influence. The results of the method showed that all used indicators reliably explain road traffic intensity with a coefficient of determination higher than 90 %. However, the statistical significance of many variables/indicators was quite low. The behavior within the individual groups of cities were in the framework of individual regimes similar and different than in other groups of cities and regimes.

Multiple linear regression shows a complex dependency of all selected indicators. The disadvantage of the method is a limit of used independent variables given by the number of input data of used cities; in other words, a sufficient number of cities for this analysis is necessary for each set of indicators. The analyses were again processed for the 1970–1990 and 1990–2005 periods. Four from six models (small, medium, big cities for two periods) had all a level of significance of all indicators higher than 0,05. Thus the indicators had a low significance. This method brings interesting results showing the differences between the regimes especially in statistical significance of individual indicators.

The last method – correlation allowed to find a dependency between road traffic intensity and individual indicators regardless other indicators. More information can be found using average road traffic intensity. Correlation shows that there are great differences between city groups. A significant impact of political change can be found in all groups of cities but in the dependency of different land use areas as well. The differences between the regimes using the correlation in big and medium cities occur in all classes except for transportation areas, in small cities only for residential and production areas. A relatively high number of correlation coefficients in the communist regime are very low and have an increasing trend either to positive or negative values. It means that the dependency between the road traffic is higher in the democratic regime than in the communist at average road traffic. This dependency of maximum road traffic intensity is substantially lower than of the average. It suggests that it is the land use of cities which raises the intensity especially in the democratic regime in the country. Each of the methods presented in this chapter proved to be a useful tool for analyzing the time series of more variables and from a different point of view.

All the results of the analyses proved that political change followed by economical change has a very strong impact on road traffic intensity. Eighty to ninety per cent of the road traffic intensity is formed by personal cars, motorcycles which cover less than 3 %, and the rest is formed by heavy vehicles. The high increase of the number of personal cars since early 1990s and developing residential areas situated usually out of city centers deteriorated the traffic situation having a doubled road traffic intensity if compared between 1970 and 2005. Both these features reflect a different state of the society in the post communist period.

There is a large scale of indicators of various types which influence the changes and development in urban areas. Geospatial science is the only really objective tool which is able to store, analyze and model urban development based on historical

data and their mutual relations. The advantage of geospatial science is its open character allowing to implement an unlimited number of available attributes and update the data on one side, and to visualize both data, and partial and/or final results of analyses and modelling using spatial and non-spatial data.

The application of remote sensing data and city maps data allows for the use of knowledge of urban architects to map the land use of urban areas. City maps combined with aerial photographs – show and help to interpret individual land use classes. Aerial photographs are – unlike city maps – accurately dated and that is necessary for additional analyses with other data. GIS analysis are a very good method how to find trends in the spatial development of features occurring on the earth, in individual countries, or regions. The key point is to decide what spatial/remote sensing data are suitable, especially their scale and thus spatial resolution, spectral bands, and temporal resolution, and to choose other data describing the features. As there are various data with similar spatial and spectral characteristics (aerial photographs and VHR data, e.g.), temporal resolution and price can become the decisive issue.

Acknowledgments The chapter presents results of the COST project with support of The Ministry of Education, Youth and Sports: *Modelling of urban areas to lower the negative influences of human activities* (OC10011)

References

- Anthony RM (2014) Bringing up the past: political experience and the distribution of urban populations. *Cities* 37:33–46
- Banister D (2011a) Cities, mobility and climate change. *J Transp Geogr* 19:1538–1546
- Banister D (2011b) The trilogy of distance, speed and time. *J Transp Geogr* 19:950–959
- Banister D, Anderton K, Bonilla D, Givoni M, Schwanen T (2011) Transportation and the environment. *Annu Rev Environ Resour* 36:247–270
- Barla P, Miranda-Moreno LF, Lee-Gosselin M (2011) Urban travel CO₂ emissions and land use: a case study for Quebec City. *Transp Res D-Transp Environ* 16(6):423–428
- Ewing R, Cervero R (2010) Travel and the built environment. *J Am Plann Assoc* 76(3):265–294
- Fan F, Wang Y, Qiu M, Wang Z (2009) Evaluating the temporal and spatial urban expansion patterns of Guangzhou from 1979 to 2003 by remote sensing and GIS methods. *Int J Geogr Inf Sci* 23:1371–1388
- Gallez C, Kaufmann V, Maksim H, Thebért M, Guerrinha C (2013) Coordinating transport and urban planning: from ideologies to local realities. *Eur Plan Stud* 21(8):1235–1255
- Halounová L, Holubec V, Těhle M, Řehák M, Vepřek K (2013) Atlas of urban development in Czech cities (since 60-ies of the 20th century). FCE CTU in Prague, Prague. ISBN: 978-80-01-05177-1
- Handy SL (1992) Regional versus local accessibility: neo-traditional development and its implications for non-work travel. *Built Environ* 18(4):253–267
- Jacobson E (2003) The transportation-land use connection. Transportation and Growth Management, School of Urban Studies and Planning, College of Urban and Public Affairs, Portland State University
- Kitamura R, Mokhtarian PL, Laidet L (1997) A micro-analysis of land use and travel in five neighborhoods in the San Francisco Bay Area. *Transportation* 24(2):125–158

- Kuzmyak JR, Baber C, Savory D (2006) Conference: 85th annual meeting of the transportation-research-board location, Washington, D.C. Date: 22–26 Jan 2006 Transportation Research Record-Series Issue 1977, pp 145–153
- Litman TA, Steele R (2013) How land use factors affect travel behaviour. Land use impacts on transport, transport policy institute. Available in pdf at: <http://www.vtpi.org/landtravel.pdf>, cited 18 Oct 2013
- Ma KR, Banister D (2007) Urban spatial change and excess commuting. *Environ Plan* 39:630–646
- Næss P, Sandberg SL (1996) Workplace location, modal split and energy use for commuting trips. *Urban Stud* 33(3):557–580
- Newton C, Schuermans N (2013) More than twenty years after the repeal of the Group Areas Act: housing, spatial planning and urban development in post-apartheid South Africa. *J Housing Built Environ* 28(4):579–587
- Ristimäki M, Kalenoja H (2011) Travel-related zones of urban form in urban and peri-urban areas. Track 11, 3rd World planning school congress, Perth
- Stead D (2001) Relationships between land use, socioeconomic factors, and travel patterns in Britain. *Environ Plann B Plan Des* 28(4):499–528
- Sykes AO (1992) An introduction to regression analysis. 1992 Coase lecture, the University of Chicago, <http://www.law.uchicago.edu/node/1309.cit>. Accessed 4 July 2014
- Vepřek K (2000) Požadavky na jednotný způsob zpracování a hodnocení analýzy vývoje funkčních ploch a českých měst v konfrontaci s vývojem infrastruktury silniční dopravy/ Demands on the unified way of processing and evaluation of analysis of functional areas in the Czech Republic vs the development of the road traffic infrastructure (in Czech only). Prague
- Vepřek K (2009) Metodika hodnocení efektivity rozvoje silniční sítě z hlediska urbanizace/ Methodology of evaluation of effectivity of the road traffic development from the urbanisation point of view. (in Czech only). Prague
- Yen L, Wu AM (2014) Urbanization, land development, and land financing: evidence from chinese cities. *J Urban Aff* 36(SI Supplement: 1):354–368

Part III
Monitoring and Mapping Environmental
Changes

Chapter 6

Mapping Sea Ice from Satellite SAR Imagery

Linlin Xu and Jonathan Li

Abstract Sea ice information is crucial for ensuring safe marine navigation and supporting climate change studies in the polar regions. Spaceborne synthetic aperture radar (SAR), due to its ability to cover large inaccessible areas without the dependence on weather condition or sun-light illumination, provides a powerful tool for sea ice mapping. This chapter provides a comprehensive overview of SAR image analysis approaches to sea ice mapping with a focus on sea ice segmentation. Sea ice segmentation is an essential step in computer-aided sea ice mapping systems. Automated segmentation of SAR sea ice imagery is a difficult task due to the complex sea ice physics and the ever-changing ocean environment, as well as the numerous sensor parameters. In light of the difficulties, an efficient segmentation method has to utilize the spatial and textural information for modeling the label correlation and increasing the discriminative capability. This Chapter presents a Bayesian method for segmentation of SAR sea ice imagery, where a novel kernel principal component analysis (KPCA) model is used for accounting for the textual information, and a Markov random field (MRF) is used for addressing the label correlation effect. The proposed method is optimized by the graph-cut approach. The results demonstrate that the proposed method is capable of effectively delineating different sea ice types. Moreover, it requires less computational time than the other advanced approaches.

Keywords Sea ice segmentation • Synthetic Aperture Radar (SAR) • Bayesian estimation • Maximum a posterior • Markov random field (MRF) • Kernel principal component analysis

L. Xu • J. Li (✉)

Department of Geography and Environmental Management, University of Waterloo,
Waterloo, ON N2L 3G1, Canada

e-mail: l44xu@uwaterloo.ca; junli@uwaterloo.ca

© Springer Science+Business Media Dordrecht 2015

J. Li, X. Yang (eds.), *Monitoring and Modeling of Global Changes: A Geomatics Perspective*, Springer Remote Sensing/Photogrammetry,
DOI 10.1007/978-94-017-9813-6_6

113

6.1 Introduction

Sea ice information in the polar regions is essential for various applications, especially for climate change study and marine navigation. Sea ice is an integral part of the Earth's climate system. It interacts with both the ocean and the atmosphere by modulating the heat and moisture fluxes. The state and dynamics of sea ice determines and alters the surface albedo and salt-freshwater redistributions (IGOS 2007). In particular, because of its high albedo, sea ice tends to reflect most of the sunlight back to the atmosphere, resulting in cold climate in the polar regions. However, with the current trend of the contraction of Arctic ice caps (Kwok et al. 2009), the failure in controlling the amount of sun ray may cause climate change in local or global scale, leading to serious influence on human life, the earth's ecosystem and natural environment. Consequently, sea ice information, such as extent, type, concentration and thickness, has been recognized as an Essential Climate Variable by both the World Meteorological Organization (WMO) and the United Nations Framework Convention on Climate Change (UNFCCC). Moreover, the sea ice information is essential for ensuring safe marine navigation. The Northern Sea Route (NSR) in the Arctic region is the shortest sailing route linking northwestern Europe and northeastern Asia. However, the navigation in this region is greatly hampered by the presence of sea ice and iceberg (Johannessen et al. 2006). Therefore, information regarding the conditions and distributions of different sea ice types is required for reducing hazards of marine transportation and offshore operations.

While optical sensors can be used for obtaining sea ice information, they depend on weather condition or sun-light illumination, and are therefore limited by clouds and darkness. Satellite synthetic aperture radar (SAR), due to its ability to penetrate the cloud and work day and night, provides a powerful tool for sea-ice monitoring. RADARSAT-1 and -2 have been the primary source for sea ice monitoring. At the Canadian Ice Service (CIS), the operational interpretation of SAR sea ice images relies on human operators to manually process a great number of image scenes annually. The sea ice charts, as the final product, label each identified region with an egg code, which indicates sea ice information (e.g., the type, concentration, stage of development, and floe size). This visual interpretation of SAR sea ice images, although capable of incorporating human knowledge and experiences, is very demanding due to the vast amount of daily sea ice observations. Hence, there is an urgent need to develop automatic programs that are capable of accurately and time-efficiently discerning the types and extends of different sea ice from SAR imagery.

This chapter is organized as follows. Section 6.2 describes the principles of SAR imaging. Section 6.3 summarizes the available satellite SAR sensors. The automatic segmentation of SAR sea ice imagery and the challenges are described in Sect. 6.4. The proposed method for SAR sea ice segmentation is introduced in Sect. 6.5. The results of experiments on both simulated and real SAR sea ice images are presented in Sect. 6.6. Lastly, Sect. 6.7 concludes the study.

6.2 Principle of SAR Imaging

SAR is a radar system (see Fig. 6.1a) where a transmitter generates successive microwave pulses (A), which are focused by radar antenna into a beam (B) to illuminate the surface obliquely, finally the receiver records the backscattered energy (C) from various objects within the beam. The time delay between the signal transmission and 'echo' reception is used to infer the distance of the targets to radar, and thus the location of the targets. With the moving of sensor platform, the continuous recording and processing of backscattered energy form a two-dimensional image of the surface.

The SAR imaging geometry contains five elements (see Fig. 6.1b), i.e. flight direction (A), nadir point (B), swath (C), range (D), azimuth (E). The spatial resolution of SAR system entails the range resolution which is determined by the pulse length, and the azimuth resolution which is determined by the angular width of the beam and slant range distance. Because beam width is inversely proportional to the length of radar antenna, a fine azimuth resolution requires antenna length longer than what can be carried on satellite platform. To overcome the antenna size limitation, the SAR system is designed to synthesize a very long antenna by taking advantage of the moving of the platform. Most SAR systems have very high spatial resolution, e.g. RADARSAT system provides resolution between 3 and 100 m. For sea ice monitoring, the most commonly used RADARSAT mode is ScanSAR narrow and wide modes which have spatial resolution of 50 m and 100 m respectively.

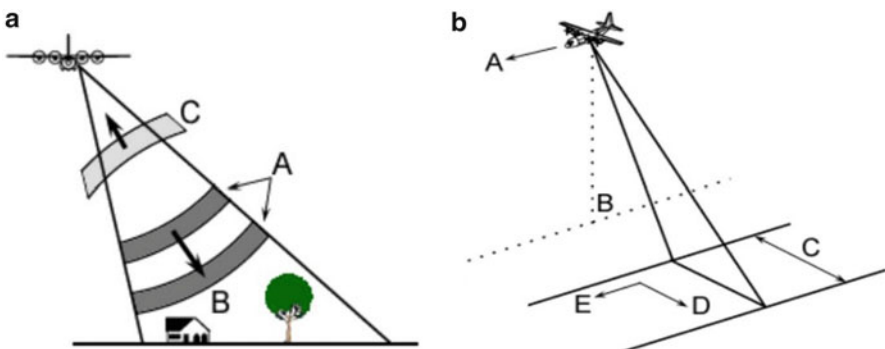


Fig. 6.1 Illustration of (a) the principle of SAR imaging, and (b) the basic elements of SAR imaging geometry (From CCRS 2009)

6.3 Summary of SAR Imaging Satellites

Remote sensing of sea ice can be performed in visible, infrared (IR) ranges, using sensors such as MODIS (Moderate Resolution Imaging Spectroradiometer), and AVHRR (Advanced Very High Resolution Radiometer) and SeaWiFS (Sea Wide Field of view Spectrometer). However, these sensors are limited by their coarse spatial resolution and the susceptibility to the influence of weather conditions.

In contrast, the SAR sensors onboard satellites have been widely used for sea ice monitoring, primarily because of the following reasons. First, SAR sensors are active sensors, which are capable of sending radiations to the earth surface, and receiving the backscattered signals. Consequently, SAR sensors do not rely on the sun illumination and are able to work 24 h a day. This characteristic is especially important for the polar regions that have long dark period in winter. Second, SAR sensors work at microwave ranges, and therefore are capable of penetrating the cloud. This feature also makes SAR sensors more suitable than the optical sensors for monitoring the polar regions, where cloud is easily formed in the melting season due to open water and the cold atmosphere. Third, SAR sensors are generally characterized by wide coverage with medium spatial resolution. And this combination is suitable for delineating sea ice without compromising too much the monitoring efficiency.

Various SAR sensors have been used for ocean monitoring, as summarized in Table 6.1. Seasat launched in 1978 is almost the earliest SAR sensor that is designed for ocean monitoring. ERS-1 and -2, launched by the European Space Agency (ESA) in 1991 and 1995 are also specifically designed for ocean surveillance. RADARSAT-1, launched by Canadian Space Agency (CSA) in 1995, has the optimal combination of spatial resolution and coverage that is suitable for detecting ocean features over large area. For example, with a spatial resolution of 50 m (100 m) and swath width of 300 km (500 km), the ScanSAR Narrow (Wide) beam mode in RADARSAT-1 is capable of providing detail information of large sea ice area. The ENVISAT, launched by ESA in 2002, carries an advanced SAR (ASAR) sensor, which is capable of providing the Precision and ScanSAR modes, with spatial resolution of 30 m and 150 m, and swath width of 100 km and 400 km respectively. In 2007, two X-band SAR satellites, the TerraSAR-X and COSMO-SkyMed were sent into space. RADARSAT-2 was launched by CSA in the same year, and it has widely been used for sea ice monitoring (Ochilov and Clausi 2012). It is worth to mention that Canada has initiated a new mission, called the RADARSAT Constellation Mission (RCM) in 2005 and intends to launch three RCM satellites in 2018. Using the three satellites, RCM will be able to provide complete coverage of Canada's land and ocean with daily revisit, as well as daily access to 95 % of the Earth's surface.

Table 6.1 Summary of SAR imaging satellites

Name (owner)	Operative	Swath width (km)	Revisit time (day)	Best spatial resolution (m)	Wavelength range (cm)	Number of channels	Incidence angle (degree)
SEASAT (NASA)	Operative 1978–off same year	100	NA	25	23.4	HH	15–25
ERS-1 (ESA)	1991–1996	100	35	30	5.7	VV	20–26
ERS-2 (ESA)	1995–operating	100	35	30	5.7	VV	20–26
JERS (Japan)	1992–1998	75	44	18	23.6	HH	32–38
RADARSAT-1 (Canada)	1995–2013	45–500	1–5	10	5.7	HH	10–58
ENVISAT (ESA)	2002–operating	30–400	1–7	30	5.7	HH & VV/cross-pol	15–45
RADARSAT-2 (CSA)	2007–operating	20–500	1–3	3	5.7	Full-pol	10–60
ALOS-PALSAR (Japan)	2006–operating	70–350	1–3	10	23.6	Full-pol	8–60
TerraSAR-X (Germany)	2007–operating	10–100	1–2.5	1	3.1	Full-pol	20–55
COSMO/SkyMed Constellation (Italy)	2007–operating	10–200	1–5	1	3.1	Full-pol	25–59

6.4 Automatic Mapping of Sea Ice in SAR Imagery

Sea ice backscatter in SAR imagery depends primarily on the surface roughness and the dielectric constant of sea ice or open seawater (Carsey 2013). Generally speaking, rougher surface enables more radiation to be backscattered to the sensor, causing brighter appearance in SAR imagery. The dielectric constant of sea ice decreases as the degree of salinity decreases. Lower dielectric constant generally causes stronger backscatter. This implies that thicker sea ice tends to assume brighter color due to its lower salinity, and new or fresh sea ice appears darker in the image due to the relatively higher dielectric constant. Therefore, different sea-ice types are generally distinguishable on SAR images because they admit different physical characteristics, i.e. salinity and surface roughness, resulting in the varying magnitudes of SAR backscattering.

Unfortunately, the complex sea ice physics and ever-changing ocean environment, as well as the numerous sensor parameters cause large inner-class gray tone variation in the observed SAR sea-ice images. First of all, SAR sensor inherently produces speckle noise, which renders the observed pixel values either brighter or darker than the true pixels values, leading to great variability in areas that should be homogeneous. This variation would reduce the separability of different sea-ice types. Moreover, the existence of ridges, rubble, rims and deformations produced by compression forces can also produce inhomogeneity in gray tone values (Shokr 1991). In addition, the same sea-ice type could appear different tone values as the changing of SAR incidence angle.

The significant inner-class variation imposes a fundamental challenge on the automatic techniques for sea ice image segmentation. Current algorithms for SAR sea ice image segmentation can be categorized as pixel-based and texture-based. The former clusters pixels based on gray tone values, e.g., local thresholding (Haverkamp et al. 1993), Gamma (Samadani 1995) and Gaussian (Karvonen 2004) mixture models, and K-Means clustering (Redmund et al. 1998). Due to the sensitivity of single pixels to speckle noise, these methods always produce many artifacts. The suppression of speckle noise by some denoising methods (Lee 1980; Frost et al. 1982; Kuan et al. 1985) however will introduce new problems, such as the blur of the ice boundaries which serve as important information to delineate sea ice.

As opposed to using single pixels, the texture-based approaches use for segmentation the texture features, which are linear or nonlinear functions of neighboring pixels, e.g., variation (Burns et al. 1982; Heolbaek-Hansen et al. 1989), gray-level co-occurrence matrix (GLCM) (Haralick et al. 1973; Shuchman et al. 1989; Baraldi and Parmiggiani 1995; Barber and LeDrew 1991; Soh and Tsatsoulis 1999; Clausi 2002), Markov random fields (MRF) (Deng and Clausi 2005) and Gabor filter (Clausi 2001). Comparing with pixel-based approach, these methods are more robust to inner-class variation. However, due to the vast amount of texture features and their varying specializations, it's difficult to select the best group of features for the current task at hand. Moreover, most texture-based approaches are

computationally intensive, thus are not suitable to support operational usage. This chapter therefore aims to explore sea ice segmentation technique that is both efficient and accurate.

6.5 Proposed Method

6.5.1 Bayesian Segmentation of SAR Sea Ice Imagery

In this chapter, we denote the discrete lattice spanned by SAR sea ice imagery by \mathcal{N} , and a site in the lattice by $t \in \mathcal{N}$. We represent the image patch centered at site t by \mathbf{y}_t , a p -dimensional random vector taking on different grayscale values, and the label of site t by l_t , a random variable taking on a class $\{1, \dots, K\}$. Then a SAR sea ice image can be denoted as $\mathbf{Y} = \{\mathbf{y}_t | t \in \mathcal{N}\}$, and the labels of this image as $\mathbf{I} = \{l_t | t \in \mathcal{N}\}$. For automated segmentation of SAR sea ice imagery, we are trying to infer \mathbf{I} based on \mathbf{Y} , which, in the Bayesian framework, can be achieved by maximizing the posterior distribution of l_t given \mathbf{y}_t , i.e.,

$$p(l_t | \mathbf{y}_t) p(\mathbf{y}_t | l_t) p(l_t) \quad (6.1)$$

where $p(\mathbf{y}_t | l_t)$ denotes the probability distribution of patch variable \mathbf{y}_t conditioned on l_t , which allows the modeling of textural information, and $p(l_t)$ is the a priori probability of labels, which allows the modeling of label correlation effect. The maximum a posterior (MAP) estimation of the labels can be expressed as:

$$\hat{\mathbf{I}} = \arg \max_{\mathbf{I}} \prod_{t \in \mathcal{N}} p(l_t | \mathbf{y}_t) \quad (6.2)$$

or

$$\hat{\mathbf{I}} = \arg \min_{\mathbf{I}} \sum_{t \in \mathcal{N}} [-\log p(\mathbf{y}_t | l_t) - \log p(l_t)] \quad (6.3)$$

In this letter, $p(\mathbf{y}_t | l_t)$ is approached by kernel principal component analysis (KPCA) to mine the most discriminative textural information, whereas $p(l_t)$ is implemented by the MRF-based multiple logistic (MLL) prior to modeling the label correlation effect. The maximum a priori (MAP) problem is solved by the graph-cut-based α -expansion algorithm.

6.5.1.1 Likelihood Implementation

Since image patches \mathbf{y}_t characterize the spatial relationship of local pixels, using image patches instead of individual pixels would allow better representation of

texture patterns and is more capable of resisting the influence of speckle noise. However, the drawbacks of using \mathbf{y}_t lie in the fact that \mathbf{y}_t assumes high level noise, high dimensionality, and that \mathbf{y}_t itself may not reveal the most discriminative texture patterns. Therefore, one essential issue for sea ice segmentation is to explore the most compact and discriminative texture features as model input. Many texture features, as linear or nonlinear transformations of \mathbf{y}_t have been used instead of \mathbf{y}_t , e.g. GLCM (Haralick et al. 1973; Clausi 2002) and Gabor filter (Clausi 2001). However, due to the vast amount of variations of these texture features and their varying specializations, it's difficult to select the best group of features for the current task at hand. Moreover, it is difficult to predict the statistical distribution of texture features.

In Sect. 6.5.2, we present a KPCA model to extract compact and discriminative texture features with Gaussian-like noise characteristics. We will illustrate that the proposed KPCA local texture features assume some meaningful characteristics that benefit sea ice segmentation. The KPCA features \mathbf{z}_t in site t can be obtained by transferring \mathbf{y}_t into KPCA domain. Accordingly the KPCA features in class $l_t = i$ can be expressed as:

$$\mathbf{z}_t^i = \boldsymbol{\mu}^i + \boldsymbol{\eta} \quad (6.4)$$

where $\boldsymbol{\mu}^i$ is the mean vector of class i , and $\boldsymbol{\eta}$ is class-independent noise. In Sect. 6.5.2, we will prove that $\boldsymbol{\eta}$ satisfies independently and identically distributed (i.i.d.) zero-mean Gaussian-like distribution:

$$p(\boldsymbol{\eta}) = (2\pi\sigma^2)^{-p/2} \exp\{-\sigma^{-2}/2\boldsymbol{\eta}^T\boldsymbol{\eta}\} \quad (6.5)$$

where σ^2 is noise variance. Accordingly, the likelihood function can be expressed as:

$$p(\mathbf{z}_t | l_t = i) = (2\pi\sigma^2)^{-p/2} \exp\{-\sigma^{-2}/2(\mathbf{z}_t - \boldsymbol{\mu}^i)^T(\mathbf{z}_t - \boldsymbol{\mu}^i)\} \quad (6.6)$$

The likelihood function in KPCA domain $p(\mathbf{z}_t | l_t)$ will be used to substitute $p(\mathbf{y}_t | l_t)$ in Eq. (6.1) for estimating the labels.

6.5.1.2 Label Prior Implementation

The MRF is a classical method for modeling contextual information (Geman and Geman 1984). It promotes identical class labels for spatially close pixels. The MRF-based approach is often implemented by the MLL model, which can be expressed as (Li 2001):

$$p(l_t) = \frac{1}{Z} \exp\left(-\sum_{t \in N} \sum_{u \in G_t} \delta(l_t, l_u)\right) \quad (6.7)$$

where Z is a constant normalization term, G_t denotes the neighborhood centered at site t ; and $\delta(l_t, l_u) = -1$ if $l_t = l_u$, whereas $\delta(l_t, l_u) = 1$ if $l_t \neq l_u$.

6.5.1.3 Complete Algorithm

The likelihood function and MLL label prior in Sects. 6.5.1.1 and 6.5.1.2 are incorporated into a Bayesian framework and solved by the MAP criterion. The optimal labeling $\hat{\mathbf{I}}$ can be obtained according to MAP criterion:

$$\hat{\mathbf{I}} = \arg \min_{\mathbf{I}} \sum_{t \in N} \left\{ \|\mathbf{z}_t - \boldsymbol{\mu}^i\|_2 + \gamma \sum_{u \in G_t} \delta(l_t, l_u) \right\} \quad (6.8)$$

where γ is the weighting parameter that determines the relative contribution of the data likelihood and the label prior. The unknown parameters include labels \mathbf{I} and class mean vectors $\{\boldsymbol{\mu}^i\}$. This is an ill-posed optimization problem, since the number of unknown parameters is more than the number of observations. The Expectation and Maximization (EM) algorithm can be used for solving this problem. The EM algorithm is a variant of the maximum likelihood estimation. It treats \mathbf{I} as missing observations and iterates the E- and M-step. In E-step, it estimate \mathbf{I} by assuming known values of $\{\boldsymbol{\mu}^i\}$, while in M-step, $\{\boldsymbol{\mu}^i\}$ is updated based on the estimate of \mathbf{I} .

The estimation of \mathbf{I} in E-step using the MLL label prior is essentially a combinatorial optimization issue. While many traditional algorithms, such as the simulated annealing (Geman and Geman 1984) and iterative conditional mode (Besag 1986) can be used for solving this problem, the more advanced method, i.e. graph-cut (Boykov et al. 2001), has not been adopted for sea ice segmentation. The graph-cut approach generally requires less computation time than other approaches and is more capable of finding the global optima. In this study, we therefore use the graph-cut alpha-expansion approach (Boykov et al. 2001; Bagon 2006) for efficient and effective MAP segmentation SAR sea ice image.

The complete algorithm is summarized into the following steps:

1. Transform the patch observations $\{y_t\}$ into KPCA domain, to get KPCA features $\{z_t\}$;
2. Estimate the initial value of $\{\boldsymbol{\mu}^i\}$ using K-means algorithm;
3. E-step: estimate $\hat{\mathbf{I}}$ using graph-cut alpha-expansion algorithm, based on the current value of $\{\boldsymbol{\mu}^i\}$;
4. M-step: update $\{\boldsymbol{\mu}^i\}$ based on the current estimate of $\hat{\mathbf{I}}$. Estimate $\boldsymbol{\mu}^i$ as the mean value of the KPCA features in the i th class $\{z_t | l_t = i\}$;
5. Repeat E- and M-step until the estimate of $\{\boldsymbol{\mu}^i\}$ stabilizes or a given number of iterations being reached.

6.5.2 Kernel PCA Texture Feature

The likelihood function is realized as the distribution of KPCA features. In this section, we introduce in detail the proposed KPCA features. This section is organized as follows. First we briefly introduce KPCA approach. Then we explain the extraction of texture features based on KPCA approach as well as the interpretation of the extracted features. Lastly, we explore the compatibility of KPCA texture features with K-Means algorithm.

6.5.2.1 Kernel Principal Component Analysis

Similar to classic PCA, the KPCA approach intends to obtain a series of orthogonal directions that explain most of data variance. However, KPCA works in nonlinear feature space rather than the original space (Schölkopf et al. 1998). As such, the KPCA is supposed to be more powerful in terms of discovering meaningful patterns hidden in the dataset. The nonlinear transformation is achieved by a mapping function $\Phi(\cdot)$ that maps the original space to feature space. Then KPCA can be achieved by performing classic PCA in nonlinear feature space. Alternatively, KPCA can be implemented by using kernel function without explicitly exploring the form of mapping function (Schölkopf et al. 1998). This purpose of approach is mainly to avoid the complexity of nonlinear mapping operation. In this chapter, we adopt the logarithmic function as the mapping function in order to take into consideration the multiplicative nature of SAR speckle noise. And we employ the mapping function instead of the kernel function, considering that the mapping function here is not complex and does not increase the dimensionality of the data.

6.5.2.2 KPCA Local Texture Features

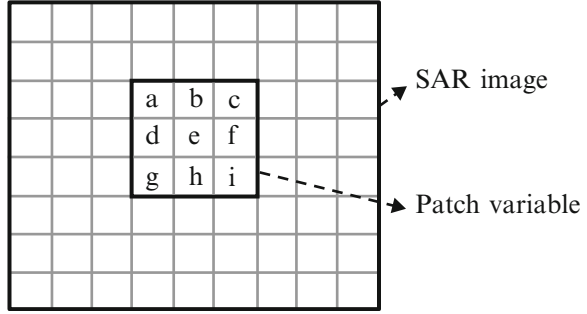
Texture features are usually predefined linear or nonlinear transformations of original image pixels. However, instead of using these predefined texture features, we design a set of totally data-driven local texture features based on KPCA technique. These adaptive features are capable of revealing meaningful information hidden in image patches, while achieving Gaussian-like noise characteristics.

Assuming that the speckle noise is fully developed, a SAR image patch variable can be modeled as (Hoekman 2001):

$$\mathbf{y} = (x_1 n_1, x_2 n_2, \dots, x_p n_p)^T \quad (6.9)$$

where x_i and n_i are respectively the terrain backscatter intensity and the speckle intensity of the i th pixel in image patch. For fully developed speckle noise, x_i and n_i are independent, and n_i is spatially uncorrelated. Accordingly, we denote the SAR image as a collection of all the image patches by a data matrix:

Fig. 6.2 Illustration of patch acquisition in SAR sea ice image



$$\mathbf{Y} = [\mathbf{y}_1, \mathbf{y}_2, \dots, \mathbf{y}_N]^T \quad (6.10)$$

where \mathbf{y}_t ($t \in N$) represents the t th patch that is obtained by placing a small square window at the t th pixel (Fig. 6.2). Essentially, the proposed KPCA model seeks linear PCA directions in nonlinearly transformed feature space instead of in the original space. The transformation can be achieved by a nonlinear mapping function $\Phi(\mathbf{y})$. To account for the multiplicative nature of SAR speckle noise, in this chapter, we define:

$$\Phi(\mathbf{y}) = \log(\mathbf{y}) \quad (6.11)$$

where $\log(\mathbf{y})$ represents performing logarithmic operation on each element of \mathbf{y} . Suppose $\Phi(\mathbf{y})$ has been centralized, the covariance matrix in logarithmic feature space is:

$$\mathbf{C} = 1/N \sum_{t=1}^N \Phi(\mathbf{y}_t) \Phi^T(\mathbf{y}_t) \quad (6.12)$$

Note that \mathbf{C} is a $p \times p$ matrix, because the mapping function $\Phi(\vec{\mathbf{y}})$ does not change the dimensionality of \mathbf{y} . The KPCA can be achieved by performing singular value decomposition (SVD) on the covariance matrix in logarithmic feature space:

$$\begin{aligned} \mathbf{C} &= \begin{pmatrix} C_{aa} & C_{ab} & \dots & C_{ai} \\ C_{ba} & C_{bb} & \dots & C_{bi} \\ \vdots & \vdots & \ddots & \vdots \\ C_{ia} & C_{ib} & \dots & C_{ii} \end{pmatrix} \\ &= \begin{pmatrix} \mathbf{w}_1^T \\ \mathbf{w}_2^T \\ \vdots \\ \mathbf{w}_p^T \end{pmatrix}^T \begin{pmatrix} \lambda_1 & 0 & \dots & 0 \\ 0 & \lambda_2 & \dots & 0 \\ \vdots & \vdots & \ddots & \vdots \\ 0 & 0 & 0 & \lambda_p \end{pmatrix} \begin{pmatrix} \mathbf{w}_1^T \\ \mathbf{w}_2^T \\ \vdots \\ \mathbf{w}_p^T \end{pmatrix} \end{aligned} \quad (6.13)$$

where element C_{AB} in \mathbf{C} represents the covariance between the two pixels at position A and B across the image in logarithmic feature space. So \mathbf{C} provides a

statistical description of relationship among pixels in SAR image. Pixels that do not belong to the same patch are considered uncorrelated. Hence the size of the patch determines the scale of spatial patterns that can be described. Generally speaking, bigger-sized patch considers larger-range correlations, and hence is more capable of capturing larger-scale textural patterns in SAR image. However, for SAR sea ice image that is usually devoid of strong texture pattern, small patch-size (e.g. 3×3) is sufficient.

The $p \times 1$ vectors $\{\mathbf{w}_j\} (j = 1, \dots, p)$, denote mutually orthogonal PCA directions of sequentially largest variances in logarithmic feature space. The KPCA texture features $\{\mathbf{z}_t\} (t = 1, \dots, N)$, can be obtained by projecting the image patch onto the PCA directions:

$$\mathbf{z}_t = \mathbf{W}^T \Phi(\mathbf{y}_t) \quad (6.14)$$

The elements $z_{ti} (i = 1, \dots, p)$ in \mathbf{z}_t are called Principal Components (PCs), whose variances are represented by $\{\lambda_i\} (i = 1, \dots, p)$. As discussed in Sect. 6.5.2.1, while we adopt the mapping function for obtaining KPCA features, it is equivalent to follow the approach presented in (Schölkopf et al. 1998) by using the kernel function: $k(\mathbf{y}_t, \mathbf{y}_q) = \log(\mathbf{y}_t) \log(\mathbf{y}_q^T)$.

The above-described KPCA texture features assume several interesting characteristics that benefit sea ice segmentation.

1. The features admit Gaussian-like noise with stable variance. Although most statistical methods, e.g. PCA, K-Means and GMM, require symmetrically-distributed noise with constant noise level, this requirement cannot be satisfied in the case of SAR image. Due to the multiplicative nature, the speckle noise renders the variance of \mathbf{y} unstable across the image, and the data distribution “heavy-tailed”. Nevertheless, the KPCA features solve this problem by adopting a mapping function that maps the original domain into logarithmic domain.

$$\vec{\mathbf{y}} = \Phi(\mathbf{y}) = \vec{\mathbf{x}} + \vec{\mathbf{n}} \quad (6.15)$$

where $\vec{\mathbf{x}}$ and $\vec{\mathbf{n}}$ are respectively the terrain backscatter intensity and speckle intensity of image patch in logarithmic domain. After being mapped nonlinearly into logarithmic domain, the probability density function (PDF) of $\vec{\mathbf{n}}$ is close to Gaussian distribution, and the mean and variance of $\vec{\mathbf{n}}$ do not change across the image (Hoekman 2001). Therefore, we can approximately treat $\vec{\mathbf{n}}$ as Gaussian noise with zero mean and isotropic variance matrix $\mathbf{I}_p \sigma^2$, where \mathbf{I}_p denotes the $p \times p$ identity matrix. Not only does the distribution of $\vec{\mathbf{n}}$ satisfy the implicit assumption of PCA model (Tipping and Bishop 1999), it also enables the resulting KPCA features to assume i.i.d. zero-mean Gaussian noise, as proved in Sect. 6.5.2.3. Because of this property, in Eq. (6.8), the MAP estimation of

labels is independent of noise variance. Therefore, the number of unknown parameters can be reduced.

2. The features are discriminative. The KPCA texture features are linear projections of image patches onto the leading principal axes. Since the principal axes reveal the largest variations in patch stack, the corresponding PCs therefore amount to linear texture patterns that reflect the greatest variations among different sea ice types. The subspace with the largest variance is highly possibly the subspace where sea ice classes demonstrate their differences. Suppose that texture patterns are similar within a certain class, but are different among different classes. Then the KPCA's goal of seeking subspaces with large variances will naturally drive it to find the subspaces that are capable of revealing between-class variations, instead of subspaces revealing within-class variations.
3. The features are compact. In KPCA domain, the signal is mainly captured by several leading PCs, while the last PCs are primarily due to noise. Therefore, dimension reduction can be achieved by preserving several leading PCs as texture features. In practice, KPCA features \mathbf{z}_t include only the first several PCs that explain a fixed amount (e.g. 80 %) of the data variance. Therefore, it can help reduce the computation in Eq. (6.8), since \mathbf{z}_t has much lower dimensionality than \mathbf{y}_t . Moreover, due to the orthogonal constraint, the variables in \mathbf{z}_t reflect mutually independent information, thus are capable of reducing information redundancy.
4. The features are adaptive. For predefined features, such as Gabor filter and GLCM, it is always a hard task to select relevant texture features from all available ones. But it is not the case for the KPCA features, because they are totally data-driven and capable of automatically adapting to the "best" transformations of the pixel values.

Therefore, the KPCA local texture features are powerful for sea ice segmentation. While in this chapter we adopt KPCA features to be combined use with MRF in a Bayesian framework for sea ice segmentation, it is also promising to combine them with other clustering or classification techniques for other SAR applications.

6.5.2.3 Noise Distribution of KPCA Texture Features

Since the data likelihood in the MAP estimation is realized by KPCA texture features, it is important to investigate the noise distribution of KPCA features.

In logarithmic feature space, following Eq. (6.15), we express the centralized patch variable as:

$$\vec{\mathbf{y}} = \vec{\mathbf{x}} + \vec{\mathbf{n}} \quad (6.14)$$

where $\vec{\mathbf{y}} = [\vec{y}_1, \vec{y}_2, \dots, \vec{y}_p]^T$, $\vec{\mathbf{x}} = [\vec{x}_1, \vec{x}_2, \dots, \vec{x}_p]^T$ and $\vec{\mathbf{n}} = [\vec{n}_1, \vec{n}_2, \dots, \vec{n}_p]^T$.

Based on Eq. (6.15), $\vec{\mathbf{n}}$ roughly satisfies i.i.d. Gaussian distribution with variance

matrix $\sigma^2 I_p$. Since \vec{x} and \vec{n} are independent for fully developed speckle noise, we can get:

$$\Sigma_{\vec{y}} = \Sigma_{\vec{x}} + \sigma^2 I_p \quad (6.15)$$

where $\Sigma_{\vec{y}}$ and $\Sigma_{\vec{x}}$ denote respectively the covariance matrices of \vec{y} and \vec{x} . The PCA analysis can be achieved by performing SVD on $\Sigma_{\vec{x}}$.

$$\Sigma_{\vec{x}} = \mathbf{W}\mathbf{S}\mathbf{W}^T \quad (6.16)$$

where the column vectors in \mathbf{W} represent the PCA bases with sequentially largest variances, and $\mathbf{S} = \text{diag}(\lambda_1, \dots, \lambda_p)$ is a diagonal matrix with the diagonal elements being the variances of PCs. Then, we have

$$\Sigma_{\vec{y}} = \mathbf{W}\mathbf{S}\mathbf{W}^T + \sigma^2 \mathbf{W}\mathbf{W}^T = \mathbf{W} \begin{bmatrix} \lambda_1 + \sigma^2 & \cdots & 0 \\ \vdots & \ddots & \vdots \\ 0 & \cdots & \lambda_p + \sigma^2 \end{bmatrix} \mathbf{W}^T \quad (6.17)$$

So we can see, $\Sigma_{\vec{x}}$ and $\Sigma_{\vec{y}}$ share the same PCA bases. As in Eq. (6.14), the texture features can be obtained by projecting the image patch onto PCA bases:

$$\mathbf{z} = \mathbf{W}^T \vec{y} = \mathbf{W}^T \vec{x} + \mathbf{W}^T \vec{n} = \mathbf{z}_x + \boldsymbol{\eta} \quad (6.18)$$

where $\mathbf{z}_x = \mathbf{W}^T \vec{x}$ and $\boldsymbol{\eta} = \mathbf{W}^T \vec{n}$ stand respectively for the signal and noise parts in texture features \mathbf{z} . Denote the variance matrix of \mathbf{z} by $\Sigma_{\mathbf{z}}$:

$$\Sigma_{\mathbf{z}} = \Sigma_{\mathbf{z}_x} + \Sigma_{\boldsymbol{\eta}} = \begin{bmatrix} \lambda_1 & \cdots & 0 \\ \vdots & \ddots & \vdots \\ 0 & \cdots & \lambda_p \end{bmatrix} + \begin{bmatrix} \sigma^2 & \cdots & 0 \\ \vdots & \ddots & \vdots \\ 0 & \cdots & \sigma^2 \end{bmatrix} \quad (6.19)$$

Since the noise of KPCA feature $\boldsymbol{\eta}$ is a linear function of \vec{n} and $\Sigma_{\boldsymbol{\eta}} = \sigma^2 \mathbf{I}$, the distribution of $\boldsymbol{\eta}$ can be approximated as:

$$p(\boldsymbol{\eta}) = (2\pi\sigma^2)^{-p/2} \exp\{-\sigma^{-2}/2\boldsymbol{\eta}^T \boldsymbol{\eta}\} \quad (6.20)$$

Since $\boldsymbol{\eta}$ assumes i.i.d. zero-mean Gaussian noise, in Eq. (6.8), the MAP estimation of labels is independent of noise variance. Therefore, the number of unknown parameters can be reduced.

6.6 Results and Discussion

In this section, the results achieved by the proposed method are reported and discussed, in comparison with several other popular methods. Before reporting the results on real SAR images, we first examine the results on simulated SAR sea ice images, where clean images with ice-like gray tones were degraded by speckle noise. In simulated study, the clean images were used as ground truth to produce numerical measures for performance evaluation. For real SAR images, the evaluation of segmentation result was by visual interpretation based on prior knowledge and ice-chart concerning sea ice types and their spatial distributions.

6.6.1 Results on Simulated Imagery

One clean image (Fig. 6.6a) was degraded by speckle noise that satisfies a squared-root Gamma distribution (Xie et al. 2002). Simulated images with different noise levels measured by equivalent number of looks (ENL) were used to feed segmentation methods, in order to examine their robustness to varying noise levels.

On the simulated images, we compared the proposed method with four popular methods, such as K-Means clustering (Redmund et al. 1998), Gamma mixture (Samadani 1995), GLCM (Clausi and Yue 2004) and VMLL technique (Deng and Clausi 2005). Moreover, we also used for comparison the combination of KPCA features and K-Means clustering model, where the KPCA features are used to feed K-Means method. For the MRF-based method, we adopted the gray tone values as features, used 150 EM iterations and 10,000 simulated-annealing iterations. For GLCM, we used 12 features (i.e. entropy, dissimilarity and correlation in four directions), 64 quantization levels and the patch-size of 15×15 .

Figure 6.3 presents the segmentation results obtained by different algorithms when $ENL = 4$. The results suggest that the proposed method outperformed the other three techniques. As we can see, Gamma mixture and K-Means approaches produced intense artifacts, due to the sensitivity of single pixel to speckle noise. The GLCM and MRF methods, although were better at resisting the influence of speckle noise, produced certain misclassifications. For example, GLCM failed to delineate the boundaries accurately; MRF also failed to provide smooth boundaries. KPCA also produced artifacts due to the fact that the label correlation effect is not addressed. The proposed Bayesian method nevertheless produced segmentation results that are very similar to the true image.

We adopt the overall accuracy for quantitative evaluation. The overall accuracy is calculated as the ratio between the number of pixels that are correctly classified and the total number of pixels. Figure 6.4 shows the overall accuracy of different algorithms as a function of noise level measured by ENL. As we can see, the values of overall accuracy of the proposed method are above all the other methods. With the increasing of noise level, Gamma mixture deteriorated sharply, while MRF

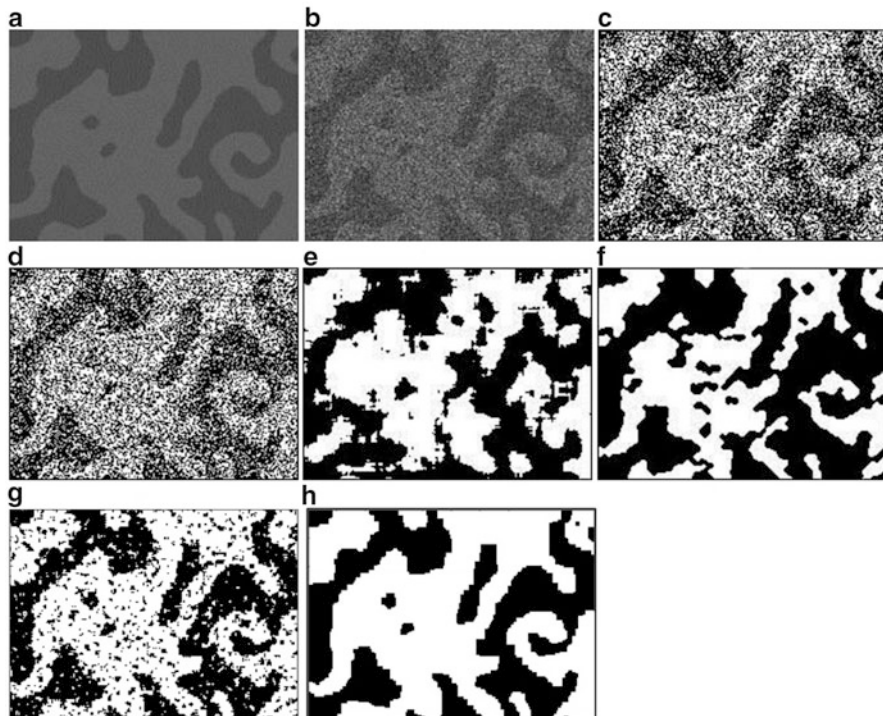


Fig. 6.3 Simulated images segmented by different techniques, (a) true image, (b) image with speckle noise ($L = 4$), (c) Gamma mixture, (d) K-Means, (e) GLCM, (f) MRF, (g) KPCA, (h) the proposed method

achieved relatively stable results. The curve of KPCA is generally above the curve of GLCM. It is remarkable that GLCM increased slightly with the increasing of noise level. It is probably because the performance of GLCM relies on strong textual patterns, which tend to be available when speckle noise is abundant. In contrast, the proposed method achieved stable overall accuracy values on different noise levels, indicating that the proposed method is robust to speckle noise.

6.6.2 Results on RADARSAT-2 Sea Ice Imagery

A HH-polarization RADARSAT-2 image comprising several sea ice types located off the coast of Newfoundland, a Canadian island province, was provided by the CIS for this study. The image was acquired in ScanSAR Wide beam mode at 22:29:36 UTC on 16 March 2009. Considering the large size ($7,291 \times 7,296$ pixels) of the original image scene (Fig. 6.5), a subset of 684×544 pixels was used for fast processing (see Fig. 6.7).

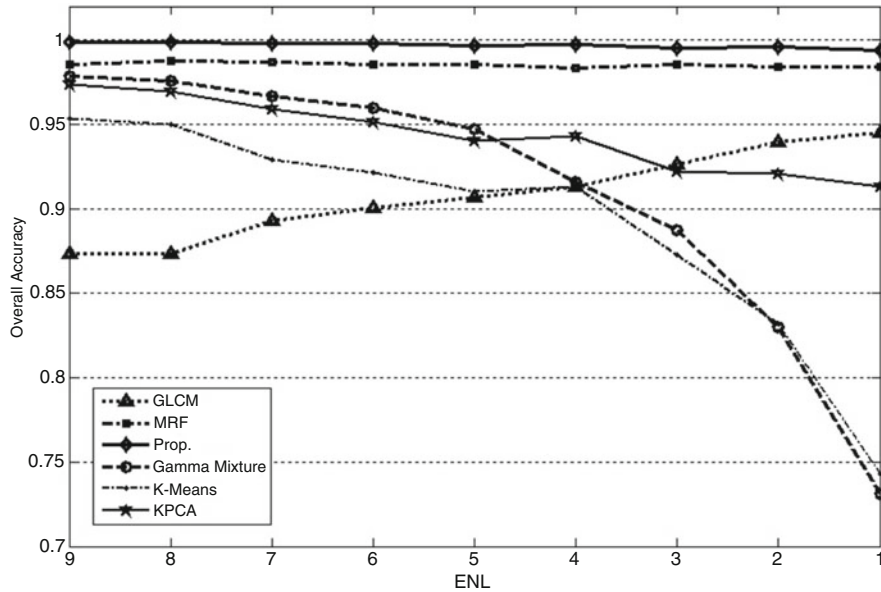


Fig. 6.4 The plot of overall accuracy as a function of noise level measured by ENL

In order to evaluate segmentation results, it is important to know accurately the location and extent of different sea ice types. The CIS website provides daily regional ice charts which provide a series of egg codes, indicating the sea ice concentrations, stages of development, and form of the ice for each segment of sea ice-covered regions. Figure 6.6 shows the daily regional ice-chart covering the study area. By carefully interpreting the egg codes for each segment of the study area, we found two sea ice types in Fig. 6.7, i.e. the gray ice with a thickness of 10–15 cm and medium thick first-year ice with a thickness of 70–120 cm.

We tested different methods on three sub-images from Fig. 6.7. In this experiment we used the same parameter setting as in the experiments on synthetic image. In order to test the log-transformation on image segmentation, we implemented a so-called log K-Means algorithm that transforms SAR images into logarithmic domain before performing K-Means clustering. The results are shown in Figs. 6.8, 6.9, and 6.10.

The results on real SAR images are consistent with simulated study. And we can extract the following conclusions based on the results. The proposed method can accurately resist the influence of speckle noise, while in the meantime discriminate different sea ice types very accurately. For example, in Fig. 6.8 suggests that KPCA can precisely delineate sea ice boundaries. Moreover, although it is challenging to identify small classes, i.e. seawater in Figs. 6.9 and 6.10, the proposed method delineated seawater areas accurately. Another powerful model, MRF although performed quite well in Fig. 6.9, confused seawater with certain gray ice in Fig. 6.10.



Fig. 6.5 RADARSAT-2 image ($7,291 \times 7,296$ pixels) covering the sea area nearby the Island of Newfoundland in Canada, ScanSAR Wide beam mode, HH polarization, taken at 22:29:36 on March 16, 2009

Logarithmic projection should be adopted as a pre-processing step for SAR sea ice image segmentation in general. Most statistical methods, e.g. PCA, K-Means and GMM rely on symmetric distributed noise with constant noise level. However, this requirement cannot be satisfied in the case of SAR imagery, where the multiplicative speckle noise assumes “heavy-tailed” distribution with unstable variance. Nevertheless, after mapping nonlinearly into logarithmic domain, the PDF of speckle noise is close to Gaussian distribution, with constant mean and variance (Hoekman 2001). This conclusion is confirmed by experiments. For example, in Figs. 6.8, 6.9, and 6.10, where the classical K-Means method misclassified seawater with gray ice, the log K-Means, which works in logarithmic domain, demonstrated better separation of different sea ice types.

Last, the proposed method is much more computationally efficient than other advanced algorithms, i.e. GLCM and MRF. All the algorithms were implemented in MATLAB, and ran on a PC with an Inter(R) 2.40GHZ Quad-Core processor. To process a 256×256 pixels sub-image, it took K-Means, proposed method, GLCM and MRF 0.038, 0.619, 113.090, and 5049.462 s, respectively.

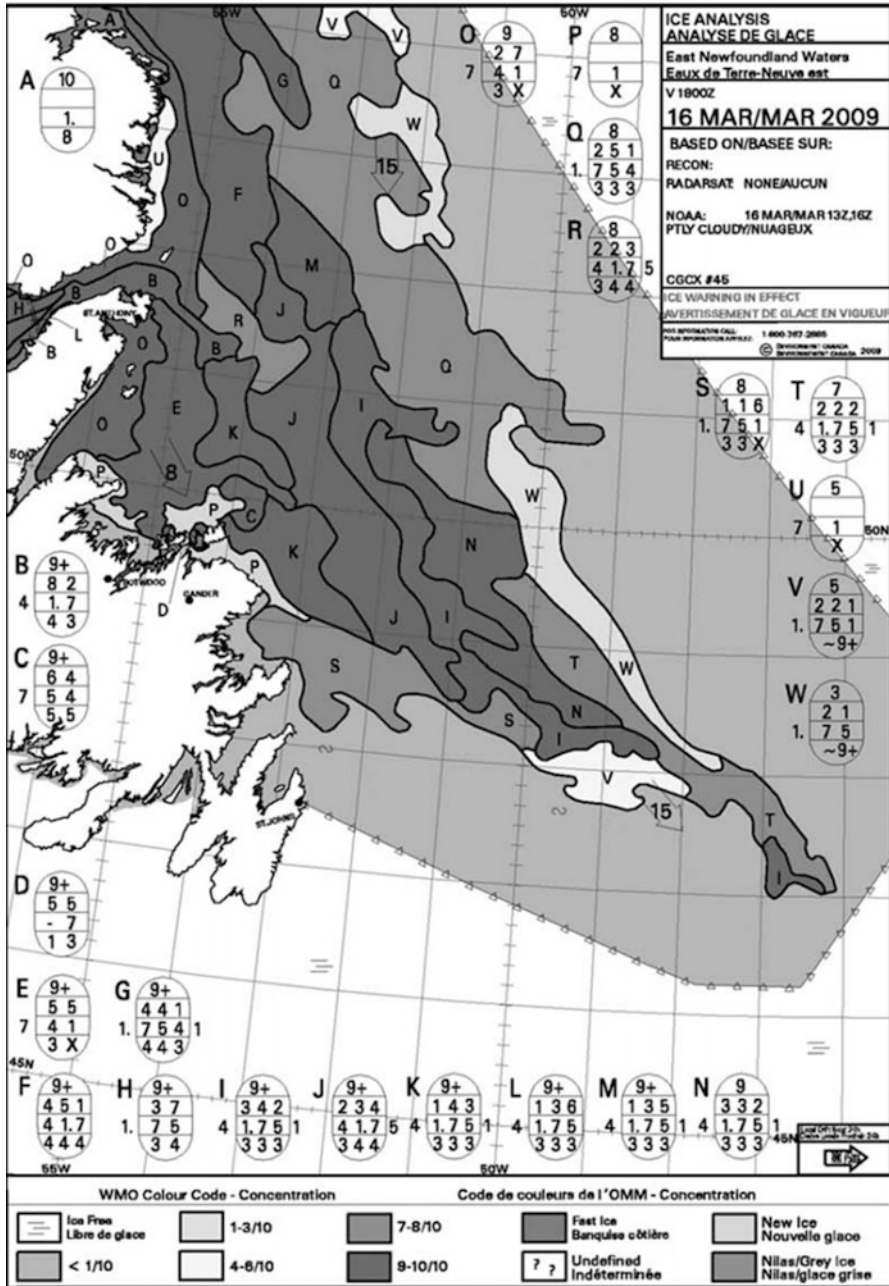


Fig. 6.6 Daily regional ice-chart covering the study area. The egg codes, i.e. the oval symbols, contain ice information of different regions, i.e. concentrations, stages of development (age) and form (floe size) of ice

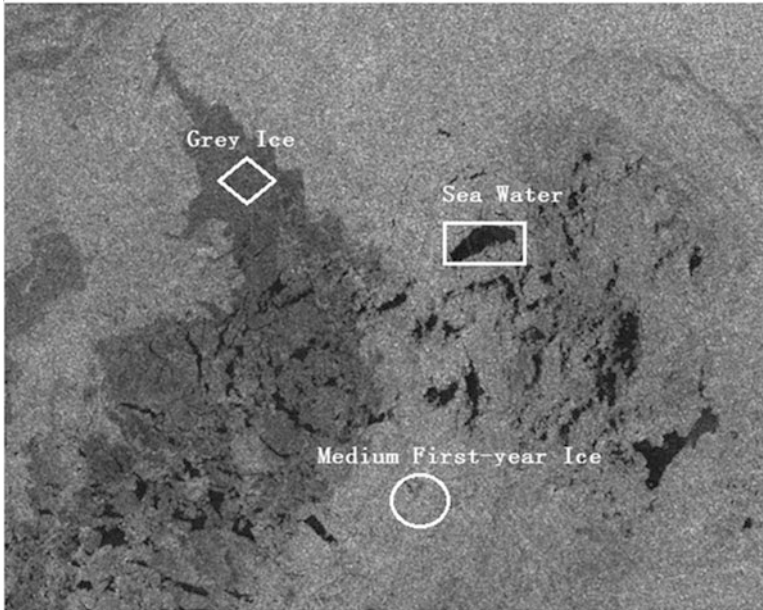


Fig. 6.7 Subset taken from the sea ice region (684×544 pixels)

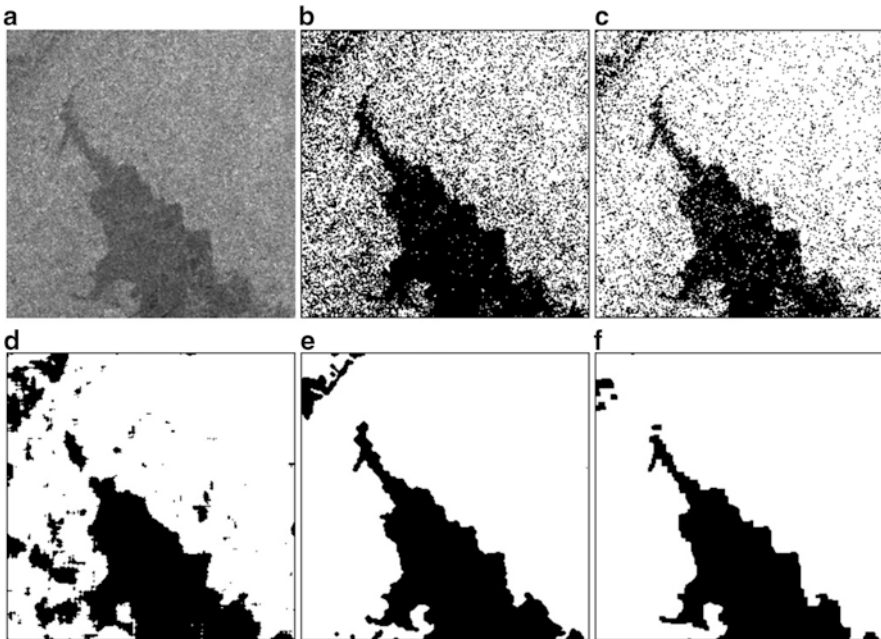


Fig. 6.8 RADARSAT-2 images with two sea ice types by different segmentation techniques, (a) original image, (b) K-means (c) Log K-means, (d) GLCM, (e) MRF, (f) the proposed method

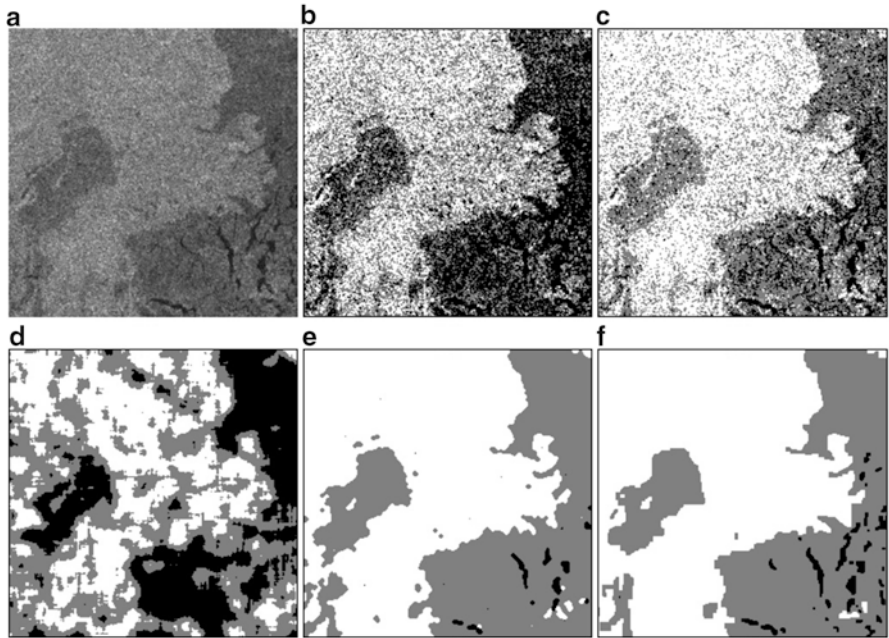


Fig. 6.9 RADARSAT-2 images with three sea ice types by different segmentation techniques, (a) original image, (b) K-means (c) Log K-means, (d) GLCM, (e) MRF, (f) the proposed method

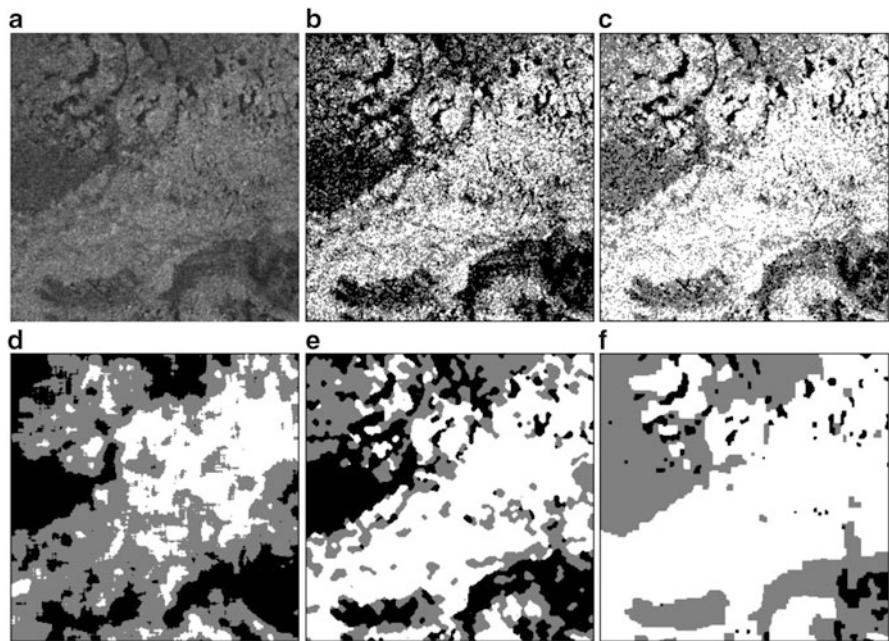


Fig. 6.10 RADARSAT-2 images with three sea ice types by different segmentation techniques, (a) original image, (b) K-means (c) Log K-means, (d) GLCM, (e) MRF, (f) the proposed method

6.7 Conclusions

In this chapter, we have provided an overview of satellite SAR image analysis techniques for sea ice mapping. Based on the characteristics of SAR sea ice imagery, we have presented a Bayesian method for fast and accurate segmentation of SAR sea ice imagery. The proposed segmentation scheme is capable of accounting for the spatial correlation effect on both pixel observations and the pixel labels. The proposed KPCA technique was performed on the image patches to extract compact and discriminative texture features with Gaussian-like noise characteristics. These KPCA texture features are totally data-driven and capable of revealing between-class variations. In the proposed Bayesian method, the combined use of KPCA feature likelihood and the MRF label prior constitutes a coherent and powerful scheme for automated segmentation of SAR sea ice imagery. Both simulated SAR images and RADARSAT-2 sea ice images were used for comparing our segmentation scheme with several other popular methods, such as K-Means, Gamma mixture, GLCM and MRF. The results evaluated by both visual interpretation and quantitative measures suggested that the proposed method achieved higher accuracy than the referenced techniques. Moreover, the proposed method achieved very high time-efficiency, thus may better support the operational segmentation of SAR sea ice imagery.

References

- Bagon S (2006) Matlab wrapper for graph cut, Dec [online] Available <http://www.wisdom.weizmann.ac.il/~bagon>
- Baraldi A, Parmiggiani F (1995) An investigation of the textural characteristics associated with gray level co-occurrence matrix statistical parameters. *IEEE Trans Geosci Remote Sens* 33(2):293–304
- Barber DG, Ledrew EF (1991) SAR sea ice discrimination using texture statistics: a multivariate approach. *Photogramm Eng Remote Sens* 57(4):385–395
- Besag J (1986) On the statistical analysis of dirty pictures. *J R Stat Soc Ser B* 48:259–302
- Boykov Y, Veksler O, Zabih R (2001) Fast approximate energy minimization via graph cuts. *IEEE Trans Pattern Anal Mach Intelligence* 20(11):1222–1239
- Burns BA, Kasischke ES, Nuesch DR (1982) Extraction of texture information from SAR data: application to ice and geological mapping. *International Symposium on Remote Sensing of Environment*, Fort Worth, TX, 6–10 Dec, pp 861–868
- Carsey FD (ed) (2013) *Microwave remote sensing of sea ice*. Online ISBN: 9781118663950, Geophysical Monograph Series, Wiley. doi:10.1029/GM068
- Clausi DA (2001) Comparison and fusion of co-occurrence, gabor and MRF texture features for classification of SAR sea-ice imagery. *Atmos-Oceans* 39(3):183
- Clausi DA (2002) An analysis of cooccurrence texture statistics as a function of grey level quantization. *Can J Remote Sens* 28(1):45–62
- Clausi D, Yue B (2004) Comparing cooccurrence probabilities and markov random fields for texture analysis of SAR sea ice imagery. *IEEE Trans Geosci Remote Sens* 42(1):215–228

- CCRS (2009) Tutorial: Fundamentals of Remote Sensing. <http://www.nrcan.gc.ca/earth-sciences/geomatics/satellite-imagery-air-photos/satellite-imagery-products/educational-resources/9309>
- Deng D, Clausi DA (2005) Unsupervised segmentation of synthetic aperture radar sea ice imagery using a novel markov random field model. *IEEE Trans Geosci Remote Sens* 43(3):528–538
- Frost VS, Stiles JA, Shanmugan KS, Holtzman JC (1982) A model for radar images and its application to adaptive digital filtering of multiplicative noise. *IEEE Trans Pattern Anal Mach Intell PAMI-4*(2):157–166
- Geman S, Geman D (1984) Stochastic relaxation, Gibbs distribution, and the Bayesian restoration of images. *IEEE Trans Pattern Anal Mach Intelligence PAMI-6*(6):721–741
- Haralick RM, Shanmugam K, Dinstein I (1973) Textural features for image classification. *IEEE Trans Syst Man Cybern* 3(6):610–621
- Havercamp D, Soh L, Tsatsoulis C (1993) A dynamic local thresholding technique for sea ice classification. In: *Proceedings of IGARSS 1993*, vol 2, Tokyo, 18–21 Aug, pp 638–640
- Heolbaek-Hansen E, Thjelmeland H, Johannessen O, Olaussen MT, Karpuz R (1989) Speckle reduction and maximum likelihood classification of SAR images from sea ice recorded during MIZEX 87. In: *Proceedings of IGARSS 1989*, vol 2, Vancouver, 10–14 July, pp 755–758
- Hoekman DH (2001) Speckle ensemble statistics of logarithmically scaled data. *IEEE Trans Geosci Remote Sens* 29:180–182
- IGOS (2007) Integrated global observing strategy cryosphere theme report -for the monitoring of our environment from space and from earth. World Meteorological Organization, Geneva, Retrieved from http://igos-cryosphere.org/docs/cryos_theme_report.pdf
- Johannessen OM, Alexandrov V, Frolov IY, Sandven S, Pettersson LH, Bobylev LP, Kloster K, Smirnov VG, Mironov YU, Babich NG (2006) Remote sensing of sea ice in the northern sea route: studies and applications. Springer, Chichester
- Karvonen J (2004) Baltic sea ice SAR segmentation and classification using modified pulse coupled neural networks. *IEEE Trans Geosci Remote Sens* 42(7):1566–1574
- Kuan DT, Sawchuk AA, Strand TC, Chavel P (1985) Adaptive noise smoothing filter for images with signal-dependent noise. *IEEE Trans Pattern Anal Mach Intell PAMI-7*(2):165–177
- Kwok R, Cunningham GF, Wensnahan M, Rigor I, Zwally HJ, Yi D (2009) Thinning and 30 volume loss of the Arctic Ocean sea ice cover: 2003–2008. *J Geophys Res* 114:C07005
- Lee JS (1980) Digital image enhancement and noisefiltering by use of local statistics. *IEEE Trans Pattern Anal Mach Intell PAMI-2*(2):165–168
- Li S (2001) Markov random field modeling in image analysis. Springer, New York
- Ochilov S, Clausi D (2012) Operational SAR sea ice image classification. *IEEE Trans Geosci Remote Sens* 50:4397–4408
- Redmund Q, Long D, Drinkwater M (1998) Polar sea ice classification using enhanced resolution NSCAT data. In: *Proceedings of IGARSS 1998*, vol 4, Seattle, 6–10 July, pp 1976–1978
- Samadani R (1995) A finite mixtures algorithm for finding proportions in SAR images. *IEEE Trans Image Process* 4(8):1182–1186
- Schölkopf B, Smola A, Müller KR (1998) Nonlinear component analysis as a kernel eigenvalue problem. *Neural Comput* 10:1299–1319
- Shokr ME (1991) Evaluation of second-order texture parameters for sea ice classification from radar images. *J Geophys Res* 96(C6):10625–10640
- Shuchman RA, Wackerman CC, Maffett AL, Onstott RG, Sutherland LL (1989) The discrimination of sea ice types using SAR backscatter statistics. In: *Proceedings of IGARSS 1989*, Vancouver, 10–14 July, pp 381–385
- Soh LK, Tsatsoulis C (1999) Texture analysis of SAR sea ice imagery using gray level cooccurrence matrices. *IEEE Trans Geosci Remote Sens* 37(2):780–795
- Tippling ME, Bishop CM (1999) Mixtures of probabilistic principal component analyzers. *Neural Comput* 11(2):443–482
- Xie H, Pierce L, Ulaby F (2002) Despeckling SAR images using a low complexity wavelet denoising process. In: *Proceedings of IGARSS 2002*, vol 1, Toronto, 24–28 June, pp 321–324

Chapter 7

Landscape Ecological Mapping for Biodiversity Evaluation Using Airborne Laser Scanning Data

Mamoru Koarai

Abstract In this chapter, we describe our method for landscape ecological mapping in support of biodiversity evaluation through the use of airborne laser survey data. Our study areas include the Siretoko Peninsula, well known as a World Natural Heritage area, and the Chugoku mountainous area in the Satoyama Region, Japan. The landscape ecological map consists of the combination of a three dimensional vegetation structure classification derived from a detailed digital surface model (DSM) and a micro landform classification generated from a detailed digital elevation model (DEM). Airborne laser survey data were used to derive micro landforms under forest areas by using the last pulse data in a Fall season. Vegetation classification was generated by using the seasonal difference of the airborne laser survey data acquired in Summer and Fall. An overlay analysis of the vegetation classification and the landform classification indicates that at the Shiretoko Peninsula, three dimensional vegetation structures are more related to terrain elevation rather than micro landforms. And at the Chugoku mountainous area, some early deciduous high thin crown trees are located in historical mining sites within several micro landform categories such as gentle slope, concave and rough texture.

Keywords Airborne laser survey • Landscape ecological mapping • Three dimensional vegetation structure • Automated micro landform classification

7.1 Introduction

For biodiversity assessment, in addition to the distribution of species and the degree of deterioration of the natural environment, the topographic conditions of the assessment area must also be examined. Thus, the importance of a landscape

M. Koarai (✉)

Survey Department, College of Land, Infrastructure, Transport and Tourism (MLIT),
2-2-1 Kihei-cho, Kodaira, Tokyo 187-8520, Japan
e-mail: koarai-m9510@mlit.go.jp

© Springer Science+Business Media Dordrecht 2015

J. Li, X. Yang (eds.), *Monitoring and Modeling of Global Changes: A Geomatics Perspective*, Springer Remote Sensing/Photogrammetry,
DOI 10.1007/978-94-017-9813-6_7

137

ecological viewpoint that allows understanding of an ecosystem based on its topographic conditions is now recognized. Since Japan is a contracting state of the Convention on Biological Diversity, the acquisition of information on its biodiversity based on landscape ecology is essential.

Landscape ecology is the science of studying and improving relationships between ecological processes in the environment and particular ecosystems. This is done within a variety of landscape scales, development spatial patterns, and organizational levels of research and policy (Wu 2006). Landscape ecological map is the thematic map which shows the distribution of eco-topes, which are the smallest ecologically distinct landscape features with uniform landform, soil and vegetation. These maps are usually consisting of the combination of landform classification and vegetation classification with middle scale such as 1/25,000 or 1/50,000. Recently, by the development of airborne laser survey technology (Light Detection and Ranging; LIDAR), it is possible to detect micro landform under the forest (Sato et al. 2007) and three dimensional forest structure (Nelson et al. 1984; Næsset 1997a, b).

This study aims at understanding the detailed topographic information and the three dimensional structure of vegetation using airborne laser survey data (airborne LIDAR data), and developing a technology to construct a dataset to be used for biodiversity assessment in Japan, based on the above understanding. In this paper, the author introduces two types of landscape ecological study and mapping using airborne LIDAR data in natural heritage area and rural area (Koarai et al. 2010a, b, 2011, 2012).

7.2 Airborne Laser Survey Data

Airborne laser survey is an active measurement method in which the distance from the sensor to the ground is measured by processing the laser beam emitted from the onboard scanner and reflected on the ground. Aircraft positions are calculated using combinations of GPS data, both on the aircraft and on the ground. Aircraft acceleration and three-axial attitude data measured by an IMU (Inertial Measurement Unit) are also used for the calculation. Furthermore, the direction data of the laser beams are measured by an onboard sensor. These data are combined to calculate the three dimensional position (X, Y, Z) on the ground (Fig. 7.1).

Akutsu et al. (2005) shows vertical accuracy of airborne laser survey. The sites which were selected as points for accuracy verification were flat ground surfaces such as parks. Coordinates of verification points acquired by airborne laser survey were compared with those derived from the ground survey using GPS and leveling. The results of comparison with the altitude value of leveling, was 0.03 m on average (maximum +0.42 m minimum -0.32 m) and the standard deviation was 0.16 m.

One of characteristics of airborne laser survey is the possibility to detect micro landform under forest. Because of the stereo matching method using aerial photos will match on a tree crown, DSM will be made from aerial photo. Since a laser pulse passes through between leaves and reflects a ground surface, it is possible to detect micro landform under the forest using airborne LIDAR data. Many researches of

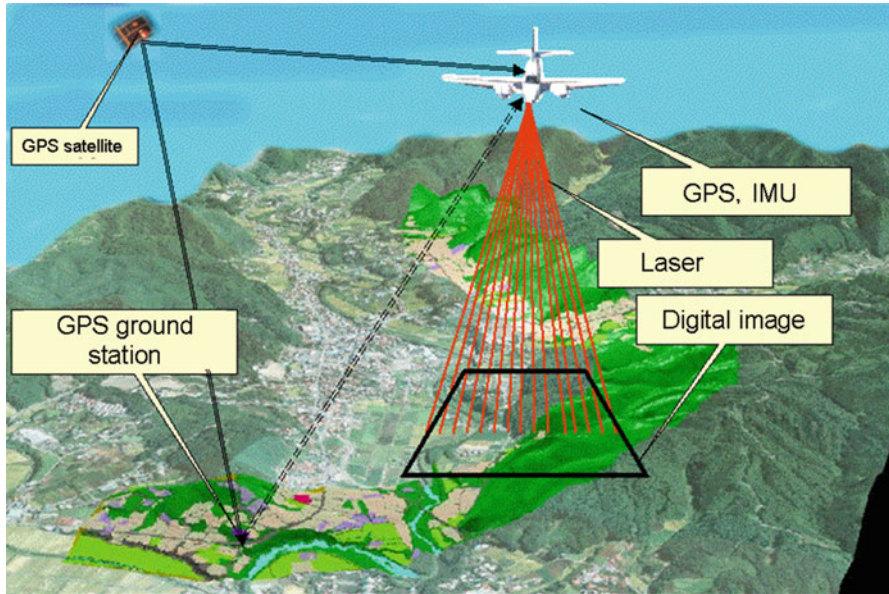


Fig. 7.1 Principle of airborne laser scanning

the automatic landform classification were carried out using DEM with 50–10 m grid size (Iwahashi and Pike 2007; Ho et al. 2011; MacMillan et al. 2003). Sato et al. (2007) was performing the automatic landform classification using airborne LIDAR data in Shirakami Mountain as the World Natural Heritage site, northeast Japan, based on the method of Iwahashi and Pike (2007).

Another characteristic of airborne laser scanning is the possibility to acquire vegetation three-dimensional information, using laser pulse reflected in leaves and branches of tree. For example, tree height can be extracted with about 1 m error (Nelson et al. 1984; Næsset 1997a, b). Næsset (1997b, 2002) show that trees numbers and sum of cross-sectional area of evergreen forest can be guessing from LIDAR data.

7.3 Study Areas

The author had selected two study areas in Japan. One is Siretoko Peninsula, Hokkaido Island as a wilderness area, and another is Chugoku Mountain, Tottori Prefecture as a Satoyama rural area (Fig. 7.2). The Shiretoko Peninsula is the World Natural Heritage Site, and a great portion of the peninsula is designated as Shiretoko National Park. The park has been subject to strict regulation as a nature preserve, and entering is prohibited in some area. The objective of the study is to understand biodiversity of this nature preserve, and to establish a landscape ecological map to ensure protection of biodiversity by using high resolution airborne

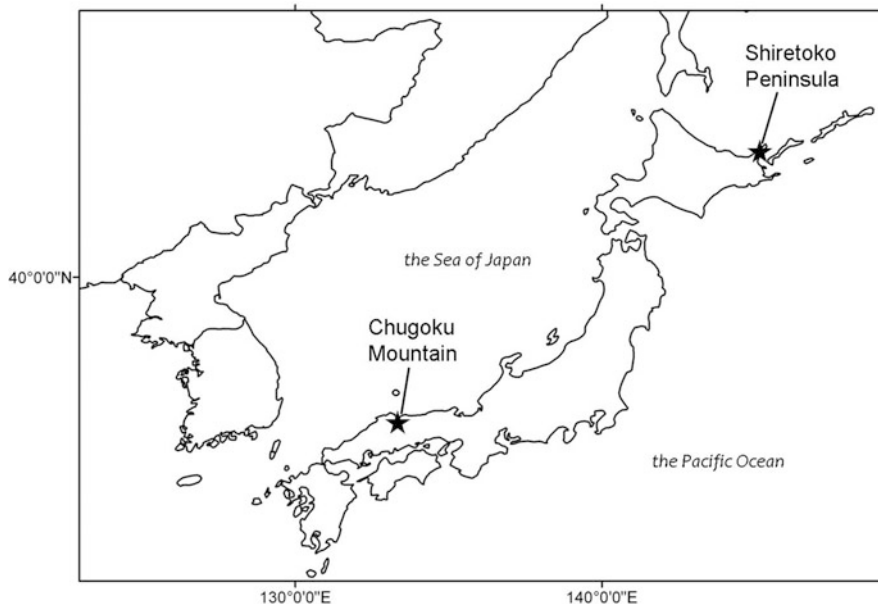


Fig. 7.2 Location map of study areas

laser survey data. The Chugoku Mountains is a typical region representing the environment of Satoyama rural areas. Research is under way to create a landscape ecological map to clarify the relationship between topography and vegetation at an iron sand mining (Kanna-Nagashi) site, and to investigate the effects of human interference activities on wildlife habitat.

7.4 Landscape Ecological Study of Shiretoko Peninsula Using Airborne Laser Data

The author tried to produce landscape ecological maps for estimation of biodiversity using airborne laser survey data. The targeted area is the south east foot of Mt. Rausu in Siretoko Peninsula, Hokkaido (Fig. 7.3). Basic legend of landscape ecological map consists of the combination of three dimensional vegetation structure classification using detailed DSM (Digital Surface Model) and micro landform classification using detailed DEM (Digital Elevation Model). The author obtained 0.5 m grid DSM and DEM of 4 km² on the south east foot of Mt. Rausu along a hiking trail in early September, 2008. The vegetation classification map with three dimensional vegetation structure was created by combining summer season (early September) 0.5 m grid LIDAR data and archived autumn season 2 m grid LIDAR data.

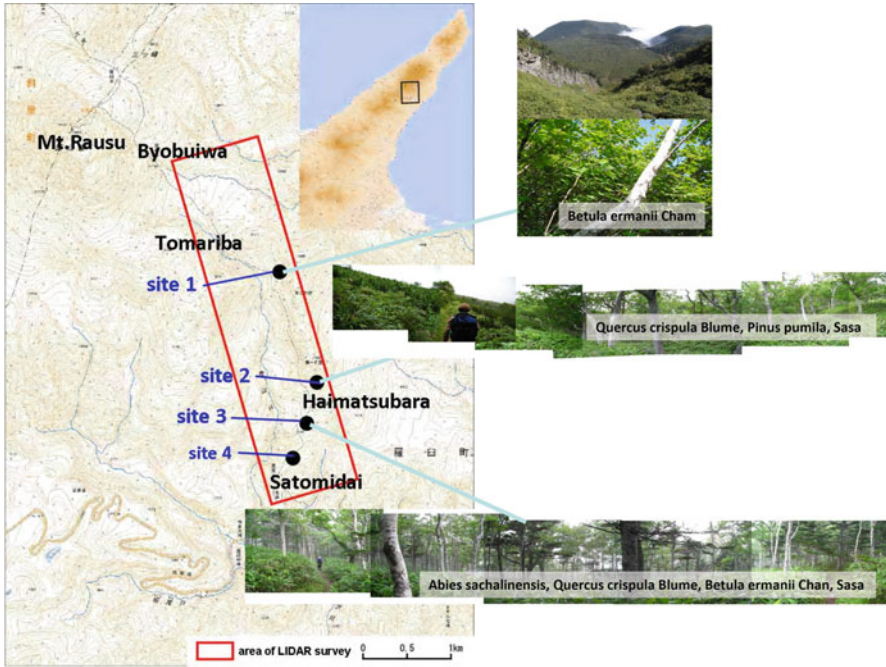


Fig. 7.3 LIDAR survey area on the south east foot of Mt. Rausu, and photos of each ground truth site

7.4.1 Produce of LIDAR Vegetation Map

Vegetation classification has been carried out using three dimensional vegetation structure detected by the difference between DSM data during the two seasons. The algorithm of producing LIDAR vegetation map (three dimensional vegetation structure map) is as follows (Koarai et al. 2010a). The legend of LIDAR vegetation map consists of the combination of vegetation height, thickness of crown and differences between the two seasons (deciduous single layer tree, deciduous multiple layer tree and evergreen tree). Vegetation height of each grid is calculated by differences between DSM and DEM. As the result of overlay analysis between vegetation height by LIDAR and Actual Vegetation Map with 1/25,000 scale by the Ministry of Environment, vegetation height is classified into four categories such as bare, grass and *Pinus pumila* (under 1.5 m), low (over 1.5 m and under 6 m), middle (over 6 m and under 10 m) and high (over 10 m). Thickness of crown of each grid is calculated by difference of max value and minimum value of random point data except ground surface. Thickness of crown of high tree is classified into two categories such as thin (under 10 m) and thick (over 10 m). The author defines that evergreen trees are those with difference between vegetation height on summer (H_s) and vegetation height on winter (H_w) under 3 m and H_s over 7 m, and other trees are deciduous trees. The deciduous tree, which H_w is over 5 m is defined to

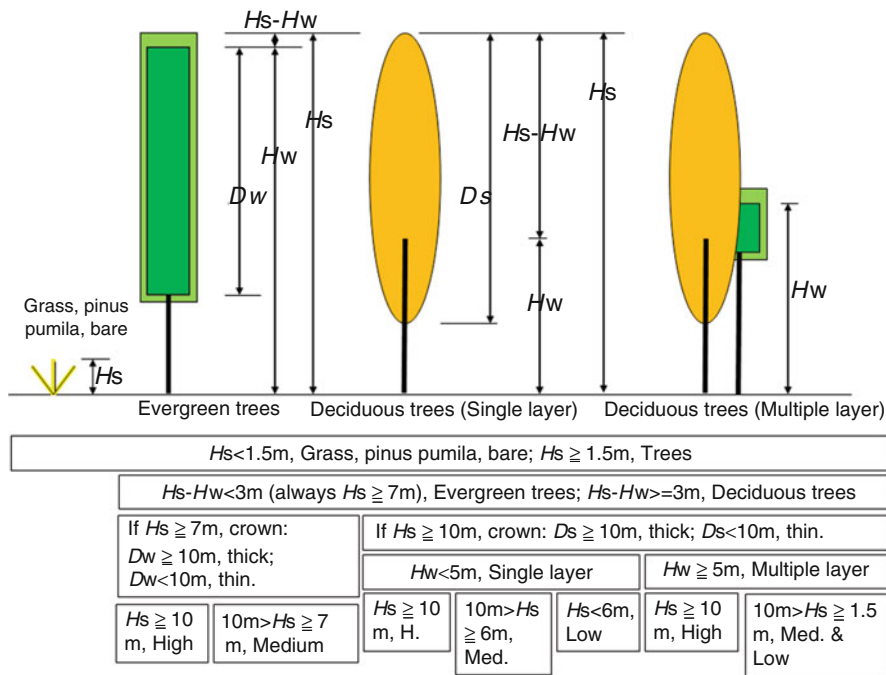


Fig. 7.4 Algorithm for vegetation classification (Koarai et al. 2010a)

deciduous multiple layer trees, because there are small evergreen trees under deciduous trees, other is deciduous single layer trees. Figure 7.4 shows the algorithm for vegetation classification of this study. Using this algorithm, it is possible to classify vegetation into 11 categories. Figure 7.5 shows LIDAR vegetation map of the south east foot of Mt. Rasue.

The results of comparison between LIDAR vegetation map and Actual Vegetation Map with 1/25,000 scale by the Ministry of Environment, shows that LIDAR vegetation map is corresponds with Actual Vegetation Map. In this study, the author carried out ground truth survey on four sites (Fig. 7.3). The results of comparison between LIDAR vegetation map and ground truth data shows that LIDAR vegetation map does not correspond completely with ground truth data on Mt. Rausu, because of the size difference between crown size of tree and grid side of LIDAR vegetation map.

7.4.2 Produce of Automated Landform Classification Map

Airborne laser survey data is useful for the detection of micro landform under forest areas by using last pulse data in autumn season. Automatic landform classification was carried out using 2 m grid autumn season DEM, by combining three categories

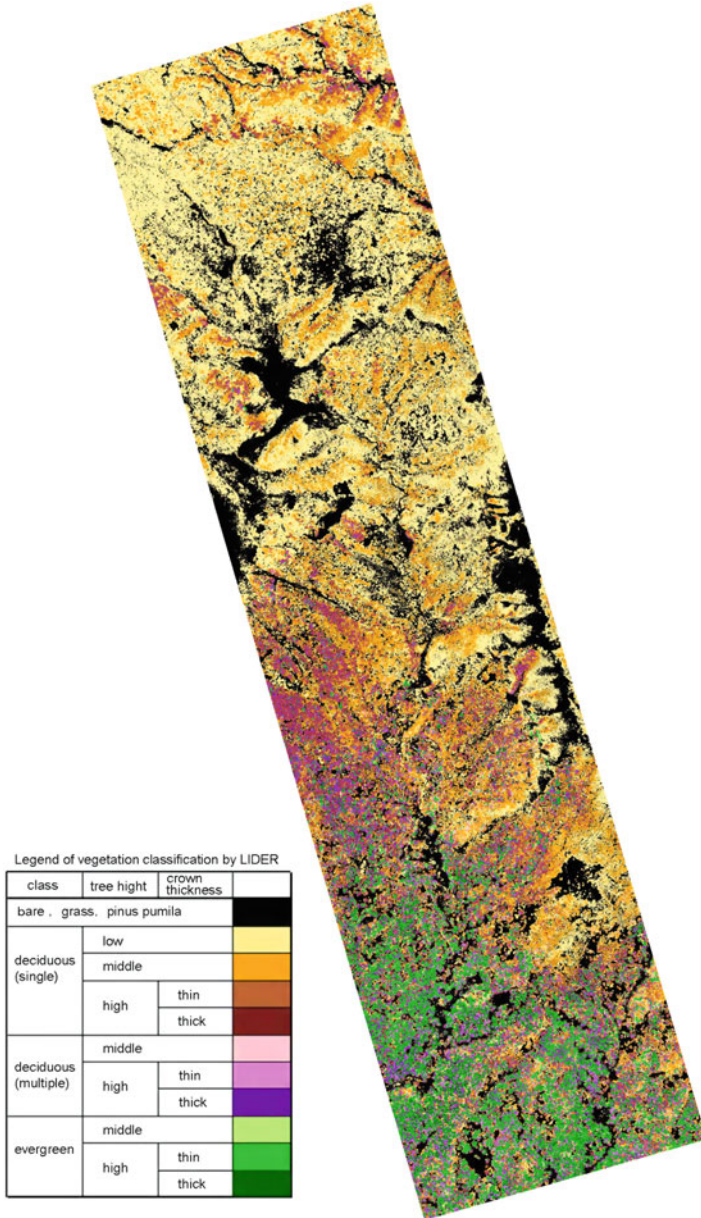


Fig. 7.5 LIDAR vegetation map on the south east foot of Mt. Rausu (Koarai et al. 2010a)

using the method by Iwahashi and Pike (2007), such as slope degree (gentle, middle and steep), convexity (convex and concave) and roughness (rough and smooth) derived from the DEM. Figure 7.6 shows automated landform classification map with 12 category (Koarai et al. 2010b).

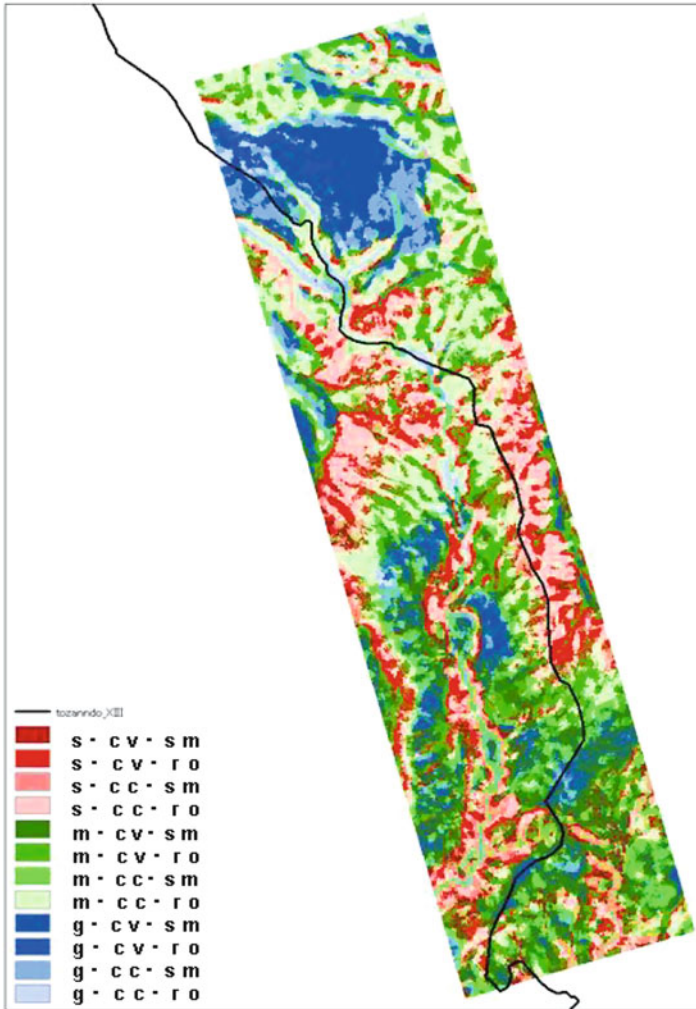


Fig. 7.6 Automated landform classification map of the south east foot of Mt. Rausu using 2 m grid DEM (*s* steep, *m* middle, *g* gentle, *cv* convex, *cc* concave, *sm* smooth, *ro* rough) (Koarai et al. 2010b)

7.4.3 Relationship Between Vegetation and Landform

The results of overlay analysis of LIDAR vegetation map and automated landform classification map are shown in Fig. 7.7. Bare, grass and *Pinus pmila*, and deciduous single layer trees have high ratio of gentle slope compared with deciduous multiple layer trees and evergreen trees. There is gentle slope of pyroclastic flow deposits on high elevation area. With these reasons, the author considers that three dimensional vegetation structures on Mt. Rausu are subject to site elevation rather than micro landform classification (Koarai et al. 2010b).

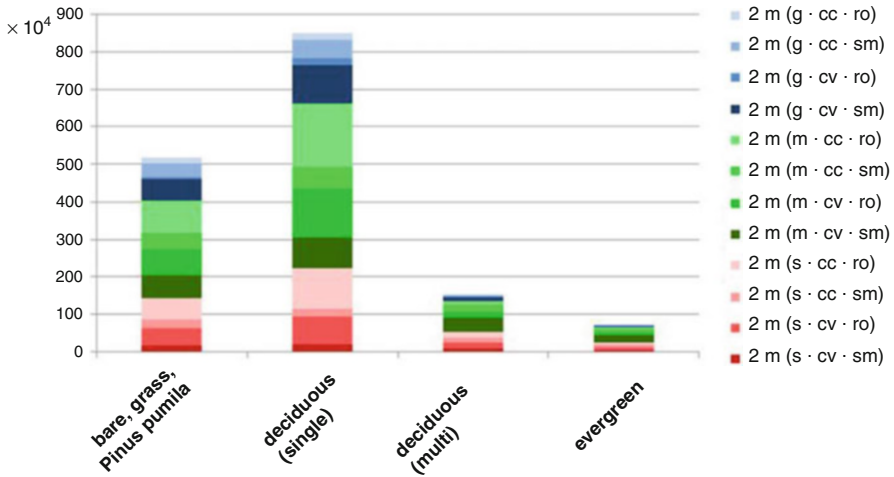


Fig. 7.7 Results of overlay analysis between LIDAR vegetation classification and 2 m grid DEM automated landform classification of Mt. Raus (Koarai et al. 2010b)

7.5 Landscape Ecological Study of Chugoku Mountain Using Lidar Data

The targeted area of Chugoku Mountain is the north foot of Mt. Dogo, Nichinan Town, Tottori Prefecture. The author obtained 1 m grid DSM and DEM of 25 km² on targeted area in November 2008, and obtained 0.5 m grid DSM of 2 km² on the north foot of Mt. Dogo in August, 2009 (Fig. 7.8). Vegetation classification map with three dimensional vegetation structure was produced by the combination of summer season airborne laser survey data and autumn season airborne laser survey data. The topographic analysis was done using autumn season airborne laser survey data.

Figure 7.9 depicts topographic counter map with 1 m interval on the north foot of Mt. Dogo by airborne laser survey data and some pictures. It is possible to detect olden iron sand mining sites (Kanna-Nagashi) with concave gentle slope area in mountain area surrounded by artificially cutting steep slope, using the method of counter line interpretation. The author interprets that areas A and B are olden Kana-Nagashi sites, and areas C and D are artificial cannels for mineral classification by specific gravity method on Kana-Nagashi site. In ground survey, *J. mandshurica* (kind of nuts) is dominated in concave gentle slope which is interpreted as Kanna-Nagashi site.

7.5.1 Produce of LIDAR Vegetation Map

Vegetation classification has been carried out using three dimensional vegetation structure detected by the difference between DSM data in two seasons. Algorithm

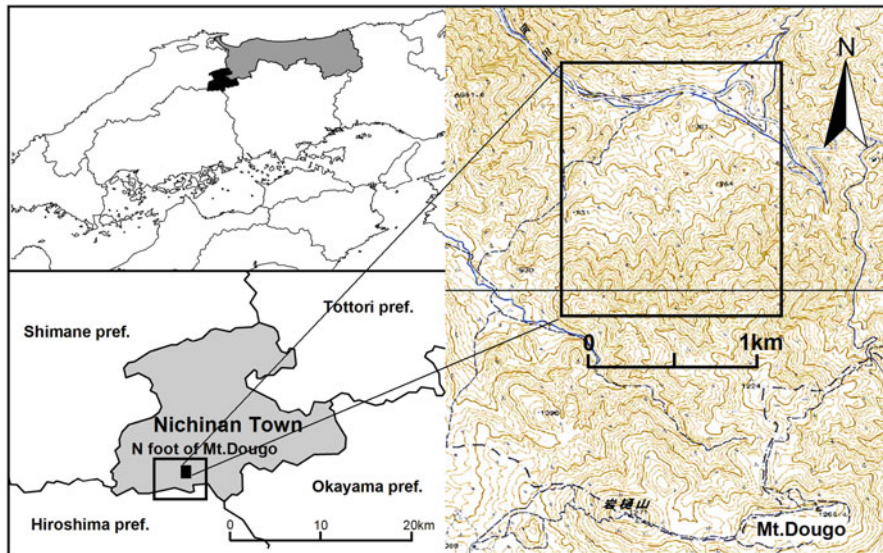


Fig. 7.8 Study area of Chugoku Mountain

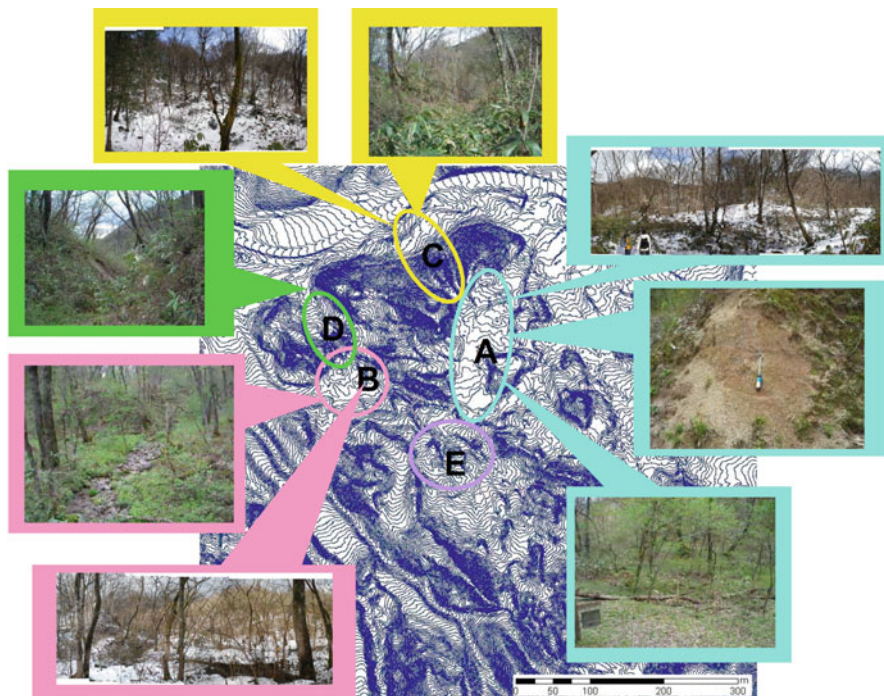


Fig. 7.9 Topographical counter map with 1 m interval of the north foot of Mt. Dougo by airborne laser data (Koarai et al. 2010b)

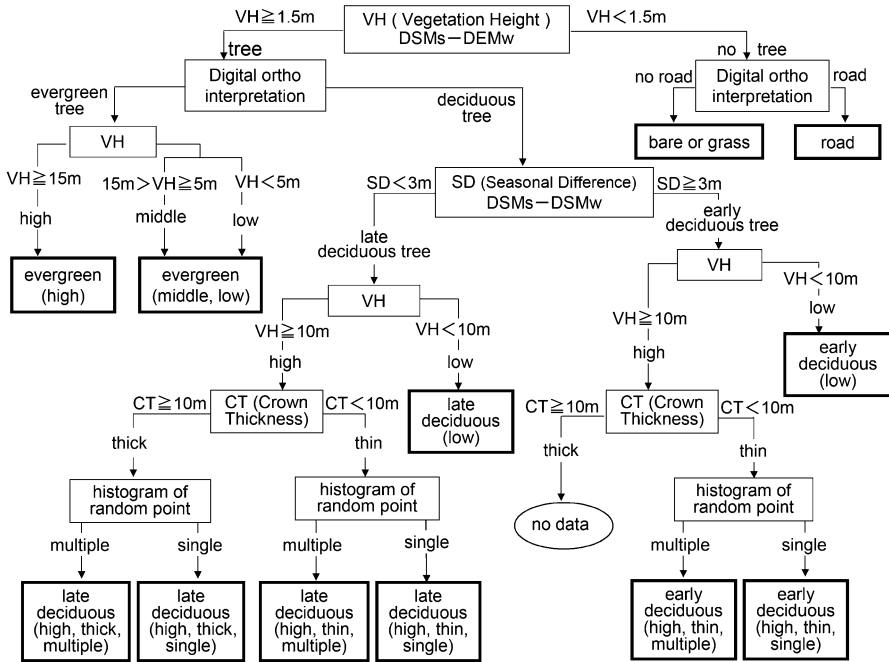


Fig. 7.10 Decision tree of vegetation classification of Chugoku Mountain using airborne laser survey data (Koarai et al. 2011)

of producing LIDAR vegetation map is as follows (Koarai et al. 2010b). The legend of LIDAR vegetation map consists of the combination of difference in two seasons (early deciduous trees, late deciduous trees and evergreen trees), vegetation height, thickness of crown and deference of forest structure (single layer or multiple layers).

The author detects evergreen trees, roads by digital imagery interpretation. And he classified areas which the vegetation height on summer (H_s) is less than 1.5 m into bare or grass, and areas which the H_s is over 1.5 m into tree. Deciduous trees area classified into two categories such as early deciduous tree which the difference between H_s and vegetation height on winter (H_w) is over 3 m, and other trees are late deciduous trees. Vegetation height is classified into three categories such as low (under 5 m), middle (over 5 m and under 15 m) and high (over 15 m) for evergreen trees, and two categories such as low (under 10 m) and high (over 10 m) for deciduous trees. Thickness of crown of high tree is classified into two categories such as thin (under 10 m) and thick (over 10 m). Deciduous trees are divided into two categories such as single layer and multiple layers using histogram of random point data in summer season. The decision tree of algorithm for vegetation classification was shown in Fig. 7.10.

Using this algorithm, it is possible to classify vegetation with 12 categories. Figure 7.11 shows LIDAR vegetation map of the north foot of Mt. Dogo. In this LIDAR vegetation map, early deciduous thin crown trees mean *J. mandshurica*.

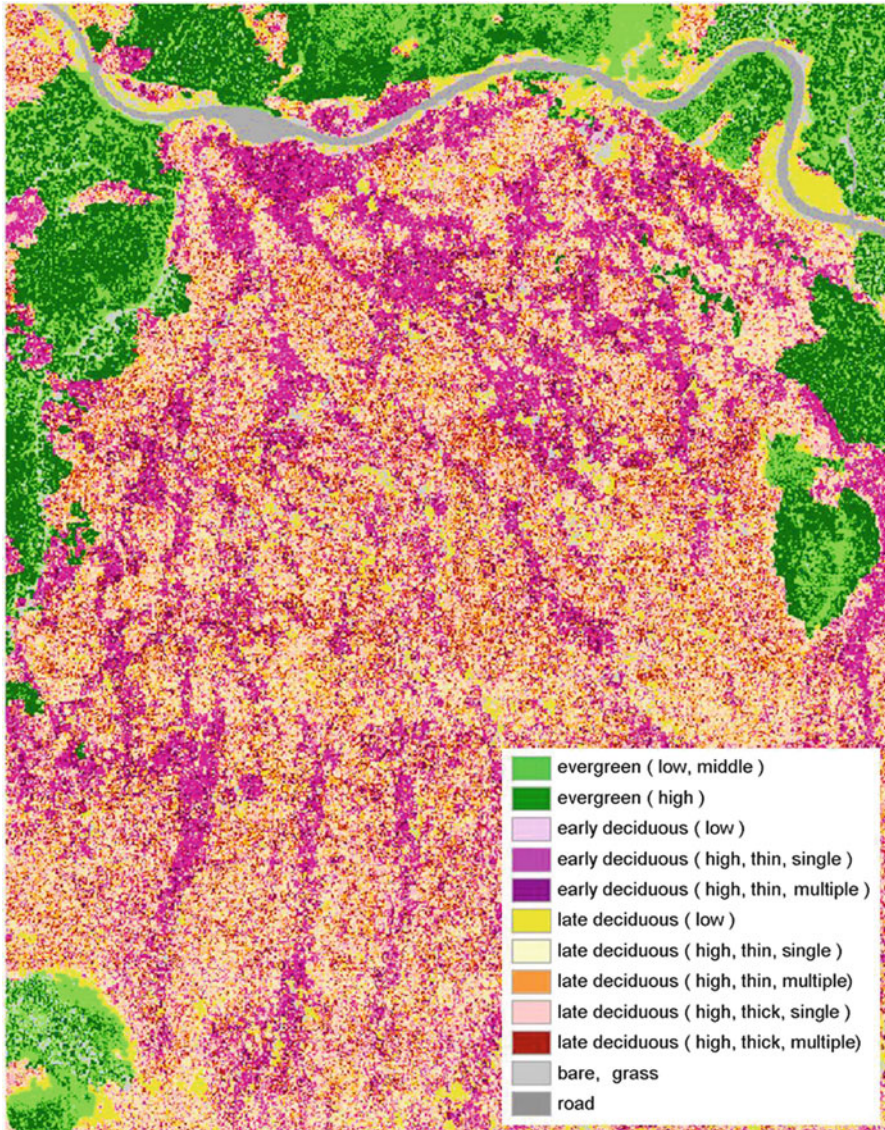


Fig. 7.11 LIDAR vegetation map on the north foot of Mt. Dogo (Koarai et al. 2010b)

7.5.2 Produce of Automated Landform Classification Map

Automatic landform classification was carried out using 1 m grid autumn season DEM, by combining three categories, such as slope degree (gentle and steep), convexity (convex and concave) and roughness (rough and smooth) derived from the DEM (Fig. 7.12).

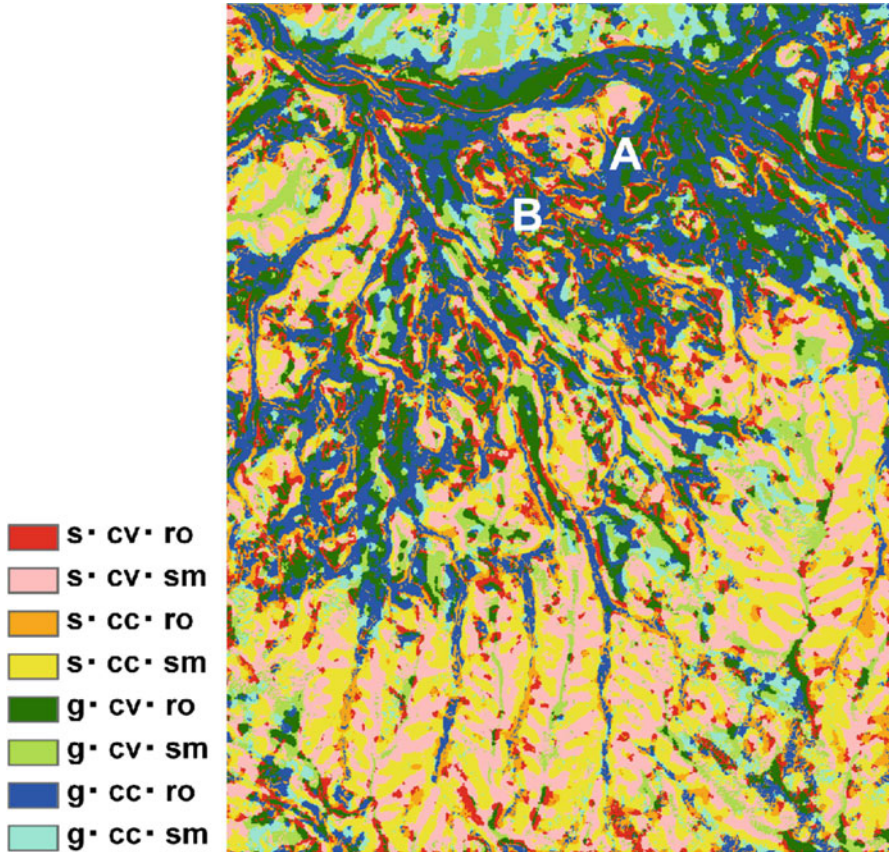


Fig. 7.12 Automated landform classification map on the north foot of Mt. Dogo (*s* steep, *g* gentle, *cv* convex, *cc* concave, *sm* smooth, *ro* rough) (Koarai et al. 2011)

Rough texture areas of 1 m grid DEM are dominated by flood plain and artificial cutting areas such as Kanna-Nagashi sites. In particular, the areas, which the values of roughness by 1 m grid DEM is approximately 0.4, correspond to Kanna-Nagashi sites located along Mt. Dogo. It is expected the value of texture indicate the existence of Kanna-Nagashi sites (Koarai et al. 2011) (Table 7.1).

7.5.3 Relationship Between Vegetation and Landform

The results of overlay analysis of LIDAR vegetation map and automated landform classification map are shown in Fig. 7.13. This result shows many forests consisting of early deciduous tree such as *J. mandshurica* were distributed in areas with gentle slope, rough texture, and concave, which were considered to be mainly created by

Table 7.1 Value of texture on each artificial sites (From Koarai et al. 2011)

Sites	Roughness (1 mDEM)	Roughness (50 mDEM)
A (Valley plain)	0.56–0.58	0.63
B (Valley plain)	0.52–0.54	0.64
C (Iron sand mining site)	0.38–0.40	0.66
D (Iron sand mining site)	0.40–0.42	0.62

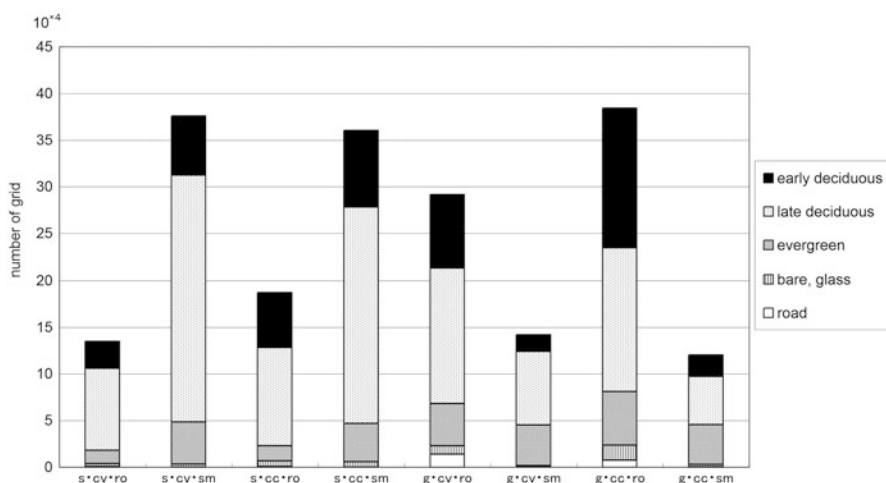


Fig. 7.13 Results of overlay analysis between LIDAR vegetation map and automated landform classification map by 1 m grid DEM (*s* steep, *g* gentle, *cv* convex, *cc* concave, *sm* smooth, *ro* rough) (Koarai et al. 2011)

Kanna-Nagashi. *J. mandshurica* is often observed as riverside vegetation and it inhabits places with abundant soil moisture. Since Kanna-Nagashi removes the soil from the mountain slopes, the slopes were flattened to become gentle slopes with rough texture and concave. Because of these unique topographic features, a riverside-like environment with abundant soil moisture was generated. *J. mandshurica* is characteristically distributed in a large area at present (Koarai et al. 2011). The eco-topo elements model in Kanna-Nagashi site are shown in Fig. 7.14.

7.6 Produce of Landscape Ecological Mapping for Biodiversity Evaluation

The author produced landscape ecological map combined with three dimensional vegetation structure and micro landform classification. Sample of landscape ecological map of the north foot of Mt. Dogo is shown in Fig. 7.15. The author

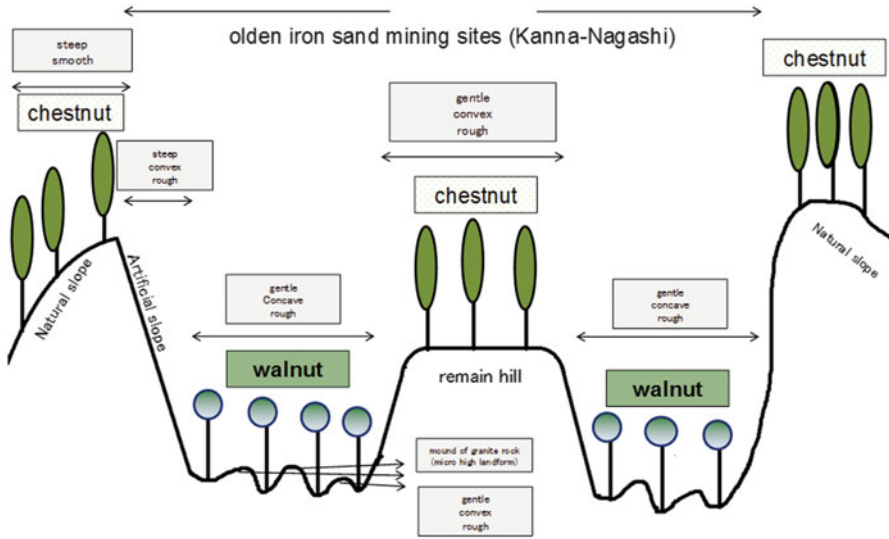


Fig. 7.14 Eco-tope elements model in Kanna-Nagashi site (old iron sand maining site) (Koarai et al. 2012)

considered new type legend of landscape ecological map of studied area in this research, using the results of overlay analysis of LIDAR vegetation maps and automated landform classification maps. The legend of this map is matrix of three dimensional vegetation map and automated landform classification map (Koarai et al. 2012). He now plans to introduce the utilization method of landscape ecological maps for natural environment conservation planning.

Since the Shiretoko Peninsula is the area currently afflicted by the vermin damage of the deer, the thin crown thickness areas of the Shiretoko Peninsula can be expected as the areas of a heavy vermin damage of a deer. In the Chugoku Mountains, old sand iron mining sites (Kanna-Nagashi), which are the artificially landform changed area, are detected as concave gentle slope areas with rough texture by landform analysis using the detailed LIDAR DEM. The specific vegetation “*J. mandshurica*”, which is an early deciduous tree with a thin crown thickness, is dominated in old sand iron mining sites.

Using landscape ecological map by LIDAR data, it is possible to extract the important eco-topes, such as a place where a special ecosystem exists or where the ecosystem is vulnerable, from all the surveyed areas. The author had given these landscape ecological maps to the local office of the Ministry of Environment and the Environmental Department of the local government. They will able to use the landscape ecological maps made from LIDAR data for the fundamental material of evaluation of biodiversity.



[Map A] 凡例 Legend

植生分類 Vegetation Classification	地形分類 Landscape Classification	緩中傾斜・凸型	緩中傾斜・凸型 人工改変の可能性あり potential historic iron sand moving site	緩中傾斜・凹型	緩中傾斜・凹型 人工改変の可能性あり potential historic iron sand moving site	急傾斜・凸型	急傾斜・凹型
		gentle / middle slope / convex	gentle / middle slope / convex	gentle / middle slope / concave	gentle / middle slope / concave	steep / convex	steep / concave
常緑樹林 (スギ・ヒノキ人工林に相当) Evergreen forest (<i>Chamaecyparis japonica</i> / <i>Chamaecyparis obtusa</i> artificial forest)	樹冠高 15m 未満 Canopy height less than 15m						
	樹冠高 15m 以上 Canopy height more than 15m						
落葉樹林 (ジュウモンジシダ・サワグルミ等類 ケルトキホウコウノ葉緑藻、ネニクムシ葉緑藻に相当) Deciduous forest (<i>Elaphoglossum phaeocarpum</i> Subsp. of <i>Dalmanella jarkoviana</i> Variant of <i>Aglaia alarhospitem</i>)	林内ギャップ Forest Gap						
	樹冠高 10m 以上、草層 Canopy height more than 10m, Sapling layer						
	樹冠高 10m 以上、落葉 Canopy height more than 10m, Deciduous layer						
落葉樹林 (クリ・ミズナラ群集に相当) Deciduous forest (<i>Castanea</i> - <i>Quercus</i> crupales)	樹冠高 10m 未満 Canopy height less than 10m						
	樹冠高 10m 以上、草層 Canopy height more than 10m, Sapling layer						
草地等 Grass land							

道路
Road
 遊歩道
Hiking trail
 等高線
Contour

Fig. 7.15 Part of landscape ecological map of the north foot of Mt. Dogo (Korai et al. 2012)

7.7 Conclusion

The landscape ecological maps using airborne laser survey data have been produced in Mt. Rausu of the Shiretoko Peninsula as World Natural Heritage area and Mt. Dogo of the Chugoku Mountains as rural area. The basic legend for landscape ecological map consists of the combination of three dimensional vegetation structure classification using detailed DSM and micro landform classification using detailed DEM. The legend of three dimensional vegetation structure maps consists of the combination of vegetation height, thickness of crown and differences between the two seasons (deciduous single layer tree, deciduous multiple layer tree and evergreen tree). Landform classification has been carried out by automatic landform classification using 1 m grid DEM, combining three categories, such as slope degree, convexity and texture. At the Mt. Rausu, three dimensional vegetation structures are subject to site elevation rather than micro landform classification. At the Mt. Dogo, some early deciduous high thin crown trees (a kind of nut) are located in historical mining sites (Kanna-Nagashi) with the following micro landform categories such as gentle slope, concave and rough texture. As the landscape ecological maps produced by LIDAR data in this study is possible to extract the important eco-topes, these maps are useful for the fundamental material of evaluation of biodiversity.

Acknowledgments This study was supported by Environment Research and Technology Development Fund (D-0805: project leader is Mamoru Koarai) from Ministry of Environment, Japan. Several collaborators are listed here: Prof. Ryota Nagasawa, Prof. Yoshiyuki Hioki, Prof. Tsuyoshi Yoshida, Prof. Akio Yamashita, Dr. Takayuki Nakano, Dr. Hiroshi P. Sato, and Mr. Kosei Otoi.

References

- Akutsu O, Ohta M, Isobe T, Ando H, Noguchi T, Shimizu M (2005) Development and utilization of high precision digital elevation data taken by airborne laser scanner. *Bull GSI* 52:13–21
- Ho LTK, Yamaguchi Y, Umitsu M (2011) Automated micro-landform classification by combination of satellite images and SRTM DEM. *Geoscience and Remote Sensing Symposium (IGARSS), IEEE International*, pp 3058–3061
- Iwahashi J, Pike RJ (2007) Automated classification of topography from DEMs by an unsupervised nested-means algorithm and a three-part geometric signature. *Geomorphology* 86:409–440
- Koarai M, Sato HP, Nakno T (2010a) Three dimensional vegetation structure map using LIDAR data. *MAP* 48–3:34–46 (in Japanese with English abstract)
- Koarai M, Nakano T, Sato HP, Yoshida T, Yamashita A, Nagasawa R, Hioki Y (2010b) Landscape ecological mapping using lidar data for biodiversity evaluation. *Int Arch Photogramm Remote Sens Spat Inf Sci*, vol XXXVIII, Part 8, Kyoto Japan: 501–506
- Koarai M, Nakno T, Sato HP, Nagasawa R, Hioki Y, Shiba E, Nakayama S (2011) Landscape ecological syudy of iron sand mining site in Chugoku Mountains using airborne laser survey (LIDAR). *J Remote Sens Soc Jpn* 31–1:36–44 (in Japanese with English abstract)
- Koarai M, Yoshida T, Nagasawa R, Nakano T, Otoi K, Hioki Y, Yamashita A, Sato HP, Shiba E, Nakayama S, Nishi K (2012) Landscape-ecological map using three dimensional vegetation

- structure and micro landform classification detected by LiDAR survey data. MAP 53-3:16-31 (in Japanese with English abstract)
- MacMillan RA, Martin TC, Earle TJ, McNabb DH (2003) Automated analysis and classification of landforms using high-resolution digital elevation data: applications and issues. *Can J Remote Sens* 29-5:592-606
- Næsset E (1997a) Determination of mean tree height of forest stands using airborne laser scanner data. *ISPRS J Photogramm Remote Sens* 52-2:49-56
- Næsset E (1997b) Estimating timber volume of forest stands using airborne laser scanner data. *Remote Sens Environ* 61-2:246-253
- Næsset E (2002) Predicting forest stand characteristics with airborne scanning laser using a practical two-stage procedure and field data. *Remote Sens Environ* 80-1:88-99
- Nelson R, Krabill W, Maclean G (1984) Determining forest canopy characteristics using airborne laser data. *Remote Sens Environ* 15:201-212
- Sato HP, Yagi H, Koarai M, Iwahashi J, Sekiguchi T (2007) Airborne LIDAR data measurement and landform classification mapping in Tomari-no-tai landslide area, Shirakami Mountains, Japan. In: Sassa K (ed) *Progress in landslide science*. Springer, Japan, pp 237-249
- Wu J (2006) Cross-disciplinarity, landscape ecology, and sustainability science. *Landsc Ecol* 21:1-4

Chapter 8

Grassland Productivity Simulation: Integrating Remote Sensing and an Ecosystem Process Model

Yuhong He, Zhangbao Ma, and Xulin Guo

Abstract The heterogeneous nature of semi-arid grasslands in Canada creates significant challenges in monitoring grassland conditions, especially in light of increasing human activities and rapid environmental changes. It is thus imperative to develop a spatially-explicit tool to monitor and predict grassland productivity and to examine its responses to land-use and environmental change processes. In response to this need, we use a spatial BIOME-BGC model to estimate spatially distributed net primary productivity (NPP) for a mixed semi-arid grassland in Canada. Given the importance of the foliar C:N ratio in modelling terrestrial biochemical cycles and the ability of remote sensing in deriving spatially distributed data, a C:N ratio map is first produced from MODIS data which is then used to drive the spatial BIOME-BGC model. The simulated NPP driven by the fixed foliar C: N (i.e., C:N = 24.0) has an average of $112.53 \text{ g C m}^{-2} \text{ years}^{-1}$, while simulated NPP driven by MODIS-derived spatial foliar C:N has an average of $107.36 \text{ g C m}^{-2} \text{ years}^{-1}$. The latter better reflects the actual NPP on the ground which is $98.29 \text{ g C m}^{-2} \text{ years}^{-1}$. The results demonstrate that spatial foliar C:N can produce a more accurate simulation of grassland biogeochemical cycles thus improving NPP simulation accuracy.

Keywords Grassland ecosystems • Productivity modelling • MODIS derived C:N ratio map

Y. He (✉)

Department of Geography, University of Toronto Mississauga,
3359 Mississauga Road, Mississauga, ON L5L1C6, Canada
e-mail: yuhong.he@utoronto.ca

Z. Ma • X. Guo

Department of Geography and Planning, University of Saskatchewan,
117 Science Place, Saskatoon, SK S7N5C8, Canada
e-mail: zhangbao.ma@usask.ca; xulin.guo@usask.ca

© Springer Science+Business Media Dordrecht 2015

J. Li, X. Yang (eds.), *Monitoring and Modeling of Global Changes:
A Geomatics Perspective*, Springer Remote Sensing/Photogrammetry,
DOI 10.1007/978-94-017-9813-6_8

155

8.1 Introduction

Globally, grasslands are important in the study of terrestrial ecosystems as they cover nearly 20 % of the Earth's surface (Lieth 1978); contain approximately 30 % of global carbon stocks (Ojima et al. 1996; Parton et al. 1996); and store at least 10 % of the global soil organic matter (Eswaran et al. 1993). There are approximately 24 M ha of mixed grasslands in Canada, serving a variety of economic, environmental, and ecological purposes. In recent years, grassland degradation has become a worldwide problem due to intense human activities and environmental changes, and the mixed grasslands of Canada are no exception. As a result, mixed grasslands have frequently been associated with fluctuating, and unreliable productivity (Curll et al. 1985a, b; Fothergill et al. 2000; He 2014; Laws and Newton 1992; Orr et al. 1990; Schwinning and Parsons 1996a, b). To ensure the sustainable development of Canadian mixed grasslands and to predict the cascading effects of human activities and climate change on these grasslands, ecosystem process modeling is required because it can simulate and predict vegetation productivity and also project ecosystem response to a wide range of environmental conditions.

Over the past 30 years, a considerable number of ecosystem process models such as BIOME-BGC (Running and Hunt 1993) and CENTURY (Parton et al. 1993) have been developed to investigate many different aspects of ecosystems, including vegetation productivity, changing vegetation distributions, and land carbon sinks (Adams et al. 2004). These models have significantly improved our understanding of the possible consequences and responses of terrestrial ecosystems to different environmental conditions (e.g. Cramer et al. 1999; Song and Woodcock 2003). At the core of most of these models is a net primary productivity (NPP) sub-model, which can be used to simulate or predict global vegetation productivity for a specific ecosystem. However, these NPP sub-models are typically site-specific, meaning they assume vegetation is homogenous within the ecosystem under study.

When applied in a spatially distributed mode, ecosystem process models can effectively integrate a diverse assemblage of data and simulate ecosystem conditions with spatial details (Turner et al. 2004). Over landscape or regional scales, remote sensing provides the only practical source of spatial information that is required to parameterize, drive and validate process-based models (Psomas et al. 2008; Turner et al. 2004). Many of the relevant data on vegetation ecosystems are now available from remotely sensed platforms, and the integration of remote sensing derived variables and process modeling is a rapidly evolving field (Cohen and Goward 2004). Examples of ecological variables that can be obtained from remote sensing data are: (1) biophysical parameters (the leaf area index and the minimum canopy resistance to evaporation), which can be assessed by spectral indices to aid biological processes that control fluxes of mass; (2) surface temperature, which can be achieved from various satellite sensors to improve simulation of energy balance components, and (3) surface soil moisture content, which can be derived from microwave data to improve the process modeling of bare soil and sparsely vegetated surfaces. The feasibility of using remote sensing data in

ecosystem models has been demonstrated in several land cover types, such as grasslands (Cayrol et al. 2000; forests (Hasenauer et al. 2012; Liu et al. 1997; Ranson et al. 2001), and croplands (Bouman 1992; Clevers and van Leeuwen 1996; Guerif and Duke 2000; Maas 1988; Weiss et al. 2001).

For Canadian mixed grassland ecosystems, a conceptual remote sensing-based BIOME-BGC model simulating spatially explicit mixed grassland productivity has already been developed (He 2008). However, there still remains a question to be addressed within this modeling framework: to what extent and with what limitations can the critical parameter(s) required by the model be derived from available remote sensing data? A critical parameter in a model is one in which minimal changes to its value would generate major changes in model output (Makler-Pick et al. 2011). When high uncertainty in a parameter coincides with high sensitivity of the model to that parameter, model predictions may not be reliable.

Foliar carbon to nitrogen ratio (C:N) drives terrestrial biogeochemical processes such as decomposition and mineralization, and is thus one of the most important parameters that significantly controls NPP in the BIOME-BGC model (White et al. 2000). Research conducted by Psomas et al. (2008) in semi-natural grassland types in the Central region of the Swiss Plateau also indicated that NPP estimates using spatial estimates of foliar C:N derived from remote sensing data are significantly different from those produced when single C:N values representing individual land cover classes were used.

Since foliar C:N ratio within the current Biome-BGC model is assumed to be constant for a given biome and given that it varies dramatically over space for different species (Psomas et al. 2008), more spatially accurate information regarding grassland spatial heterogeneity of this key parameter (i.e. foliar C:N ratio) obtained from remote sensing is needed to improve model predictions. Thus, the objectives of this research are to: (1) develop methodology for the estimation of spatially distributed foliar C:N ratio from remote sensing data; (2) test the sensitivity of the model to foliar C:N ratio; and (3) evaluate spatial C:N ratio driven modelling results.

8.2 Study Area and Field Data

The study area is located in the West Block of the Grasslands National Park (GNP) and its surroundings in southwest Saskatchewan, Canada (Fig. 8.1). A detailed description of this area could be found from He (2014). Field data were collected in mid-June 2005, the approximate date of peak growing season. A total of 24 randomly selected sites were visited, 10 of which are located in upland areas, and the remaining 14 in sloped areas. Each field site is limited to a homogeneous area of at least 1 ha in size in order to accommodate positional errors. In each field site, fresh biomass samples were collected from ten 50×50 cm quadrats. A detailed description of field sampling design and field data collection protocol can be found in

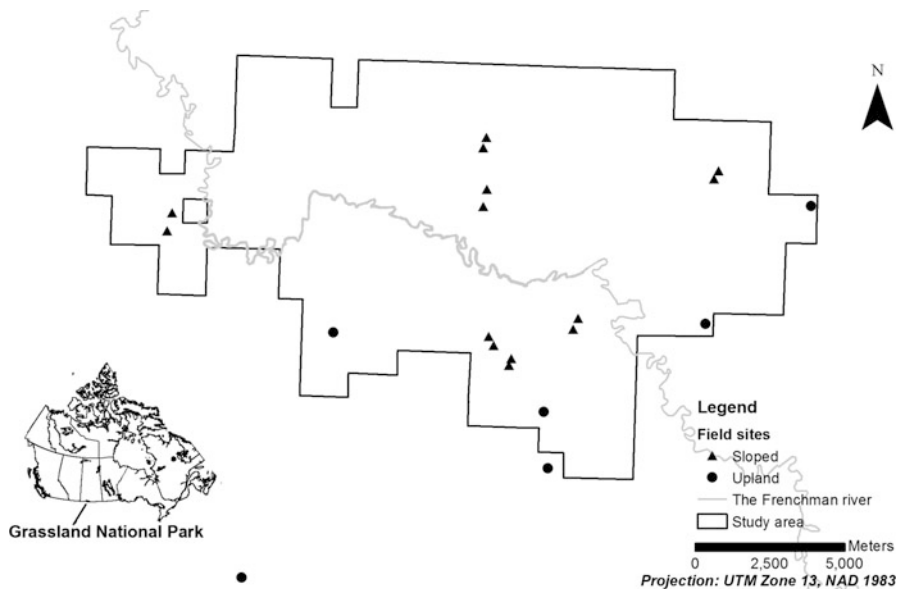


Fig. 8.1 Study area and distribution of sites in Grasslands National Park, Saskatchewan, Canada and surrounding pastures

He (2014). The dominant native grass species found in the study sites are needle-and-thread grass (*Stipa comata*), western wheat grass (*Agropyron smithii*), June grass (*Koeleria gracilis*) and blue grama (*Bouteloua gracilis*). Fresh biomass samples were dried in an oven for 48 h at 60 °C and weighed.

8.3 Integration of Remote Sensing Data and Modeling Approach

The methodology section (Fig. 8.2) starts with a brief overview of the BIOME-BGC model, is followed by the description of C:N ratio mapping for the study area, and ends with an assessment of modeling results based on field observations. The main focuses are on producing a C:N ratio map from MODIS data and on the comparisons between field-based NPP, the fixed C:N ratio driven modeling results, and the C:N ratio map driving NPP.

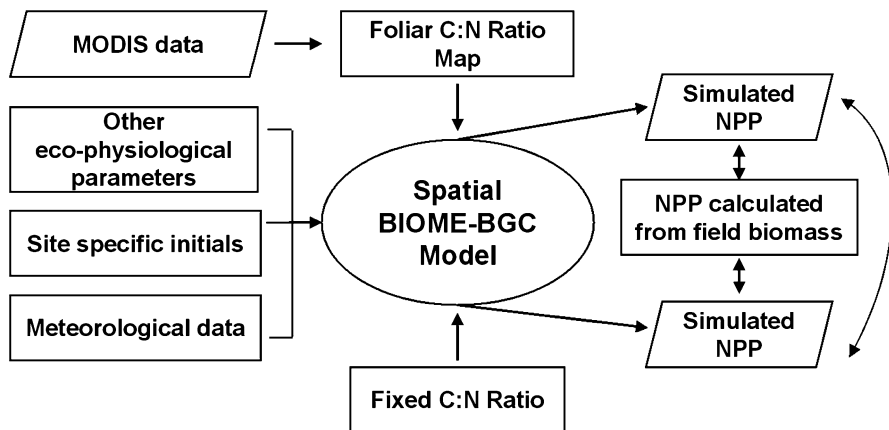


Fig. 8.2 Flowchart for running the model using spatial C:N ratio map and fixed C:N ratio

8.3.1 Model Description and Parameterization

The ecosystem process model used in this study is the BIOME-BGC, which simulates daily fluxes and storage of carbon, nitrogen, and water at specified locations when provided with appropriate weather data, physiographic information, and eco-physiological traits of the vegetation (Thornton et al. 2002). The site-specific Biome-BGC model is free to use and the program is designed to operate on the UNIX and Windows environment. The model was developed and is maintained by the Numerical Terradynamics Simulation Group in the School of Forestry at the University of Montana. Further development of the site-based model has led to the grid-based (spatial) BIOME-BGC model by the Max-Planck-Institut für Biogeochemie and also freely available (Trusilova and Churkina 2008).

The Biome-BGC model operates by using at least three input files to compute a simulation. The three basic input files include but are not limited to the initialization, meteorological, and eco-physiological data files. The initialization file provides general information about the simulation, including a description of the physical characteristics of the simulation site, a description of the time-frame for the simulation, the names of all the other required input files, the names for output files that will be generated, and lists of variables to store in the output files. The primary driving variables for estimating ecosystem processes with Biome-BGC are daily meteorological data. The model also uses a list of parameters to differentiate biomes on the basis of their eco-physiological characteristics. There are a total of 43 such parameters that must be specified for each model simulation. Most of the required parameters can be measured in the field, or can be derived from other measurements. For implementation at a particular site, field-based measurements should be used to set the relevant eco-physiological constants of the model. A list of basic inputs for each file type can be found in Thornton et al. (2002).

In this study, BIOME-BGC was applied in a pixel mode of 250×250 m, the same resolution as MODIS data. Initial modeling inputs, daily meteorological data, and parameters other than foliar C:N ratio for the study area are described in He (2008).

8.3.2 Mapping C:N Ratio Using Remote Sensing Data

To derive a C:N ratio map from remote sensing, experimental data and methods from recent literature were adopted. Specifically, the foliar C:N values were calculated by using a constant C_{CNT} value (i.e., mean C value measured at the 27 grass sampling plots measured by Psomas et al. (2008), $C_{\text{CNT}} = 44.05$) over the N predictions from a MODIS NDVI exponential model ($y = 9.98^{(-3.49x)}$; Hansen and Schjoerring 2003). In this study, MODIS Band 3 (459–479 nm) was used to replace r_{440} in the equation, and MODIS Band 4 (545–565 nm) was used to replace r_{573} (Hansen and Schjoerring 2003). Two MODIS images acquired on July 11 of 2005 (the same period that field data were collected) were obtained from the Canadian Centre of Remote Sensing and used to calculate a vegetation index and C:N ratio map.

8.3.3 Sensitivity Analysis of the Model to C:N Ratio

Sensitivity analysis (SA) is a commonly-used method to quantify the variation of the model outputs to variation in model parameters (Saltelli et al. 2000). SA of model parameters is carried out by changing them and observing the corresponding response in the output variables. When local SA techniques are applied, parameter values are changed one at a time, while fixing all other parameter values (Bar Massada and Carmel 2008). Global SA alters a subset or all the parameters simultaneously in a given model simulation (Helton et al. 2006). Two foliar C:N ratio scenarios were applied in this study to examine the sensitivity of the BIOME-BGC model, and to estimate the advantage of spatially distributed foliar C:N ratio over the constant values. First, the “global C:N” scenario was applied using C:N values ranging from 5 to 45 to drive the model. This range of foliar C:N ratio values was determined by a previous study in which grassland foliar C:N ratio was found to vary from 5.83 to 44.98 (Psomas et al. 2008). At the same time, special attention was paid to the accuracy of simulated NPP while using the default C:N ratio defined by the BIOME-BGC model (i.e., C:N = 24.0) which is most frequently used in ecosystem process modeling studies. Second, the “Remote Sensing C:N” scenario was applied using the foliar C:N map derived from MODIS data to drive the model.

8.3.4 *Modeling Results Evaluation*

Above ground biomass data collected from the study area in the peak growing season of 2005 were converted to NPP for the purpose of model evaluation. This conversion is needed because simulated NPP is the total annual production which includes both above ground and below ground production. Specifically, total biomass was calculated using a ratio of 0.57 between above ground NPP and total NPP. This ratio is adapted from Bradford et al. (2005), whereby above ground NPP of native Northern American vegetation in the Great Plains was estimated to be 164 g C/m², while below ground NPP averaged 122 g C/m². The assumptions behind the above-ground biomass and NPP conversion are: (1) any standing dead or litter was carried over from the previous year, and dead vegetation in the current year is negligible; and (2) live biomass was not carried over from previous years.

To ensure that the biomass data collected in 100 × 100 m² sites could be used to evaluate simulated NPP at a 250 × 250 m² scale, SPOT 5 imagery acquired in the summer of 2005 was utilized to investigate the homogeneity of each site and for visual comparison between vegetation density and modeling results. Mean NDVI values were calculated from the SPOT image for the 100 × 100 m² sites and also for the surrounding buffered 250 × 250 m² areas. If a significant difference of NDVI values was found between 100 × 100 m² and 250 × 250 m² areas, the site was ruled out for model evaluation.

8.4 Results and Discussion

8.4.1 *MODIS-Based Foliar C:N Ratio*

Using the two MODIS images, a foliar C:N ratio map was produced for the entire study area – the West Block of the GNP (Fig. 8.3). In the park, the foliar C:N ratio values range from 9.5 to 25.4 with a low ratio in the majority of the park area and a high ratio along the Frenchman River. The descriptive statistical analysis of the map indicates that mean C:N ratio in the park is 15.8 with a standard deviation of 5.5. The mean C:N ratio of 15.8 is much lower than the model default C:N ratio of 24 for C3 grass. Visually comparing the C:N ratio map with the SPOT 5 image (Fig. 8.3) indicates that foliar C:N ratio is high in areas with high vegetation cover (e.g. river bank), and low in areas with low vegetation cover.

8.4.2 *Sensitivity of the Model to Foliar C:N Ratio*

Figure 8.4 shows averaged model-simulated NPP, the highest simulated NPP values, and the lowest simulated NPP values from the study area in 2005, as a

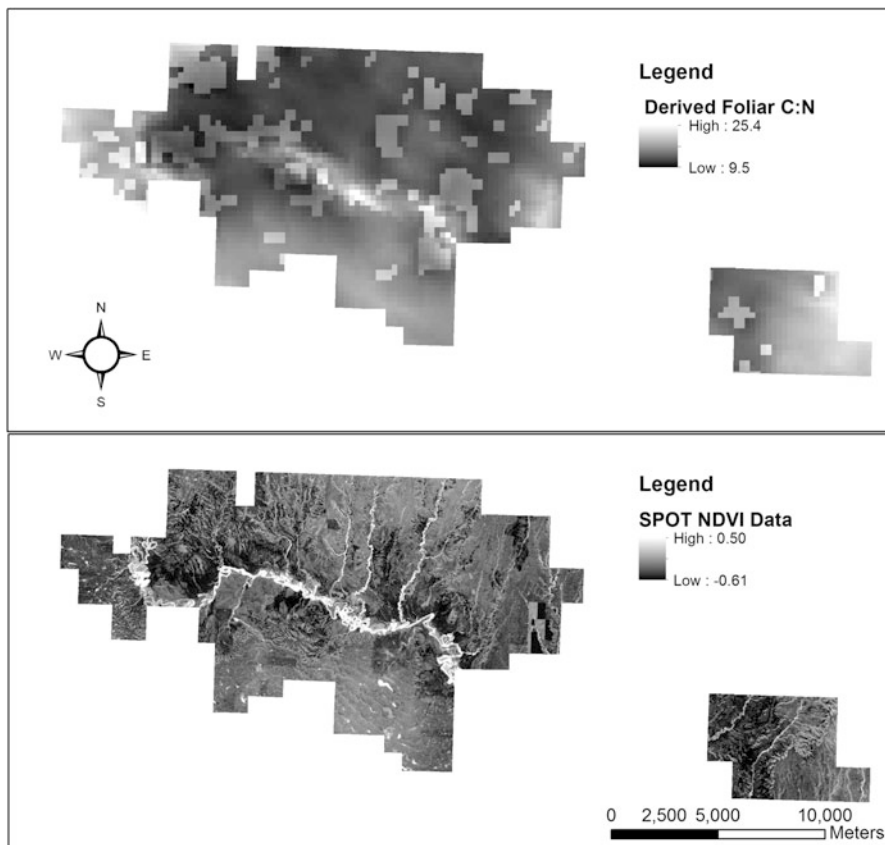
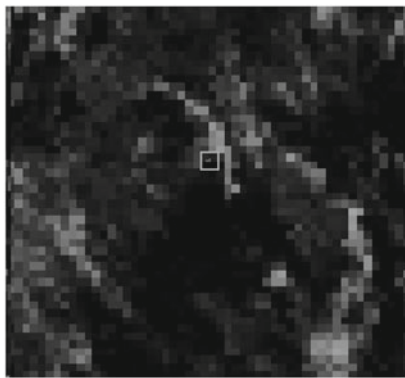
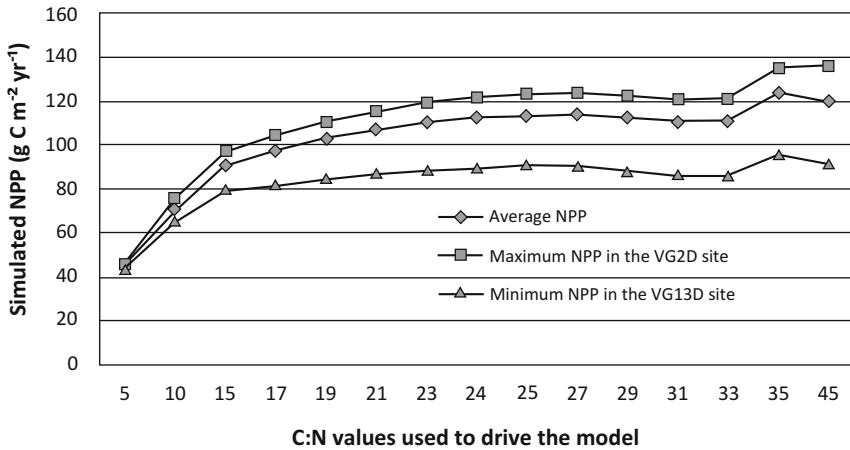


Fig. 8.3 A map of foliar C:N ratio derived from MODIS images for the West Block of the GNP (*Top*) and a SPOT NDVI image (*Bottom*)

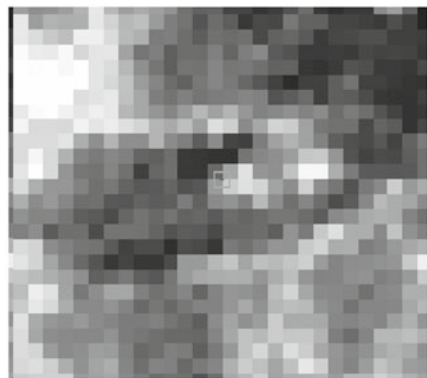
function of foliar C:N ratio. As foliar C:N ratio values changes from 5 to 45, the modelled NPP varies from 44 to 120 g C m⁻² years⁻¹ on average, from 46 to 136 g C m⁻² years⁻¹ for a site with high vegetation cover, and from 44 to 92 g C m⁻² years⁻¹ for a site with low vegetation cover.

The model has a similar response to prescribed changes in foliar C:N ratio. In general, modeled NPP increases greatly when the foliar C:N value is less than 15, and has marginal variation when foliar C:N values vary between 15 and 33, and either increases or decreases under higher foliar C:N values. Consistently, higher simulated NPP always appears in the site with higher vegetation cover (the site VG2D), and lower simulated NPP always appears in the site with lower vegetation cover (e.g. the site VG13D).

Results from sensitivity analysis of simulated NPP to foliar C:N parameter reveal that spatial BIOME-BGC model is strongly sensitive to the critical parameter foliar C:N ratio, especially when foliar C:N value is high or low.



VG13D site – Minimum Simulated NPP



VG2D site – Maximum Simulated NPP

Fig. 8.4 The sensitivity of spatial BIOME-BGC model to foliar C:N ratio. The SPOT 5 NDVI scene showing VG13D site in the *bottom left* and VG2D site in the *bottom right* (The tone from *black to white* indicating NDVI values from low to high)

8.4.3 Total Biomass Data and Their Usefulness for Model Evaluations

Total biomass data for 24 sites have been calculated based on field-collected above ground biomass in 2005 (Fig. 8.5). Total biomass averaged 95.6 g/m², with a range from 43 to 172 g/m².

To test the usefulness of the biomass data for model evaluation, each sampling site was examined to see how well it can represent its surrounding area using the SPOT 5 image. Figure 8.6 shows that only three sampling sites (SG2C, SG9C, and U4T3) have a consistent NDVI between 100 × 100 m² site and its surrounding areas, while the rest (21 sampled sites) shows a moderate to large difference. Dramatic differences between 100 × 100 m² NDVI and 250 × 250 m² NDVI can

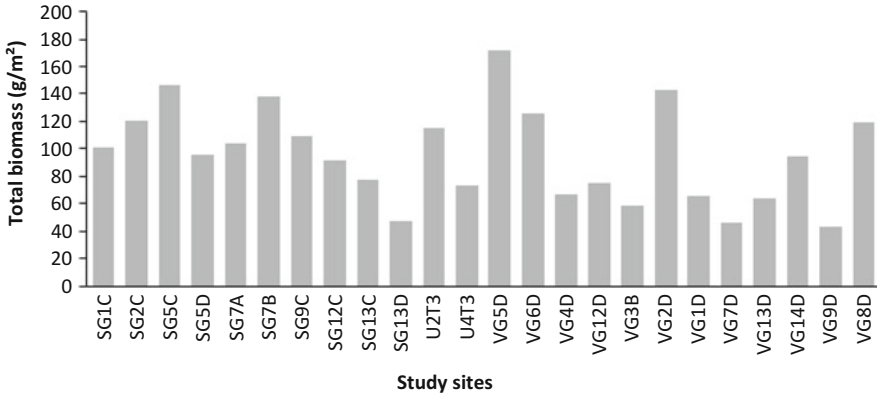


Fig. 8.5 Total biomass data calculated based on collected above ground biomass

be found in six sites (VG4D, VG5D, VG7D, VG8D, VG9D, and VG14D). Visual interpretation of these sites in the SPOT 5 image in a standard false color composite indicates that all six sites were adjacent to the Frenchmen river, with the most heterogeneous vegetation composition at a scale of $250 \times 250 \text{ m}^2$ in the study area. As a result, the biomass data from these six sites had to be removed when evaluating model NPP, as the biomass data collected in the areas of $100 \times 100 \text{ m}^2$ cannot represent modeled NPP at the $250 \times 250 \text{ m}^2$ scale.

8.4.4 Evaluating Model Simulated NPP Data

After removing the sites that were not able to represent a $250 \times 250 \text{ m}^2$ study area, the field NPP averaged from 18 sites was $98.29 \text{ g C m}^{-2} \text{ years}^{-1}$ with a standard deviation of $43.49 \text{ g C m}^{-2} \text{ years}^{-1}$. The simulated NPP based on the fixed foliar C:N has an average of $112.53 \text{ g C m}^{-2} \text{ years}^{-1}$ with a standard deviation of $21.08 \text{ g C m}^{-2} \text{ years}^{-1}$, while simulated NPP based on remote sensing derived spatial foliar C:N has an average of $107.36 \text{ g C m}^{-2} \text{ years}^{-1}$ with a standard deviation of $35.38 \text{ g C m}^{-2} \text{ years}^{-1}$ (Table 8.1). The results demonstrated that simulated NPP based on remote sensing derived spatial foliar C:N parameters are better than those based on the fixed C:N parameter for reflecting actual ground conditions.

In general, the model overestimated NPP in the area (Fig. 8.7). The relationships and RMSE between simulated NPP and observed NPP (Figs. 8.7 and 8.8 – $R^2 = 0.17$ using fixed C:N and 0.34 using spatial C:N; $\text{RMSE} = 27 \text{ g C m}^{-2} \text{ years}^{-1}$ using the fixed C:N and $22.6 \text{ g C m}^{-2} \text{ years}^{-1}$ using spatial C:N) indicate a relatively poor model predictability. Nevertheless, in comparison with fixed C:N values, spatial C:N greatly increases the accuracy of modeling results.

Even when using the foliar C:N ratio map to drive the model, the modeling accuracy is not very high. This is considered an acceptable deviation given that

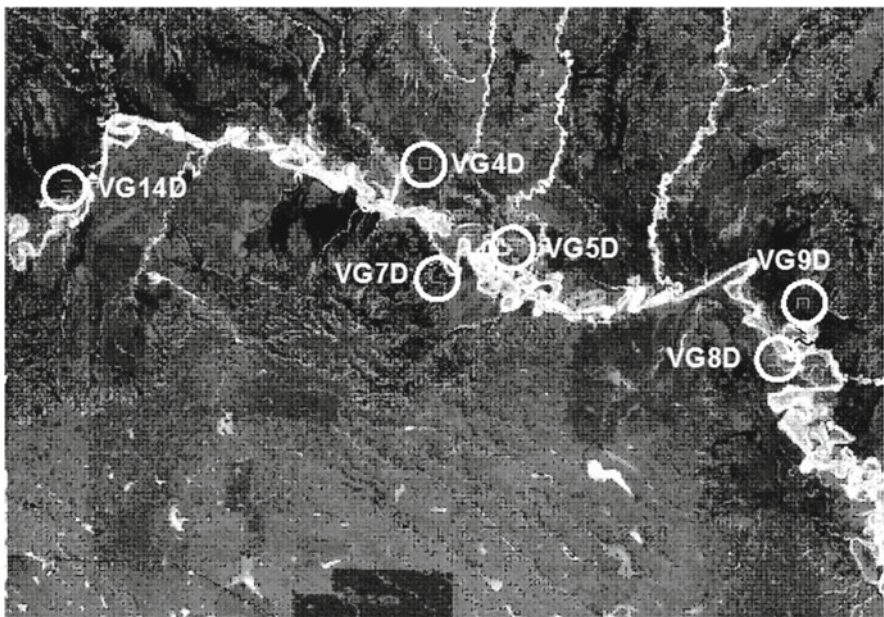
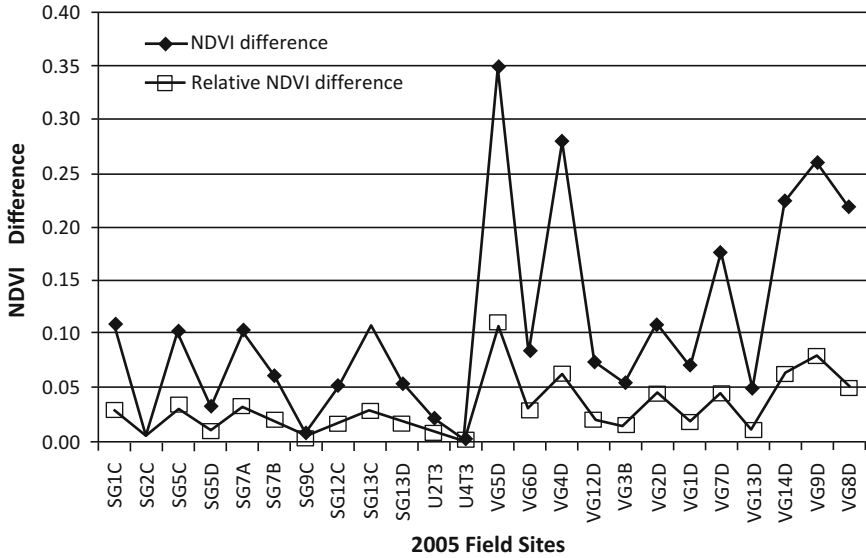


Fig. 8.6 The SPOT 5 NDVI image showing the differences of NDVI values in the $100 \times 100 \text{ m}^2$ sites and its $250 \times 250 \text{ m}^2$ surrounding area. The larger NDVI differences indicate that the $100 \times 100 \text{ m}^2$ sites could not represent their surrounding areas; therefore, the collected biomass values from these sites were not used for calculations

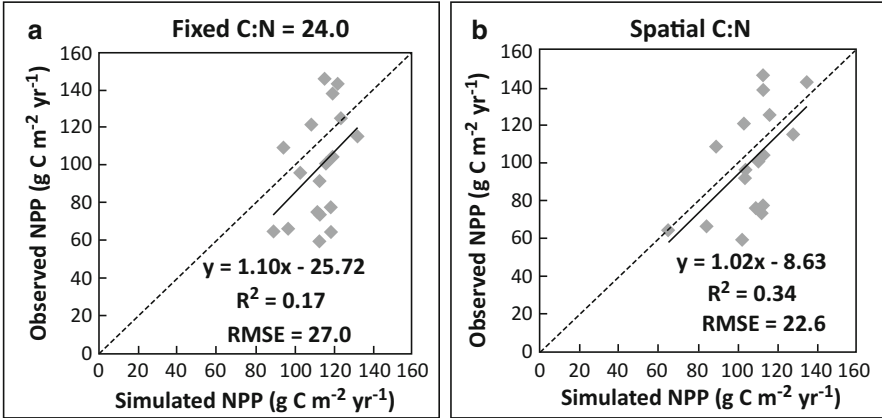


Fig. 8.7 The relationships between observed NPP and simulated NPP

Table 8.1 Descriptive statistics of field NPP ($\text{g C m}^{-2} \text{ years}^{-1}$), simulated NPP ($\text{g C m}^{-2} \text{ years}^{-1}$) from the model outputs driven by fixed foliar C:N ratio and MODIS derived spatial foliar C:N ratio

Descriptive statistics	Observed NPP	Simulated NPP driven by fixed C:N	Simulated NPP driven by spatial C:N
Average	98.29	112.53	107.36
Max	146.00	131.72	135.65
Min	59.15	89.62	65.32
STD	43.49	21.08	35.38

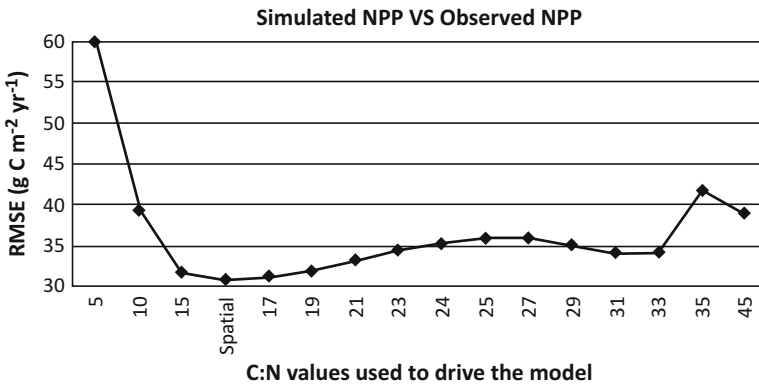


Fig. 8.8 RMSE between observed NPP and simulated NPP as a function of different leaf C:N values

there is high uncertainty in the measured NPP, the C:N ratio map, and other parameters used for the model prediction (Mitchell and Csillag 2001). In the spatial

C:N driven modeling process, two major factors may have contributed to the uncertainty of the NPP prediction: the constant C that is used for C:N ratio prediction and the N prediction model. As a result of unavailable field C and N data, this study only contributes on narrowing the uncertainty in NPP simulation that is introduced by the constant C:N ratio for Canadian mixed grasslands.

8.5 Conclusions

This study describes a method for integrating a critical remote sensing derived model parameter with the spatial BIOME-BGC model to estimate NPP in Canadian mixed grasslands. Consistent with previous findings in the literature (Psomas et al. 2008), the spatial BIOME-BGC model was also found to be highly sensitive to the critical model parameter foliar C:N ratio. Given the importance of the foliar C:N ratio in terrestrial biochemical cycles and the ability of remote sensing in providing spatially distributed foliar C:N, we coupled remote sensing derived C:N maps and ecosystem modeling in order to increase model accuracy for Canadian mixed grasslands.

MODIS data were used to derive spatial foliar C:N values for the study area. The foliar C:N ratio map indicated that MODIS derived C:N ratio has a much lower mean than the model default C:N ratio. Grassland NPP was simulated using a foliar C:N ratio map to drive the BIOME-BGC model, and field NPP data collected in 2005 were used to evaluate the model results. We found that simulated NPP based on spatially-derived foliar C:N parameter is better than that based on the fixed C:N parameter to reflect actual ground conditions. Further analysis indicated that simulated and observed NPP displayed acceptable correlations and RMSE. In comparison with fixed C:N values, spatial C:N greatly increased the accuracy of modeling results, although both simulated NPP outputs overestimated observed NPP. These results demonstrate the importance of using spatially explicated foliar biochemical parameters as an input to ecosystem process models. The use of spatial foliar C:N ratio could also lead to a better understanding of local interactions on biogeochemical cycles thus improving model accuracy.

Further work will focus on developing an experimental-based carbon and nitrogen dataset for different vegetation communities in the study area, and establishing remote sensing based C:N ratio models for these vegetation communities. In the longer term, we will also investigate other important model parameters and develop methodologies to provide spatially explicit parameters to further improve model accuracy.

Acknowledgements This research was supported by ISTPCanada C4507 to Dr. Xulin Guo and NSERC to Dr. Yuhong He. Grateful thanks to Kristina Trusilova for Max-Planck-Institut für Biogeochemie, Germany for generously sharing the codes for the terrestrial ecosystem model GBIME-BGCv1.0.

References

- Adams B, White A, Lenton TM (2004) An analysis of some diverse approaches to modeling terrestrial net primary productivity. *Ecol Model* 177:353–391
- Bar Massada A, Carmel Y (2008) Incorporating output variance in local sensitivity analysis for stochastic models. *Ecol Model* 213:463–467
- Bradford JB, Lauenroth WK, Burke IC (2005) The impact of cropping on primary production in the U.S. Great Plains. *Ecology* 86(7): 1863–1872
- Bouman BAM (1992) Linking physical remote sensing models with crop growth simulation models, applied for sugar beet. *Int J Remote Sens* 13:2565–2581
- Cayrol P, Kergoat L, Moulin S, Dedieu G, Chehbouni A (2000) Calibrating a coupled SVAT-vegetation growth model with remotely sensed reflectance and surface temperature – a case study for the HAPEX-Sahel grassland sites. *J Appl Meteorol* 39:2452–2473
- Clevers JGPW, van Leeuwen HJC (1996) Combined use of optical and microwave remote sensing data for crop growth monitoring. *Remote Sens Environ* 56:42–51
- Cohen WB, Goward SN (2004) Landsat's role in ecological applications of remote sensing. *BioScience* 54:535–545
- Cramer W, Kicklighter DW, Bondeau A, Moore B, Churkina C, Nemry B, Ruimy A, Schloss AL (1999) Comparing global models of terrestrial net primary productivity (NPP): overview and key results. *Glob Chang Biol* 5:1–15
- Curl MJ, Wilkins RJ, Snaydon RW, Shanmugalingam VS (1985a) The effects of stocking rate and nitrogen fertiliser on a perennial ryegrass-white clover sward: 1. Sward and sheep performance. *Grass Forage Sci* 40:129–140
- Curl MJ, Wilkins RJ, Snaydon RW, Shanmugalingam VS (1985b) The effects of stocking rate and nitrogen fertilizer on a perennial ryegrass-white clover sward: 2. Subsequent sward and sheep performance. *Grass Forage Sci* 40:141–149
- Eswaran H, van den Berg E, Reich P (1993) Organic carbon in soils of the world. *Soil Sci Soc Am J* 57:192–194
- Fothergill M, Davies DA, Morgan CT (2000) Sheep grazing and white clover. A rest is best? In: Rook AJ, Penning PD (eds) *Grazing management. Occasional Symposium No. 34*. Harrogate, 29 Feb–2 Mar 2000. The British Grassland Society
- Guerif M, Duke CL (2000) Adjustment procedures of a crop model to the site specific characteristics of soil and crop using remote sensing data assimilation. *Agric Ecosyst Environ* 81:57–69
- Hansen PM, Schjoerring JK (2003) Reflectance measurement of canopy biomass and nitrogen status in wheat crops using normalized difference vegetation indices and partial least squares regression. *Remote Sens Environ* 86:542–553
- Hasenauer H, Petritsch R, Zhao M, Boisvenue C, Running SW (2012) Reconciling satellite with ground data to estimate forest productivity at national scales. *For Ecol Manage* 276:196–208
- He Y (2008) Modeling grassland productivity through remote sensing products. Ph.D. thesis, University of Saskatchewan
- He Y (2014) The effect of precipitation on vegetation cover over three landscape units in a protected semi-arid grassland: temporal dynamics and suitable climatic index. *Journal of Arid Environments* 109:74–82
- Helton JC, Johnson J, Sallaberry C, Storlie C (2006) Survey of sampling-based methods for uncertainty and sensitivity analysis. *Reliab Eng Syst Saf* 91:1175–1209
- Laws JA, Newton E (1992) The grazing management of sheep on grass white clover permanent pasture. *Ir J Agric Food Res* 31:143–156
- Lieth HFH (1978) Patterns of primary productivity in the biosphere. Hutchinson Ross, Stroudsburg, p 342
- Liu J, Chen JM, Cihlar J, Park W (1997) A process-based boreal ecosystems productivity simulator using remote sensing inputs. *Remote Sens Environ* 62:158–175
- Maas SJ (1988) Use of remotely-sensed information in agricultural crop growth models. *Ecol Model* 41:247–268

- Makler-Pick V, Gal G, Gorfine M, Hipsey MR, Carmel Y (2011) Sensitivity analysis for complex ecological models: a new approach. *Environ Model Softw* 26:124–134
- Mitchell SW, Csillag F (2001) Assessing the stability and uncertainty of predicted vegetation growth under climatic variability: northern mixed grass prairie. *Ecol Model*, 139(2-3): 101–121
- Ojima DS, Parton WJ, Coughenor MB, Scurlock JMO, Kirchner TB, Kittel TGF, Hall DO, Schimel DS, Moya EG, Gilmanov TG, Seastedt TR, Kamnalrut A, Kinyamario JI, Long SP, Menaut JC, Sala OE, Scholes RJ, Veen JA (1996) Impact of climate and atmospheric carbon dioxide changes on grasslands of the world. In: Hall DO, Breymeyer AI, Melillo JM, Argen GI (eds) *Global change: effects on coniferous forests and grasslands*. Wiley, London, pp 271–311
- Orr RJ, Parsons AJ, Penning PD, Treacher TT (1990) Sward composition, animal performance and the potential of grass/white clover swards continuously stocked with sheep. *Grass Forage Sci* 45:325–336
- Parton W, Scurlock J, Ojima D (1993) Observations and modelling of biomass and soil organic matter dynamics for the grassland biome worldwide. *Global Biogeochem Cycles* 7:785–809
- Parton WJ, Coughenor MB, Scurlock JMO, Ojima DS, Gilmanov TG, Kirchner TB, Menaut JC, Seastedt TR, Moya EG, Kamnalrut A, Kinyamario JI, Hall DO (1996) Global grassland ecosystem modeling: development and test of ecosystem models for grassland system. In: Hall DO, Breymeyer AI, Melillo JM, Argen GI (eds) *Global change: effects on coniferous forests and grasslands*. Wiley, London, pp 229–269
- Psomas A, Kneubühler M, Huber S, Itten K, Zimmermann NE (2008) Coupling imaging spectroscopy and ecosystem process modelling – the importance of spatially distributed foliar biochemical concentration estimates for modelling NPP of grassland habitats. In: *IEEE Geoscience and Remote Sensing Symposium (IGARSS 2008)*, IEEE Boston (USA), CD-ROM
- Ranson KJ, Sun G, Knox RG, Levine ER, Weishampel JF, Fifer ST (2001) Northern forest ecosystem dynamics using coupled models and remote sensing. *Remote Sens Environ* 75:291–302
- Running SW, Hunt ER (1993) Generalization of a forest ecosystem process model for other biomes, BIOME-BGC and an application for global-scale models. In: Ehleringer JC (ed) *Field scaling physiological processes: leaf to globe*. Academic, San Diego, pp 141–158
- Saltelli A, Tarantola S, Campolongo F (2000) Sensitivity analysis as an ingredient of modeling. *Stat Sci* 15:377–395
- Schwinning S, Parsons AJ (1996a) Analysis of the coexistence mechanisms for grasses and legumes in grazing systems. *J Ecol* 84:799–813
- Schwinning S, Parsons AJ (1996b) A spatially explicit population model of stoloniferous N-fixing legumes in mixed pastures with grass. *J Ecol* 84:815–826
- Song CH, Woodcock EC (2003) A regional forest ecosystem carbon budget model: impacts of forest age structure and landuse history. *Ecol Model* 164:33–47
- Thornton PE, Law BE, Gholz HL, Clark KL, Falge E, Ellsworth DS, Goldstein AH, Monson RK, Hollinger D, Paw UJC, Sparks JP (2002) Modeling and measuring the effects of disturbance history and climate on carbon and water budgets in evergreen needle leaf forests. *Agric For Meteorol* 113:185–222
- Trusilova K, Churkina G (2008) The terrestrial ecosystem model GBIOME-BGCv1. Tech Rep Max-Planck-Institut für Biogeochemie 14:1–61
- Turner DP, Ollinger SV, Kimball JS (2004) Integrating remote sensing and ecosystem process models for landscape to regional scale analysis of the carbon cycle. *BioScience* 54:573–584
- Weiss M, Troufleau D, Baret F, Chauki H, Prevot L, Olioso A, Bruguier N, Brisson N (2001) Coupling canopy functioning and radiative transfer models for remote sensing data assimilation. *Agr Forest Meteorol* 108:113–128
- White MA, Thornton PE, Running SW, Nemani RR (2000) Parameterization and sensitivity analysis of the BIOME-BGC terrestrial ecosystem model: net primary production controls. *Earth Interact* 4(3):1–84

Part IV
Environmental Modeling and Risk
Assessment

Chapter 9

Glaciological Studies at Pasterze Glacier (Austria) Based on Aerial Photographs

Viktor Kaufmann, Andreas Kellerer-Pirklbauer, Gerhard Karl Lieb, Heinz Slupetzky, and Michael Avian

Abstract This chapter describes and analyses glacier recession observed at Pasterze Glacier, Hohe Tauern Range, Austria, for the time period 2003–2009. Pasterze Glacier is the largest glacier of the entire Eastern Alps, and it is highly indicative of ongoing glacier melt in the Alps. We evaluated three glacier stages (2003, 2006 and 2009) and the glaciological changes between them. The quantitative analysis is based on aerial surveys carried out during the summer of these years. The photogrammetric workflow provided high resolution datasets, such as digital elevation models and orthophotos of each stage. We evaluated the extent, surface elevation, flow velocity field, supraglacial debris cover, and geomorphological changes at the glacier surface and the adjacent paraglacial environment. The main numerical results can be summarized as follows: the glacier covered $17.3 \pm 0.1 \text{ km}^2$ in 2009, the mean surface elevation change was $-1.31 \pm 0.07 \text{ m a}^{-1}$ for the period 2003–2009, the glacier surface flow velocity in two test areas at the glacier tongue decelerated from 2003–2006 to 2006–2009 (-4% and -31%), and the debris cover of the glacier tongue increased from 63% (2003) to 72% (2009). We conclude that Pasterze Glacier is far from equilibrium and that its glacier tongue will turn into a large dead ice body in the near future.

V. Kaufmann (✉)

Institute of Remote Sensing and Photogrammetry, Graz University of Technology,
Steyrergasse 30, 8010 Graz, Austria
e-mail: viktor.kaufmann@tugraz.at

A. Kellerer-Pirklbauer • G.K. Lieb

Department of Geography and Regional Science, University of Graz,
Heinrichstraße 36, 8010 Graz, Austria
e-mail: andreas.kellerer@uni-graz.at; gerhard.lieb@uni-graz.at

H. Slupetzky

Department of Geography and Geology, University of Salzburg,
Hellbrunnerstraße 34, 5101 Bergheim, Austria
e-mail: heinz.slupetzky@sbg.ac.at

M. Avian

Institute of Earth Sciences, University of Graz, Heinrichstraße 26, 8010 Graz, Austria
e-mail: michael.avian@uni-graz.at

© Springer Science+Business Media Dordrecht 2015

J. Li, X. Yang (eds.), *Monitoring and Modeling of Global Changes: A Geomatics Perspective*, Springer Remote Sensing/Photogrammetry,
DOI 10.1007/978-94-017-9813-6_9

173

Keywords Pasterze Glacier • Glacier change • Glacier recession • Photogrammetric mapping • Geomorphological mapping

9.1 Introduction

Glaciers in the European Alps have lost around 50 % of their volume between the end of the Little Ice Age (LIA, ~1850 AD) and 1975, approx. 10 % in the period 1975–2000, and again 10 % in the period 2000–2009 (Haeberli et al. 2007, 2013a). These values highlight the strong influence of the first decade of this century on glacier recession in the European Alps. Furthermore, projected future atmospheric warming will cause almost complete deglaciation in the European Alps within a matter of decades. However, predicting this evolution gets more complicated when considering various feedbacks such as size effects (small/large glaciers), thermal aspects (temperature/cold firn/ice areas), albedo, insulation (debris cover), surface elevation (glacier surface lowering into warmer climate) and process changes (ice collapse; lake formation) (Haeberli et al. 2013a, b; Vaughan et al. 2013). Glaciers that persist tend to be (i) small ice patches on very high and/or radiation-sheltered locations or (ii) mighty glacier tongues with large ice thickness which need longer time periods to melt (Zemp et al. 2006; Haeberli et al. 2013b).

This study focuses on Pasterze Glacier, the largest glacier of the Eastern European Alps with a present (2009) area of 17.3 km². As all other glaciers in the Alps, it has more or less continuously receded since the end of the LIA maximum (~1850 AD), interrupted by relatively short periods of minor advances and stagnations. During the LIA maximum the glacier covered 26.5 km² (Paschinger 1969) and has thus lost about one third of its area during the past 160 years.

Atmospheric warming is the driving force behind glacial recession. Temperatures in the Alps increased by about +2 °C over the last 100 years (Auer et al. 2007). The warming is indicated by long-term climatic observations at the Meteorological Observatory Hoher Sonnblick (Schöner et al. 2000) located approx. 16 km to the east of Pasterze Glacier. During the last few years accelerated recession and decline of the glacier tongue has been observed (Avian et al. 2007; Kellerer-Pirklbauer et al. 2008) accompanied by a considerable increase in the areal extent of the supraglacial debris cover (Kellerer-Pirklbauer 2008). Ongoing mass balance studies at Pasterze Glacier applying the glaciological method confirm the observed mass loss (ZAMG 2013).

The glaciological and geomorphological changes examined in this paper are largely connected to the specific topographical setting of the glacier. The upper part is separated from the lower one by a distinct icefall known as ‘Hufeisenbruch’ (German for ‘horseshoe’). The icefall has changed its appearance substantially since the 1990s with a steady increase in bedrock outcrops (hereafter termed ‘rock windows’) within the icefall on the one hand and a steady decrease in the glacier motion through the icefall on the other. Rapid glacier disintegration created circular collapse structures which occur more frequently at the glacier tongue

(Avian et al. 2007). The morphology of the glacier tongue is peculiar: its right side (as seen in the flow direction) is strongly debris-covered, whereas the left side is relatively debris-free and bare ice occurs at the surface. The accelerated glacier recession has important paraglacial implications (Ballantyne 2002) on the vicinity of the glacier, e.g. by the exposure of unstable rock walls prone to rock fall events (Kellerer-Pirklbauer et al. 2012) or by the development of a chaotic and highly dynamic proglacial area where large volumes of sediments are stored (Geilhausen et al. 2011).

The specific aim of this study is to analyze glaciological and related paraglacial changes at Pasterze Glacier and its surroundings in the two time periods 2003–2006 and 2006–2009. We used high-resolution aerial photographs and products derived therefrom, such as topographic line information, digital elevation models (DEMs) and orthophotos. We (a) quantified changes of the entire glacier regarding surface extent, elevation and volume, and (b) analyzed glacier velocities and the extent of the supraglacial debris cover at the glacier tongue. In a further step (c) we quantified major glacier-related morphological changes such as the evolution of rock windows in the massive icefall of Pasterze Glacier and a large paraglacial rock fall event.

9.2 The Study Area

Pasterze Glacier is a valley glacier located in the central part of the Hohe Tauern Range, Austria (Fig. 9.1). The glacier catchment consists of different metamorphic rocks which are part of the Penninic tectonic unit. These rocks are predominantly calcareous mica schist and prasinite (a type of greenschist derived from basalts) with some amphibolite from the Jurassic to Cretaceous periods (Höck and Pestal 1994). The climatic conditions are largely continental. At an automatic weather station (AWS) near Pasterze Glacier located at 2,070 m a.s.l. (AWS-MA; see Fig. 9.1), the annual precipitation in the period 2003–2009 was 1,000 mm and the mean annual air temperature (MAAT) about 2.1 °C (data provided by VERBUND-Austrian Hydro Power). The potential upper timberline can be estimated at 2,150 m a.s.l. (Lieb 2007). The mean lower limit of discontinuous permafrost depends on substrate and aspect and is at around 2,900 m a.s.l. on south-facing slopes and 2,600 m a.s.l. on northeast-facing slopes (Kellerer-Pirklbauer et al. 2012).

The glacier has a length of 8.3 km and a maximum ice thickness of about 190 m considering georadar data (Span et al. 2005) and recent glacier thickness losses based on own measurements (see below). Together with the nearby Großglockner (3,798 m), Austria's highest mountain peak, Pasterze Glacier forms a unique Alpine landscape which attracts up to a million visitors a year. Glaciological surveys have been carried out at Pasterze Glacier almost annually since 1878 (initiated by Ferdinand Seeland) representing one of the longest time series of continuous glacier monitoring globally (Wakonigg and Lieb 1996). The surveys include measurements of glacier length, surface velocity and surface elevation change. The annual campaigns have been organized by the Department of Geography and Regional

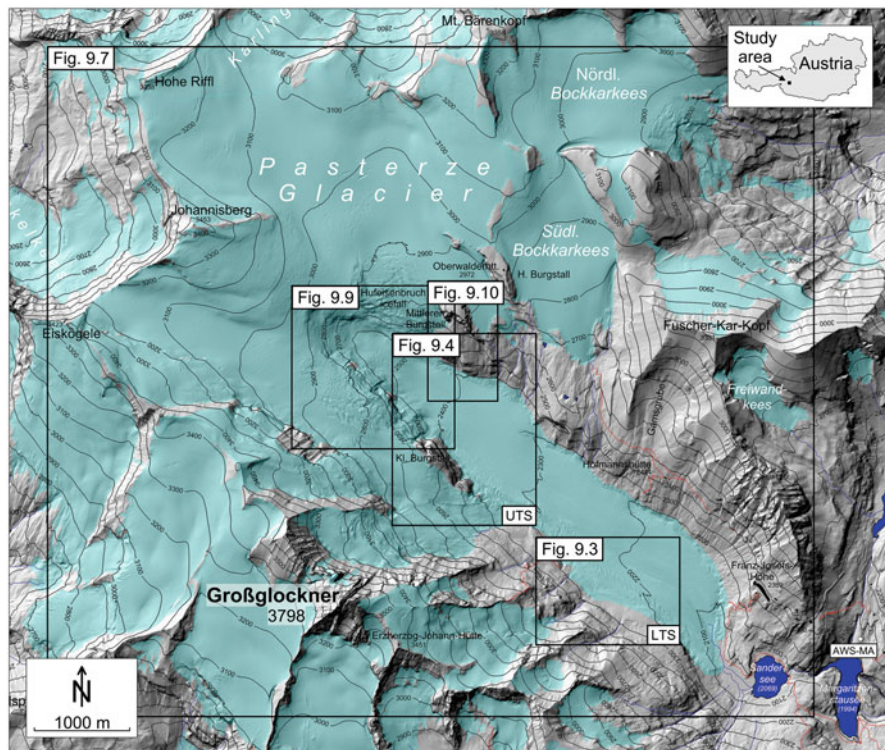


Fig. 9.1 Location map of the study area. The glacial stage shown was retrieved from the 1998 Austrian glacier inventory. Relief depiction is based on the 2003DEM

Science, University of Graz, since 1958. These data and a large number of paintings, photographs (Fig. 9.2) and topographic maps provide very detailed information on the spatio-temporal changes of the glacier. These changes are in good accordance with those observed for other alpine glaciers showing a strong recession after the LIA maximum, a decelerated recession from the end of the nineteenth century until the 1930s – although with intermittent periods of glacier advances in the 1890s and 1920s –, and again a rapid recession from the mid-twentieth century onwards with a slightly more favorable climatic phase between the mid-1960s and early 1980s (Zemp 2006). Approximately two thirds of the Austrian glaciers advanced during that period (Patzelt 1985). Years with mass gain did not last long enough, however, to trigger advances of Pasterze Glacier, which can be attributed to its long response time (Zuo and Oerlemans 1997). The mass surplus flowed through the icefall with accelerated velocity, but melted gradually on its way towards the glacier terminus (Wakonigg and Lieb 1996).

A massive rock fall was released at the southeast ridge of the mountain Mittlerer Burgstall (2,933 m a.s.l.) in 2007 (Fig. 9.1 for location). This mountain is characterized by a flat mountain plateau and steep rock walls, except for one facing

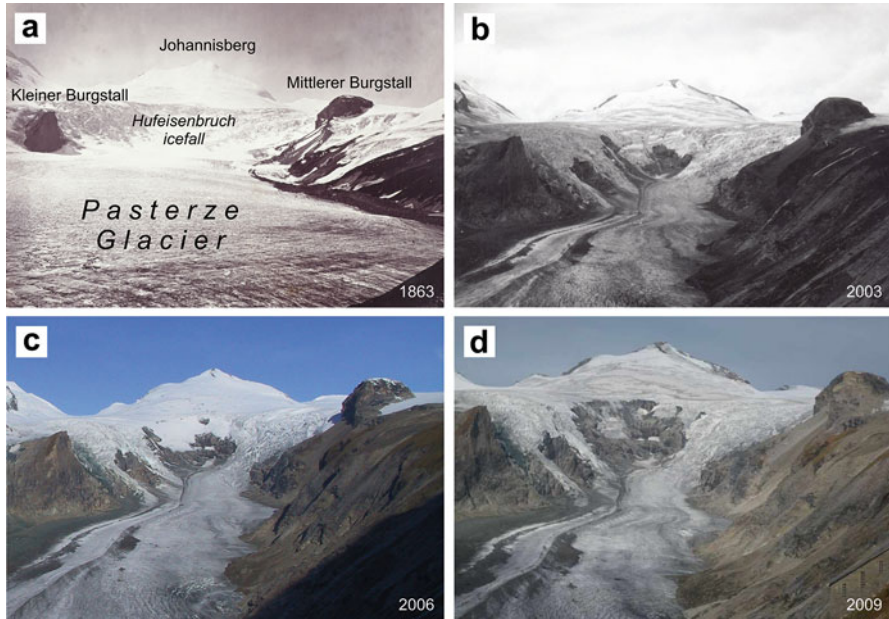


Fig. 9.2 Set of four terrestrial photographs taken in northwesterly direction showing Pasterze Glacier with its prominent Hufeisenbruch icefall. Date of photography: (a) 1863 (Photo by Jägermayer G, © Albertina, Vienna, <http://www.albertina.at/>), (b) 8 August 2003 (Photo by Lieb GK), (c) 21 September 2006 (Photo by Lieb GK) and (d) 8 October 2009 (Photo by Hohenwarter G)

northwest where the mountain slopes gently towards Pasterze Glacier. During the LIA, Mittlerer Burgstall was fully surrounded by two glacier tongues of Pasterze Glacier. Kellerer-Pirklbauer et al. (2012) presented possible causes (deglaciation, permafrost degradation, unfavorable geology, unusually warm winter 2006/2007) for this rock fall event and gave a first estimation on the displaced rock volume. In the present paper we provide more detailed geomorphometric information.

9.3 Material and Methods

9.3.1 Aerial Surveys 2003, 2006 and 2009

In summer 2003 the temperature in Central Europe was extremely high (Beniston and Diaz 2004). Due to the heat Austria's glaciers were almost free of snow from the previous winter by early summer (mid-August), thus favoring strong glacier ice melt (Slupetzky and Wiesenegger 2005). An aerial survey of the study area was carried out on 13 August.

Table 9.1 Technical parameters of the aerial surveys 2003, 2006 and 2009

Aerial survey	Acquisition date	f [mm]	Mean scale	Mean GSD [cm]	ns/np
2003	13 August	150	1:16,800	20	3/32
2006	22 September	300	1:16,700	25	4/36
2009	24 August	300	1:16,300	23	5/59

Mean elevation of the study area is 2,635 m a.s.l.

f mean focal length of camera, GSD ground sampling distance, ns number of strips, np number of photos

Aerial survey 2003 Color-positive photographs were acquired in three adjacent flight strips oriented parallel to the main axis of the glacier tongue of Pasterze Glacier. The technical details are listed in Table 9.1. Because of the short focal length of the wide-angle camera used the photographs show large geometric distortions at steep mountain slopes, thus causing problems in the photogrammetric evaluation. Furthermore, cloud cover and associated shadows are considerable (around 20 %), creating additional problems in achieving complete spatial coverage. Irregular photo orientation is attributed to bumpy flight conditions. Additional flight navigation data (e.g. from GPS) was not available. Marking of ground control points (GCPs) for aerotriangulation (AT) was not considered. Despite these limitations, all glacier areas can be delimited clearly.

Aerial survey 2006 Since appropriate GCPs for the AT of the 2003 data were lacking and project funds did not allow the required GCPs to be measured in the field, we decided to retrieve the relevant information from triangulated (geo-referenced) image data. One data set dates from 2006 and the other one from 2009 (Table 9.1). From a photogrammetric point of view the 2006 photographs (color-positive) are not ideal since the terrain above approx. 2,750 m a.s.l. is covered by fresh snow, which partly hides the upper parts of the glaciers to be mapped. Furthermore, high albedo of the snow-covered areas obstructs 3D surface perception. Nevertheless, this data set (provided by the Federal Office of Metrology and Surveying, BEV, Vienna) was taken to retrieve the GCPs for the AT of the 2003 data.

Aerial survey 2009 The time series of aerial photographs used in this study was complemented by image data from 2009 (TIRIS 2014). The glaciers are shown in good contrast. However, although the temporal snow line of 2009 was higher than that of 2006, glaciological studies were complicated by snow in terrain depressions at the glacier surface. The image data from both 2006 and 2009 were supported by appropriate photogrammetric orientation files.

9.3.2 Photogrammetric Workflow

9.3.2.1 Aerotriangulation

In the present study we selected the Austrian Gauss-Krüger coordinate system (strip M31) as a coordinate reference. As already indicated in the previous section, we built on available photogrammetric projects carried out by federal (BEV) and regional mapping (TIRIS) authorities. All photogrammetric work of the present study was carried out using an *ImageStation* of Intergraph and Bentley's CAD *MicroStation*. We manually measured 364 distinct natural GCPs in the various stereomodels of 2006 of which we finally used 221 in the AT of the 2003 photo block. Due to the difficulties arising from the imaging geometry, i.e. foreshortening and occlusions, cloud cover and shadows of the 2003 image data we had to measure all tie points semi-automatically. This means that prospective points were selected manually, followed by automatic point transfer using image matching. The quality of the geo-referencing process was checked (1) absolutely by measuring cadastral triangulation points provided by BEV (mainly mountain peaks), and (2) relatively by superimposing contour lines derived from the 2006 and 2009 DEMs onto the 2003 stereomodels at a later stage of the photogrammetric workflow. Planimetric accuracy of single point measurements is better than ± 20 cm. Height accuracy is in the order of ± 25 – 30 cm. Areas with limited photo overlap may suffer occasionally from small systematic model deformations which, however, were not quantified.

The accuracy of the 2009 stereo models was checked visually by superimposing all available GCPs and official triangulation points, onto the respective stereomodels. Control measurements confirmed a similar accuracy as for the 2003 result.

9.3.2.2 Digital Elevation Models

A primary source of glaciological studies are high-resolution multi-temporal DEMs which can be efficiently provided either by airborne laser scanning (ALS) or by digital photogrammetry (Baltsavias et al. 2001; Würländer et al. 2004; Abermann et al. 2009, 2010). DEMs, along with digital orthophotos and glacier boundaries form the basis of a glacier inventory system (Eder et al. 2000; Kääb 2005).

Data capture for surface reconstruction of the three glacial stages consisted of two steps: (1) automatic computation of surface points with a grid spacing of 5 m for the whole study area using *ImageStation Automatic Elevations (ISAE)* of Intergraph applying image matching and (2) manual adaptation of erroneous results located in areas with cloud cover, shadows, occlusions, missing texture and low contrast, and filling up the voids by 3D mapping of additional surface points using image data of all three epochs. Finally, the data captured was intermeshed to form a triangulated irregular network (TIN) using the *MGE Terrain Analyst* of Intergraph. Grid-based DEMs of the same size (12×12 km, see Fig. 9.1) with a grid spacing of

5 m were interpolated for each epoch in order to support further data manipulation and analysis. Missing elevation data of areas not covered by the photo flights was complemented by a DEM (10×10 m grid spacing) provided by BEV.

9.3.2.3 Digital Orthophotos

High-resolution orthophotos with a spatial resolution of 0.5 m were generated using *ImageStation OrthoPro* of Intergraph. These were used as a basis for deriving datasets of lower resolution (1 m, 2 m, 5 m and 10 m) to facilitate image processing (cp. Sect. 9.3.2.5) and cartographic work. The mosaicing process of stitching together the overlapping orthophotos was time consuming for the 2003 data since cloud cover, shadows, strong relief distortion and occlusions forced us to work with small tiles and to check each tile separately.

9.3.2.4 Glacier Boundaries

Glacier boundaries of the three epochs were interactively mapped as 3D polylines using the photogrammetric workstation. The glacier boundaries of the Austrian glacier inventory of 1998 (Lambrecht and Kuhn 2007) were taken as a reference for the consistent delineation of directly neighboring glaciers. In cases of continuous snow cover at higher elevations (for 2006), snow accumulation in depressions at the glacier limits (for 2009) and dense debris cover (for all epochs, Pasterze Glacier tongue) the delimitation of the glacier boundaries was often only vague or sometimes even impossible. In areas with debris cover we were successful in precisely mapping the glacier boundaries by superimposing the interpolated contour lines of the DEM of a younger epoch with the stereo model (cp. Abermann et al. 2010). The glacier boundaries of 2009 could thus not be checked using this 3D technique, assuming overall glacier recession.

9.3.2.5 Glacier Flow Velocity

Glacier flow velocity is an important parameter describing the state of a glacier, and it is also needed for numerical modeling in glaciological research (Oerlemans 2001). Surface flow velocity can be measured by various techniques (Kääb 2005; Bollmann et al. 2012). In the present study we applied an image-based technique based on optical flow estimation.

Kaufmann and Ladstädter (2003) describe a rigorous photogrammetric technique of how to retrieve a dense field of 3D displacement vectors in multi-temporal stereomodels using image matching. The authors propose to use pre-rectified image data, i.e. quasi-orthophotos, for image matching. However, quasi-orthophotos obtained using accurate and high-resolution DEMs will become 'true-orthophotos'. Based on this presumption, the 3D problem can be reduced to a 2D problem. A wide

variety of methods exists for finding corresponding points in two images (Goshtasby 2012). Successful examples of mapping the kinematics of glaciers, rock glaciers and other mass movements by remote sensing techniques are given, for example, by Kääb (2005).

In the present study we focused on the kinematics of the tongue of Pasterze Glacier. Feature tracking, i.e., finding corresponding points in the multi-temporal dataset, was accomplished by means of automatic image matching maximizing the normalized cross-correlation coefficient (NCC) at pre-defined grid points. Sub-pixel accuracy was achieved by interpolation of a parabola at the position of the peak-value of the correlation function. Back-matching, i.e. applying the image matching algorithm in the reverse direction for consistency check, helped to sort out most of the gross errors. Remaining outliers of the 2D displacement vectors were identified visually and eliminated manually. The accuracy obtained was quantified at stable regions, e.g. bedrock, where no surface movements can be expected.

Two morphologically interesting areas at Pasterze Glacier were investigated (Figs. 9.3 and 9.4). The image matching technique applied will fail if (1) the geometry of the two patches to be compared has changed excessively, (2) the surface textures have decorrelated in time, or (3) sufficient surface texture is completely lacking. The results of both test sites show that areas with bare ice are prone to rapid decorrelation of surface texture, and thus image matching fails. Best results are obtained on completely debris-covered areas and on bedrock. In order to fully benefit from the high resolution of the original photographs additional orthophotos with a spatial resolution of 0.25 m were computed for both test sites.

Lower test site (LTS) The window size for image matching was 41 pixel \times 41 pixel. Flow velocities obtained are accurate to $\pm 0.17 \text{ m a}^{-1}$ (2003–2006) and $\pm 0.12 \text{ m a}^{-1}$ (2006–2009).

Upper test site (UTS) Here the surface texture is mostly determined by supraglacial debris and ogive-type structures. The flow velocities are much higher than in the lower test site, resulting in faster surface texture decorrelation. This problem was overcome by re-computing the orthophotos at a relatively large GSD of 2 m, and increasing the window size for successful image matching to 101 pixel \times 101 pixel. Subsequently, accuracies of flow velocities obtained are lower than for the lower test site, i.e., $\pm 0.24 \text{ m a}^{-1}$ in the best case for stable areas.

9.3.2.6 Glacier Surface Elevation Change

Glacier mass balance can be computed using the geodetic method or the glaciological method. Both methods have advantages and disadvantages (Benn and Evans 2010; Fischer 2011; Zemp et al. 2013). The geodetic method is based on simple glacier surface elevation change. The numerical transformation of volume change to mass loss or gain requires spatial information on the density of the material involved, i.e. ice, firn and snow. Most glacier studies assume a mean density of 900 kg m^{-3} for glacier ice (Huss 2013). Specific mass balances are often calculated in mm water equivalent (w.e.).

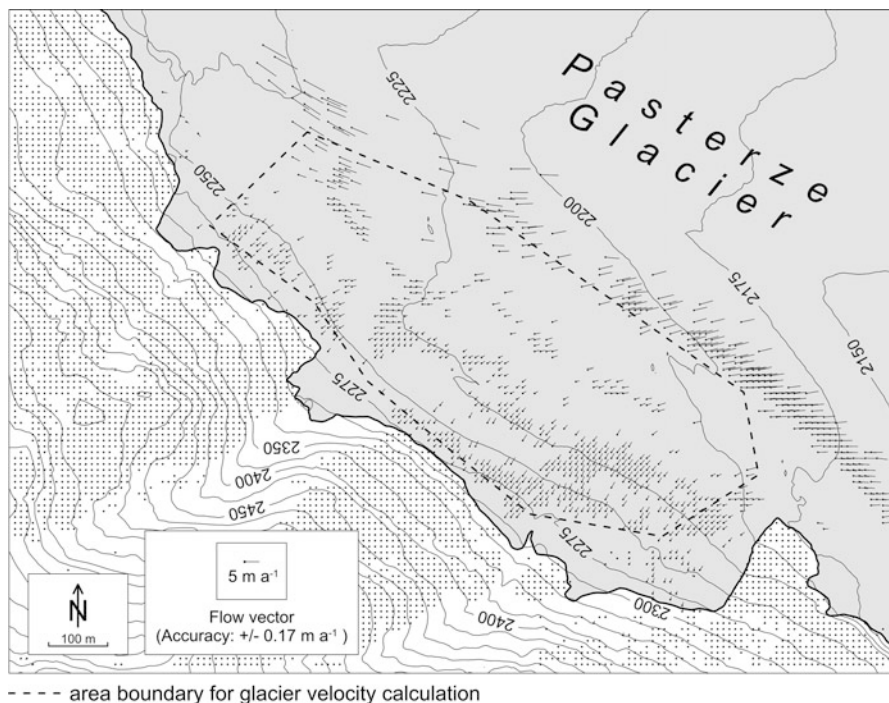


Fig. 9.3 Surface flow vector field at the lower test site (LTS) of the glacier tongue (see Fig. 9.1 for location) for 2003–2006 indicating the complex movement pattern (combination of valley-center and downvalley flow)

Surface elevation change can be easily computed by subtracting multi-temporal DEMs. A prerequisite is the perfect geometric co-registration of the DEMs involved. A computer program (Kaufmann and Plösch 2000) was used to exploit the available data, i.e. DEMs and glacier masks, following glaciological standards and needs. Outputs are hypsometric curves of the glacier (Fig. 9.5), detailed information on glacier elevation/volume change for discrete altitude intervals (Fig. 9.6), and other glaciological parameters.

9.3.2.7 Evolution of the Supraglacial Debris Cover and Meltwater Channels

A supervised classification was performed within *ArcGIS* 10.1 in order to differentiate between debris-covered glacier parts and bare-ice parts. This approach involves manually selecting training areas for the categories to be mapped in order to develop the spectral signatures of these classes (Kääb 2005). The aerial photographs for 2003, 2006 and 2009 contain no thermal information but only the three color bands RGB. Thermal and multispectral remote sensing information of

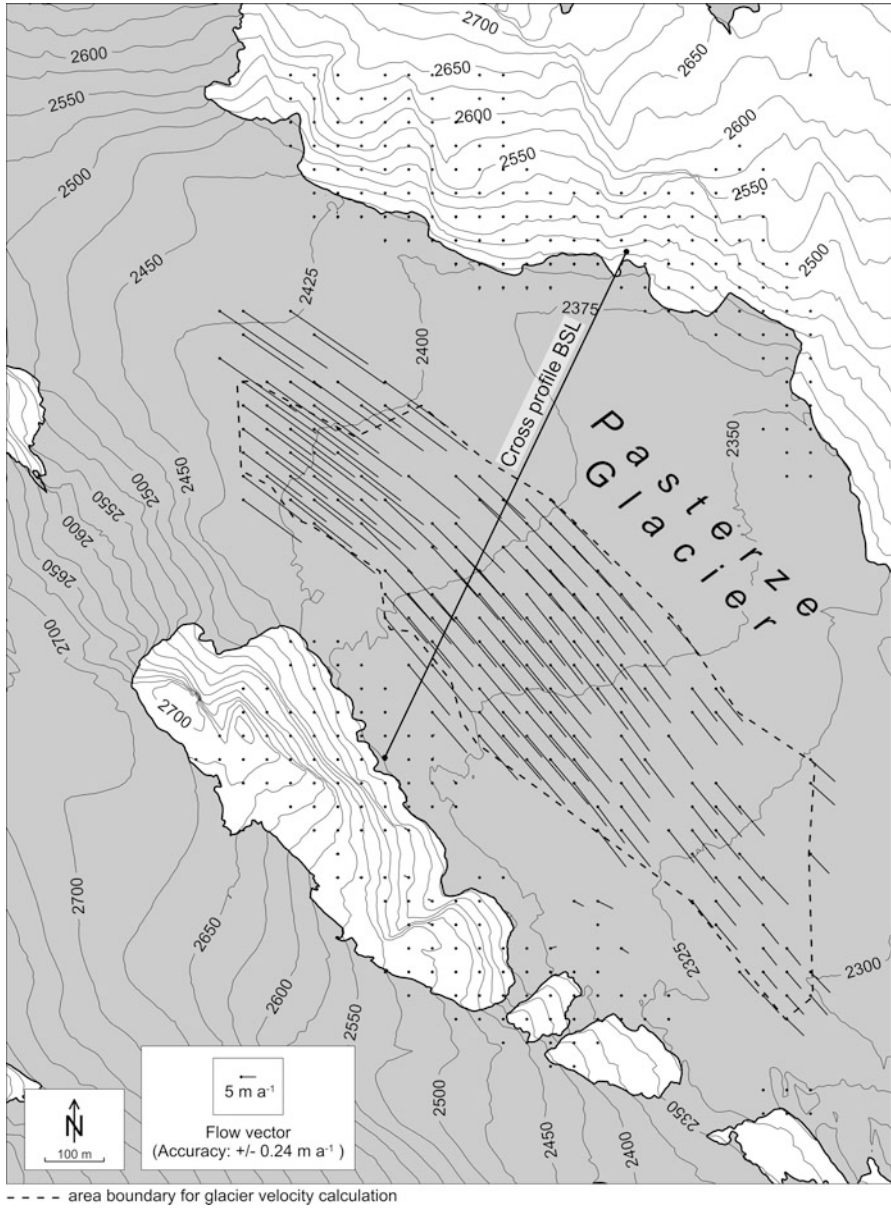


Fig. 9.4 Surface flow vector field at the upper test site (UTS) of the glacier tongue (see Fig. 9.1 for location) for 2003–2006 indicating a dominantly downvalley flow pattern

this type, including infrared, is commonly used for mapping debris-covered glaciers (e.g., Paul et al. 2004; Bolch et al. 2007; Karimi et al. 2012). In our classification approach we: (a) defined five types of training samples with respective spectral

Fig. 9.5 Area-altitude distribution (hypsometric curve) for the glacial stages 2003 and 2009 based on 50 m altitude intervals

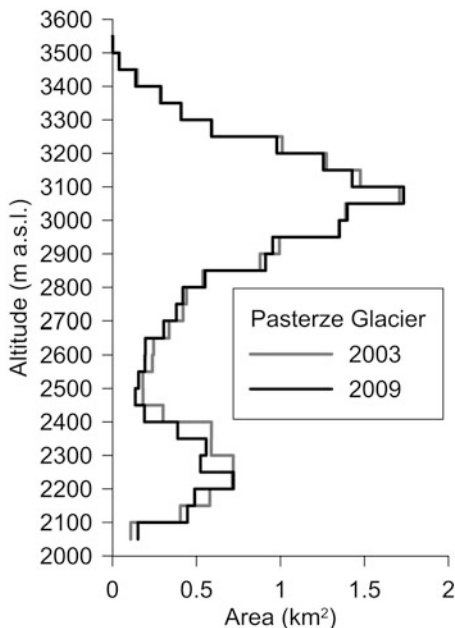
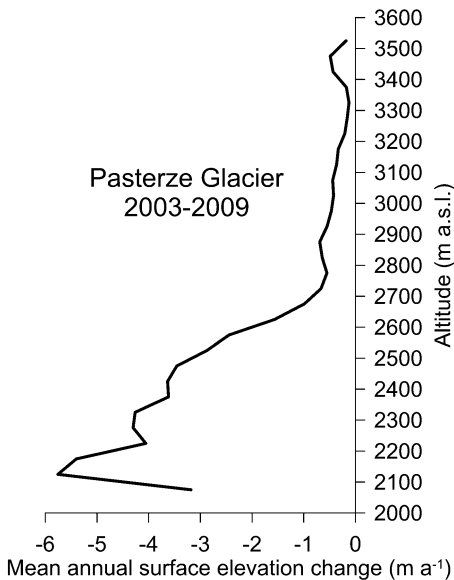


Fig. 9.6 Mean annual surface elevation change for the time period 2003–2009 based on 50 m altitude intervals



signatures at the glacier tongue (classes ‘debris-1’, ‘debris-2’, ‘dirty-ice-1’, ‘dirty-ice-2’, and ‘clean-ice’), (b) ran the classification procedure applying the maximum likelihood method, (c) reclassified the produced file by combining the two classes ‘debris-1’ and ‘debris-2’ to the class ‘debris-covered’ and the remaining three

classes to the class 'bare ice', and used (d) a low-pass filter (applying 3×3 window) to smooth the classification result. Errors in the supervised classification procedure occurred due to identical spectral signatures for some sparsely debris-covered glacier ice and illuminated debris-covered slopes near the glacier terminus. Furthermore, glacier crevasses with shadows showed similar spectral signatures to debris-covered areas. This led in some cases to wrong classifications. However, the areal extent of these classification problems is minor as judged from direct visual comparison of the orthophotos and the classification result. Therefore, and in order to keep the classification procedure consistent, the supervised classification results were not manually corrected. Additionally, the main supraglacial meltwater channel near the glacier terminus was manually mapped for the three stages. This channel separates the continuously debris-covered part (southwestern part) from the sparsely debris-covered and bare-ice parts during all three relevant glacier stages.

9.4 Results

9.4.1 *Glaciation Changes*

Pasterze Glacier covered an area of 18.14 km^2 in 2003, 17.65 km^2 in 2006 and only 17.28 km^2 in 2009. The accuracy of the areal extents given can be estimated at $\pm 0.05\text{--}0.10 \text{ km}^2$, which is due to the uncertain mapping of the glacier boundaries, e.g. in areas with snow cover or shadow. Thus, the areal extent of the glacier was reduced significantly by 4.8 % or 0.86 km^2 within only 6 years. The areal distribution of the glacier surface with respect to altitude (at 50 m intervals) for 2003 and 2009 is indicated in Fig. 9.5. An asymmetric bimodal hypsometric distribution is evident. As shown in this graph, no change has occurred for altitude intervals above 3,250 m ASL and for the interval 2,800–2,850 m ASL. Areal losses prevailed between 2,150 and 2,800 m ASL, which is basically the entire glacier tongue below the icefall. The pattern can be explained by the area-wide lowering of the entire glacier tongue. The areal extent of the interval 2,200–2,250 m ASL was almost identical in 2003 and 2009, although this altitude interval shifted up-valley. The lowest two intervals (2,050–2,150 m ASL) increased from 0.51 km^2 in 2003 to 0.60 km^2 in 2009. Changes above the icefall were less distinct with small gains or losses at the individual altitude intervals. This is also indicated by the total glaciated area above 2,900 m a.s.l. which was almost identical in 2003 (10.7 km^2) and 2009 (10.6 km^2).

Changes in surface elevation during the six years of monitoring are indicated in Figs. 9.6 and 9.7. Figure 9.6 depicts the mean annual values at different altitude intervals and hence the gradient. It clearly indicates that there is no altitude interval (in contrast to specific areas; see Fig. 9.7) with a positive surface elevation change. Figure 9.7 shows the spatial distribution of the mean annual surface elevation

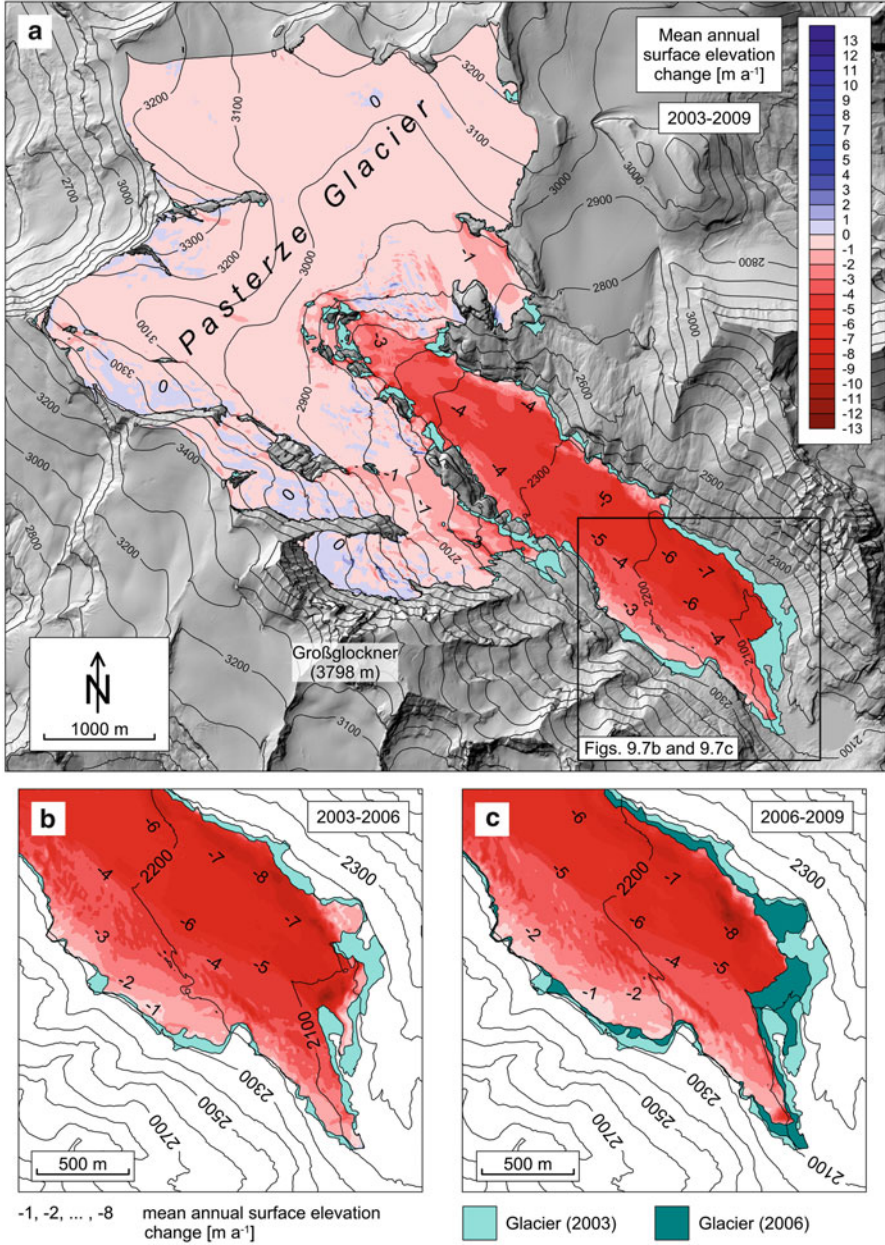


Fig. 9.7 Mean annual surface elevation change: (a) for the entire glacier for 2003–2009, (b) and (c) for the lower part of the glacier tongue for 2003–2006 and 2006–2009, respectively

Table 9.2 Changes in volume and surface elevation between 2003 and 2009 for the entire glacier and for the glacier tongue (as delineated in Fig. 9.8) for the two 3-year periods

Area	Period	Volume change (ice/firn/snow) [10^6 m^3]	Mean surface elevation change [m a^{-1}]
Entire glacier	2003–2009	−144.53	−1.31
Glacier tongue	2003–2006	−56.46	−4.52
(Below icefall)	2006–2009	−46.74	−4.07
	2003–2009	−103.20	−4.32

change. This figure reveals substantial elevation losses particularly at the glacier tongue and even some elevation gains at the highest northeast-facing cirques. During the period 2003–2009 the glacier lost about $144 \times 10^6 \text{ m}^3$ of ice, firn and snow (Table 9.2). The mean surface elevation change for the entire glacier during this 6-year period was $-1.31 \pm 0.07 \text{ m a}^{-1}$. For the glacier tongue, however, this value is much higher (-4.32 m a^{-1}) with a slightly higher mean annual value for the second 3-year period.

9.4.2 Glacier Velocity

Figures 9.3 and 9.4 show the flow vector field for the lower (LTS) and upper test sites (UTS) at the glacier tongue for the period 2003–2006. The accuracy of the horizontal flow velocities obtained has already been described above and is in the order of $0.1\text{--}0.3 \text{ m a}^{-1}$. The results of the calculated surface flow velocities for both 3-year periods are summarized in Table 9.3. Additionally, the glacier movement was visualized in an animated GIF (Kaufmann 2013). The vector fields measured for the LTS are almost identical during both 3-year periods. The mean flow velocity – derived from a 0.29 km^2 large area at the glacier surface with valid data for both periods – is 2.3 m a^{-1} in the first period and 2.2 m a^{-1} in the second. The observed change in the overall velocity is, however, not significant. Of particular interest in the LTS is the movement pattern, i.e. the direction of the individual flow vectors. The ones calculated for the area close to the glacier margin moved perpendicular to the glacier’s main axis, hence towards the valley center. This is related to the fact that those point measurements are located on northeast-facing and relatively steep slopes ($20\text{--}30^\circ$). Further away from the glacier margin (lower right part of Fig. 9.3) the flow direction changes gradually from northeast to east and velocities increase correspondingly. Flow vectors at the upper part of the LTS point first towards southeast following the main valley axis/main flow direction of the glacier. Further below, however, vectors change to east, i.e. towards the valley center. This change is related to the change in glacier surface slope.

Table 9.3 Glacier velocities at two areas (LTS, UTS) of the glacier tongue for both time periods

Area	Period	Measurements [n]	Mean [m a ⁻¹]	Minimum [m a ⁻¹]	Maximum [m a ⁻¹]
LTS (Fig. 9.3)	2003–2006	–	2.3	0.6	5.4
	2006–2009	–	2.2	0.7	4.9
	Difference in %		–4.3		
UTS (Fig. 9.4)	2003–2006	172	20.7	7.3	30.4
	2006–2009	263	14.3	3.3	23.9
	Difference in %		–30.9		

The locations of LTS and UTS are indicated in Fig. 9.1, values given refer to the areas outlined in Figs. 9.3 and 9.4

LTS: GSD of 0.25 m, correlation window 41 pixels × 41 pixels

UTS: GSD of 2 m, correlation window 101 pixels × 101 pixels

n number of measurements

The UTS is located below the icefall resulting in higher flow velocities. The mean velocity exceeded 20 m a⁻¹ in the first period and was only about 14 m a⁻¹ in the second one, which is a statistically significant velocity change of 31 %. The general flow direction, however, did not change during the two periods. The flow vectors of the central part of the glacier are parallel to the main valley axis, which is in contrast to the LTS.

9.4.2.1 Supraglacial Debris Cover

Supraglacial debris covered about 62.8 % of the glacier tongue in 2003, 73.3 % in 2006 and 72.1 % in 2009 (Table 9.4). Therefore, the density of the supraglacial debris cover increased by 9.3 % during the 6 years of observation, whereas in the same time the area of the glacier tongue was reduced by 14.5 %. The slight decrease in debris density between 2006 and 2009 is related to the fact that previously connected glacier parts near the terminus of the glacier either lost their connection to the main glacier tongue or melted. Furthermore, one debris-covered ice stream tributary lost its connection to the glacier tongue (Fig. 9.8).

The spatial distribution of the debris cover did not change significantly throughout the observation period. A largely continuous debris cover at the right side of the glacier tongue is in contrast to the left side, which is only partly covered by a discontinuous debris cover. A closer look, however, reveals various changes. For instance, the boundary between the continuous and discontinuous debris-covered part was shifted towards the valley center, in particular close to the terminus. This is illustrated by the displacement of the main supraglacial meltwater channel. The strongly meandering channel shifted by about 30 m within the 6 years (Fig. 9.8d). This change can be explained by the increase in the difference of the surface elevation between the two parts as a result of differential ablation. The gradually changing glacier surface topography led to a strong valley-center flow component

Table 9.4 Extent of supraglacial debris cover of Pasterze Glacier at the glacier tongue in 2003, 2006 and 2006

Area	Debris-covered		Bare ice		Total area	Relative to 2003
	[km ²]	[%]	[km ²]	[%]	[km ²]	[%]
2003	2.81	62.8	1.66	37.2	4.47	100.0
2006	3.00	73.3	1.09	26.7	4.09	91.6
2009	2.75	72.1	1.07	27.9	3.82	85.5

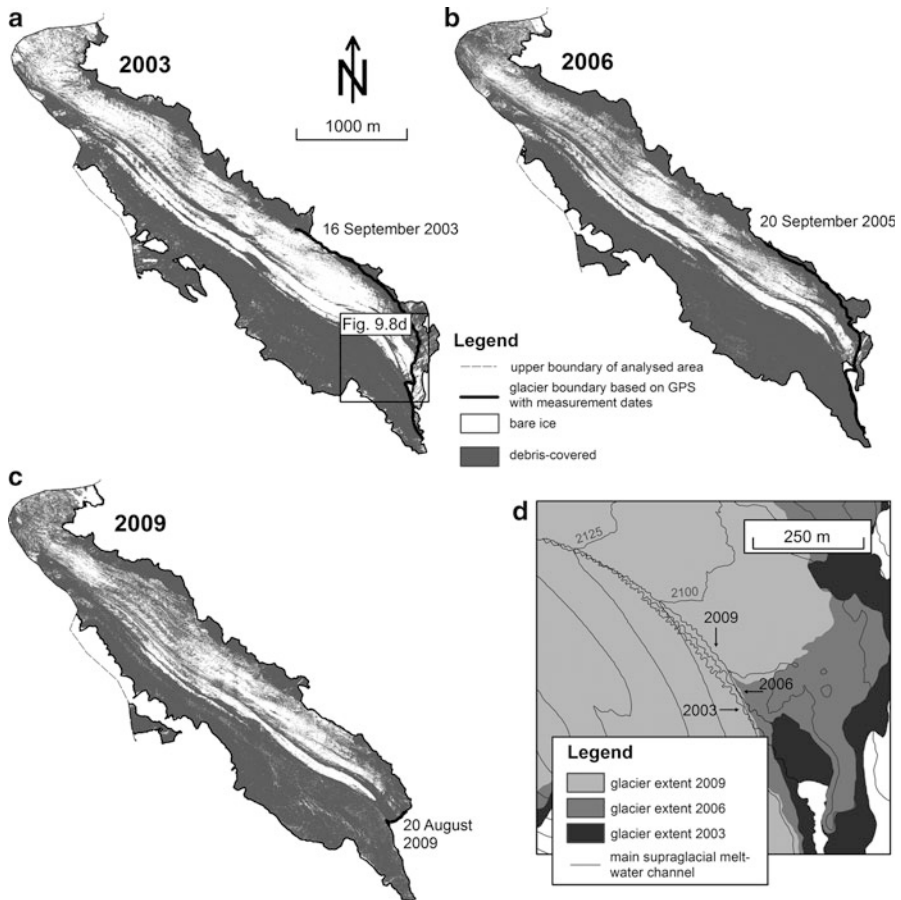


Fig. 9.8 Evolution of supraglacial debris cover and the main supraglacial meltwater channel at the glacier tongue between 2003 and 2009. Contour lines in (d) are based on the 2009DEM

(similar to the one shown in Fig. 9.3 at the glacier margin) of the continuously debris-covered part.

Supraglacial debris cover influences the ablation rate in two different ways. A thin layer (less than approx. 2 cm in thickness) lowers the albedo, influences the

Table 9.5 Mean surface elevation changes below the icefall (for extent see Fig. 9.8) for debris-covered and bare ice parts for the periods 2003–2006 and 2006–2009

Period	Surface type during both stages	Area [km ²]	Mean surface elevation change [m]
2003–2006	Bare ice	0.89	16.1
	Debris-covered	2.28	12.1
	Difference		4.0 (24.9 %)
2006–2009	Bare ice	0.66	14.3
	Debris-covered	2.33	10.4
	Difference		3.9 (27.1 %)

superficial thermal regime and increases ablation. In contrast, a thicker layer reduces ablation by shielding the ice underneath the debris mantle (e.g. Østrem 1959; Mattson et al. 1993). We compared the differential ablation at the glacier tongue below the icefall (Fig. 9.8 for extent). As shown in Table 9.5, the mean surface lowering for the debris-covered area was about 4.0 m less than for the bare-ice area in both periods. The annual difference in mean surface lowering amounts to 1.32 m a^{-1} . Hence, the shielding effect of the debris cover was clearly dominant in both periods.

9.4.3 Morphological Changes

We quantified two major glacier-related morphological changes in our study area. First, we focused on areal extent of the rock windows in the massive icefall of Pasterze Glacier. Second, we quantified the volume of the relocated rock mass released in a large rock fall event in 2007.

Figure 9.9 depicts the evolution of several large rock windows in the icefall. In this figure, areas 1 and 2 covered 0.072 km^2 in 2003, 0.131 km^2 in 2006 and 0.190 km^2 in 2009. The rock outcrops in this area thus increased 2.6 times in the 6 years of observation. The ice-free areas at the left (area 4) and right (area 3) margins of the glacier in the icefall also increased substantially. The deglaciation caused a substantial reduction in ice transport through the icefall. By 2009 only two minor ice streams at the southwest side of the icefall were still connected with the glacier tongue. Both are insignificant for glacier ice transport and hence for the nourishment of the glacier tongue. Only the main glacier ice stream transports significant amounts of glacier ice to the glacier tongue.

The mass relocation of a major rock fall event in 2007 at Mittlerer Burgstall is depicted in Fig. 9.10. We quantified the total area influenced by the rock fall as $89,300 \text{ m}^2$ (detachment area $13,800 \text{ m}^2$, deposition area $75,500 \text{ m}^2$). A rock volume of $428,000 \text{ m}^3$ was detached by this event at the sharp and distinct mountain ridge. The highest change in elevation in this area was -67 m and the mean was -31 m . In contrast, the total volume of the deposited rock material was $523,000 \text{ m}^3$, resulting

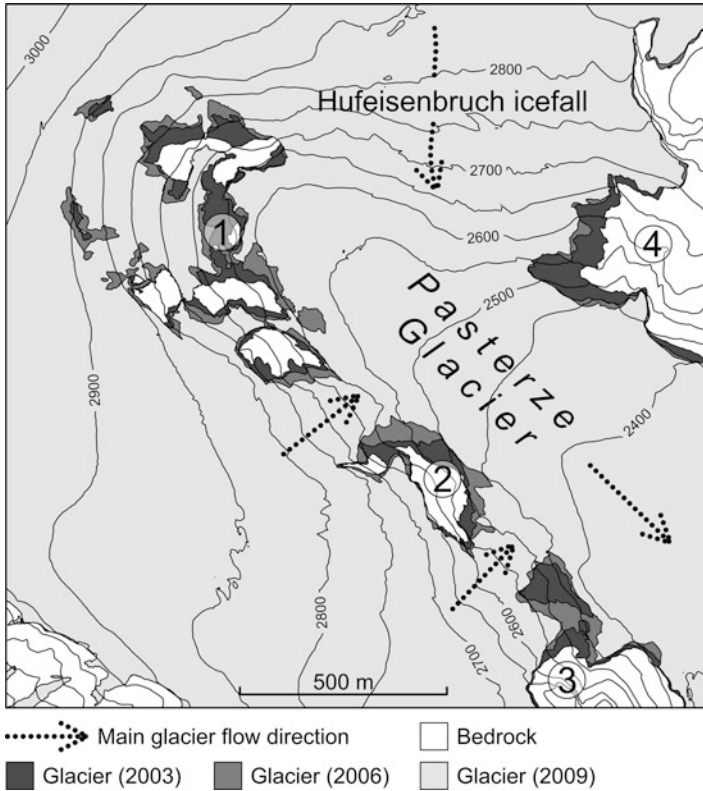


Fig. 9.9 Evolution of the rock windows (areas 1–4) in the Hufeisenbruch icefall between 2003 and 2009

in an estimated pore volume of 18 %. The mean increase in elevation in the deposition area was +7 m and the maximum value (at the northeast side of the former ridge) was +32 m.

9.5 Discussion

9.5.1 *The Fading of a Glacier*

At present Pasterze Glacier is far from equilibrium. As indicated by our analyses there is basically no accumulation area left. The surface elevation change at Pasterze Glacier (Fig. 9.6) below 2,500 m a.s.l. is strongly influenced by the presence of supraglacial debris. The general increase in debris cover thickness towards the glacier terminus (as shown by Kellerer-Pirklbauer 2008) offsets the effect of increasing air temperature at lower elevations. This effect is not as strong

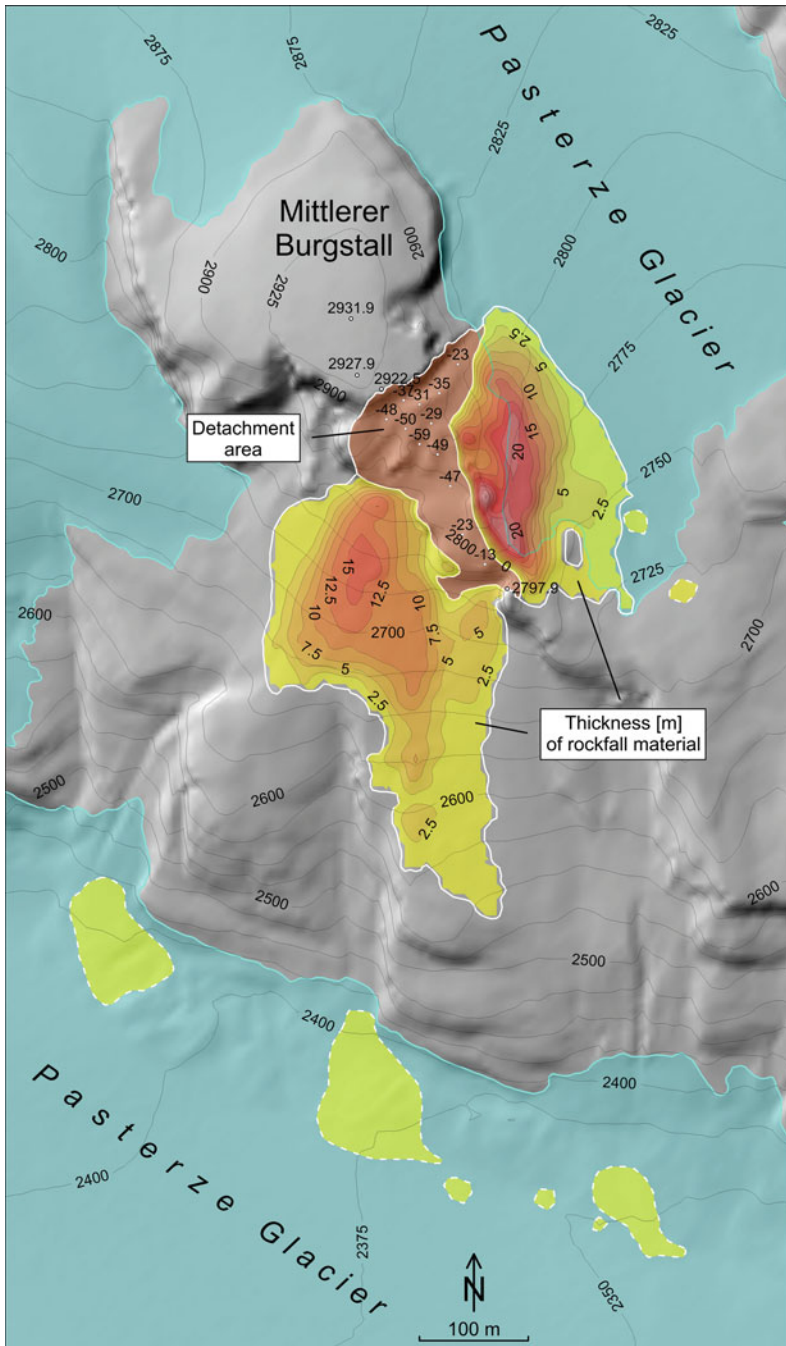


Fig. 9.10 Mass relocation caused by a massive rock fall event at Mittlerer Burgstall in 2007: spatial extent of the areas of detachment and deposition, and surface elevation change in both areas

as for heavily debris-covered glaciers where the net ablation at the glacier terminus might even be zero (e.g. Khumbu Glacier, Nepal; Inoue 1977; Benn and Lehmkuhl 2000). As shown in an earlier study (Kellerer-Pirklbauer et al. 2008), the debris-covered part of Pasterze Glacier exhibited almost identical net ablation rates over a wide range of altitude intervals during the period 1981–2000. The present study shows that the steadily growing supraglacial debris cover conserves the glacier ice and significantly reduces the amount of ice mass loss by about 25 %.

Figure 9.7 reveals that small areas show an increase in surface elevation over the period 2003–2009. This is related to the fact that there was almost no winter snow left in 2003 and the firn line was substantially higher than in 2009. The positive elevation changes observed between 2003 and 2009 at higher altitudes and in areas less exposed to solar radiation are thus the result of both glacier-hostile conditions in 2003 and glacier-friendly conditions in 2009. The massive ice loss during the observation period 2003–2009 is also evident in other places in the European Alps. Haerberli et al. (2013a) report that the mean specific mass balance of nine Alpine glaciers (Gries, Silvretta, Vernagt, Hintereis, Kesselwand, Careser, Saint Sorlin, Sarennes, Stubacher Sonnblick) was -1.2 m a^{-1} during the period 1999–2009. This specific mass balance value is the highest decadal mean measured during the period 1949–2009. A similar accelerated trend in glacier mass loss since the turn of this century has also been revealed on a global scale at 30 reference glaciers in nine mountain ranges (Haerberli et al. 2013b).

Direct measurement data on the specific mass balance at Pasterze Glacier have been available from the Central Institute for Meteorology and Geodynamics (ZAMG 2013) since the glaciological year 2004–2005 (Table 9.6). The comparison of mean surface elevation changes obtained using the photogrammetric method (2003–2009) and direct measurements (2004–2009) reveals very similar results and confirms the reliability of our method, notwithstanding the caveats mentioned in Sect. 9.3.2.6. Submergence and emergence velocities of glacier ice cannot be measured photogrammetrically. Recent measurements at the tongue of Pasterze Glacier by ZAMG revealed notable emergence velocities only at ablation stakes close to the icefall (W. Schöner; personal communication 2006). Thus, the photogrammetrically derived volume change of the glacier in the period 2003–2009 is presumably close to the real mass loss.

9.5.2 *Towards a Big Dead Ice Body*

The successful computation of displacement vectors depends on the stability of the surface texture and the time elapsed between two glacial stages. Ice surfaces are difficult to monitor over a longer (multi-annual) time span because of changing surface texture and associated decorrelation of surface radiometry. On the contrary, a too short observation period would not allow the detection of significant changes. This is a substantial problem in monitoring the kinematics of glaciers (Kääb 2005). Kaufmann et al. (2008) estimated the surface flow velocity at Pasterze Glacier by

Table 9.6 Mean surface elevation changes at Pasterze Glacier during the period 2004–2009 based on direct mass balance measurements

Period	Mean surface elevation change [m a^{-1}]
2004–2005	–0.990
2005–2006	–1.355
Mean 2004–2006	–1.173
2006–2007	–1.491
2007–2008	–1.563
2008–2009	–1.232
Mean 2006–2009	–1.429
Mean 2004–2009	–1.326

Data from ZAMG (2013)

using differential SAR interferometry. Their study revealed that only ERS-1/2 Tandem Mission images with a time interval of 1 day can be successfully applied for surface flow analyses of mid-latitude glaciers during the summer period. On a large scale, Heid and Kääb (2012) studied regional signals of glacier flow changes using Landsat data. These authors calculated the average rate of decline of glacier flow velocity per decade for five regions with negative specific mass balances (Pamir, Caucasus, Penny Ice Cap of Baffin Island, Alaska Range and Patagonia). Their results show that velocity decreased in recent decades (mid-1980s up to 2011) at an average rate per decade of 43 % in the Pamir, 25 % on Penny Ice Cap, 20 % in Patagonia, 11 % in the Alaska Range and 8 % in the Caucasus.

We successfully quantified surface flow velocity at two Pasterze Glacier test sites (LTS, UTS) with supraglacial debris despite the decorrelation problem outlined above. LTS shows a distinct flow component from the valley side towards the valley center. This movement pattern is related to the effect of differential ablation. Recent changes in the glacier flow pattern are also revealed by morphological evidence at bedrock outcrops in the proglacial area showing two different striation generations. The dominant striation direction detected is parallel to the valley axis. These older striations are superimposed by younger striations pointing towards the valley center (Kellerer-Pirklbauer 2009). UTS is located below the icefall, which is well known for the fastest flow velocities at Pasterze Glacier (Wakonigg and Lieb 1996; Kaufmann et al. 2008). Long-term glacier flow data from the cross profile BSL (see Fig. 9.4) indicate that the mean decadal velocity at this profile decreased from 46 m a^{-1} in 1981–1990 to 21 m a^{-1} in 2001–2010. Our measurements confirm this recent decline of flow velocity in this fast moving area.

A further decline in flow velocity of the glacier tongue is very likely if we consider the ongoing disintegration of the icefall. The pace in the separation of the glacier tongue from the main glacier is high considering the rapidly increasing rock outcrops in the icefall. It is very likely that the two remaining glacier-ice connections at the southwest side of the icefall will separate in the near future. The main remaining icefall at the north side will last substantially longer. However, if glacier recession continues at this pace, the tongue of Pasterze Glacier will – at least for a brief period of time – form a regenerated glacier (Benn and Evans 2010) within the next few decades. By then, the tongue of the remaining glacier will only be fed by

ice avalanches. A prominent example of a present regenerated glacier is Morsarjökull in south Iceland. Morsarjökull lost its connection with Vatnajökull in recent times (Barry and Gan 2011).

Once the tongue of Pasterze Glacier is separated from the upper part of the glacier, ice-flow movement pointing down-valley will decrease eventually to zero. This will presumably not be the case for the ice movement towards the valley center assuming further topographical changes due to differential ablation. The areal extent of the supraglacial debris cover and the debris thickness will further increase if we project the evolution seen between 1964 and 2009 into the future. In 1964, 21.0 % of the glacier tongue was debris-covered (Kellerer-Pirklbauer et al. 2008) whereas 45 years later this percentage had increased to 72.1 %.

9.6 Conclusions and Outlook

The high resolution photographs of 2003, 2006 and 2009 allowed the preparation of base data, i.e. DEMs, orthophotos and glacier boundaries, needed for the anticipated glaciological and geomorphological studies. This base data helped us to quantify important glacial and paraglacial processes associated with the recession of Pasterze Glacier. We applied the geodetic method for glacier mass balance measurements for the period 2003–2009. Our results correspond very well with the annual mass balance measurements carried out by ZAMG (2013) using the glaciological method, keeping in mind the limitations of both methods (Fischer 2011). Our study gives clear evidence that Pasterze Glacier is far from equilibrium. Furthermore, we demonstrated that the icefall connecting the glacier tongue with the main glacier is rapidly disintegrating. We thus assume that the remaining glacier tongue will turn into a large dead ice body in the near future. However, the supraglacial debris cover will most likely increase in extent and thickness, hence reducing the ablation rate. The evaluation of further aerial surveys (e.g. 2012) is planned in order to continue the high resolution glacier monitoring. We presented a selection of possible evaluations of the base data. Exemplary fields of interest in further studies could be: (a) in-depth analysis of surface flow pattern, (b) analysis of ice collapse structures, and (c) mapping and quantifying paraglacial landforms and processes in recently deglaciated areas.

Acknowledgments The aerial photographs of 2003 were made available by Heinz Slupetzky and the Hydrological Service of the Regional Government of Salzburg. Photogrammetric work was financially supported by the Austrian Federal Ministry of Science and Research and the Salzburg Hydrological Service. The aerial photographs of 2009 were provided free of charge by the Department of Geoinformation of the Regional Government of Tyrol (TIRIS). Field campaigns at Pasterze Glacier were supported by the project ‘ALPCHANGE – Climate change and impacts in southern Austrian alpine regions’ funded by the Austrian Science Fund (FWF) through project FWF P18304-N10 and by the Austrian Alpine Club (OeAV) within the framework of the annual glaciological surveys. VERBUND-Austrian Hydro Power provided meteorological data from the automatic weather station AWS-MA. An anonymous reviewer is very much thanked for his constructive criticism on an earlier version of this paper.

References

- Abermann J, Lambrecht A, Fischer A, Kuhn M (2009) Quantifying changes and trends in glacier area and volume in the Austrian Ötztal Alps (1969–1997–2006). *Cryosphere* 3(2):205–215
- Abermann J, Fischer A, Lambrecht A, Geist T (2010) On the potential of very high-resolution repeat DEMs in glacial and periglacial environments. *Cryosphere* 4(1):53–65
- Auer I, Böhm R, Jurkovic A, Lipa W, Orlik A, Potzmann R, Schöner W, Ungersböck M, Matulla C, Briffa K, Jones PD, Efthymiadis D, Brunetti M, Nanni T, Maugeri M, Mercalli L, Mestre O, Moisselin J-M, Begert M, Müller-Westermeier G, Kveton V, Bochnicek O, Stastny P, Lapin M, Szalai S, Szentimrey T, Cegnar T, Dolinar M, Gajic-Capka M, Zaninovic K, Majstorovic Z, Nieplova E (2007) HISTALP – historical instrumental climatological surface time series of the greater Alpine region 1760–2003. *Int J Climatol* 27:17–46
- Avian M, Lieb GK, Kellerer-Pirklbauer A, Bauer A (2007) Variations of Pasterze Glacier (Austria) between 1994 and 2006 – combination of different data sets for spatial analysis. In: Proceedings of the 9th international symposium on high mountain remote sensing cartography, Graz, 2006. *Grazer Schriften der Geographie und Raumforschung* 43:79–88
- Ballantyne CK (2002) Paraglacial geomorphology. *Quat Sci Rev* 21:1935–2017
- Baltsavias EP, Favey E, Bauder A, Bösch H, Pateraki M (2001) Digital surface modelling by airborne laser scanning and digital Photogrammetry for glacier monitoring. *Photogramm Rec* 17(98):243–273
- Barry R, Gan TY (2011) The global cryosphere: past, present and future. Cambridge University Press, Cambridge, UK
- Beniston M, Diaz HF (2004) The 2003 heat wave as an example of summers in a greenhouse climate? Observations and climate model simulations for Basel, Switzerland. *Global Planet Change* 44(1–4):73–81
- Benn DI, Evans DJA (2010) *Glaciers and glaciation*, 2nd edn. Hodder Arnold Publication, London
- Benn DI, Lehmkuhl F (2000) Mass balance and equilibrium-line altitudes of glaciers in high mountain environments. *Quat Int* 65–66:15–29
- Bolch T, Buchroithner MF, Kunert A, Kamp U (2007) Automated delineation of debris-covered glaciers based on ASTER data. In: Gomasasca (ed) *Geoinformation in Europe*, Proceedings of the 27th Symposium of the EARSel. Millpress Science Publishers, pp 403–410
- Bollmann E, Klug C, Sailer R, Stötter J, Abermann J (2012) Quantifying rock glacier creep using airborne laser scanning: a case study from two rock glaciers in the Austrian Alps. In: Hinkel KM (ed) *10th International Conference on Permafrost*. The Northern Publisher, Salekhard, Russia, pp 49–54
- Eder K, Würländer R, Rentsch H (2000) Digital photogrammetry for the new glacier inventory of Austria. In: *International archives of photogrammetry and remote sensing*, vol XXXIII, Part B4, Amsterdam, pp 254–261
- Fischer A (2011) Comparison of direct and geodetic mass balances on a multi-annual time scale. *Cryosphere* 5(1):107–124
- Geilhausen M, Otto JC, Schrott L (2011) Geomorphic system analysis and paraglacial landform adjustment in two glacier forefields (Pasterze & Obersulzbachkees, Hohe Tauern, Austria). *Geophys Res Abstr* 13:EGU2011–EGU10496
- Goshtasby AA (2012) *Image registration – principles, tools and methods*. Advances in computer vision and pattern recognition. Springer, London, p 441
- Haeblerli W, Hoelzle M, Paul F, Zemp M (2007) Integrated monitoring of mountain glaciers as key indicators of global climate change: the European Alps. *Ann Glaciol* 46(1):150–160
- Haeblerli W, Huggel C, Paul F, Zemp M (2013a) Glacial responses to climate change. In: *Treatise on geomorphology*, vol 13. Academic, San Diego, pp 152–175
- Haeblerli W, Paul F, Zemp M (2013b) Vanishing glaciers in the European Alps. In: *Fate of Mountain glaciers in the anthropocene*. Pontifical Academy of Sciences, *Scripta Varia*, 118:1–9

- Heid T, Kääb A (2012) Repeat optical satellite images reveal widespread and long term decrease in land-terminating glacier speeds. *Cryosphere* 6(2):467–478
- Höck V, Pestal G (1994) Geological map of Austria 1:50.000, GK sheet 153 “Grossglockner”. Geological Survey of Austria, Vienna
- Huss M (2013) Density assumptions for converting geodetic glacier volume change to mass change. *Cryosphere* 7(3):877–887
- Inoue J (1977) Mass budget of the Khumbu Glacier. *Seppyo* 39:15–19
- Kääb A (2005) Remote sensing of mountain glaciers and permafrost creep, vol 48, Schriftenreihe Physische Geographie. Geographisches Institut der Universität Zürich, Switzerland
- Karimi N, Farokhnia A, Karimi L, Eftekhari M, Ghalkhani H (2012) Combining optical and thermal remote sensing data for mapping debris-covered glaciers (Alamkouh Glaciers, Iran). *Cold Reg Sci Technol* 71:73–83
- Kaufmann V (2013) http://www.geoimaging.tugraz.at/viktor.kaufmann/Pasterze_2003-2006-2009_2m.gif. Accessed 14 Dec 2013
- Kaufmann V, Ladstädter R (2003) Quantitative analysis of rock glacier creep by means of digital photogrammetry using multi-temporal aerial photographs: two case studies in the Austrian Alps. In: *Permafrost. Proceedings of the 8th international conference on permafrost, Zurich*, vol 1. A.A. Balkema Publishers, pp 525–530
- Kaufmann V, Plösch R (2000) Mapping and visualization of the retreat of two cirque glaciers in the Austrian Hohe Tauern National Park. In: *International archives of photogrammetry and remote sensing*, vol XXXIII, Part B4, Amsterdam, pp 446–453
- Kaufmann V, Kellerer-Pirklbauer A, Kenyi LW (2008) Gletscherbewegungsmessung mittels Satellitengestützter Radar-Interferometrie: Die Pasterze (Glocknergruppe, Hohe Tauern, Kärnten). *Z Gletscherk Glazialgeol* 42(1):85–104
- Kellerer-Pirklbauer A (2008) The supraglacial debris system at the Pasterze Glacier, Austria: spatial distribution, characteristics and transport of debris. *Z Gemorphol, Supplementar Issue* 52(1):3–25
- Kellerer-Pirklbauer A (2009) The use of GPS and DGPS for glacier monitoring at the tongue of Pasterze Glacier between 2003 and 2008. In: *Proceedings of the 4th symposium of the Hohe Tauern National Park for research in protected areas, Kaprun, Austria, Sept 2009*, pp 163–167
- Kellerer-Pirklbauer A, Lieb GK, Avian M, Gspurning J (2008) The response of partially debris-covered valley glaciers to climate change: the example of the Pasterze Glacier (Austria) in the period 1964 to 2006. *Geogr Ann Ser A Phys Geogr* 90(A/4):269–285
- Kellerer-Pirklbauer A, Lieb GK, Avian M, Carrivick J (2012) Climate change and rock fall events in high mountain areas: numerous and extensive rock falls in 2007 at Mittlerer Burgstall, central Austria. *Geogr Ann Ser A Phys Geogr* 94(1):59–78
- Lambrecht A, Kuhn M (2007) Glacier changes in the Austrian Alps during the last three decades, derived from the new Austrian glacier inventory. *Ann Glaciol* 46(1):177–184
- Lieb GK (2007) Southeastern and Central Austria Field Guide of the HMRSC-IX (2006) post-symposium excursion. In: *Proceedings of the 9th international symposium on high mountain remote sensing cartography, Graz, 2006*. Grazer Schriften der Geographie und Raumforschung 43:257–292
- Mattson LE, Gardner JS, Young GJ (1993) Ablation on debris covered glaciers: an example from the Rakhiot Glacier, Panjab, Himalaya. *IAHS Publ* 218:289–269
- Oerlemans J (2001) *Glaciers and climate change*. Swets & Zeitlinger BV, Lisse
- Østrem G (1959) Ice melting under a thin layer of moraine and the existence of ice cores in moraine ridges. *Geogr Ann* 41A:228–230
- Paschinger H (1969) Die Pasterze in den Jahren 1924 bis 1968. *Wiss Alpenvereinshefte* 21:267–290
- Patzelt G (1985) Glacier advances in the Alps 1965 to 1980. *Z Gletscherk Glazialgeol* 21(1–2):403–407
- Paul F, Huggel C, Kääb A (2004) Combining satellite multispectral image data and a digital elevation model for mapping debris-covered glaciers. *Remote Sens Environ* 89:510–518

- Schöner W, Auer I, Böhm R (2000) Klimaänderung und Gletscherverhalten in den Hohen Tauern. *Salzburger Geogr Arb* 36:97–113
- Slupetzky H, Wiesenegger H (2005) Glazialhydrologische Aspekte des Jahres 2003 im “Hohe Tauern Einzugsgebiet” der Salzach. *Mitteilungsblatt Hydrographischen Dienstes Österr* 83:61–81
- Span N, Fischer A, Kuhn M, Massimo M, Butschek M (2005) Radarmessungen der Eisdicke Österreichischer Gletscher. Band 1: Messungen 1995 bis 1998, Österreichische Beiträge zu Meteorologie und Geophysik 33
- TIRIS (2014) <https://portal.tirol.gv.at/LBAWeb/luftbilduebersicht.show>. Accessed 23 May 2014
- Vaughan DG, Comiso JC, Allison I, Carrasco J, Kaser G, Kwok R, Mote P, Murray T, Paul F, Ren J, Rignot E, Solomina O, Steffen K, Zhang T (2013) Observations: cryosphere. In: Stocker TF, Qin D, Plattner G-K, Tignor M, Allen SK, Boschung J, Nauels A, Xia Y, Bex V, Midgley PM (eds) *Climate change 2013: the physical science basis. Contribution of working group I to the fifth assessment report of the intergovernmental panel on climate change*. Cambridge University Press, Cambridge, UK
- Wakonigg H, Lieb GK (1996) Die Pasterze und ihre Erforschung im Rahmen der Gletschermessungen. *Wiss Nationalpark Hohe Tauern Kärnten Kärntner Nationalpark-Schriften* 8:99–115
- Würländer R, Eder K, Geist T (2004) High quality DEMs for glacier monitoring – image matching versus laser scanning. In: *ISPRS archives*, vol XXXV, Part B7, Istanbul, pp 753–758
- ZAMG (2013) <http://www.zamg.ac.at/cms/de/klima/informationsportal-klimawandel/daten-download/glatscherdaten>. Accessed 6 Nov 2013
- Zemp M (2006) *Glaciers and climate change – spatio-temporal analysis of glacier fluctuations in the European Alps after 1850*. PhD thesis, University of Zurich, 201 p
- Zemp M, Haeblerli W, Hoelzle M, Paul F (2006) Alpine glaciers to disappear within decades? *Geophys Res Lett* 33(13):L13504. doi:10.1029/2006GL026319
- Zemp M, Thibert E, Huss M, Stumm D, Rolstad Denby C, Nuth C, Nussbaumer SU, Moholdt G, Mercer A, Mayer C, Joerg PC, Jansson P, Hynek B, Fischer A, Escher-Vetter H, Elvehøy H, Andreassen LM (2013) Reanalysing glacier mass balance measurement series. *Cryosphere* 7(2):1227–1245
- Zuo Z, Oerlemans J (1997) Numerical modelling of the historic front variation and the future behavior of the Pasterze glacier, Austria. *Ann Glaciol* 24:234–241

Chapter 10

Mapping Coastal Erosion Risk in the Southern Red River Delta, Vietnam

Mizue Murooka, Yasuhiro Kuwahara, and Shigeko Haruyama

Abstract In recent years, the Red River Delta has suffered from coastal erosion due mainly to human activities. To determine the characteristics of coastal erosion, a coastal dynamic index was calculated by overlapping eight JERS-1 SAR (Synthetic Aperture Rader) images from 1994 to 1998. After combining the features of natural environment and land use, 74 meshes covering 500 m along the coastline were classified by cluster analysis of UPGMA (unweighted pair-group method using arithmetic averages) using the three major factors, i.e., costal dynamics index, banks, and land elevation. A coastal erosion risk map was produced by clustering 686 meshes, including the inland area. The coastline clusters and distance from the sea were used in the clustering. Finally, a vulnerability map of coastal erosion considering land use was constructed. The present land use was assessed by randomization of land use, and it became clear that the current land use was vulnerable to coastal erosion. This study indicates that when other information is not available, satellite data can be very useful for coastal erosion risk mapping.

Keywords Red River Delta • Coastal erosion • JERS-1/SAR • Risk mapping

10.1 Introduction

In recent years, coastal erosion has become a worldwide phenomenon. The cause of coastal erosion includes natural factors and human activities, and the damage from coastal erosion can be tremendous. In the Red River Delta, Vietnam, coastal erosion has been a serious problem. In this area, cultivation has occurred without an appropriate land use planning (Asian Development Bank and Ministry of Agriculture and

M. Murooka (✉) • Y. Kuwahara
Abashiri Fisheries Research Institute, 1-1-1 Masuura, Abashiri, Hokkaido, Japan
e-mail: murooka-mizue@hro.or.jp; fp7y-kwahr@asahi-net.or.jp

S. Haruyama
Graduate School of Bioresources, Mie University, 1577 Kurimachiyacho, Tsu City,
Mie Prefecture, Japan
e-mail: haruyama@bio.mie-u.ac.jp

Rural Development 2000; Haruyama 2004). Rice is the main agricultural product of the delta, and paddy fields and their concomitant villages extend to the shoreline. Coastal erosion extends from the agricultural land or villages to the inland areas, causing higher soil salinity, salty water wells, and crop damage.

In Vietnam, the data related to the natural hazards are not easily available. In a previous study conducted by the authors (Murooka and Haruyama 2005), satellite remote sensor data were used to assess coastal erosion risk in the Red River Delta. In the current study, we will try to reconstruct the methodology to assess the coastal erosion risk using satellite remote sensor data.

10.2 The Red River Delta

10.2.1 Geographical Settings

The Red River rises in China and flows southeast for about 1,300 km before entering the Gulf of Tonkin. The extensive delta covers 17,000 km². The Red River Delta, a fluvial plain located in the crustal movement region, is in the northern part of Vietnam.

Vietnam is the second largest rice exporting country in the world. The Red River Delta has been cultivated for a very long period of time, and the population density is the highest in Vietnam. Because of the excellent agricultural conditions, the Delta has become the nation's primary farming region. Agriculture land accounted for 37 % of the entire Delta, forestry 25 %, and homestead land 7 % in January 2012 (GSO 2014).

Deltas are generally formed by the soil deposits of streams. The Red River has expanded because the people have created embankments along its course to protect against flooding. The delta has expanded a maximum of 80–100 m per year at the Red River mouth during the last 70 years (Nguyen 1992). The Red River Delta was affected by the tides and waves when the delta expanded (Hori 2012). The study area is a wave-dominated system and is composed of a fine-grained tidal flat and marsh sediments (Mathers and Zalasiewicz 1999).

There are many sand ridges in the southern Red River Delta. Because the sand ridges are dry and slightly higher than the surrounding ground, they are conducive to human settlement. The sand ridges are smaller and well developed in the inland area and larger in the coastal area. Most of the sand ridges are in the area between the Ninh Co River and the Red River.

10.2.2 Climate

The Red River Delta is affected by tropical monsoons during the dry and cold winters. In summer, it is hot and humid with heavy rains or typhoons. The region is a part of Köppen Cwa, warm, humid and subtropical with plentiful precipitation.

The annual rainfall is 1,650 mm in Hanoi; around 70–80 % of the precipitation occurs from May to October. From July to October, the coastal area of the Red River Delta is affected by low pressure systems from the South China Sea. The low pressure systems result in inclement weather ranging from tropical storms to typhoons. The storm surges resulting from those typhoons or tropical depressions cause severe coastal erosion and flood damage.

Typhoons often attack coastal regions. The typhoon season lasts from June to September. The average number of typhoons which yearly hit the northern coastal region in Vietnam is between 1 and 2. In the Red River Delta, typhoons cause enormous damage to both the national economy and society. The maximum wind speed exceeds a scale of 12. High winds generated by strong typhoons directly approach the coastline of Hai Phong, Ninh Binh and Thanh Hoa (Cao et al. 2007).

10.2.3 Floods and Reservoirs

The Red River is characterized by its seasonal variation of water level. Floods occur almost every year when typhoons come. When floods occur, the water level of the river rises 188 cm per day. Because the Red River is a raised bed river, the river water sometimes overflows its banks. The fluctuation band of the river's water level is 1,141 cm in a year. At the Son Tay, the flood records are as follows, 25,100 m³/s in 1915, 33,500 m³/s in 1945, 28,300 m³/s in 1969, 37,400 m³/s in 1971 (Haruyama 2004). The flood of 1971 exhibited a discharge rate of 37,400 m³/s. Dangerous water levels continued for 36 days. The flood disaster lasted for more than 1 month in the Red River and the Day River Basins (Haruyama and Van 2002). Booij (2004) described the flood situation of 26 provinces in the Red River Delta for the period 1990–2001. The flood in 1996 was extremely severe, and the flood damage was enormous in Ninh Binh Province.

The Red River that flows through Hanoi, the capital city of Vietnam, is comprised of three major tributaries: the Da, Thao, and Lo rivers, which bring annual floods threatening the capital and the delta. Upstream reservoirs, namely Hoa Binh, Thac Ba, Tuyen Quang, and Son La, have a total storage capacity of 8.5 billion m³ for flood control (Dang et al. 2011).

The reservoir system in the Red River Basin plays a very important role in the socio-economic development of Vietnam. The major reservoirs include:

1. Thac Ba reservoir (since 1964). It has the following features: high water level: 59 m; total storage: 3.6 billion m³; flood regulation storage: 0.45 billion m³; and installed capacity: 120 MW.
2. Hoa Binh reservoir (since 1994): It is the biggest in Vietnam in 2007. Main features: high water level: 120 m; total storage: 9.45 billion m³; flood regulation storage: 5.6 billion m³, and installed capacity: 1,920 MW.

3. Tuyen Quang reservoir (since 2007): Main features: high water level: 123 m; total storage: 2.3 billion m³; flood regulation storage 1–1.5 billion m³, and installed capacity: 234 MW.
4. Son La reservoir (since 2010): Main features: high water level: 217 m; total storage: 9.26 billion m³; flood regulation storage 5.5 billion m³, and installed capacity 2,400 MW (Nguyen et al. 2007).

The policies and laws to prevent the floods are still in the development stage in Vietnam. The lack of comprehensive institutional framework has caused losses and failures in water resources management practices in Vietnam (Nguyen et al. 2007).

10.2.4 Coastal Erosion in the Southern Red River Delta

The coastal erosion in the southern Red River Delta was estimated at 30–50 m per year in 1905–1960, 20–35 m per year in 1960–1973, and 10 m per year in 1973–1992 (Imamura and Dang 1997). The mouth of the Red River expanded until the middle of the twentieth century by embankment and reclamation projects. Vinh et al. (1996) clarified the coastline development from 1905 to 1992 in Nam Ha province. Deposition occurred near the mouths of the Red River, the Ninh Co, and the Day River. This resulted in shoreline developments in these areas of 2.5–6.5 km in the seaward direction over the 87 year period. However, in Hai Hau district the development was just the opposite. Over the last 87 years a strip some 16 km long and about 2.5 km wide was lost to the sea. This is a time averaged shoreline retreat of about 29 m per year. Duc et al. (2012) mentioned that the erosion coasts are distributed either between the river mouths (Hai Hau) or near them (Giao Long, Giao Phong, and Nghia Phuc). Erosion in Hai Hau is accelerated by sea level rise and upstream dams. Sea dike stability is seriously threatened by erosion-induced lowering of beach profiles, sea level rise, typhoons, and storm surges.

In the last 30 years, farmers in the Nam Dinh and Thanh Hoa provinces relocated to Dac Lac province because the paddy fields had been washed away by coastal erosion (Haruyama 1995, 2002). Based on the tidal activity data collected from Hon Dau Observation Station in North Vietnam, it was determined that coastal erosion is also affected by the recent sea level rise in the Gulf of Tonkin (Haruyama 2002).

Foreign non-governmental organizations (NGOs) headed by Sweden have started to repair the sea-walls since 1990. At the same time, foreign assistance groups planted mangrove trees with the aim of stopping spatial enlargement of coastal erosion (Haruyama 2004). Coastal erosion in the southern Red River Delta is mainly due to several major human activities including: the construction of the Hoa Binh Dam beginning in 1994 in the upper part of the Red River. It is now the largest dam in South East Asia. This dam has trapped sediments, thereby resulting in decreased sedimentation in the lower part of the river; the destruction of the natural sea-wall system by cutting the mangrove forests to make aquaculture farms; a decrease in the amount of river sand because of dredging from the river bed for

brick and building materials; ground subsidence caused by pumping up underground water; and changing mass balance in the watershed area (Haruyama 2000, 2002). Therefore, the sand supply has been decreasing since the construction of the tidal irrigation system in the coastal zone. This decrease in the amount of sand in the Red River consequently has resulted in the coastline's receding (Vu and Nguyen 1992; Haruyama et al. 2002).

The banks have been constructed near the sea shore with a standard height of 4 m. These banks are not strong enough and are sometimes washed away by typhoons. The budget for constructing banks is insufficient, so the village people make the banks the primitive way, by heaping up soil. Some NGO plant mangroves in the eroded area to protect the shoreline, but mangroves are easily washed away when they are little.

10.3 Research Methods

10.3.1 *Altitude Map*

SRTM (Shuttle Rader Topography Mission) provides the altitude data for this study. C-band and X-band SAR (Synthetic Aperture Radar) were mounted on the Space Shuttle for 11 days in February 2000. SRTM covers 80 % of the continent except for polar areas. There are two kinds of SRTM data: SRTM-3 has 3 s (about 90 m) meshes covering the whole world except for the polar areas, and SRTM-1 has 1 s (about 30 m) meshes in the U.S. SRTM-3 was used in this study, the altitude rounded to the nearest whole meter. To illustrate the altitude map, the software of Kashmir 3D Ver. 9 on a PC was used.

10.3.2 *Climate Analysis*

Climate analysis is an important tool for assessing the damage caused by coastal erosion. In this study, wind data was available. In the Van Ly Observatory Station, wind speeds and directions are recorded four times a day. In this study, the highest wind speed and its direction from 1991 to 2000 were used. The average numbers of days with strongest wind speed were calculated. The directions and the average wind speeds were calculated respectively.

10.3.3 Coastal Dynamics Index (CDI)

To investigate the coastline change, JERS-1/SAR data were used. JERS-1 is the satellite which was launched by NASDA (National Space Development Agency of Japan) in 1992 and discontinued in 1998. JERS-1 loaded the SAR (Synthetic Aperture Radar). The SAR sensor is an active microwave sensor. SAR emits microwaves and receives the reflected waves from the earth. Therefore, SAR can acquire images even at night or on rainy, cloudy, and smoky days. JERS-1/SAR used the L-band which was long wave. L-band can observe the ground regardless of forest cover because the wave passes through the trees and reflects from the land surface. The digital value of the data is called the backscattering coefficient. When the soil water is high, the pixel shows blackish and the water surface shows black. Conversely, artificial things show whitish because the radio wave reflection is high; and the backscattering coefficient is high.

The 1990s in the Red River Delta is an important era. Construction of Hoa Binh Dam began, and the areas of the paddy fields rapidly expanded (GSO 2014) and coastal erosion accelerated remarkably. In this study, eight sheets of satellite images, which were taken from 1994 to 1998 were collected: September 30, 1994; February 9, 1995; September 17, 1995; January 27, 1996; January 13, 1997; October 4, 1997; February 13, 1998; September 21, 1998. JERS-1/SAR provided by NASDA had been running from 1992 to 1998. However, the satellite images in the first two years could not be used because of strong noise. So data after 1994 was used to calculate CDI in this analysis.

A total of 149 measuring points were tracked across the coastline with an interval of 500 m. The measurement lines, which were perpendicular to the coastline, were laid down on the each measuring point. The coastline change was recorded based on the coastline on September 30, 1994. Next, the CDIs of seasonal change were calculated by subtracting a CDI from the CDI of the next season.

PCI Geomatica Ver. 7 software in a PC was used to conduct the image analysis. The nearest neighbor interpolation was used in all of the JERS-1/SAR Images, and 15 GCP points were secured in each satellite image based on the topographic map with a 1:50,000 scale.

The RMS error between the topographic map and the satellite image was 1.2, and the RMS error between each satellite image was under 0.5. Frost Filtering was used to diminish the speckle noise in each satellite image (Frost et al. 1982).

10.3.4 Production of the Coastal Erosion Risk Map

10.3.4.1 Parameters for Assessing Coastal Erosion

CDIs are closely related to coastal erosion in the southern Red River Delta. Therefore, a risk map of the coastal erosion based on CDIs was prepared.

Considering the CDI measurement scale is 500 m, the map is divided into 500 m meshes, covering all CDIs on the coastline. The average CDI is calculated to represent the CDI value in each mesh. For example, if there is only 1 CDI in 1 mesh, this CDI value represents this mesh; if there are 2 CDIs in 1 mesh, then the average of the CDIs represents the CDI value in this mesh.

The authors made the 500 m mesh map of embankment locality by using data from the documents preserved in provincial government offices. In the field study, the authors measured the height of the sea wall, along with the relative heights of sand dunes or sand ridges and the swampy lowlands between the ridges using HANDLEVEL K50-1560 (Nobel) among Hai Hau, Nghia Hung, Thanh Hoa areas, etc. The authors used the longest embankment to represent each mesh. There are some geomorphological features along the coast: the tidal plain, former river courses, sand ridges, sand dunes, and offshore beaches. The authors also used HANDLEVEL to measure the height of the coastline and the inland area of banks. The heights of areas were taken into account also. However, only CDIs, the heights of the banks, and heights of land can be taken into consideration since all the other information was quite fragmentary and incomplete.

The risk map now can be built by integrating those three major factors: CDIs, banks, and height of land. CDIs are subtracted from immediately succeeding CDIs using data from eight sheets of JERS-1 image, that is, these CDIs directly measure the coastline changes of the terms. To measure the risk of the banks, a risk ranking from 0 to 2 is assigned to each bank by using the height of the banks. The standard height of bank in this study area is 4 m. Risk level 0 is assigned to those existing banks with the height more than 4 m; risk level 1 is assigned to those banks less than 4 m; risk level 2 is assigned to those areas without any banks. The risk measurement regarding sea level can be classified into two categories: risk ranking 0 represents the land level of the coastal area being higher than sea level; risk ranking 1 results if the land level is lower than sea level. Based on the above nine items (seven sets of CDI data, bank data, and heights of land data), 74 meshes in 500 m squares were subjected to cluster analysis.

10.3.4.2 Numerical Estimation Using Hierarchical Cluster Analysis

In this study, cluster analysis was used to categorize the meshes. Cluster analysis has been used by evolutionary biologists as a tool for phylogenetic relationship studies since the 1960s. Hierarchical cluster analysis is one of the classical methods in dynamic programming (DP) in multivariate analyses and often is used as a heuristic approach.

The results of cluster analyses are normally expressed as the dendrograms. Similarities and dissimilarities can be applied to the all calculable dataset. From the perspective of pattern recognition, hierarchical cluster analysis is categorized as the uncensored learning method. The objective of hierarchical cluster analyses is the discovery of the cluster by classification of the ranks. The rank is absolutely determined by the range of the similarities or the dissimilarities. Commonly used

hierarchical cluster analyses techniques are; the single linkage clustering method, complete linkage clustering method, Ward's clustering method, WPGMA (weighted pair-group method using arithmetic average) and UPGMA (unweighted pair-group method using arithmetic average) (Sneath and Sokal 1973; Romesburg 1989).

The calculated dendrogram is assessed by the CPCC (cophenetic correlation coefficient) (Sneath and Sokal 1973). CPCC is the coefficient of correlation between the similarity matrix (or the dissimilarity matrix) and cluster topology, arrived at by calculating the data. If CPCC is near 1, the topology is a highly reproducible result. Because UPGMA is simple and useful and shows the higher CPCC (Farris 1969), it is considered a highly reproducible cluster analysis.

In the numerical vulnerability estimation, the shoreline is divided into 108 meshes. These shoreline meshes are called an Operational Taxonomic Unit (OTU) and the intermediate node is called a Hypothetical Taxonomic Unit (HTU). Here, the Pearson's product moment correlation coefficient is used as the similarity.

UPGMA algorithm is expressed as follows:

i, j, k, l, m_k, m_l, n and N are natural numbers and S is a real symmetric square matrix of order N .

1. Substitute n for N and calculate a similarity matrix S .
2. Select a taxonomic unit (TU) pair, i and j , with a maximum similarity value $S(i, j)$.
3. Replace a TU pair to HTU k . Substitute $N-1$ for N and update the similarity matrix S . When m_k and m_l are numbers of OTUs in cluster k and l , an update formula is

$$S(k, l) = \frac{1}{m_k m_l} \sum_{i=1}^{m_k} \sum_{j=1}^{m_l} S(k_i, l_j),$$

$k_i \in \{i \text{ th unit of cluster } k, 1 \leq i \leq m_k\}$, $l_j \in \{j \text{ th unit of cluster } l, 1 \leq j \leq m_l\}$.

4. If N is not 1, return to 2.
 5. Stop.
- If S is a dissimilarity matrix, select a TU pair with minimum dissimilarity at 2.

10.3.5 Land Use Vulnerability

10.3.5.1 Distance from the Sea

The inland areas also suffer damage from coastal erosion. Salt water from the sea damages the crops and seawater intrudes into ground water, but the damage is less than that in the coastal area. In this study, an extra factor, "distance from the sea," was included to assess the coastal erosion risks.

The authors define a total of 686 meshes and use the same clustering calculation as coastal 74 meshes. The coastal meshes are assigned to clusters which were calculated in a previous paragraph. The inland meshes are identified as the same group of the nearest coastline meshes. The meshes which are on the opposite side of the Day River are identified as those whose CDIs are small. If a mesh is on the coastline, the distance is 0 km from the sea; otherwise, the distance is calculated in km by multiplying the number of meshes to the coastline by the length of the diagonal line or side line.

10.3.5.2 Land Use

Current land use is important in assessing the coastal erosion risk due to human factors as well as to natural factors. In this study, the authors used the land use data by the Ministry of Agriculture and Rural Development in 1996. Five types of land use are classified as follows: village, rice paddy, rush field, saltpan, and mangrove forest. The village has been destroyed by coastal erosion; and houses, churches and other buildings ceased to exist. The people living there had to move to another area. Then, the importance of the villages is assigned as the highest, 4. The paddy fields were also destroyed or contaminated by salty sea water. Because the produce of the paddies is very valuable, damage to them entails serious economic loss. Therefore, the importance of the paddy field is assigned as 3. The saltpan uses sea water, and salt is not so expensive so the importance of a saltpan is assigned as 2. There are rush forests in the deposition area because the rush is highly resistant to salt water; and the produce of the rush forests is less valuable than that of the paddies. There are mangrove forests in some areas, but the mangroves are not salable. The importance of rush field and mangrove forest are assigned as 1, the lowest. The land use mesh map is Fig. 10.8 below.

10.4 Results

10.4.1 Altitude Map

An altitude map of the southern Red River Delta was constructed (Fig. 10.1). The delta is very flat and low with an altitude varying from 0–5 m. There are some patchy areas of 0 m. The Red River and Day River are partly raised bed rivers. Upstream of the Red River and Day River, the altitude of the rivers is higher than that of the surrounding area.

There are some sand ridges which are perpendicular to the rivers. The sand ridges show how the delta has been expanded. The Giao Thuy area has been formed by the Red River and Hai Hau, The Nghia Hung and Kim Son areas have been formed by the Day River and Ninh Co River. There are islands formed by

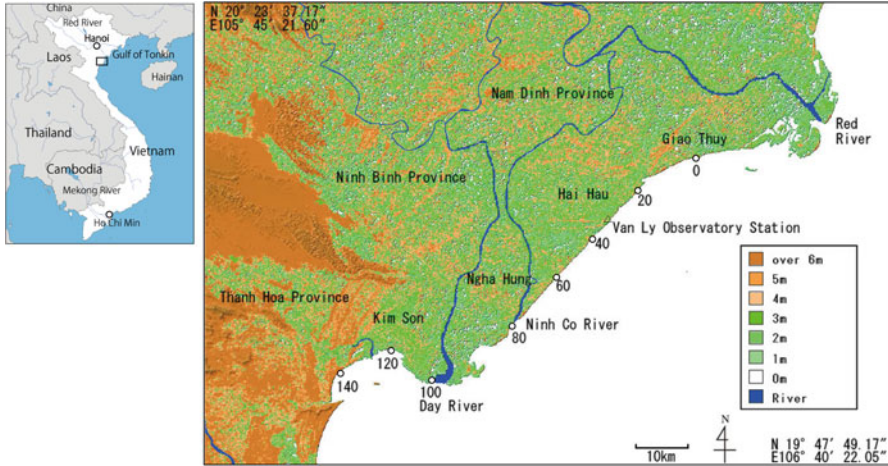


Fig. 10.1 Altitude map made by SRTM (Shuttle Rader Topography Mission) (The numbers are the measuring points of the Coastal Dynamics Index in Fig. 10.2)

sedimentation in the mouths of the rivers. These islands will become a peninsula when they connect to the mainland.

10.4.2 Climate Analysis

Table 10.1 shows the result of calculating the wind data by Van Ly Obserbatory Station, the average number of days by month and by directions.

From May to September, the typhoon season, the winds from E, ESE, SE, SSE, S are strong. The wind directions in the typhoon season are from the sea to inland. Not only is the coastal damage great, there is severe damage to the paddies from salty sea water. Hainan Island of China protects the northern coast from the wind and waves. The damage is less than in the southern part of the northern area of the coastline of the Red River Delta,

From October to the following April, the winter season, the winds from NE, ENE, E are strong. The wind in the winter damages the banks of the coastline and washes away the planted mangroves. In all seasons, the wind is from NE–SE. The wind heaves the waves up and they attack perpendicularly the banks of the coastline. Also, paddies are damaged by the saline water blown from the sea.

Table 10.1 Average number of days from 1991 to 2000 (with strongest wind among four times observation in a day, parenthesis numbers are the average wind speed)

	Jan	Feb	Mar	Apr	May	Jun	Jul	Aug	Sep	Oct	Nov	Dec
N	1.2 (7.1)	0.6 (6.3)	1.0 (6.3)	0.4 (8.5)	0.6 (8.0)	0.7 (6.3)	0.3 (8.3)	1.0 (6.3)	2.2 (6.2)	2.4 (8.5)	3.0 (6.6)	3.3 (6.8)
NNE	0.3 (8.0)	0.4 (7.5)	0.1 (8.0)	0.2 (7.5)	0.4 (6.8)	0.2 (6.0)	0.1 (12.0)	0.7 (9.0)	0.9 (8.7)	1.1 (7.3)	1.2 (7.4)	1.3 (7.5)
NE	2.2 (9.2)	3.0 (9.1)	1.9 (7.5)	1.7 (7.8)	1.6 (11.3)	0.3 (8.3)	0.3 (11.7)	1.1 (10.5)	2.2 (9.8)	3.6 (9.5)	3.2 (8.3)	3.2 (8.9)
ENE	7.4 (10.0)	8.4 (8.6)	8.2 (8.4)	4.7 (8.9)	3.0 (9.6)	0.8 (9.3)	0.5 (7.0)	0.4 (10.0)	3 (8.5)	5.1 (8.3)	5.5 (8.5)	6.1 (8.7)
E	6.0 (7.9)	7.5 (7.7)	10.7 (8.6)	9.5 (7.4)	4.3 (8.6)	1.3 (8.9)	1.7 (8.2)	2.6 (7.7)	4.4 (8.0)	5.1 (7.7)	5.1 (7.5)	5.6 (7.7)
ESE	2.6 (7.3)	1.3 (6.2)	1.7 (6.4)	1.8 (5.8)	1.4 (7.4)	0.5 (9.4)	0.7 (8.1)	1.1 (8.4)	2.9 (9.7)	1.3 (7.2)	2.1 (7.5)	1.5 (6.3)
SE	1.6 (6.2)	1.5 (6.9)	2.9 (6.9)	3.5 (6.7)	6.5 (7.8)	6.0 (8.0)	4.3 (8.2)	5.5 (8.1)	4.5 (6.6)	3.2 (7.5)	2.1 (6.9)	1.7 (6.2)
SSE	0.4 (6.0)	0.5 (9.4)	1.7 (8.9)	3.3 (8.0)	5.4 (8.7)	7.1 (9.4)	8.6 (8.8)	6.5 (8.0)	2.3 (7.3)	2.0 (7.7)	0.2 (7.0)	0.2 (6.5)
S	0.3 (6.3)	0.3 (7.0)	0.4 (5.5)	2.3 (7.3)	4.1 (8.4)	6.0 (9.2)	5.3 (8.6)	3.1 (8.0)	1.5 (5.9)	0.4 (5.5)	0.2 (8.0)	0.6 (6.2)
SSW	0.3 (7.0)		0.1 (6.0)	0.9 (11.3)	0.9 (9.0)	3.7 (8.6)	4.4 (9.0)	2.4 (7.8)	0.5 (8.2)	0.3 (5.7)	0.5 (6.6)	
SW				0.1 (8.0)	0.3 (8.7)	0.9 (8.7)	1.8 (9.9)	1.3 (7.0)		0.2 (8.5)	0.1 (8.0)	
WSW						0.1 (5.0)	0.3 (8.3)	0.7 (9.4)	0.1 (6.0)	0.1 (7.0)		
W		0.1 (4.0)			0.4 (8.3)	0.4 (7.8)	0.5 (6.2)	0.6 (7.7)	0.2 (6.0)			0.1 (6.0)
WNW					0.2 (15.0)	0.1 (28.0)	0.1 (9.0)	0.3 (5.0)	0.1 (5.0)		0.1 (4.0)	0.1 (7.0)
NW	1.7 (7.4)	1.1 (7.0)	1.1 (6.6)	0.9 (7.6)	0.3 (7.7)	1.2 (8.5)	1.4 (8.1)	2.1 (6.8)	2.2 (7.2)	1.2 (7.3)	2.0 (7.3)	1.1 (6.8)
NNW	7.0 (9.8)	3.6 (7.5)	1.2 (6.6)	0.7 (6.6)	1.6 (8.7)	0.7 (7.6)	0.7 (9.3)	1.5 (7.6)	3.0 (7.4)	5.0 (7.6)	4.7 (8.1)	6.2 (6.9)

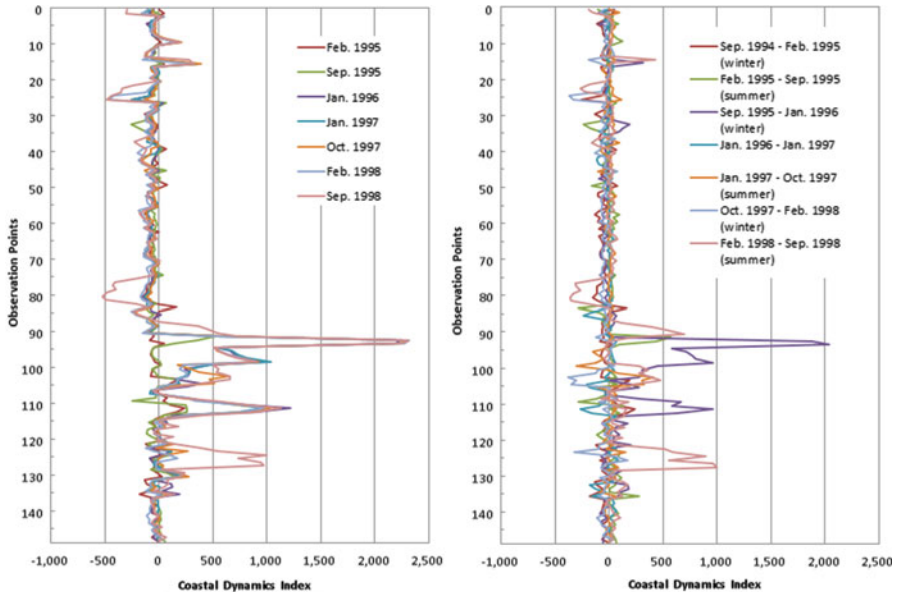


Fig. 10.2 Coastal Dynamics Index (CDI) from 1995 to 1998 calculated by JERS-1/SAR. The negative numeric means erosion and plus numeric means the deposition in metric units. The vertical axis shows the measuring points which were shown in Fig. 10.1. (a) Shows the accumulate CDI where 0 is the September 1994 coastal line; (b) shows the seasonal CDI where 0 is the beginning coastal line of the season

10.4.3 Coastal Dynamics Index (CDI)

Figure 10.2 shows the Coastal Dynamics Index (CDI) from 1995 to 1998; Fig. 10.2a shows the accumulated CDI and the Fig. 10.2b shows the seasonal CDI. Figure 10.2a can be roughly divided into two parts, a positive section and a negative section. Measuring points from the 20th to the 80th shows a negative sign, indicating an erosion zone. The location is from the northern Hai Hau to the mouth of the Ninh Co River. Measuring points from the 85th to the 130th shows a positive sign, representing a deposition zone. The location is from the mouth of the Ninh Co River to the Day River. The maximum expansion captured through CDIs is more than 1 km per year in the western part of the Ninh Co River mouth. The minimum is – 500 m in northern Hai Hau to the mouth of the Ninh Co River.

The average CDI in the erosion section from 20th to 80th is – 50 m from 1994 to 1998. CDIs in the year 1998 indicate that more serious erosion occurred in this area. Almost all CDIs in this erosion area exhibit the same tendencies every other year.

As for the seasonal CDI in Fig. 10.2b, coastal erosion occurs in the winter and deposition occurs in the summer season. In summer, some big erosion occurs locally. It is because of high precipitation in the summer season, sometimes with typhoons, which brings sediment from upstream, that the deposition occurs in

summer. The typhoons have destroyed the banks and much coastal erosion has therefore occurred locally. In winter, because the precipitation is low, sedimentation is insufficient; and therefore coastal erosion occurs.

The tidal effect needs to be considered. However the time of the satellite images could not be obtained. The tide amplitudes were 1.1–3 m in September 30, 1994; 1.3–2.3 m in February 9, 1995; 1.3–2.9 m in September 17, 1995; 1.8–2.1 m in January 27, 1996; 0.8–3.2 m January 13, 1997; 2–2.5 m October 4, 1997; 1–2.9 m in February 13, 1998; 1.7–2.7 m September 21, 1998. The tide amplitude was large only on January 13, 1997. The other dates had narrow tide amplitudes. The coastline changes because of the tide are narrow, while the coastline changes due to erosion are larger than those resulting from the tidal change. Additionally, Thuy et al. (2012) analyzed the coastline change in Hai Hau area by satellite data, determining the times of high, middle and low tides. The results showed the coastline is apparently less affected by the tide than by erosion and deposition.

10.4.4 Coastal Erosion Risk Map

By using the CDIs, banks, and, heights of land, the authors classified the 74 coastal meshes. The coastline was divided into four large clusters (Fig. 10.3). The CPCC (cophenetic correlation coefficient) was 0.941. The features of those four groups are as follows: Group I – regardless of CDIs, most parts of the banks in each mesh are not over 4 m; Group II – coastal erosion occurs, land level is below sea level; Group III – coastal erosion or small deposition occurs, the land level is above sea level; Group IV – large deposition occurs. Therefore, the construction of a coastal erosion risk map was possible (Fig. 10.4).

10.4.5 Risk Map of Coastal Erosion

By using the CDIs, banks, and, heights of land, the authors classified the 74 coastal meshes. The coastline was divided into four large clusters (Fig. 10.5). The CPCC (cophenetic correlation coefficient) was 0.941. The features of those four groups are as follows: Group I – regardless of CDIs, the greater part of the banks in each mesh are not over 4 m; Group II – coastal erosion occurs; land level is below sea level; Group III – coastal erosion or small deposition occurs; the land level is above sea level; Group IV – large deposition occurs. Therefore, the construction of a coastal erosion risk map was possible (Fig. 10.4)

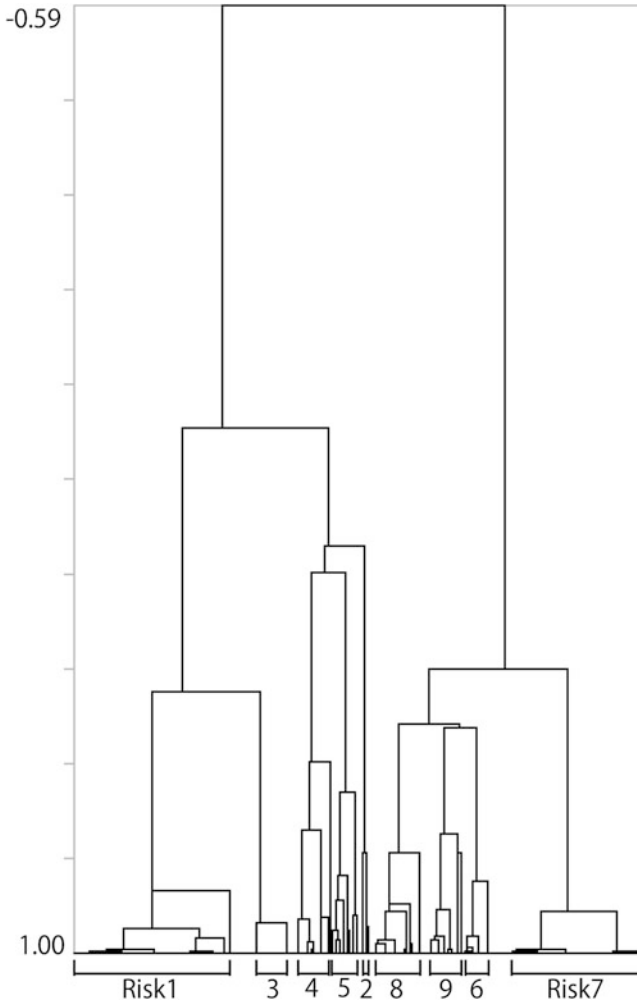


Fig. 10.3 Dendrogram based on UPGMA cluster analysis, with Coastal Dynamics Index (*CDI*), banks and height of land. The cophenetic correlation coefficient (*CPCC*) was 0.941. If the *CPCC* is near 1, the topology is highly reproducible

10.5 Land Use Vulnerability Map

10.5.1 Risk Ranks

With another factor, “distance from the sea,” added to the previous four groups, a total of 686 meshes and 9 new clusters were classified (Fig. 10.5). The *CPCC* was 0.897. Since the inland area had a lower erosion risk than did the coastal area, the risk ranking assigned to the new clusters were as follows (from the highest risk

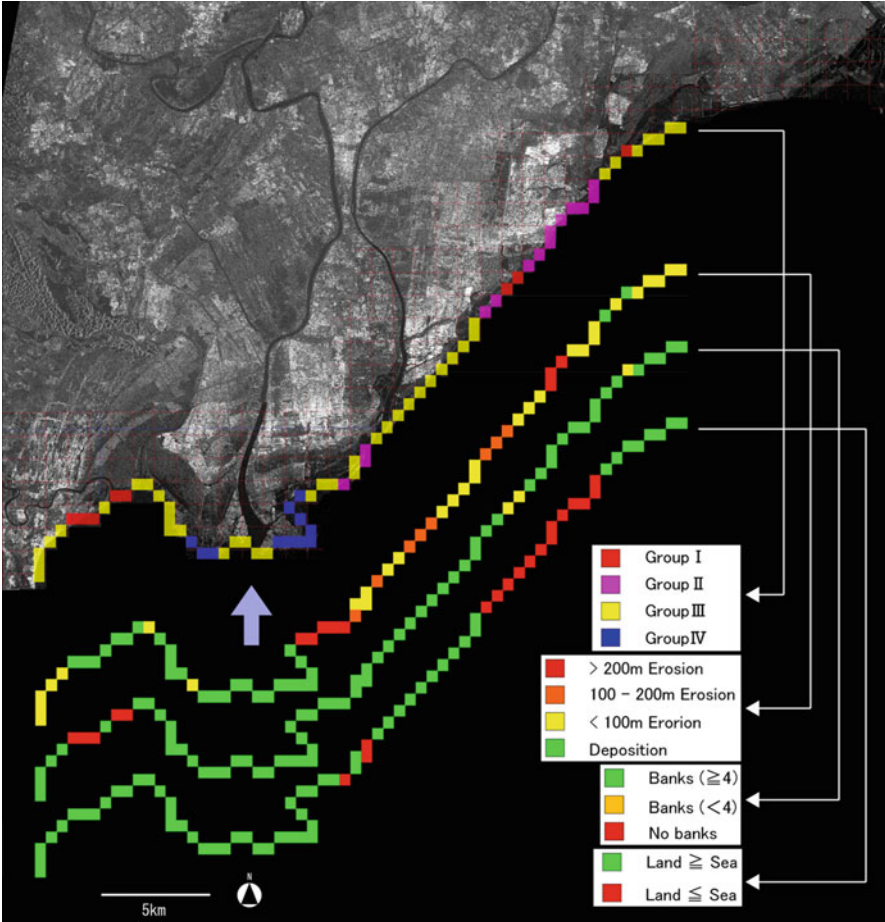


Fig. 10.4 Risk map of the coastal erosion by calculating the cluster analysis of UPGMA with the items of Coastal Dynamics Index (*CDI*), banks and height of land. In the calculation, actual *CDI* numeric value was used

ranking to the lowest): Risk 9 – the coastal area in Group I; Risk 8 – the coastal area in Group II; Risk 7 – the coastal area in Group III; Risk 6 – the coastal area in Group IV; Risk 5 – the inland area in Group I; Risk 4 – the inland area of Group II; Risk 3 – the inland area of Group III; Risk 2 – the inland area of Group IV; Risk 1 – interior of Risk 2–5 areas. The illustrated risk map is in the middle section of Fig. 10.8 The risk map shows the coastal areas such as Giao Thuy, Hai Hau, and Hoang Hoa are the most dangerous places – they have the highest probability of encountering a land loss problem in the near future. The deposition areas consist of new and soft soils and are therefore easily affected by coastal erosion. The risks of the deposition areas are also higher than those of the inland areas.

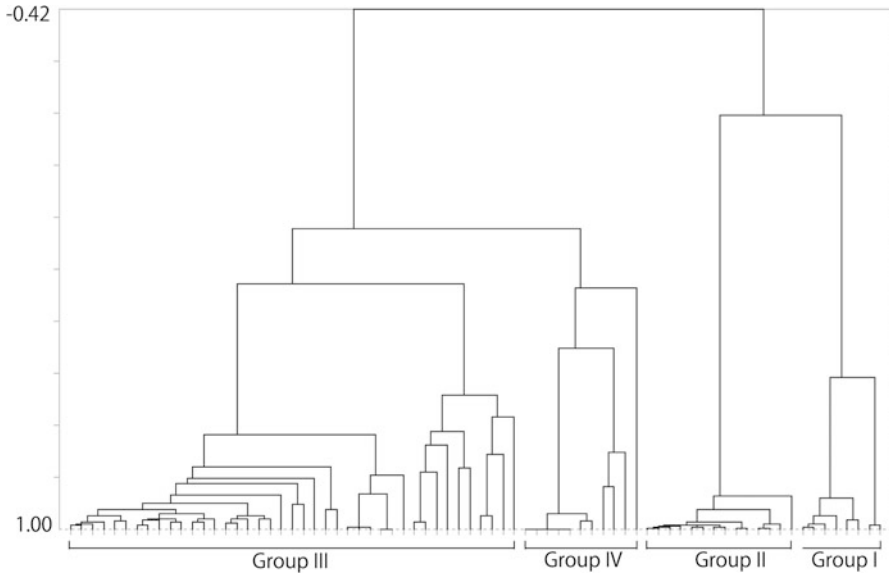


Fig. 10.5 Dendrogram of risk ranks of 686 meshes based on UPGMA cluster analysis with the group I–IV in Fig. 10.4 and the distance from the sea. The cophenetic correlation coefficient was 0.897. If the CPCC is near 1, the topology is highly reproducible

10.5.2 Vulnerability Diagnosis: Spatial Randomization for Current Land Use

Is current land use in the southern Red River Delta vulnerable? Because of the importance of the problem, we introduce a vulnerability index (Murooka and Haruyama 2005).

Where one study area is divided into n meshes, the vulnerability of i -th mesh, v_i , is a product of coastal erosion risk and land use importance,

$$v_i = c_i l_i,$$

c_i : coastal erosion risk of i -th mesh, l_i : land use importance of i -th mesh.

v_i is the original vulnerability index.

Where an area vulnerability is defined as a total sum of all vulnerabilities,

$$V_{area} = \sum_{i=1}^n v_i.$$

V_{area} is a unique measurement based on observation. Furthermore an average mesh vulnerability is

$$V_{mesh} = \frac{1}{n}V_{area}.$$

Hence a V_{mesh} is not only a mean value of the area vulnerability but also an expected value of a vulnerability distribution. If there are some areas with different mesh sizes, we can compare the vulnerability of those areas using V_{mesh} ,

where V_{area} is the inner product of two same rank vectors, coastal erosion risk vector, C , and land use importance vector, L ,

$$\begin{aligned} V_{area} &= \sum_{i=1}^n v_i \\ &= v_1 + v_2 + \dots + v_n, \\ &= c_1l_1 + c_2l_2 + \dots + c_nl_n, \\ &= C \cdot L \end{aligned}$$

where C is a parameter vector and L is a variable vector, V_{mesh} is the following function;

$$\begin{aligned} f_{mesh}(L; C) &= V_{mesh} \cdot \\ &= \frac{1}{n}V_{area} \end{aligned}$$

where $f_{mesh}(L; C) = 0$, the trivial solution, $L = 0$, indicates an area unused by humans. Because C and L are usually positive in coastal areas, there is no nontrivial solution. The positive index value thereby means that there exists the possibility of a mitigation solution, $L_m \in \{L: 0 < f_{mesh}(L; C) \leq V_{mesh}\}$.

How do we use these indices as vulnerability diagnosis tools? A solution was achieved by the arrangement of spatial randomization tests (Manly 1997). Spatial randomization techniques are usually used to statistically test for geographical structure in various problems, i.e., epidemiology, biogeography, etc.

In spatial randomization, an empirical distribution which is constructed by random permutation is used to examine this hypothesis. Why did we use random permutation? For example, in a 20 mesh case, the number of permutation series is 2,432,902,008,176,640,000. It is usually impossible to generate all permutation series in this example, and the ordinary scale of the meshes is too large to generate all permutation series. Therefore, we should construct an approximate permutation distribution based on a set of permutation series randomly sampled without replacement.

First, one area is divided into n meshes and each one is sequentially numbered from first to n -th. Second, area vulnerability values are calculated from rearranged mesh sequences by generated random permutation. Finally one permutation distribution is constructed by a set of area vulnerabilities. Furthermore we calculate the lower area of the area vulnerability values of the current land use on the permutation distribution as a probability, generalized vulnerability score ($0 \leq V_{general} \leq 1$). Where number of meshes, N , is 4, all possible permutations are 24 in Fig. 10.6, $V_{area} = 30$ and $V_{mesh} = 7.50$. Bold frames show results based on observed data.

1) Observed Costal Erosion Risk and Land Use Importance

Coastal Erosion Risk Map

1	2
3	4

Current Land Use Importance Map

1	2
3	4

2) Possible Land Use Importance Maps

1	2	2	1	3	1	4	1
3	4	3	4	2	4	2	3

1	2	2	1	3	1	4	1
4	3	4	3	4	2	3	2

1	3	2	3	3	2	4	2
2	4	1	4	1	4	1	3

1	3	2	3	3	2	4	2
4	2	4	1	4	1	3	1

1	4	2	4	3	4	4	3
2	3	1	3	1	2	1	2

1	4	2	4	3	4	4	3
3	2	3	1	2	1	2	1

3) Possible Vulnerability Maps

1	4	2	2	3	2	4	2
9	16	9	16	6	16	6	12

1	4	2	2	3	2	4	2
12	12	12	12	12	8	9	8

1	6	2	6	3	4	4	4
6	16	3	16	3	16	3	12

1	6	2	6	3	4	4	4
12	8	12	4	12	4	9	4

1	8	2	8	3	8	4	6
6	12	3	12	3	8	3	8

1	8	2	8	3	8	4	6
9	8	9	4	6	4	6	4

4) Area Vulnerability Table

30	29	27	24
29	28	25	23
29	27	26	23
27	24	23	21
27	25	22	21
26	23	21	20

5) Average Mesh Vulnerability Table

7.50	7.25	6.75	6.00
7.25	7.00	6.25	5.75
7.25	6.75	6.50	5.75
6.75	6.00	5.75	5.25
6.75	6.25	5.50	5.25
6.50	5.75	5.25	5.00

Fig. 10.6 Calculation process of average mesh vulnerability

Figure 10.6-2 shows the importance of all possible land uses and Fig. 10.6-3 is all possible vulnerability maps. Figure 10.6-4 is all V_{area} table and Fig. 10.6-5 is all V_{mesh} table. Finally $V_{general}$ is $\frac{23}{24} = 0.96$. Figure 10.7 shows a histogram example constructed by Fig. 10.6-4. In this example current land use is estimated to be the most vulnerable, and L_m with $V_{area} = 20$ and $V_{mesh} = 5.50$ is the least vulnerable land use.

Where $V_{general}$ indicates a high score, the current land use is vulnerable in a set of all possible land use conditions in the area. On the other hand, a high score indicates the possibility for a mitigation policy concerning land use, L_m .

The random permutation algorithm is as follows;

1. Set an observed coastal erosion risk set to parameter vector C .
2. Set an observed land use importance set to variable vector L
3. Calculate $V_{observed}$ using $f_{mesh}(L; C)$.
4. Generate a new random permutation series, L_{new} , without duplication.
5. Calculate V_{mesh} using $f_{mesh}(L_{new}; C)$ for every permutation.
6. Return to 4 until repetitions are of sufficient number, M .
7. Construct a distribution based on the V_{area} set.
8. Store m with the number of elements less than $V_{observed}$ in the V_{mesh} set.
9. Calculate a generalized vulnerability score $V_{general} = \frac{m}{M}$.

For $N \leq 7$, It is possible to easily construct a complete permutation distribution; but for $N \geq 8$, random permutation distribution is most practical.

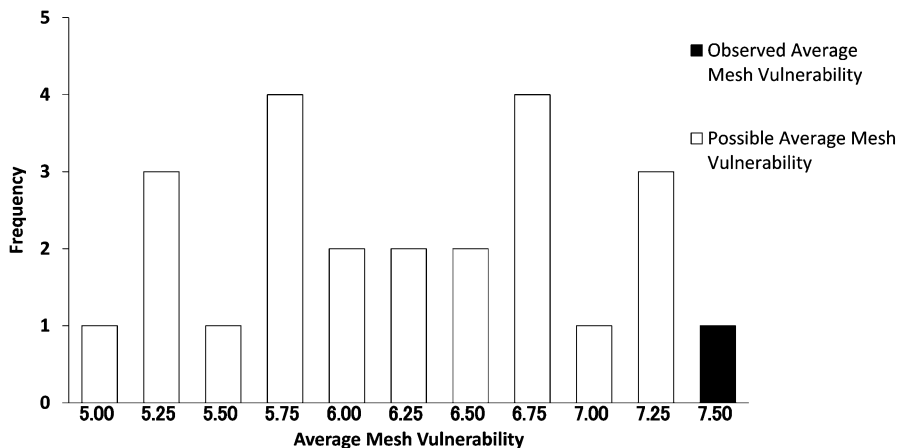


Fig. 10.7 Permutation distribution constructed by table in Fig. 10.6-5

10.5.3 Vulnerability Map of the Coastal Erosion

Vulnerability was ranked by six levels as follows; (1) 0–4, (2) 5–9, (3) 10–14, (4) 15–19, (5) 20–24, and (6) 25–27. The total number of meshes was 686. The numbers and percentage of meshes of each vulnerability were as follows: vulnerability 1 had 332 meshes (48.4 %), 2 had 124 meshes (18.1 %), 3 had 88 meshes (12.8 %), 4 had 59 meshes (8.6 %), 5 had 70 meshes (10.2 %), 6 had 13 meshes (1.9 %). The average vulnerability was 2.2 and standard error was 0.46.

The land use vulnerability map indicated that the coastal erosion risk from the aspect of land use was highest at the Van Ly area and the village in Hoang Hoa. The coastal erosion risk of rice paddies was highest in the coastal area of Giao Thuy and inland area of Van Ly.

There were rush fields in the inland area of Nghia Hung and Kim Son which was the deposition area. These rush fields could be considered to be of low vulnerability to the threat of coastal erosion (Fig. 10.8).

10.6 Conclusions

In this study, making a risk map for coastal erosion was accomplished through the use of UPGMA cluster analysis of the fragmentary data in the Red River Delta, Vietnam. Not only in Vietnam, but also in other developing countries, the necessary data are almost always lacking. Under these circumstances, satellite remote sensor data can be quite useful. Coastline changes can be assessed by using satellite remote sensor data. This study could be employed to make a vulnerability map, including land use, banks and salinity, by using the UPGMA cluster analysis. The Coastal

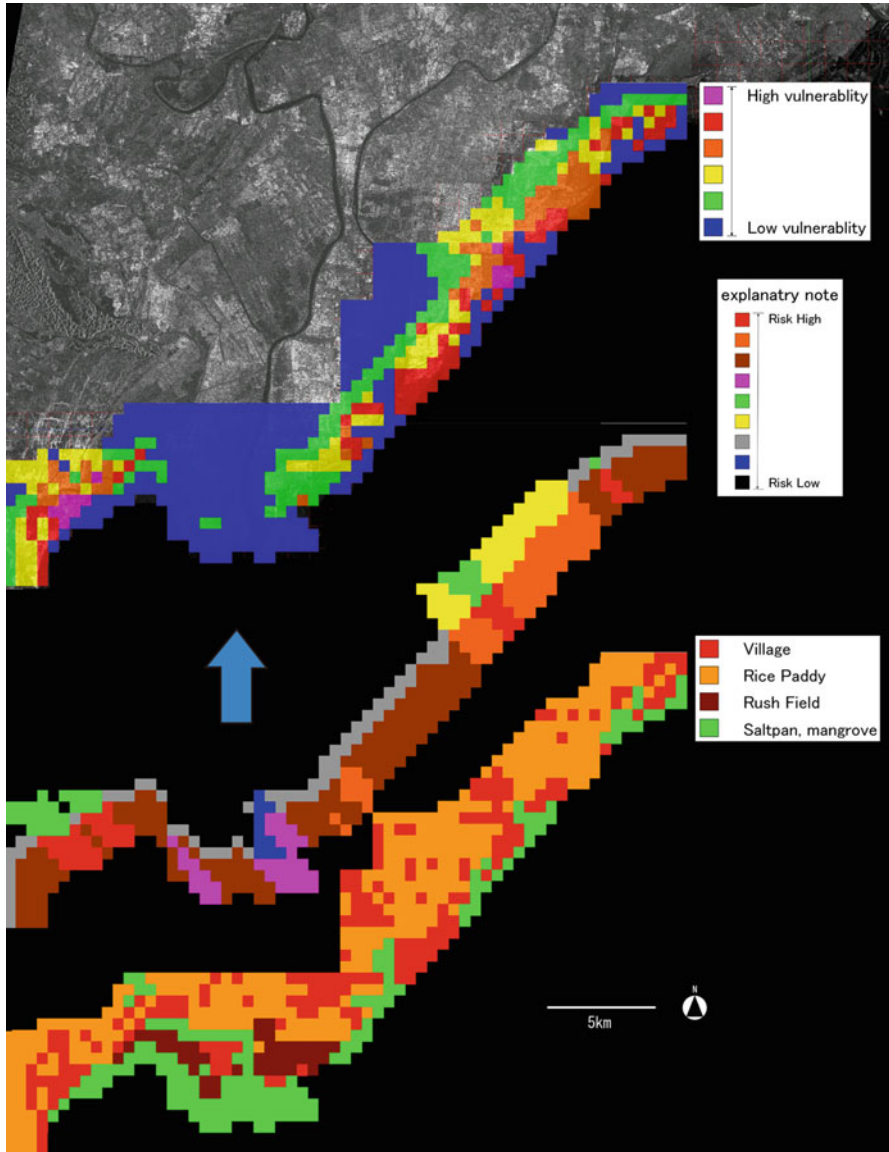


Fig. 10.8 Coastal erosion vulnerability mesh map, coastal erosion risk ranking map illustration of the dendrogram of Fig. 10.5 and land use map

Dynamics Index (CDI) calculated from JERS-1/SAR images was created to construct the coastal erosion risk map. The most important thing is that land use was included in the risk assessment. Land use is a key matter to consider in mitigation.

In Vietnam, the land use planning resembles forecasting. The plan targets are realistic and feasible, but it may not be favorable for water resources management

(Asian Development Bank and Ministry of Agriculture and Rural Development 2000). However, a proper land use policy is absolutely necessary because it can enable local areas to overcome natural hazards.

Based on the natural environmental characteristics of coastal erosion and the affected areas, erosion potential can be assessed by using remote sensing data analysis. This methodology can also apply to the other regions in Vietnam and beyond. In high risk areas, suitable means, corresponding to the particular conditions of the area, must be taken for disaster prevention.

References

- Asian Development Bank and Ministry of Agriculture and Rural Development (2000) Final report on management study on land use and water management, Asian Development Bank, TA No 2871-VIE, Red River Basin Water Resources Management Project
- Booij MJ (2004) Flood damage assessment and modelling in the Red River basin in Vietnam, International Workshop on Flood Controls Decision Support Systems (Flocods), Vietnam
- Cao DT, Nguyen XC, Nguyen DM, Nguyen HH, Bui TC (2007) Typhoons and technical solutions recommended for existing and new houses in the cyclonic regions in Vietnam, EJSE special issue: selected key note papers from MDCMS 1 1st international conference on modern design, construction and maintenance of structures, Hanoi, Dec 2007, pp 8–18
- Dang NM, Babel MS, Luong HT (2011) Evaluation of food risk parameters in the Day River Flood Diversion Area, Red River Delta, Vietnam. *Nat Hazards* 56:169–194
- Duc DM, Nhuan MT, Ngoi CV (2012) An analysis of coastal erosion in the tropical rapid accretion delta of the Red River, Vietnam. *J Asian Earth Sci* 43(1):98–109
- Farris JS (1969) On the cophenetic correlation coefficient. *Syst Zool* 18:279–285
- Frost VS, Stiles JA, Shanmugan JA, Holtzman JC (1982) A model for radar images and its application to adaptive digital filtering of multiplicative noise. *IEEE Trans Pattern Anal Mach Intell* 4(2):157–166
- General Statistics office of Vietnam: http://www.gso.gov.vn/default_en.aspx?tabid=491. 14 June 2014
- Haruyama S (1995) Geomorphologic features of the Song Hong delta. *J Int Relat Stud* 21:1–13
- Haruyama S (2000) Natural environmental change and disaster of agriculture land on the Red River delta. *J Soc Irrig Drain Reclam Eng* 68–9:15–20 (In Japanese)
- Haruyama S (2002) Natural environmental change and correspondence for rice society of the coastal area of the North Vietnam. *J Suirikagaku* 266:1–13
- Haruyama S (2004) Natural environmental study applied for agriculture in the northern Vietnam: natural hazard and their diffence policy against disaster, the Red River Delta. Kokon Shoin, Tokyo (in Japanese)
- Haruyama S, Van PV (2002) Coastal change in the Southern Song Hong Delta. *J Geogr* 111(1):126–132
- Haruyama S, Le QD, Le VT, Le KP, Vu VP, Hori K, Tanabe S, Saito Y (2002) Geomorphology of the Red River Delta and their Fluvial Process of Geomorphologic development, Northern Vietnam
- Hori K (2012) Case study of the alluvial lowland. In: Oya M (ed) *Geomorphological ecology in the alluvial lowland*. Kokon Shoin, Tokyo, pp 71–78 (in Japanese)
- Imamura F, Dang VT (1997) Flood and typhoon disasters in Viet Nam in the half century since 1950. *Nat Hazards* 15:71–87
- Manly BJ (1997) *Randmization, and bootstrap and Monte Carlo methods in biology*, 2nd edn. Chapman & Hall, London, xx+397 p

- Mathers S, Zalasiewicz J (1999) Holocene sedimentary architecture of the Red River Delta, Vietnam. *J Coast Res* 15(2):314–325
- Murooka M, Haruyama S (2005) Risk assessment of coastal erosion for suitable rural planning? Southern Red River Delta, Vietnam. *J Rural Plan* 24(Special Issue):109–114
- Nguyen TD (1992) *Geography of Vietnam*. Foreign Languages Publishing House, Hanoi
- Nguyen VD, Nguyen HK, Nguyen MS, Nguyen VH, Huntjes P (2007) Integrated water resource management in the Red river basin: problems and cooperation opportunity, International Conference on Adaptive & Integrated Water Management (CAIWA), Nov 2007, Switzerland
- Romesburg HC (1989) *Cluster analysis for researchers*. Robert E. Krieger, Malabar
- Sneath PHA, Sokal RR (1973) *Numerical taxonomy*. W. H. Freeman, San Francisco, xvi+573 pp
- Thuy MTT, Nagatsuka S, Nishihata T, Takewaka S, Mimura N, Yasuhara K, Duc DM (2012) Analysis of a large-scale erosion in Hai Hau coast, Northern Vietnam. *J JSCE B2* 68(2): I_1441–I_1445
- Vinh TT, Kant G, Nguyen NH, Pruszek Z (1996) Sea dike erosion and coastal retreat at Nam Ha Province, Vietnam, Proceedings of 25th conference on coastal engineering, Orlando, pp 2820–2828
- Vu VP, Nguyen XT (1992) Lich su Phat Trien bo Bien Ria Delta Song Hong Trong Thoi Ky Gan Day. *Tap Chi Cac Khoa Ve Trai Dat* 14:57–60 (In Vietnamese)

Chapter 11

Modelling Shallow Landslide Risk Using GIS and a Distributed Hydro-geotechnical Model

Pingping Luo, Apip, Bin He, Kaoru Takara, Weili Duan, Maochuan Hu, and Daniel Nover

Abstract GIS and distributed hydrological models are important tools for shallow landslide prediction, particularly as such disasters are exacerbated by global change driven changes in precipitation regimes. The main objective of this chapter is to outline a detailed methodology for shallow landslide risk assessment using GIS and a hydrological model. We have developed a method to assess shallow landslide risk using GIS tools and a distributed hydrological model and further used this method to analyze the probability of shallow landslides in a case study. The physically

P. Luo (✉)

Institute for the Advanced Study of Sustainability (UNU-IAS), United Nations University, Shibuya, Tokyo, Japan

Disaster Prevention Research Institute (DPRI), Kyoto University, Uji, Kyoto, Japan

e-mail: luoping198121@gmail.com

Apip

Research Centre for Limnology, Indonesian Institute of Sciences (LIPI), Cibinong, Indonesia

e-mail: apip@limnologi.lipi.go.id

B. He (✉) • W. Duan

CAS Key Laboratory of Watershed Geographic Sciences, Chinese Academy of Sciences, Nanjing Institute of Geography and Limnology, Nanjing, China

e-mail: hebin@niglas.ac.cn; wlduan@niglas.ac.cn

K. Takara

Disaster Prevention Research Institute (DPRI), Kyoto University, Uji, Kyoto, Japan

e-mail: takara.kaoru.7v@kyoto-u.ac.jp

M. Hu (✉)

Department of Civil and Earth Resources Engineering, Graduate School of Engineering, Kyoto University, Kyoto daigaku-Kastura, Nishikyo-ku, Kyoto 615-8530, Japan

e-mail: hu-maochuan@163.com

D. Nover

Global Change Research Program, U.S. Environmental Protection Agency, Washington, DC, USA

e-mail: dmnover@gmail.com

© Springer Science+Business Media Dordrecht 2015

J. Li, X. Yang (eds.), *Monitoring and Modeling of Global Changes: A Geomatics Perspective*, Springer Remote Sensing/Photogrammetry, DOI 10.1007/978-94-017-9813-6_11

221

based distributed landslide model was developed by integrating a grid-based distributed kinematic wave rainfall-runoff model combined with an infinite slope stability module. Application of the model to assess shallow landslide risk using rainfall data for Kyushu Island shows that the model can successfully predict the effect of rainfall distribution and intensity on the driving variables that trigger shallow landslides. The modeling system has broad applicability for shallow landslide prediction and warning.

Keywords GIS • Distributed hydro-geotechnical model • Shallow landslide risk • Probability • Kyushu Island

11.1 Introduction

As climate change intensifies during the twenty-first century, extreme events such as typhoons, extreme rainfall, droughts, etc. are expected to become more common. Recent decades have seen more frequent shallow landslides, driven by typhoons and extreme rainfall events (Duan et al. 2014). Shallow landslide risk mapping is a necessary tool for the risk management community. Recent developments in GIS tools and hydrological/geotechnical modeling enable researchers and resource managers to analyze land surfaces for shallow landslide potential.

As GIS tools have become more commonplace, they have been widely used in hydrological modeling. The Soil and Water Assessment Tool (SWAT) combined with ArcGIS (called ArcSWAT) is becoming a popular modeling tool applied for studying water resources in the USA (CEAP 2008; Gassman et al. 2007), China (Zhang et al. 2008), Japan (Luo et al. 2012), and West Africa (Schuol et al. 2008). Hydrological models such as grid-Cell Distributed Rainfall Runoff Model Version 3 (CDRMV3) take input hydrological data including flow accumulation, flow direction and so on from ArcGIS (Luo et al. 2014a). The Geospatial Hydrologic Modeling Extension (HEC-GeoHMS) is a public-domain software package also linked with ArcGIS. TOPMODEL, originally developed at the University of Leeds (United Kingdom) in the mid-1970s has recently been coupled with the Geographic Resources Analysis Support System (GRASS) GIS software. A GIS-based framework for systematic landslide hazard analysis was developed and applied in Hong Kong with geologic, climatic, historical landslide data and rainfall data (Chau et al. 2004). Safety maps for slope stability in the northern part of the Rasuwa district in Nepal were generated through an analysis of physical processes using GIS tools (Acharya et al. 2006). Spatial analysis and prediction of landslide hazards have also used GIS techniques in the Xiaojiang watershed in Southwest China (Lan et al. 2004). Using GIS, the dynamic characteristics of shallow landslides can be analyzed in response to rainfall events (Lan et al. 2005). A grid-based GIS framework is required for susceptibility and hazard assessment of shallow landslides (Godt et al. 2008). The proliferation of GIS tools and extensions has vastly expanded the potential for hydrological modeling and shallow landslide analysis.

Shallow landslide studies generally require a distributed hydrological model coupled with a slope stability model. For example, a topography-based hydrological model linked with a slope stability model was applied to predict the location of shallow landslides in a mountain catchment in the Dolomites, Italy (Borga et al. 1998). SHETRAN is a physically based distributed basin hydrology and sediment transport model system coupled with a geotechnical stability model to assess the impact of forest cover on shallow landslides (Bathurst et al. 2010). The TIN (triangulated irregular network) based Real-Time Integrated Basin Simulator (tRIBS) implemented with the Stability module and Movement module are also tools used to simulate spatio-temporal hydrologic processes (infiltration, evapotranspiration, groundwater dynamics and soil moisture conditions) affecting shallow landslides (Arnone et al. 2011). Distributed hydrologic rainfall-runoff models linked with geotechnical models have also been developed and applied for shallow landslide prediction using satellite-derived estimated rainfall in the upper Citarum catchment, Indonesia (Apip et al. 2010). Previous studies show numerous instances where hydrological rainfall-runoff models coupled with geotechnical models are developed and applied in large-scale areas for assessing the triggering conditions of shallow landslides. However, the detail assessment of shallow landslide risk in a large scale by using the improved hydro-geotechnical model has not been done yet.

This chapter presents a GIS framework and a distributed hydrological-geotechnical model that together identify the location and likelihood of shallow landslide on Kyushu Island, Japan. Additionally, spatial shallow landslide hazard maps are presented using results from modeling simulations and ArcGIS. The results of this study provide guidelines for spatial shallow landslide risk analysis. This chapter is organized in the following sections: Section 11.2 “Methodology”; Section 11.3 “Application Study in Kyushu Island”; Section 11.4 “Analysis Results”; Section 11.5 “Discussion”; Section 11.6 “Conclusion”.

11.2 Methodology

This section describes the methodology through which GIS and hydro-geotechnical modeling systems can be used to analyze shallow landslide risk. GIS is used to prepare input data and display outputs for the hydro-geotechnical modeling system. A detailed introduction to hydrological and slope stability models is also given in this section. The methodology is applied in the context of a large island, Kyushu, Japan, and results are presented in Sect. 11.3.

11.2.1 GIS Process and Framework of the Modeling System

There are three main parts to the GIS process including Automated Meteorological Data Acquisition System (AmeDAS) rainfall data, hydrological and soil types and

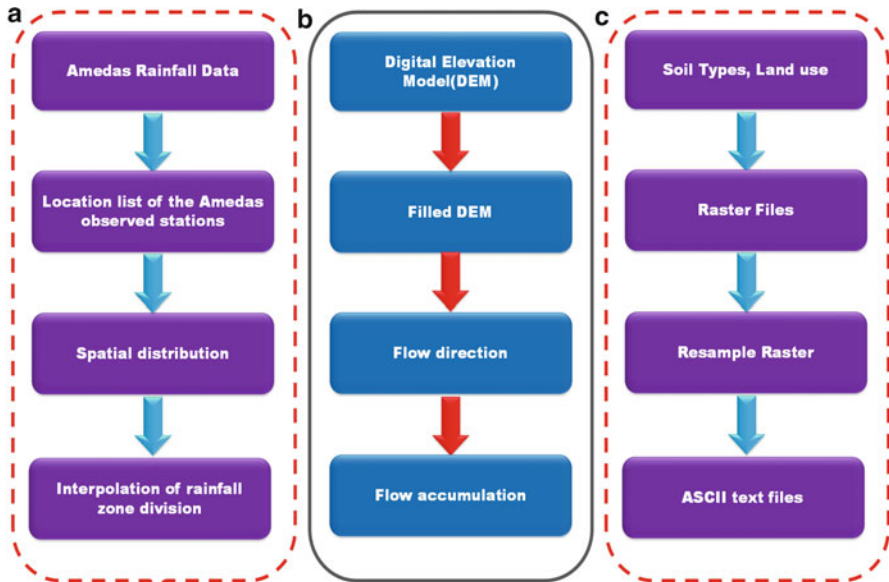


Fig. 11.1 Process of the preparing the input data using ArcGIS

land use GIS processing (Fig. 11.1a–c). ArcGIS 10 (ESRI Company) has been used to deal with the GIS processing in this study.

AmeDAS rainfall data was obtained from the Japan Meteorology Agency (JMA). We selected 120 AmeDAS observed rainfall stations and made a location list of the selected AmeDAS stations including station ID, latitude and longitude as an excel file or a comma-separated values (CSV) file. The location list made in the previous step is imported from “File” → “Add Data” → “Add XY Data” in the ArcGIS 10 Tools bar. The spatial distribution of selected AmeDAS rainfall stations is displayed in ArcGIS 10. To get the rainfall zone for modeling input data, the inverse distance weighted (IDW) interpolation was selected from “Arc Toolbox” → “Spatial Analyst Tools” → “Interpolation”. The interpolation raster file of rainfall zone is converted into ASCII file.

The hydrology tools from “Spatial Analyst Tools” in ArcGIS were used to make the hydrological dataset in Fig. 11.1b. Based on the original DEM from the Ministry of Land, Infrastructure, Transport and Tourism (MLIT), Japan, the coordinate system has been changed from Japanese Geodetic Datum 2000 (JGD 2000) to World Geodetic System 1984 (WGS 1984). The hydrology tools are used to fill all depressions or sinks in the original DEM where there is no flow from pixel to pixel within a hydrologic unit. Flow accumulation is analyzed using ArcGIS and the filled DEM. Flow accumulation was calculated from the flow direction. Finally, we convert the raster files of filled DEM, flow accumulation and flow direction to ASCII files as the input file for the hydro-geotechnical model.

In order to prepare the input file for the model, the land use and soil type shape files are converted into raster files as shown in Fig. 11.1c. The grid-cells size of land

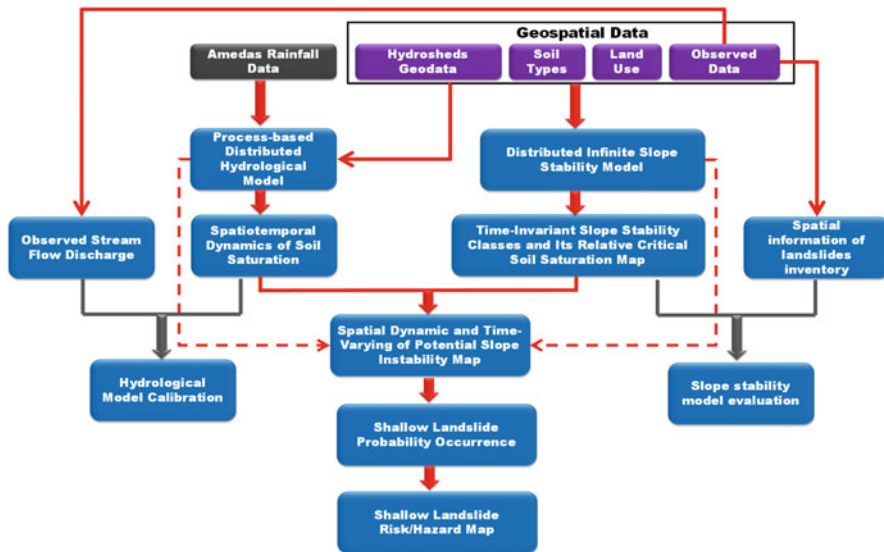


Fig. 11.2 Framework of shallow landslide risk/hazard mapping system

use and soil type raster files is different from the DEM. Therefore, the raster files of land use and soil type have been resampled into the same grid-cell size raster file with the DEM. The resample raster files are converted into ASCII files.

We present a framework for shallow landslide modeling characterized by rapidly moving flows of mixed soil and rock. These shallow landslides often occur along saturated hill slopes under heavy or extreme rainfall. The purpose of this Modeling System is mapping areas of potential slope instability over river catchments.

The framework of the modeling system (Fig. 11.2) is aimed to identify where shallow landslides have occurred in the past, and “where” shallow landslides with high potential risk may occur in the future at a large scale. The detailed description of the process is given below.

1. The geospatial data and AmeDAS rainfall data are collected for this study. The geospatial data includes hydrological geo-data, soil types, land use, observed data (i.e. rainfall data, discharge data, landslides location data). The hydrological geo-data including flow direction and flow accumulation are made by ArcGIS 10 from the DEM. The rainfall in Kyushu Island is interpolated using ArcGIS 10 on the basis of 120 AmeDAS rainfall stations.
2. Geospatial data is input into the distributed infinite slope stability model intended to derive a time-invariant spatial distribution map of the areas susceptible to slope instability, where the catchment area is classified into stability classes according to critical relative soil saturation. The effect of quasi-static land surface variables such as geometric characteristics of the slope,

- geotechnical properties, and strength parameters of the soil on slope instability is described in the time-invariant spatial distribution map.
3. The process-based distributed hydrological model which is described in the next section is calculated using the observed AmedAS rainfall data and Geospatial data from step 1.
 4. Evaluation of the hydrological model performance through calibration of the hydrological model response was carried out using observed stream flow discharge.
 5. The slope stability evaluation was analysed by comparing the spatial pattern of landslides inventory data with the pattern of simulated time-invariant slope stability classes.
 6. Based on the evaluated time-invariant slope stability distribution map, the long-term spatial dynamic and time-varying of potential slope instability map can be drawn. The hydrological model predicts the dynamic of soil saturation in each grid element, which is then used to update the state of relative soil saturation and to assess local slope instability for whole areas defined as potentially stable/unstable.
 7. Shallow landslide probability of occurrence is simulated from the Spatial Dynamic and Time-varying of Potential Slope Instability Map.
 8. Finally, the shallow landslides hazard map can be created with the simulation of shallow landslide occurrences probability.

11.2.2 Physical Based Hydrological Model

A physically based hydrological model coupled with a slope stability model was developed to assess shallow landslide risk analysis over large areas. The distributed hydrological model is the grid-Cell Distributed Rainfall Runoff Model Version 3 (CDRMV3) which was developed at the Innovative Disaster Prevention Technology and Policy Research Laboratory, DPRI, Kyoto University. The CDRMV3 model solves the Kinematic wave equation using the Lax-Wendroff scheme at every node of each cell (Kojima et al. 2003). An automatic calibration program using the Monte Carlo method was added to the evaluation of model performance and uncertainty analysis of the CDRMV3 (Sayama et al. 2003; Apip et al. 2010). Using a steady state assumption, a lumped sediment-runoff model was developed and applied by Apip et al. (2012) based on the CDRMV3 model structure.

The catchment topography is taken from the digital elevation model (DEM) which is divided into square grid-cells. A square area with four node points is called a grid-cell. The analyzed catchment is calculated as a network of grid-cells. The flow of each grid-cell receives the flows from upper grid-cells and direct rainfall. Connected grid-cells receive flow based on the drainage path defined by selecting the steepest direction from eight-directions. Discharge and water depth flow to the next grid-cell according to the predefined eight-directional flow map and routine order determined in accordance with DEM and river channel network data. Flow is

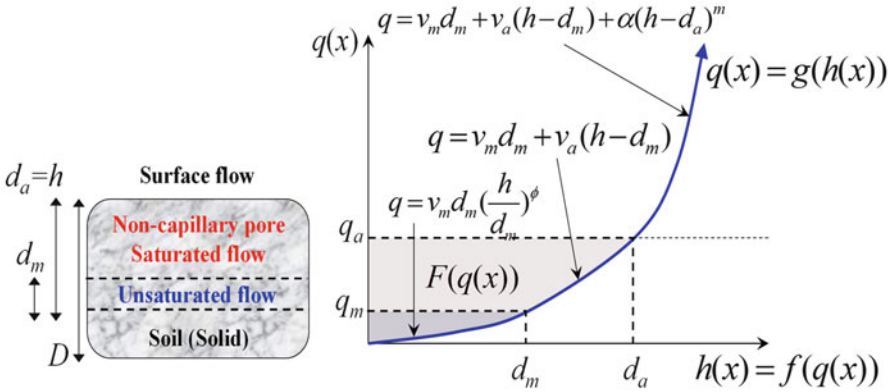


Fig. 11.3 Soil model structure and stage-discharge relationship of each particular grid-cell

routed from hill slopes to the river channel and ultimately to the outlet. The surface and subsurface hydrological processes of CDRMV3 are provided in each grid cell based on the kinematic wave method. The hydrological processes of this model have been divided into three lateral flow mechanisms including (1) subsurface flow through the unsaturated layer, (2) subsurface flow through the saturated layer and (3) surface flow on the soil layer (Luo et al. 2012). At each grid-cell, when the water depth is lower than the equivalent water depth for unsaturated flow ($0 \leq h \leq d_m$), flow is simulated by Darcy’s law with an unsaturated hydraulic conductivity k_m . The model includes a stage-discharge, q - h relationship for both surface and subsurface runoff processes (Eq. 11.1, Fig. 11.3) (Luo et al. 2014a):

$$q = \begin{cases} v_m d_m \left(\frac{h}{d_m}\right)^\phi, & 0 \leq h \leq d_m \\ v_m d_m + v_a (h - d_m), & d_m < h \leq d_a \\ v_m d_m + v_a (h - d_m) + \frac{\sqrt{i}}{n} (h - d_a)^m, & d_a < h \end{cases} \quad (11.1)$$

$$v_m = k_m i, v_a = k_a i, k_m = \frac{k_a}{\phi}$$

$$d_m = D \rho_m, d_a = D \rho_a$$

where q (mms-1) is the discharge per unit width, h (mm) is the water depth, i is the slope gradient, k_m (mms-1) is the saturated hydraulic conductivity of the capillary soil layer, k_a (mms-1) is the hydraulic conductivity of the non-capillary soil layer (saturated), d_m (mm) is the depth of the capillary soil layer (unsaturated), d_a (mm) is the depth of the capillary and non-capillary soil layer, v_m and v_a are the flow velocities of unsaturated and saturated subsurface flows respectively, ϕ is a non-dimensional parameter for unsaturated flow, ρ_a is the effective porosity of the soil layer (D), ρ_m is the effective porosity of the unsaturated layer, and n (m-1/3 s) is the Manning’s roughness coefficient based on the land cover classes.

Initial conditions at each grid-cell are assumed to be in steady-state. Given the observed discharge at the catchment outlet, the discharge from every grid-cell is assigned in proportion to each of the grid-cells upstream to it, and the assigned discharge in each grid-cell is converted to the value of the water depth according to the stage-discharge relationship (Eq. 11.1).

11.2.3 Slope Stability Model

Based on the concept of the infinite slope model, the slope stability model is developed by using a factor of safety (FS) with considering a failure surface. There are five important points which has been concluded in the slope stability model, such as (i) failure is the result of translation sliding, (ii) the failure plane and water table are parallel to the ground surface, (iii) failure occurs as a single layer, (iv) the failure plane is of infinite length, and (v) the impacts of adjacent factors are not taken into account (Apip et al. 2010). In the hill slopes, the safety factor is generally calculated as the ratio of the available resisting force (shear strength) to the driving force (shear stress). Instability occurs due to the shear strength of a soil layer becomes smaller than the shear stress acting on the soil. In this study, the Mohr-Coulomb failure criterion has been used for the governing equation of the safety factor (Apip et al. 2010).

In Fig. 11.4, it presents the detail structure of the forces acting on a point along a slope with potential for failure. The resisting force of a soil layer is the shear strength (s) as a combination of forces, including the normal stress (σ), pore pressure within the soil material (p), cohesion factors (c), and the effective angle of internal friction (β). The difference between normal stress and pore pressure is the effective normal stress. Shear strength based on the Mohr-Coulomb law is presented as follows:

$$s = c + (\sigma - p) \tan \beta \quad (11.2)$$

Normal stress is the vertical component of gravity that resists down-slope movement as follows:

$$\sigma = \delta_s g h \cos \theta, \quad (11.3)$$

where δ_s is the wet soil density (kg/m^3), g is the gravitational acceleration ($= 9.81 \text{ m/s}^2$), h is the vertical soil depth perpendicular to the slope (ψ), and θ is the slope angle (deg). Soil moisture increases the unit weight of soil material and therefore increases both the resisting and driving forces. Soil moisture creates pore pressure, which reduces the effective normal stress and shear strength. Pore pressure in the slope differs among sites and also has large temporal variation. It is difficult to estimate these values and to include them in this model of a large catchment. Therefore, we simplified the condition of pore pressure in the slope by

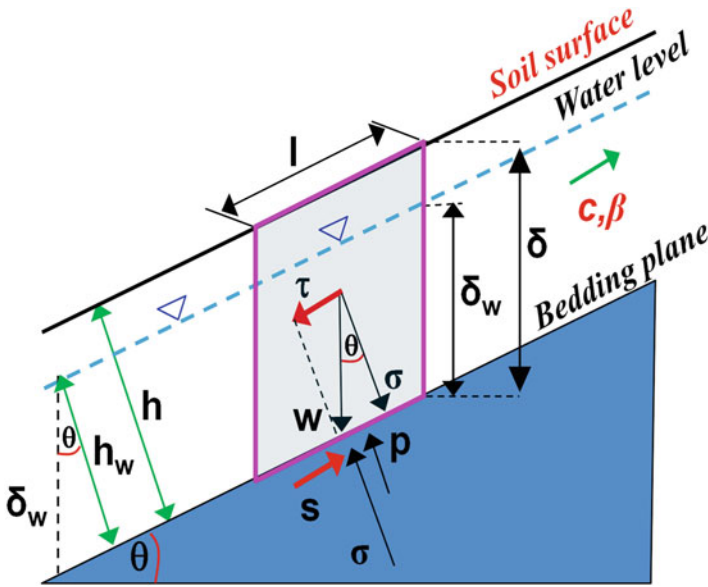


Fig. 11.4 Forces structure of the slope stability model

assuming that the pore pressure in the slope is always under the static state condition. Pore water pressure:

$$p = \delta_w g h_w \cos \theta, \tag{11.4}$$

where δ_w is the density of water ($=1,000 \text{ kg/m}^3$) and h_w is the height of the water depth perpendicular to the slope (m). This assumption ascribes greater pressure in the rising process of the subsurface water and smaller pressure in the descending process of the subsurface water.

The shear stress as driving force, defined by the down-slope parallel component of gravity, can be expressed as follows:

$$\tau = \delta_s g h \sin \theta. \tag{11.5}$$

By substituting the formula for shear strength and shear stress, the factor of safety without considering root cohesion and vegetative surcharge equals

$$FS = \frac{c^* + \cos \theta [1 - r_p] \tan \beta}{\sin \theta}; \begin{cases} c^* = \frac{c}{\delta_s g h} \\ r_u = \frac{h_w \delta_w}{h \delta_s} \end{cases} \tag{11.6}$$

The dimensionless form of Eq. (11.6) has been widely used to analyze the stability of shallow soil using digital terrain models (Borga et al. 2002; D'Odorico and Fagherazzi 2003).

In Eq. (11.6) most of the variables could be set up as spatially distributed, but it is assumed that only h_w is time-varying. Water depth, h_w , is determined by the flux of subsurface water flow computed by the hydrological model (see Eq. 11.1). Here the ratio ($\psi = h_w/h$) shows that the relative saturated depth is time-dependent (range numerically between 0.0 and 1.0). Through an inversion of the standard factor of safety (Eq. 11.6), a fixed time-invariant critical relative soil saturation (m^c) (Burton and Bathurst 1998) triggering slope instability (i.e., relative soil saturation that yields $FS = 1.0$) for each grid element can be approximated as

$$m^c = \left(\frac{h_w}{h}\right)^c = \frac{\delta_s}{\delta_w} \left(1 - \frac{\tan \theta}{\tan \beta}\right) + \frac{c}{h \delta_w g \cos \theta \tan \beta} \quad (11.7)$$

The probability of shallow landslide occurrence is calculated by Eq. (11.7) in this study.

$$P(\%) = \frac{1}{n} \sum_{k=1}^n \left(\frac{1}{t} \left(\sum_{f=1}^j FS_f \right) \times 100 \% \right)_k \quad (11.8)$$

P is the probability of shallow landslide occurrence; n is the total year of each period; t is the total time (hours) in a year (365×24); j is the total time in a year with the safety factor of slope, $FS < 1.0$.

A detailed description of the hydrological-geotechnical model used in this study can be found in Apip et al. (2010). We carried out an hourly simulation for 8 years (2000–2008). For each grid we account for the total time in each month where the FS is less than 1.0 (called X). The probability (P) is the ratio between X and total time in a month (called Y). P is multiplied by 100 %. Based on monthly probability information for the period 2000–2008, we made mean monthly shallow landslide probability risk maps and its mean annual probability risk map.

11.3 Application Study in Kyushu Island

11.3.1 Study Site

Kyushu Island, the third largest island of Japan is connected with the mainland and close to Shikoku Island. The Kyushu Mountains are aligned in a north-south direction in the center of Kyushu Island. Kyushu Island has four large calderas called Aso, Aira, Ata, and Kikai calderas. The spatial distribution of total yearly rainfall in Kyushu Island is quite high compared to other regions in Japan. The

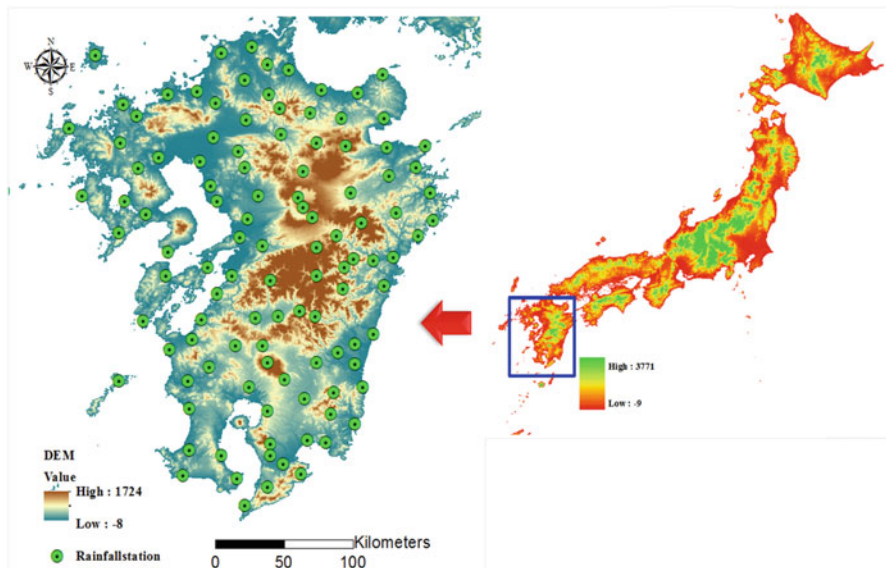


Fig. 11.5 Location of AmeDAS rainfall stations and digital elevation model at Kyushu Island

Digital Elevation Model and the 120 selected AmeDAS rainfall stations are presented in Fig. 11.5a).

11.3.2 Data

We collected the Digital Elevation Model (DEM) (Fig. 11.5), land use, soil type, observed AmeDAS rainfall, observed discharge and observed landslides distribution map. The original DEM and 100 m mesh land use data were obtained from the Ministry of Land, Infrastructure, Transport and Tourism (MLIT), Japan. The observed rainfall data from 2000 to 2008 of 120 selected AmeDAS rainfall stations is from the Japan Meteorology Agency (JMA). The observed landslide location map was downloaded from the website of Landslides Distribution Maps database published by the National Research Institute for Earth Science and Disaster Prevention (NIED).

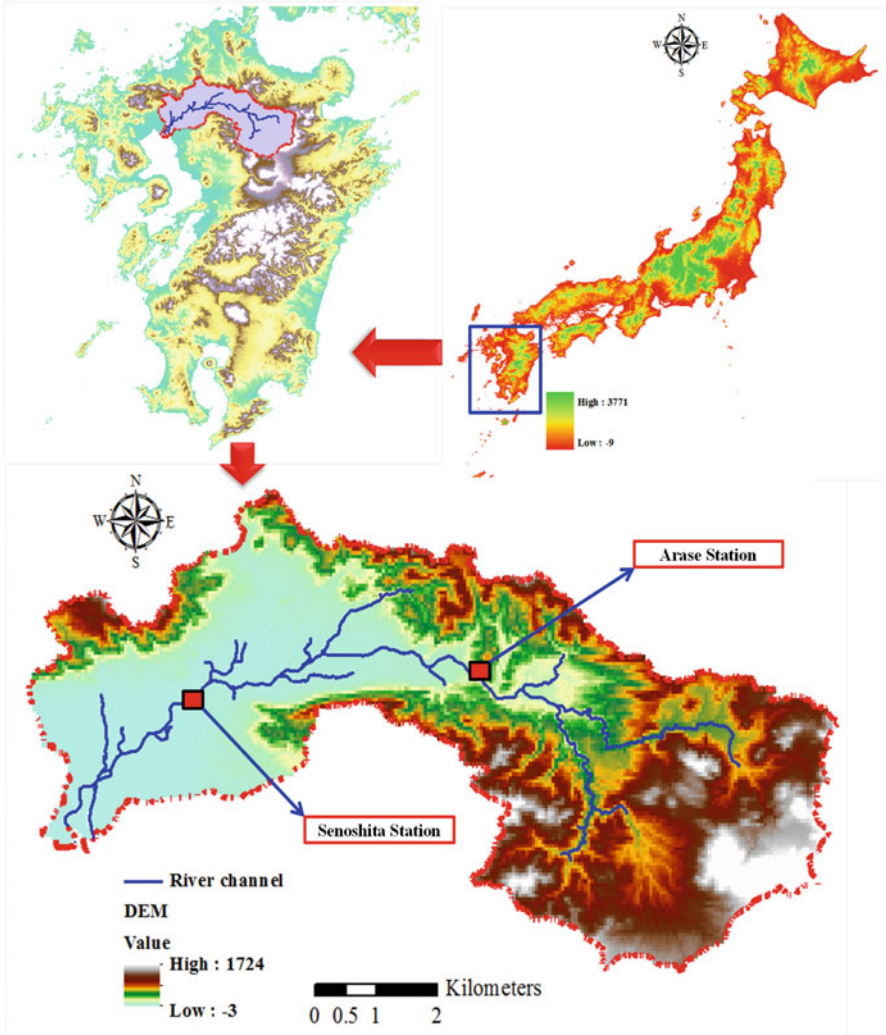


Fig. 11.6 Location of Chikugo river with the observed discharge stations, river channel and DEM

11.4 Results and Discussion

11.4.1 Hydrological Model Performance

Hydrologic model performance was evaluated by modelling hydrological response at the Senoshita and Arase Stations of the Chikugo River (Fig. 11.6). The elevation of Chikugo River basin ranges from -3 m to $1,724$ m with a main stream channel 143 m long with 70% forest coverage. Calibration results at Arase Station (Fig.

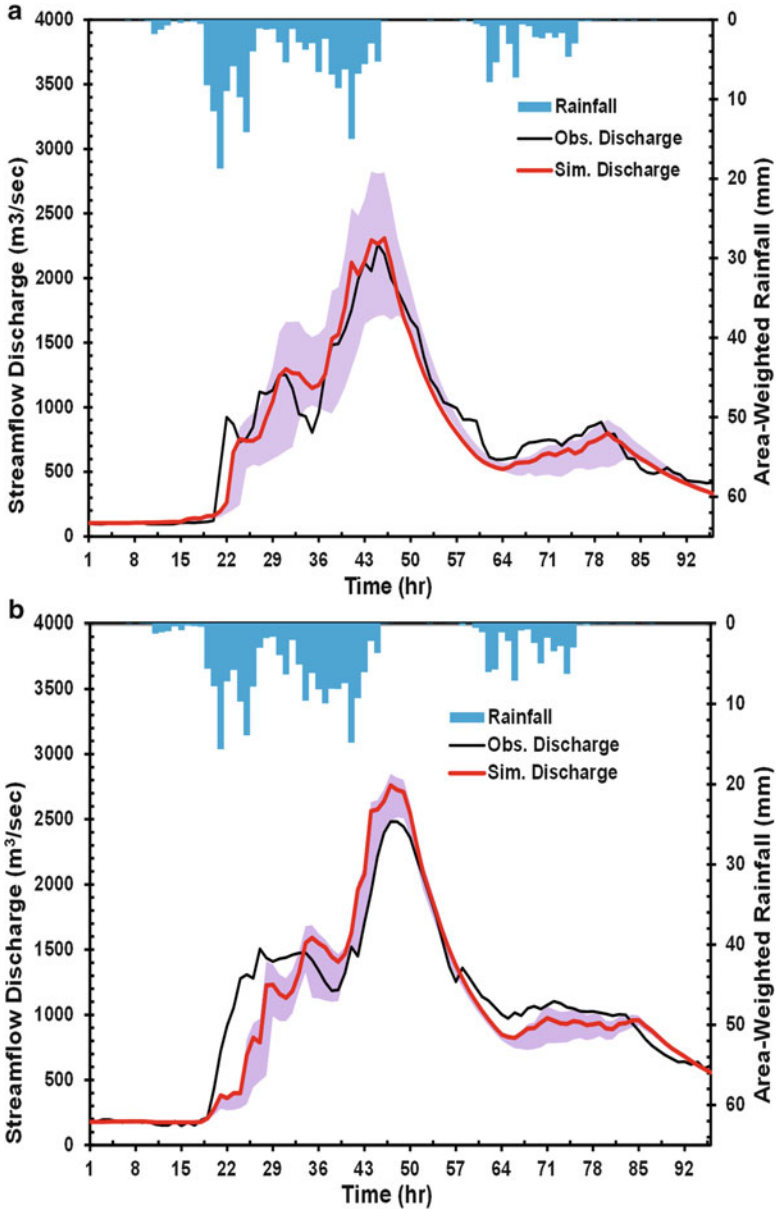


Fig. 11.7 Hydrological performance of hourly discharge at (a) Arase Station and (b) Senoshita Station

11.7a) show that simulated discharge matches observed discharge very well with a Nash-Sutcliffe (NS) coefficient of 0.93. Simulated peak discharge is similar to observed peak discharge. The overall trend in simulated discharge also closely

Table 11.1 Hydrological model calibrated parameter value of each sub-basin

Model parameter	Description	Arase outlet	Senoshita outlet
n of forest ($m^{-1/3} s$)	Manning's roughness coefficient	0.79197	0.43245
n of cropland ($m^{-1/3} s$)	Manning's roughness coefficient	0.26058	0.39511
n of paddy ($m^{-1/3} s$)	Manning's roughness coefficient	0.26458	0.21702
n of urban ($m^{-1/3} s$)	Manning's roughness coefficient	0.18070	0.15405
n of river ($m^{-1/3} s$)	Manning's roughness coefficient	0.00957	0.00714
D (mm)	Total soil depth	1602.65	2878.41
k_a ($mm s^{-1}$)	Hydraulic conductivity of saturated soil layer	0.00152	0.00159
β	Exponent constant of unsaturated flow	6.61	5.40

matches observed discharge. Simulated discharge at Senoshita Station is very similar to observed discharge with a Nash-Sutcliffe (NS) coefficient of 0.86 (Fig. 11.7b). However, simulation results overestimate observed discharge. Simulated discharge from the 22nd hour to the 36th hour and from the 57th hour to 82nd hour underestimate observed discharge. The calibrated parameters are shown in Table 11.1.

11.4.2 Performance of the Slope Stability Model

The potential for shallow landslides was defined only for stable/unstable grids, where the critical relative soil saturated depth values ranged between 0.0 and 1.0. Comparison of observed landslides with the slope stability model predictions provides an assessment of geotechnical parameters calibration. The comparison was obtained by mapping predicted critical relative saturated depth on a map of observed landslide locations and comparing the proportion of catchment area placed in the various critical relative saturated depth ranges (the zone of potential instability) with the corresponding fraction of the observed landslide grids. The soil type data is taken into account for calculating the shallow landslides in this study. The hydro-geotechnical model for shallow landslide prediction was simply calibrated by comparing the spatial pattern of shallow landslides between these two maps. This model is not intended to simulate the size of the landslide and its eroded soil distribution.

Figure 11.8 shows the critical relative saturation level map. Red color with a value equal or less than 0 represents the area of highest landslide potential. The area with the critical relative saturation level of 0.8 is the most stable area where shallow landslides are rare. The area around the Aso Mountains presents high potential for shallow landslide occurrence. The central area of Kyushu Island shows high potential for shallow landslide occurrence. Elevation maps indicate that the Aso Mountain area has steep slopes. The main reason of the high potential

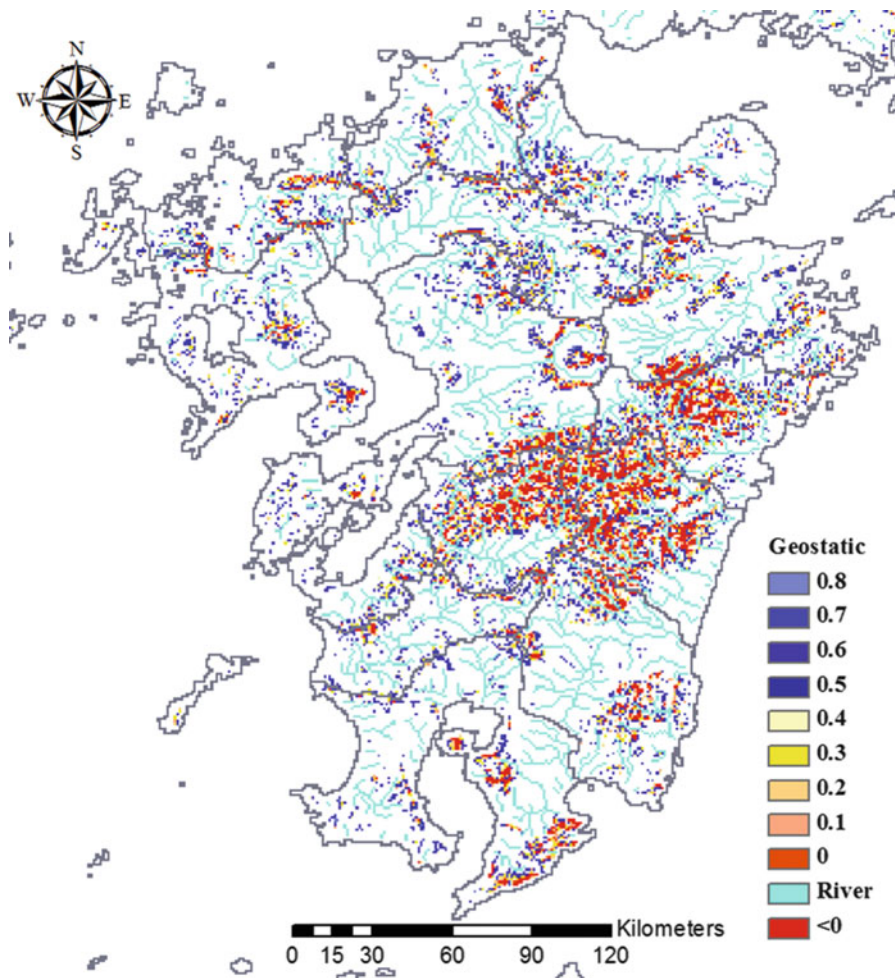


Fig. 11.8 Spatial critical relative saturation level map (Luo et al. 2014b)

occurrences level in the central area of Kyushu Island may be due to the extreme rainfall events and the steep slope. The highest potential area of the shallow landslide occurrences is quite fixed with the observed landslide locations map (Fig. 11.9). However, this observed location map includes all the types of landslides.

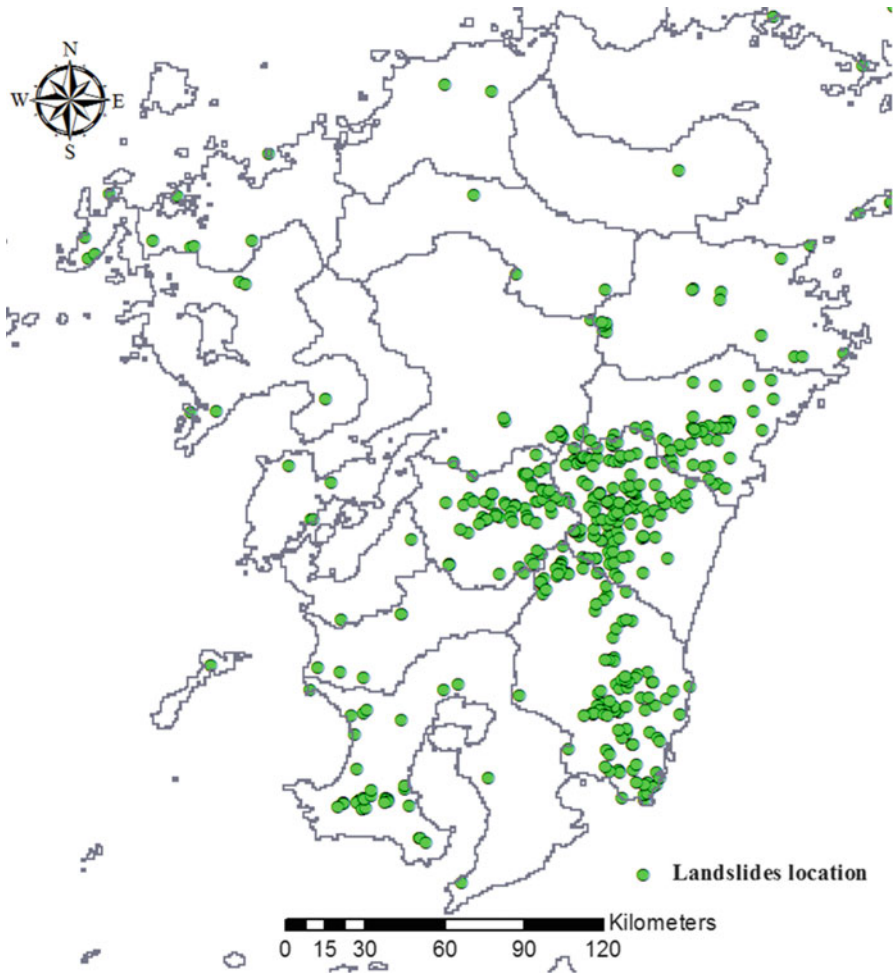


Fig. 11.9 Observed landslide Locations map (the *green point* is the detail locations of landslides) (NIED 2013)

11.4.3 Analysis Result of Mean Shallow Landslide Risk

Based on the simulation result from the hydro-geotechnical model, the monthly shallow landslide risk has been calculated as a percentage. The different risk levels have been divided into five levels which are 0–10 %, 10–30 %, 30–85 %, 85–98 %, 98–100 % levels (Table 11.2). Stable conditions are reflected by a score of 0–10 %. The detailed description of the other five risk levels is shown in Table 11.2. Figure 11.10 shows the mean shallow landslide risk, which is calculated based on the monthly shallow landslide information and presents a spatial distribution of the shallow landslide risk. Figure 11.10 shows that landslide risk is principally located

Table 11.2 Shallow landslide potential risk levels

Percentage (%)	Risk levels
0–10	Stable
10–30	Low potential risk
30–85	Middle potential risk
85–98	High potential risk
98–100	Highest potential risk

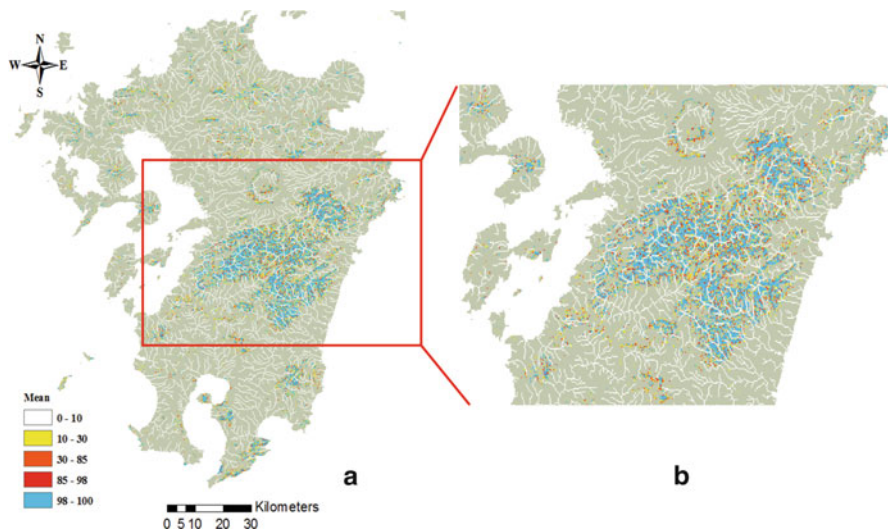


Fig. 11.10 Mean risk of the shallow landslides (2000–2008): (a) Mean risk of whole Kyushu Island, (b) Mean risk of the center part in Kyushu Island

in the area of Aso Mountain and the central part of Kyushu Island. Aso Mountain is an active volcano with steep slopes. Volcano activity may be considered one of the major reasons for frequent shallow landslides in this area. The high potential risk in central Kyushu Island may be related to the steep slope of the mountain area and the extreme rainfall events such as typhoons which often pass through central Kyushu Island.

11.5 Discussion

The mean monthly shallow landslide risk map can be used to identify where the most dangerous area of shallow landslides is and inform local residents of areas to avoid during the extreme rainfall events. The hydrogeotechnical model is a grid-cell distributed model which has two main sub models; namely hydrological sub model and infinite slope instability model. The hydrological sub model considers

two soil layers namely capillary and non-capillary layers. The water movement in the soil layers and land surface (overland flow) is accounted for numerically using a kinematic wave approach. This model is very good for use in the hill slope and humid areas like Japan. This study reflects advances on previous studies which for the most part use a simple hydrological model and assume a steady state condition in simulating hydrological responses and shallow landslide risk.

The limitation of this study is lack of a detailed deposition map for shallow landslides. Using only the deposition map for all landslide types makes it difficult to identify shallow landslides, the most common form of landslide in Japan. Our hydro-geotechnical model was not constructed for this purpose. The resolution of DEM is sufficient for shallow landslide risk analysis on a large scale, because we are not trying to identify the detail basin scale shallow landslide events. In future 100 m mesh land use data will be used as input data. Land use type is also an important driver of shallow landslide risk.

11.6 Conclusion

We use GIS tools and hydrological modeling linked with a slope stability model to estimate shallow landslide risk levels. A detailed introduction on the framework of the GIS process and hydrological modeling for large-scale shallow landslide risk analysis is presented. Model performance was evaluated with a NSE of 0.93 at the Arase station and 0.86 at the Senoshita Stations of Chikugo River compared with the observed discharge. We calculated the shallow landslide risk map in Kyushu Island, and divided the risk into five levels for better understanding. The central part of Kyushu Island presented the highest risk levels. In order to capture the intricacy of many related hydro-geotechnical processes combined hydro-geotechnical modeling for analysis of large-scale shallow landslide risk. This combined modeling system can be applied in the other large scale study areas for shallow landslide risk simulation. The results of this study can provide scientific information for future shallow landslide management to reduce economic loss and contribute to developing sustainable and survivable societies.

Acknowledgments The authors thanks the supports from the Japan Institute of Country-ology and Engineering (JICE) Grant Number 13003, Water and Urban Initiative Project at The United Nations University Institute for the Advanced Study of Sustainability (UNU-IAS), the Kyoto University Inter-Graduate School Program for Sustainable Development and Survivable Societies (GSS), MEXT Program for Leading Graduate Schools 2011–2018, Designing Local Frameworks for Integrated Water Resources Management at the Research Institute for Humanity and Nature (RIHN), Japan Society for the Promotion of Science (JSPS) Grant-in-Aid for Scientific Research (A) Grant Number 24248041.

References

- Acharya G, De Smedt F, Long NT (2006) Assessing landslide hazard in GIS: a case study from Rasuwa, Nepal. *Bull Eng Geol Environ* 65(1):99–107
- Apip, Takara K, Yamashiki Y, Sassa K, Ibrahim AB, Fukuoka H (2010) A distributed hydrological–geotechnical model using satellite-derived rainfall estimates for shallow landslide prediction system at a catchment scale. *Landslides* 7(3):237–258
- Apip ST, Tachikawa Y, Takara K (2012) Spatial lumping of a distributed rainfall sediment runoff model and effective lumping scale. *Hydrol Process* 26(6):855–871
- Arnone E, Noto LV, Lepore C, Bras RL (2011) Physically-based and distributed approach to analyze rainfall-triggered landslides at watershed scale. *Geomorphology* 133(3–4):121–131
- Bathurst JC, Bovolo CI, Cisneros F (2010) Modelling the effect of forest cover on shallow landslides at the river basin scale. *Ecol Eng* 36(3):317–327
- Borga M, Dalla Fontana G, Da Ros D, Marchi L (1998) Shallow landslide hazard assessment using a physically based model and digital elevation data. *Environ Geol* 35(2–3):81–88
- Borga M, Fontana GD, Gregoretti C, Marchi L (2002) Assessment of shallow landsliding by using a physically based of hillslope stability. *Hydrol Process* 16:2833–2851
- Burton A, Bathurst JC (1998) Physically based modelling of shallow landslide sediment yield at a catchment scale. *Environ Geol* 35(2–3):89–99
- Chau KT, Sze YL, Fung MK, Wong WY, Fong EL, Chan LCP (2004) Landslide hazard analysis for Hong Kong using landslide inventory and GIS. *Comput Geosci* 30(4):429–443
- CEAP (2008) Conservation effects assessment project. USDA Natural Resources Conservation Service, Washington, DC. Available at: <http://www.nrcs.usda.gov/wps/portal/nrcs/main/national/technical/nra/ceap/>. Accessed 22 Apr 2015
- D’Odorico P, Fagherazzi S (2003) A probabilistic model of rainfall-triggered shallow landslides in hollows: a long-term analysis. *Water Resour Res* 39(9):1262
- Duan W, He B, Takara K, Luo P, Nover D, Yamashiki Y, Huang W (2014) Anomalous atmospheric events leading to Kyushu’s flash floods, July 11–14, 2012. *Nat Hazards* 73(3):1255–1267
- Gassman PW, Reyes MR, Green CH, Arnold JG (2007) The soil and water assessment tool: historical development, applications, and future research directions. *Trans ASABE* 50(4):1211–1250
- Godt JW, Baum RL, Savage WZ, Salciarini D, Schulz WH, Harp EI (2008) Transient deterministic shallow landslide modeling: requirements for susceptibility and hazard assessments in a GIS framework. *Eng Geol* 102(3–4):214–226
- Kojima T, Takara K (2003) Grid-cell based distributed flood-runoff model and its performance, weather radar information and distributed hydrological modeling. *IAHS Publ* 282:234–240
- Lan HX, Zhou CH, Wang LJ, Zhang HY, Li RH (2004) Landslide hazard spatial analysis and prediction using GIS in the Xiaojiang watershed, Yunnan, China. *Eng Geol* 76(1–2):109–128
- Lan HX, Lee CF, Zhou CH, Martin CD (2005) Dynamic characteristics analysis of shallow landslides in response to rainfall event using GIS. *Environ Geol* 47(2):254–267
- Luo P, Takara K, He B, Cao W, Yamashiki Y, Nover D (2012) Calibration and uncertainty analysis of SWAT model in a Japanese river catchment. *J Jpn Soc Civ Eng Ser B1 (Hydraul Eng)* 67(4):I_61–I_66. doi:10.2208/jscejhe.67.I_61
- Luo P, Takara K, Apip, He B, Nover D (2014a) Palaeoflood simulation of the Kamo River basin using a grid-cell distributed rainfall run-off model. *J Flood Risk Manag* 7(2):182–192
- Luo P, Takara K, Apip, He B, Duan W, Hu M (2014b) Landslide science for a safer geo-environment, Chapter 62, “Assessment of Shallow Landslide Using the Distributed

- Hydrological–Geotechnical Model in a Large Scale”, Springer, ISBN 978-3-319-04998-4, doi:[10.1007/978-3-319-04999-1_62](https://doi.org/10.1007/978-3-319-04999-1_62), pp 443–450
- Sayama T, Takara K, Tachikawa Y (2003) Reliability evaluation of rainfall-sediment- runoff models. IAHS Publ 279:131–141
- Schuol J, Abbaspour KC, Srinivasan R et al (2008) Estimation of freshwater availability in the West African sub-continent using the SWAT hydrologic model. J Hydrol 352:30–49
- Zhang X, Srinivasan R, Debele B et al (2008) Runoff simulation of the headwaters of the yellow river using the SWAT model with three snowmelt algorithms. JAWRA J Am Water Resour Assoc 44:48–61

Chapter 12

An Integrated Model for Assessing Carbon Dioxide Emissions Considering Climate Change Mitigation and Flood Risk Adaptation Interaction

Kumiko Nakamichi, Yoshiki Yamagata, and Hajime Seya

Abstract Planning for climate change mitigation/adaptation for enhancing urban resilience against natural disaster risks is an important issue in Japan. For such planning to be effective, studies suggest that it is important to consider the interaction (co-benefits and trade-offs) between adaptation and mitigation measures. For example, climate change mitigation and adaptation measures could be compatible if our government got people to move from flood prone areas with considering urban structure (e.g., compact city). In order to simulate the effectiveness of such interactions, we propose an integrated assessment model for carbon dioxide (CO₂) emissions under several urban land-use scenarios considering (i) urban form (dispersion/compact city) (ii) urban resilience (adaptation to flood risks) and (iii) diffusion of electric vehicles (EVs) and photovoltaic (PV) panels at a local town level in Tokyo. The developed model can be used to evaluate the co-benefits of both mitigation and adaptation measures from the viewpoint of CO₂ emissions. Indirect emissions based on households' expenditure are also estimated in addition to direct

K. Nakamichi (✉)

Center for Global Environmental Research (CGER), National Institute for Environmental Studies (NIES), 16-2 Onogawa, Tsukuba City, Ibaraki 305-8506, Japan

Graduate School of Science and Engineering, Tokyo Institute of Technology, 2-12-1 O-Okayama, Meguro-ku, Tokyo 125-8550, Japan
e-mail: nakamichi.kumiko@nies.go.jp

Y. Yamagata

Center for Global Environmental Research (CGER), National Institute for Environmental Studies (NIES), 16-2 Onogawa, Tsukuba City, Ibaraki 305-8506, Japan
e-mail: yamagata@nies.go.jp

H. Seya

Center for Global Environmental Research (CGER), National Institute for Environmental Studies (NIES), 16-2 Onogawa, Tsukuba City, Ibaraki 305-8506, Japan

Graduate School for International Development and Cooperation, Hiroshima University, 1-5-1Kagamiyama, Higashi-hiroshima, Hiroshima 739-8529, Japan
e-mail: hseya@hiroshima-u.ac.jp

© Springer Science+Business Media Dordrecht 2015

J. Li, X. Yang (eds.), *Monitoring and Modeling of Global Changes: A Geomatics Perspective*, Springer Remote Sensing/Photogrammetry, DOI 10.1007/978-94-017-9813-6_12

241

emissions. The obtained results suggest that climate change mitigation and adaptation can generate a synergistic effect from the viewpoint of CO₂ emissions.

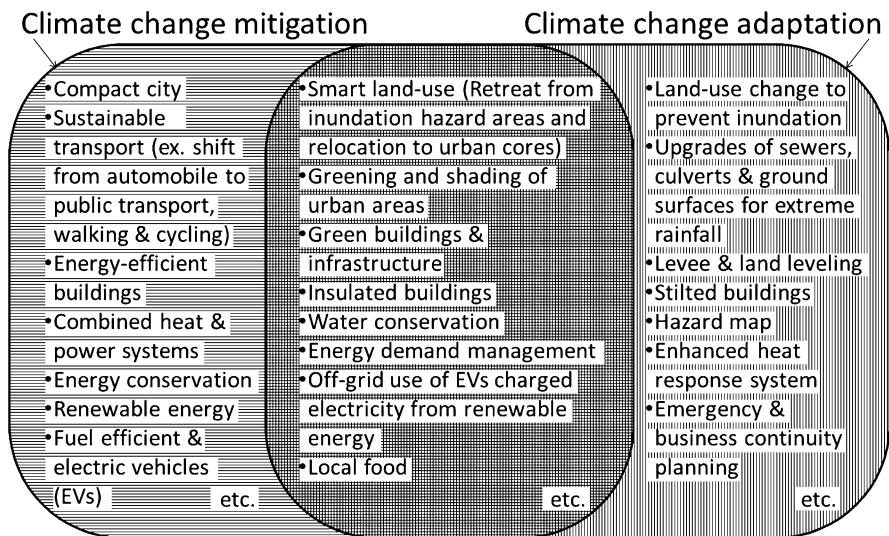
Keywords Climate change mitigation and adaptation • Direct and indirect CO₂ emissions • Land-use scenario • Electric vehicles • Photovoltaic panels

12.1 Introduction

12.1.1 Climate Change Mitigation and Adaptation Options

Scientific forecasts predict that climate change will raise the risk of climate disasters in the future. The 4th Assessment Report of Intergovernmental Panel on Climate Change (IPCC 2007) emphasizes the importance of both climate change mitigation and adaptation strategies in order to deal with the challenges of climate change. Climate change mitigation options include not only a direct reduction of greenhouse gases (GHGs) but also an enhancement of the carbon sinks of GHGs. Climate change adaptation options involve adjustments in natural or human systems in order to minimize or prevent the harmful impacts produced by climate change. Figure 12.1, adapted from Penney (2008), illustrates the overlap between climate change mitigation and adaptation in the urban context.

The 5th Assessment Report (AR5) of IPCC (2014) stated that many global risks of climate change are concentrated in urban areas. Climate change will be gradual, but extreme weather events will increase in intensity. Vulnerability created by floods is



Adopted from Penney (2008)

Fig. 12.1 Climate change mitigation and adaptation options in the urban context

especially important to consider for megacities in which many assets are located. So, we need to address climate change mitigation and adaptation at the same time. The AR5 (IPCC 2014) also points out that significant co-benefits, synergies, and trade-offs exist between mitigation and adaptation and among different adaptation responses. Increasing efforts to mitigate and adapt to climate change imply an increasing complexity of interactions, particularly at the intersections among water, energy, land use, and biodiversity, but tools to understand and manage these interactions remain limited. Under the present circumstances, there are not enough prospects for efficient GHG mitigation measures on the global scale. We must adapt to the impacts of climate change in such a case where global mean temperatures could rise about 4 °C in the present century compared with past preindustrial averages.

Current conventional urban policy has difficulty in coping with complex disasters (e.g. extreme weather events such as local heavy rainfall, sea level rise and tsunami caused by typhoons and so on). After the Great East Japan Earthquake, the concept of urban resilience has been discussed more widely in Japan. Resilient cities cannot be realized without considering energy and natural disaster risks. In case of sea-level change, the eco-system is also affected, and managed retreat can be effective as one way of climate change adaptation (Gilman et al. 2008). The risk characteristics of the frequency and intensity of flood disasters and the vulnerability of social systems including land-use change need to be analyzed. Although almost all local governments are pursuing measures for climate change mitigation, they have not focused on climate change adaptation as a priority policy yet. There is a need to review the interaction between climate change mitigation and adaptation measures, especially the co-benefits and trade-offs.

12.1.2 Land Use Approach for Climate Change Mitigation/Adaptation

In the field of urban planning, climate change adaptation is already addressed in some projects such as the Auckland Sustainability Framework and Suburban Neighborhood Adaptation to Changing Climate (SNACC). In this chapter, we focus on the adaptation to flood risk, especially considering land-use change. It is effective to reduce the damage by land-use regulations which distinguish between areas with disaster prevention measures and areas with little infrastructure and buildings. For example, land use is regulated depending on the degree of inundation height. Such regulation is introduced in Germany, Nicaragua, Ecuador and Czech. In Nagoya, Japan, buildings are controlled in the flood-hazard areas. However, the combination of other land-use regulations such as compact city is not considered. OECD (2012) defined the key characteristics of a compact city as (i) dense and proximate development patterns, (ii) urban areas linked by transport systems and (iii) accessibility to local services and jobs. It can contribute to achieving urban sustainability including environmental, social and economic benefits as well as a reduction of CO₂ emissions from automobiles due to shorter intra-urban distances

and a shift to public transportation. As flood disaster prevention, it would be easiest and most effective if people could retreat from flood-hazard areas. In addition, if retreated people moved to the city center and located around train stations, GHG emissions could also be reduced. In this case, climate change mitigation and adaptation measures are compatible.

In fact, the automobile fuel consumption under land-use scenarios considering flood disaster prevention and compact city design in local cities has been quantitatively evaluated (Taniguchi et al. 2005). Nagao et al. (2012) considered safety against disasters as one of the quality of life (QOL) indexes, and selected retreat and cohesion areas in a local city. However, the Tokyo Metropolitan Area, which is still by far the largest megacity in the world, is extremely vulnerable against climate risks, especially flood risk, because a large part of the assets is concentrating near the bay area. On the other hand, researchers are projecting the increase of flood risks in the Tokyo Metropolitan Area, due to climate change as well as tsunamis from future big earthquakes. We need to consider appropriate land uses that are more resilient against climate risks in megacities (Yamagata et al. 2013).

As for the carbon dioxide (CO₂) emission reduction potentials for the land-use scenarios, especially compact city, many studies have indicated that cities with low residential density rely on automobile transportation. Therefore the reduction of CO₂ emissions caused by transportation use would be attained by changing the urban layout to a more compact one, which would lead to the increase of the use of public transportation and the reduction of trip length by car (e.g. Newman and Kenworthy 1999; Hayashi et al. 1995; Jenks et al. 1996; Naess 1996; Roo and Miller 2000; Williams et al. 2000; Taniguchi et al. 2005, 2008; Nakamichi et al. 2007).

Also, it is necessary to estimate indirect emissions as well as direct emissions to clarify the liability of daily energy consumption-based CO₂ emissions. Recently, many studies have started considering also the indirect emissions (Abe et al. 2002; Nakamura and Otoma 2004; Yamashita et al. 2007; Dhakal 2009; Kennedy et al. 2010; Xi et al. 2011; Shigeto et al. 2012). Hence, in this paper, we also estimated the indirect emissions by allocating the emissions to the regions where the energy was consumed, using the data on the expenditure for households' daily living items.

12.1.3 Technological Approach for Climate Change Mitigation/Adaptation

In addition to the above mentioned mitigation measures with compact city scenarios, we also need to consider those with renewable energy use. Since the 2011 Great East Japan Earthquake, the Japanese Government has gradually changed its energy policies toward distributed renewable energy generation. As a part of such efforts, the Japanese Diet has approved the "Act on the Purchase of Renewable Energy Sourced Electricity by Electric Utilities (Act)", which is a feed-in tariff regime for renewable energy, effective from 1 July 2012. Under the Act, electric utility

operators are obligated to purchase electricity generated from renewable energy including solar photovoltaic (PV) power from suppliers for fixed feed-in tariff prices. The prices are higher than normal contractual prices and are applicable for a fixed duration of 10 years in case of residential PV power.

This regime is widely expected to spur the introduction of PV panels and electric vehicles (EVs). If EVs were introduced in sets with PVs, they would be useful for zero-emission power generation. They would also serve as a power storage facility in the form of mobile batteries in the case of a blackout since they are disconnected by the loss of AC power (Yamagata and Seya 2013). It means that the introduction of PVs and EVs can contribute not only to climate change mitigation but also to resilience from the energy-use perspective if they will be used as an off-grid power source.

In the Yamagata and Seya (2013) scenarios, it was expected that EVs and PV panels will be widely diffused in 2050. This paper considered the large-scale introduction of EVs and PV panels on the roofs of detached houses as a mitigation measure. Taniguchi and Ochiai (2011) evaluated the suitability of smart grids with an emphasis on the characteristics of each block and the behavior of residents and households on a residential block scale, on the premise of existing technological level. Taniguchi and Ochiai (2012) analyzed the influence of future technological innovation on the suitability of smart grids on a block scale. Yokoi et al. (2010) estimated the CO₂ reduction potential of smart grids considering plans of block renewal on a regional scale. It is important to evaluate the CO₂ reduction potential combining both the large-scale introduction of smart grids and land-use change, namely considering not only climate change mitigation but also adaptation.

12.1.4 Our Approach for Integrated CO₂ Emission Assessment Model

In this chapter, we introduce our integrated model for the assessment of indirect and direct CO₂ emissions and some results in terms of the interaction between climate change mitigation and flood risk adaptation. The objective of this study is to develop an integrated evaluation system for direct/indirect CO₂ emissions under several urban land-use scenarios (Yamagata and Seya 2013; Yamagata et al. 2013) which consider (i) land-use change (a compact city and retreat from flood-hazard areas) and (ii) introduction of EVs and PVs by using GIS, in order to assess the co-benefits or trade-offs of mitigation and adaptation. This study integrates an estimation model for direct/indirect CO₂ emissions with spatially explicit land-use scenarios at a local town level. In this study, the Tokyo Metropolitan Area, which is still by far the largest megacity in the world, was selected as a case study for the application of the developed evaluation system.

12.2 Data and Methodologies

12.2.1 *Estimation Model for Direct/Indirect CO₂ Emissions*

12.2.1.1 Definition of Direct and Indirect CO₂ Emissions

CO₂ emissions fall into two types, direct emissions and indirect emissions. Easier to measure are the direct emissions that we are responsible for. These include the amount of gas and kerosene we use in our houses and the amount of petrol or diesel we burn in our cars. Getting the CO₂ figures right for gas, petrol and diesel is quite straightforward, because a standard amount is released when each fuel is burnt. CO₂ in the electricity production process is emitted at power plants. Thus, it is defined as the direct emissions of the industrial sector. In contrast, the indirect emissions for households are defined as the CO₂ emissions allocated to the regions where the energy is consumed according to the expenditure of money on the items for households' daily life. In this study, the boundary of CO₂ emissions was extended to fuel production for household fuel use, agriculture for food production, and other production for consumption items including energy use for both production and transportation processes. The electricity, gas and kerosene used in houses were allocated as direct emissions of households. The petrol or diesel consumption was allocated to car registration place as direct emissions. It is useful to make a clear distinction among the CO₂ emissions caused by household consumption and to formulate an effective policy for the reduction of the total GHG emissions.

We defined the direct and indirect CO₂ emissions as below.

1. Direct emissions: CO₂ emissions from different CO₂ emitting regions of each sector,
2. Indirect emissions: CO₂ emissions from the regions where the commodities are consumed according to expenditure of money on the items for households' daily life.

12.2.1.2 Data

With regard to the emission intensity (emission factor) data, we employed Embodied Energy and Emission Intensity Data (3EID). These data contain embodied environmental burden intensity data calculated using Japanese input-output tables. The Japanese input-output tables consist of approximately 400 commodity sectors. They represent the economic relationships among these sectors based on annual transactions. 3EID includes data on direct and indirect energy consumption or CO₂ emissions (i.e. environmental burden) from unit production activity (equivalent to 1 million yen). In this study, we employed the CO₂ emission intensity data estimated from consumer prices excluding imports. The emission intensity by prefecture and household type was calculated by Tanaka et al. (2008)'s method mentioned above.

For calculating the annual expenditure on each item, we employed the Household Expenditure Survey (HES). This is a survey conducted to investigate the actual state of household incomes and expenditures in terms of expenditure and consumption. We used the data collected in 2005 as the base year. This survey is performed every month for 981 consumption items for 8,000 households in 168 villages, towns and cities all over Japan by the Statistics Bureau, Ministry of Internal Affairs and Communications. The results of the survey are announced monthly and yearly for cities, regions, types of households (i.e. total number of households, households of more than two, single person households). In order to estimate CO₂ emissions from household consumption within a zone, we correlated the items of HES to 3EID. For a detailed specification, see Table 12.1.

Table 12.1 Emission groups of items

Emission group	Number of items
1. Food	
Cereals	6
Fish and shellfish	5
Meat	6
Dairy products and eggs	3
Vegetables and seaweeds	9
Fruits	1
Oils, fats and seasonings	2
Cakes and candies	1
Cooked food	13
Beverages	3
Alcoholic drinks	4
Eating out	12
Providing meals	1
2. Housing	2
3. Fuel, light and water charges	6
Electricity	
City gas	
LP gas	
Kerosene	
Water and sewerage charges	
Others	
4. Furniture and household utensils	31
5. Clothes and footwear	8
6. Medical care	8
7. Transportation and communication	
Public transportation	10
Private transportation (Gasoline)	13
Communication	6
8. Education	12
9. Reading and recreation	47
10. Others	27

12.2.1.3 Estimation of Direct/Indirect CO₂ Emissions

For the evaluation of land-use scenarios, we estimated the direct and indirect emissions on the neighborhood scale. Because urban improvement projects are implemented on such micro zone scales, the evaluation of the effect on CO₂ emissions should be localized. In order to accurately estimate the lifecycle CO₂ (LC-CO₂) related to household consumption, the emission intensity of each consumer goods (expenditure item), such as gasoline, food, etc. must be estimated. The categories of the items used in this study are shown in Table 12.1. Because emission intensity differs by region and by consumer (household) type, it is important to consider its heterogeneity. We employed the algorithm proposed by Tanaka et al. (2008), who had employed statistical methods (Bayesian estimation method and Genetic Algorithm) for estimating the emission intensity of each expenditure item by prefecture by seven household types (Table 12.2). The annual CO₂ emissions (kg-CO₂/year) in each zone (micro district on the neighborhood scale) *i* was calculated in the following manner:

$$CE_i = \sum_j H_{ij} \left[\sum_k E_{ijk} (ic_{ik} + dc_{ik}) \right] \tag{12.1}$$

where,

CE_i: annual CO₂ emissions in each zone *i* (kg-CO₂/year)

H_{ij}: the number of household type *j* in zone *i*

E_{ijk}: annual expenditure on item *k* by household type *j* in zone *i* (yen/household/year)

ic_{ik}: emission intensity of indirect CO₂ emissions for item *k* (kg-CO₂/yen)

dc_{ik}: emission intensity of direct CO₂ emissions for item *k* (Gas, kerosene and gasoline) (kg-CO₂/yen)

The estimated CO₂ emissions of each household were allocated on the basis of the number of households in each of the seven household types in each micro zone. The number of households was taken from the 2005 census. Table 12.3 shows the estimated average CO₂ emissions per household of Yokohama City in 2005 as an example.

Table 12.2 Seven household types

Household type
a. One-person households (65 years of age or over)
b. One-person households (under 65 years of age)
c. Married couple only (either of them 65 years of age or over)
d. Married couple only (both under 65 years of age)
e. Married couple with child(ren)
f. Single parent and child(ren)
g. Other types

Table 12.3 Average CO₂ emissions per household (Yokohama)

Emission group	Indirect CO ₂ emissions (kgCO ₂ /year)	Direct CO ₂ emissions (kgCO ₂ /year)
1. Food	1,530	0
2. Housing	154	0
3. Fuel, light and water charges	3,719	1,304
Electricity	(2,242)	(0)
City gas	(866)	(795)
LP gas	(420)	(383)
Kerosene	(136)	(126)
Water and sewerage charges	(55)	(0)
Others	(0)	(0)
4. Furniture and household utensils	187	0
5. Clothes and footwear	349	0
6. Medical care	256	0
7. Transportation and communication	1,459	484
(Gasoline)	(559)	(484)
8. Education	136	0
9. Reading and recreation	655	0
10. Others	290	0
Total	8,735	1,788

12.2.2 Spatially Explicit Land Use Model

So far, many integrated land-use and transportation models have been applied to real urban policy planning and the creation of land-use change scenarios. The present study employed a multi-market static economic equilibrium model based on urban economic theory (e.g., Ueda et al. 2013). In this study, we developed a spatially explicit land-use model which was created based on micro district level zones.

The structure of our model is given in Fig. 12.2. The major assumptions of this model are as follows: (1) There exists a spatial economy whose coverage is divided into zones i . (2) The total number of each household type j , say H_j in the metropolitan area is given (closed city). (3) The society is composed of three types of agents: households, developers, and absentee landlords. The behavior of each agent is formulated on the basis of microeconomic principles, that is, utility maximization by households and profit maximization by developers and absentee landlords. (4) Households belonging to the same type j have identical preferences. The households choose their locations in accordance with maximized utility. (5) There is one residential land market and residential (building) floor market in each zone. These markets reach equilibrium simultaneously. The model can output

• Supply-demand balance

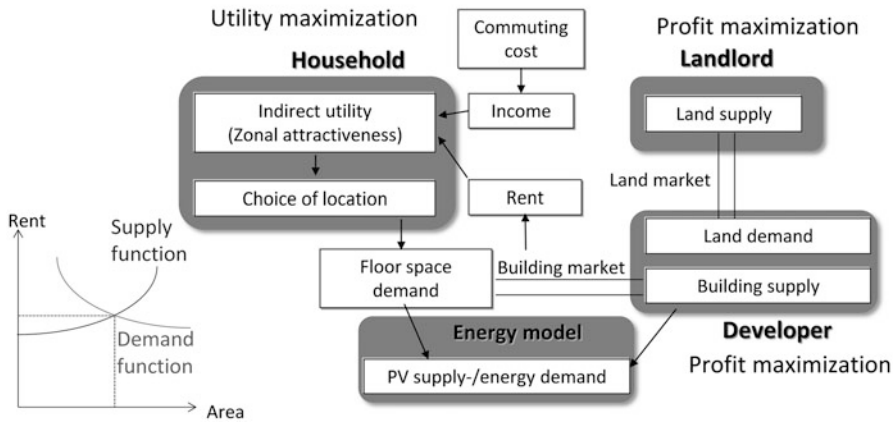


Fig. 12.2 Structure of our spatially explicit land-use model

a set of variables which describe a real urban economy such as distribution of locators (households), distribution of land rent and building floor rent, land and building floor area, etc. The detailed mathematical description of our model and the input data is given in Yamagata and Seya (2013) and Yamagata et al. (2013). The ratio of detached houses was estimated using the projected population density using the relationship shown in Fig. 12.3.

12.2.3 Integrated CO₂ Emission Evaluation System

The structure of our integrated CO₂ emission evaluation system is seen in Fig. 12.4. We can use HES data not only for the estimation of CO₂ emissions but also for the estimation of energy demand. Energy demand change can be projected even if EVs and PVs will be introduced. The installable area of roofs depends on the supply-demand balance of buildings which is provided by the land-use model. The details are given in Nakamichi et al. (2013b).

As to EVs, the CO₂ emission rate could be estimated as shown in Table 12.4. In order to consider the change of percentage of the electricity supply source (from nuclear to thermal) after the Great East Japan Earthquake, we calculated the CO₂ emission factor from April 2011 to March 2012 to be 0.50 (kgCO₂/kWh) using the reports of the federation of electric power companies of Japan.

As to PVs, we assumed that PVs were installed on the roofs of all detached houses in the study area. Following Yokoi et al. (2010), the hourly average of unit electric supply by PVs (kWh/h) can be estimated as

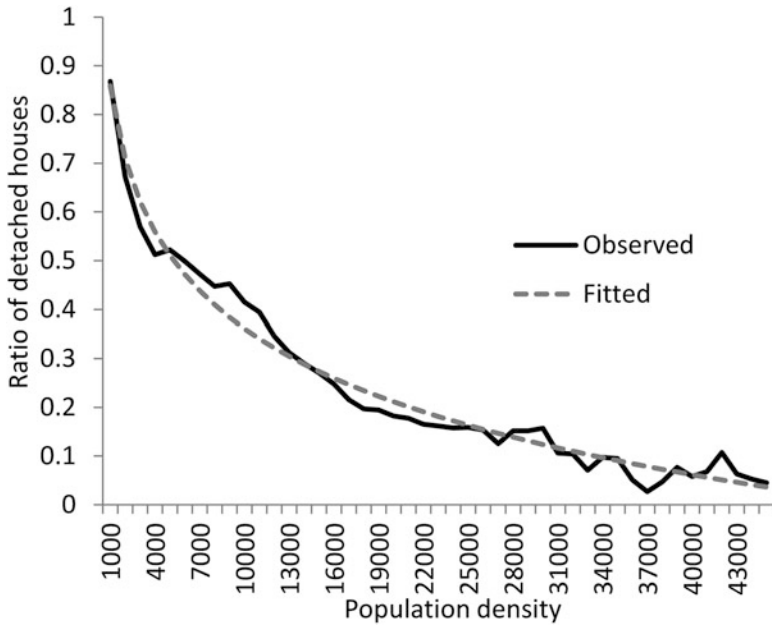


Fig. 12.3 Relationship between the ratio of detached houses and population density

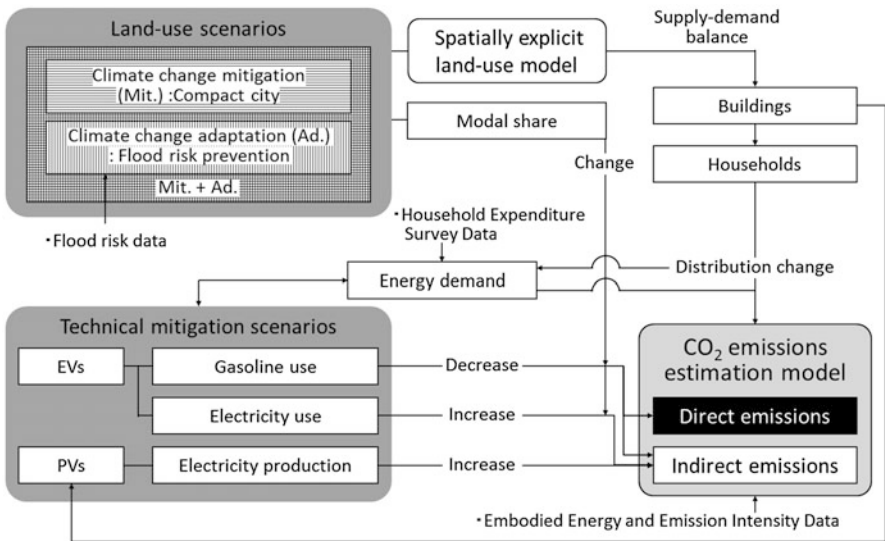


Fig. 12.4 Structure of integrated evaluation system for direct/indirect CO₂ emissions under land-use scenarios considering climate mitigation and flood risk adaptation

Table 12.4 CO₂ emission rate of EVs

Transportation method	CO ₂ emissions (gCO ₂ /km)	
General gasoline car	136.0	^a
EV (Lief)	62.1	^b
EV (i-MiEV)	55.1	^c

^aCalculated from Fuel consumption: 17.0 km/L (MLIT 2012)

^bCalculated from AC power consumption rate: 124 Wh/km (Nissan 2012)

^cCalculated from AC power consumption rate: 110 Wh/km (Mitsubishi 2012) (JC08 mode)

All calculations are based on uniquely estimated CO₂ emission factors after the Great East Japan Earthquake (2011): 0.50 kgCO₂/kWh

$$PV_i = I \times \tau \times L_i^{PV} \times \eta pc \times K_{pt} \times T \quad (12.2)$$

where I denotes the total (solar) irradiance (kWh/m²/h); τ : array conversion efficiency (=0.1); L_i^{PV} : installation area (m²); ηpc : running efficiency of power conditioner (=0.95); K_{pt} : temperature correction coefficient (=0.9221 for May to October, =1 for the other months); T : performance ratio (=0.89). I was taken from METPV-2 database. L_i^{PV} is defined as

$$L_i^{PV} = L_i \times \xi \times \iota \times 1 / \cos \psi \quad (12.3)$$

where ξ denotes the building-to-land ratio; ι : possible area of installation on the roof (=0.3); ψ : optimal angle of inclination (=30°). L_i was projected using our land-use model.

The introduction of EVs has the potential to reduce both direct and indirect emissions by gasoline use. Instead, indirect emissions for electricity use would increase for the battery charge of EVs. As to the introduction of PVs, the indirect emissions could be reduced because people would save electricity which was supplied by the electric power company.

The outline of scenarios which could be assessed by our integrated CO₂ emissions evaluation system is described in Fig. 12.5. This evaluation system can be used as a decision support system for evaluation of CO₂ emissions under land-use scenarios considering climate mitigation and flood risk adaptation.

12.3 The Case Study

12.3.1 Scenario Building for the Tokyo Metropolitan Area in 2050

The base year for the projection was 2005, while 2050 was set as the target year by taking into account the reliability of projection results. The study area is shown in

- Land-use scenarios

	Do nothing	Climate change adaptation
Do nothing	BAU :Dispersed city	Adaptation (Ad.) : Flood risk prevention
Climate change mitigation	Mitigation (Mit.) : Compact city	Mit. + Ad.



- Technological mitigation scenarios:
Introduction of photovoltaic (PV) panels and Electric vehicles (EVs)

Fig. 12.5 Scenario outline

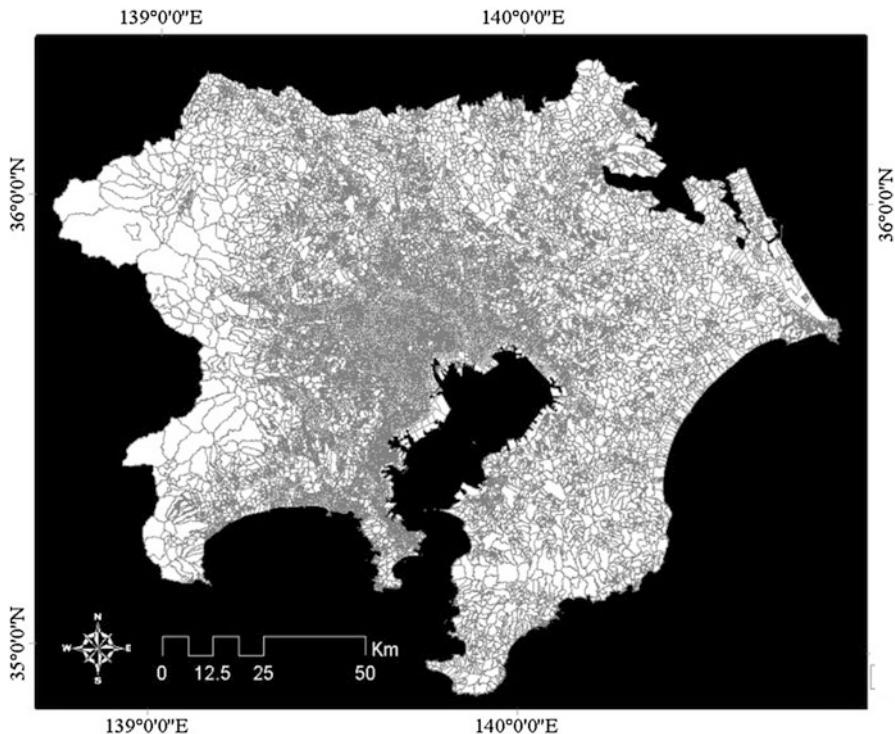


Fig. 12.6 Study area (Tokyo Metropolitan Area)

Fig. 12.6. We assumed that the number of households in each household type in 2050 would change and the ratios to the numbers in 2005 would be as follows: type 1: 2.07, 2: 1.07, 3: 1.39, 4: 0.66, 5: 0.69, 6: 1.32, 7: 0.85 This was estimated by the log-linear extrapolation of the estimates for 2030 by the National Institute of Population and Society Research, Japan.

Table 12.5 Scenarios for the Tokyo Metropolitan Area in 2050

Technological mitigation		With introduction of PVs and EVs (Technological mitigation measures, resilient from energy use perspective)
Land use	Without introduction of PVs and EVs	
Climate change mitigation (Mit.): compact city	Shrinking urbanized areas in suburbs	In addition to the left column,
	Available area of the residential land will be ½ (if distance to station is >500 m)	Cars will be replaced by EVs
	Subsidy to living in the central district	Gasoline consumption will be zero but the electricity consumption for charging EVs will increase
	100,000 yen/year (if distance to station is <250 m)	PV panels will be installed on the roofs of all the detached houses
	Modal share will be changed	Generated electricity from PVs will be subtracted from the electricity consumption of households
	Car trips around the train stations will be reduced by 50 % (if distance to station is <250 m)	Cars will be replaced by EVs PV panels will be installed on the roofs of all the detached houses
Climate change adaptation (Ad.): flood risk prevention	Retreat from the flood-hazard areas	
	Available area of the residential land will be ½ (if the liquefaction risk index is 2 (middle) or 3 (high))	
Climate change mitigation and adaptation (Mit. + Ad.)	Retreat from the flood-hazard areas	
	Shrinking urbanized areas in suburbs	
	Subsidy to living in the central district	
	Modal share will be changed	
Dispersion (BAU)	Business as usual	
	The suburban development will continue	

Our future urban scenario is described in Table 12.5. We set four land-use scenarios and five scenarios of PVs and EVs introduction. We combined each other.

12.3.1.1 Land Use Scenarios

We created four land-use scenarios: climate change mitigation (compact city), adaptation (flood risk prevention), mitigation + adaptation and a dispersion city

(BAU), to show the possible range of future land-use changes based on Yamagata and Seya (2013) and Yamagata et al. (2013).

- **Business-as-usual (BAU)**
We assumed that the suburban development will continue to compare with other scenarios.
- **Climate change mitigation scenario (Mit.)**
Regulations of land use will be introduced based on the concept of compact city. The compact city is known as one of the climate change mitigation measures. People will retreat from the suburbs and live in the city center and around train stations.
- **Climate change adaptation scenario (Ad.)**
As a way of flood disaster prevention, we assumed that people retreat from flood-hazard areas. The liquefaction risk index was used as a proxy index of flood and tsunami risk because both indexes are high near bay areas and rivers. The liquefaction risk index is calculated based on the methodology of Wakamatsu et al. (2005). The index runs from 0 (no risk) to 3 (high risk) as seen in Fig. 12.7. We defined 2 (middle risk) and 3 (high risk) as flood-hazard areas.
- **Climate change mitigation and adaptation scenario (Mit. + Ad.)**
We set a combination scenario that satisfies the conditions of both climate change mitigation and adaptation scenario. People will retreat from suburban and flood-hazard areas and will live in the city center and around train stations.

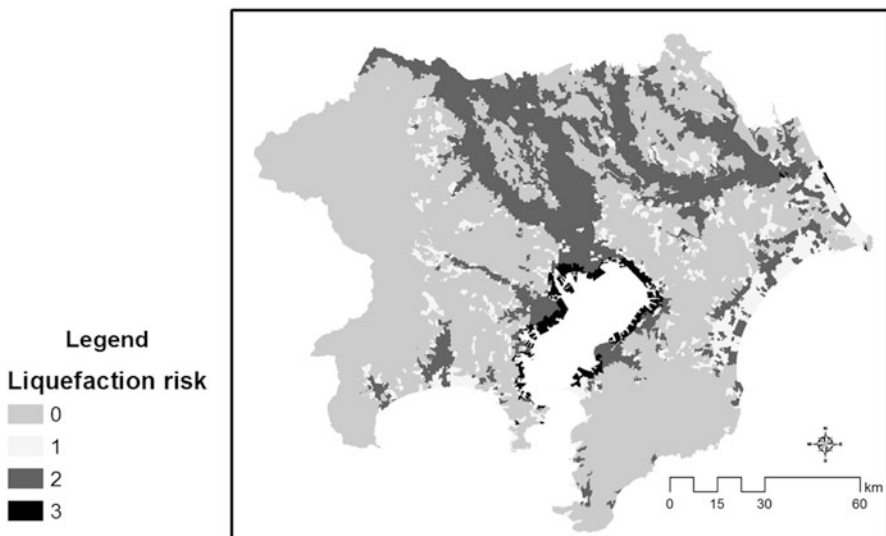


Fig. 12.7 Calculation results of the liquefaction risk index

12.3.1.2 Scenarios of Pvs and Evs Introduction

As mitigation measures, we considered not only land-use change like a compact city but also the large-scale introduction of EVs and PVs. In each land-use scenario, we set a different rate of diffusion for EVs and PVs (Table 12.6).

12.3.2 Results and Discussion

The spatial distributions of population under each land-use scenario are shown in Fig. 12.8. Figure 12.9 shows the distribution of CO₂ emissions in the Tokyo Metropolitan Area under different scenarios. The total CO₂ emissions from households could be reduced as seen in Fig. 12.10.

Even without technological mitigation measures (introduction of PVs and EVs), the estimated CO₂ emissions are likely to decrease by 3.2 % depending on the population decline in the Tokyo Metropolitan Area in 2050. The reduction rate of scenario Mit.+Ad.1 (5.0 %) is higher than that of scenario Ad.1 (4.8 %) implying that CO₂ emissions can be reduced if compact city is realized. Taniguchi et al. (2005) estimated the reduction rate of transportation energy for a local city to be about 3 % under the compact city scenario and 6 % under the scenario considering both compact city and flood disaster prevention. The depopulation of the whole city was not considered in their study. Nakai and Morimoto (2008) calculated the change of both automobile energy consumption in the transportation sector and electric power consumption in the residential sector in cases when a compact city policy was implemented for the central city of a local area. In their study, the reduction rates were 2.5–4.2 % in the transportation sector and 1.5–4.0 % in the residential sector. The target year was 2020 and the depopulation of the whole city was included in these scenarios. Such energy consumption has a direct correlation with CO₂ emissions. Because these cities are automobile dependent cities, the reduction rate in the transportation sector generally becomes higher than in the cities in the metropolitan area. Nakamichi et al. (2013a) assumed a more compact city scenario in Yokohama city included in the Tokyo Metropolitan Area, and estimated the CO₂ emissions (direct and indirect emissions) from all sectors. The reduction rate was 5.4 % under the compact city scenario. The assumptions, the target year and target area were not the same among these scenarios. However, they

Table 12.6 Scenarios of PV and EV introduction

Scenarios of PV and EV introduction	Diffusion rate of EVs (%)	Diffusion rate of PVs (%)
1	0	0
2-i	100	100
2-ii	50	50
2-iii	100	50
2-iv	100	30

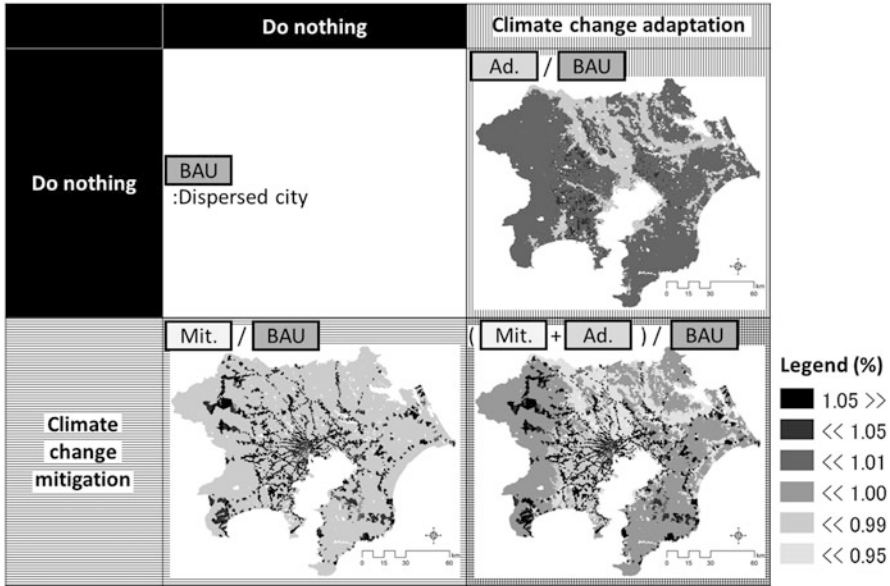


Fig. 12.8 Change rate of population distribution

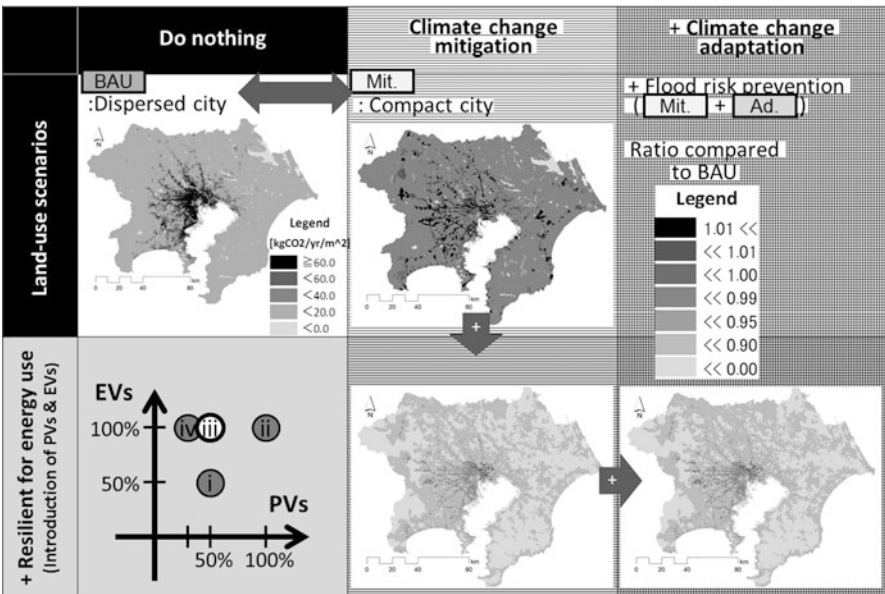


Fig. 12.9 Spatial distribution of direct and indirect CO₂ emissions of households under each scenario in the Tokyo Metropolitan Area

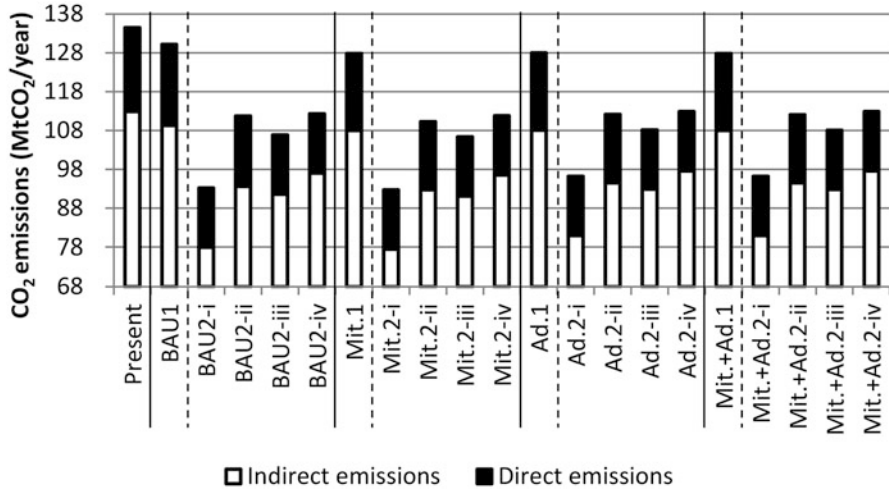


Fig. 12.10 CO₂ emissions of all the households under different scenarios

showed that the reduction rates were only several percentages or more. Compared with these studies, the estimated reduction rate of the present study is not so low.

Under the scenarios with technological mitigation measures (BAU2, Mit.2, Ad.2, Mit.+Ad.2), the introduction of EVs has the potential to reduce both direct and indirect emissions from gasoline use (Emission group: 7. Transportation and communication). Instead, indirect emissions in Emission group 3 (Fuel, light and water charges) would increase due to the battery charge of EVs. As to the introduction of PVs, some or all of the electric power demand of each household could be covered by PV power generation. The indirect emissions in Emission group 3 could be reduced because people would save electricity supplied by the electric power company.

With technological mitigation measures, the CO₂ reduction rate of scenario Mit.2 (16.9–31.0 %) is higher than that of scenario BAU2 (16.5–30.7 %) while, on the other hand, the CO₂ reduction rate of scenario Ad.2 (16.1–28.4 %) is lower than that of scenario BAU2. The order of reduction rates of CO₂ emissions is Mit.2-i>BAU2-i>Ad.2-i, Mit.2-ii>BAU2-ii>Ad.2-ii, Mit.2-iii>BAU2-iii>Ad.2-iii, Mit.2-iv>BAU2-iv>Ad.2-iv. Even under the Mit.+Ad.2 scenarios, the CO₂ emissions are much more than in the BAU2 scenarios. The reduction rate of CO₂ (16.1–28.5 %) is lower by 2.0 % compared with scenario Mit.2 only. This is due to the fact that depending on the decrease in the number of people living in flood-hazardous areas, there would be fewer detached houses, thus fewer PV panels that could be installed. It is important to formulate compatible ways between climate mitigation and adaptation. However, we can achieve more CO₂ reduction through parallel efforts in climate mitigation and adaptation measures because the reduction rate by technological mitigation measures is very high. Simultaneous discussions on both mitigation and adaptation are necessary.

12.4 Conclusions

This study developed an integrated evaluation system for CO₂ emissions under (i) land-use scenarios considering both climate change mitigation and adaptation and (ii) technological mitigation scenarios considering the introduction of PVs and EVs. The land-use scenarios built by using a spatially explicit land-use model which had been based on real estate data, were applied for the case study of this evaluation system. Our CO₂ emission estimation model could estimate not only direct emissions but also indirect emissions based on household expenditure. As a case study, we showed the future spatial distribution of CO₂ emissions by using this integrated evaluation system.

This evaluation system could be used as a decision support system for the evaluation of CO₂ emissions under land-use scenarios considering climate mitigation and flood risk adaptation for resilient cities. Urban and regional planners might implement economically-based planning of urban improvement projects, spatial distribution of population density, public transportation projects and energy saving of households. They could also select retreat and cohesion areas considering compact city design and disaster prevention on the neighborhood scale. A different diffusion rate of PVs and EVs in each zone could be set as scenarios. Policy-makers could compare each effect on CO₂ emission reduction.

The results of this case study suggest that climate change mitigation and adaptation can generate both a synergistic and trade-off effect from the viewpoint of CO₂ emissions. We have to find a strategy for compatibility between mitigation and adaptation using an evaluation system like the one in this study.

The results suggest that the compactness of land use and the introduction of PV panels installed on detached houses are not compatible from the viewpoint of CO₂ emission reduction because more compactness means fewer detached houses. In the future, we should consider scenarios assuming the installation of PV panels on the top of apartment/office buildings in the city center or around stations, and the introduction of mega solar power plants in suburban areas where people retreated. We postpone these considerations to future research. It is necessary to consider the interchange of surplus electricity generated by PVs. The electric power interchange among household types with different living hours should also be considered, as pointed out by Taniguchi and Ochiai (2012). In this study, the indirect emissions were estimated per year. The variations in time for both PV supply and household demand must be considered as pointed out by Esteban et al. (2012). The emissions were related to energy and gasoline change by scenarios. Emissions from other sources should be considered from the viewpoint of Life Cycle Assessment. Also, the cost for realizing land-use scenarios such as people's move should be calculated and compared with the cost of infrastructure for flood disaster prevention such as levee and padding based on cost-benefit analysis. The dispersed city has the potential of making services inefficient in the city and of increasing the cost for infrastructure. Because the compact city may be economical and efficient in consideration of CO₂ emissions by logistics, further studies are

needed from this viewpoint, too. Furthermore, the scenarios should be evaluated in terms of QOL such as accessibility and amenity. In order to realize a climate change adaptation scenario, risk communication tools like those suggested by Burch et al. (2010) and resilience against multiple disasters including earthquake and tsunami are also important.

Acknowledgements This study was funded by the “Research Program on Climate Change Adaptation (RECCA)” of the Ministry of Education, Culture, Sports, Science and Technology (MEXT), Japan.

We thank Professor Yutaka TONOOKA and Mr. Satoshi KOUHA of Saitama University, Special Appointed Professor Akio TANAKA of Kumamoto University, Mr. Ryota II of Pacific Consultants CO., LTD and Mr. Kohei SAKAI of the National Institute for Environmental Studies for the estimation of CO₂ emissions.

References

- Abe J, Miura S, Tonooka Y (2002) Study on the characteristics of CO₂ emissions caused by family life based on the LCA database. *J Archit Plan Environ Eng AIJ* 551:93–98 (in Japanese)
- Auckland Sustainability Framework: <http://www.arc.govt.nz/albany/fms/main/Documents/Auckland/Sustainability/Auckland%20Sustainability%20Framework.pdf>. Access date: 31 Jan 2014
- Burch S, Sheppard SRJ, Shaw A, Flanders D (2010) Planning for climate change in a flood-prone community: municipal barriers to policy action and the use of visualizations as decision-support tools. *J Flood Risk Manag* 3:126–139
- Dhokal S (2009) Urban energy use and carbon emissions from cities in China and policy implications. *Energy Policy* 37:4208–4219
- Esteban M, Zhang Q, Utama A (2012) Estimation of the energy storage requirement of a future 100% renewable energy system in Japan. *Energy Policy* 47:22–31
- Gilman EL, Ellison J, Duke NC, Field C (2008) Threats to mangroves from climate change and adaptation options: a review. *Aquat Bot* 89:237–250
- Hayashi Y, Kato H, Kimoto J, Sugawara T (1995) Estimation of reduction in CO₂ emission by modal shift policy in urban passenger transport. *Infrastruct Plan Rev* 12:277–282
- IPCC (2007) In: Parry ML, Canziani OF, Palutikof JP, van der Linden PJ, Hanson CE (eds) *Climate change 2007: impacts, adaptation and vulnerability, contribution of working group II to the fourth assessment report of the Intergovernmental Panel on Climate Change (IPCC)*. Cambridge University Press, Cambridge, UK
- IPCC (2014) *Climate change 2014: impacts, adaptation and vulnerability, contribution of working group II to the fifth assessment report of the Intergovernmental Panel on Climate Change (IPCC)*. In: Aldunce P, Ometto JP, Rahlolijao N, Yasuhara K (eds) <https://www.ipcc.ch/report/ar5/wg2/>
- Jenks M, Burton E, Williams K (eds) (1996) *The compact city: a sustainable urban form?* Routledge
- Kennedy C, Steinberger J, Gasson B, Hansen Y, Hillman T, Havránek M, Pataki D, Phdungsilp A, Ramaswami A, Mendez GV (2010) Methodology for inventorying greenhouse gas emissions from global cities. *Energy Policy* 38:4828–4837
- Ministry of Land, Infrastructure, Transport and Tourism (MLIT) (2012) The list of car fuel consumption. http://www.mlit.go.jp/jidosha/jidosha_fr10_000014.html. Access date: 31 Jan 2014 (in Japanese)
- Mitsubishi Motors Corporation (2012) i-MiEV specification sheet. http://www.mitsubishi-motors.co.jp/i-miev/spec/spe_02.html. Access date: 31 Jan 2014 (in Japanese)

- Naess P (1996) Workplace location, modal split, and energy use for commuting trips. *Urban Stud* 33:557–580
- Nagao M, Aono T, Togawa T, Kato H, Sano M (2012) An application of genetic algorithm to select retreat and cohesion areas. *J Jpn Soc Civ Eng D3* 68-3:1_339–1_348
- Nakai H, Morimoto A (2008) A study on the energy consumption in residential and traffic sector in case of practicing a compact city policy. *J Jpn Soc Civ Eng D* 64:1–10 (in Japanese)
- Nakamichi K, Taniguchi M, Matsunaka R (2007) A pictorial encyclopedia of residential zones in world class cities for sustainable urban planning – Japanese cases–. The 7th international conference on urban planning and environment, Bangkok
- Nakamichi K, Seya H, Yamagata Y (2013a) Geographically explicit direct/indirect CO₂ emission scenarios for a compact city in 2050. Proceeding of the 10th Symposium of the International Urban Planning and Environment Association (UPE10 Next City): 14–26, <http://static.icms.com.au/upe10/proceedings.pdf>. Access date: 31 Jan 2014
- Nakamichi K, Yamagata Y, Seya H (2013b) CO₂ emissions evaluation considering introduction of EVs and PVs under land-use scenarios for climate change mitigation and adaptation – focusing on the change of emission factor after the Tohoku earthquake. *J East Asia Soc Transp Stud* 10:1025–1044
- Nakamura M, Otoma S (2004) Analysis of CO₂ emission originating from household consumption –taking attributes of families into account-. *Environ Sci* 17:389–401 (in Japanese)
- Newman P, Kenworthy J (1999) *Sustainability and cities: overcoming automobile dependence*. Island Press, Washington, DC
- Nissan Motor Co., Ltd. (2012) Leaf specification sheet. http://ev.nissan.co.jp/LEAF/PDF/leaf_specification.pdf. Access date: 31 Jan 20134 (in Japanese)
- OECD (2012) *Compact city policies: a comparative assessment*, OECD green growth studies. OECD Publishing
- Penney J (2008) *Climate change adaptation in the city of Toronto: lessons for Great Lakes Communities*, Clean Air Partnership
- Roo G, Miller D (2000) *Compact cities and urban development*. Ashgate, Aldershot
- Shigeto S, Yamagata Y, Ii R, Hidaka M, Horio M (2012) An easily traceable scenario for 80% CO₂ emission reduction in Japan through the final consumption-based CO₂ emission approach: a case study of Kyoto-city. *Appl Energy* 90:201–205
- Suburban Neighbourhood Adaptation to Changing Climate (SNACC): <http://www.bne.uwe.ac.uk/cep/snacc/>. Access date: 31 Jan 2014
- Tanaka A, Kubo R, Nakagami H, Ishihara O (2008) Attribution analyses of family area and of household energy use and its future prediction. *J Environ Eng* 628:823–830 (in Japanese)
- Taniguchi M, Ochiai J (2011) Suitability of introducing smart grids on a residential block scale. *Jpn J Real Estate Sci* 25:100–109 (in Japanese)
- Taniguchi M, Ochiai J (2012) Influence of technological innovation on the introduction and suitability of smart grids at residential block scale. In: *Proceedings of 28th annual meeting of the Japan Association for Real Estate Science*, pp 29–38 (in Japanese)
- Taniguchi M, Matsunaka R, Nakamichi K (2005) SLIM CITY (Smart Layout Indicators to Materialize Compact City), as the new package to evaluate compact urban layout – how to manage land recycle and flood disaster prevention. *Computers in Urban Planning and Urban Management (CUPUM) 05*, London, 98
- Taniguchi M, Matsunaka R, Nakamichi K (2008) A time-series analysis of relationship between urban layout and automobile reliance -have cities shifted to integrate land use and transport? *Urban Transp XIV*:415–424
- Ueda T, Tsutsumi M, Muto S, Yamasaki K (2012) Unified computable urban economic model. *Ann Reg Sci* 50:341–362
- Wakamatsu K, Matsuoka M, Sugiura M, Kubo J, Hasegawa K (2005) *Japan engineering geomorphologic classification map*. University of Tokyo Press, Tokyo (in Japanese)
- Williams K, Burton E, Jenks M (eds) (2000) *Achieving a sustainable urban form*. Routledge

- Xi F, Geng Y, Chen X, Zhang Y, Wang X, Xue B, Dong H, Liu Z, Ren W, Fujita T, Zhu Q (2011) Contributing to local policy making on GHG emission reduction through inventorying and attribution: a case study of Shenyang, China. *Energy Policy* 39:5999–6010
- Yamagata Y, Seya H (2013) Simulating a future smart city: an integrated land use-energy model. *Appl Energy* 12:1466–1474
- Yamagata Y, Seya H, Nakamichi K (2013) Creation of future urban environmental scenarios using a geographically explicit land-use model: a case study of Tokyo. *Ann GIS* 19–3:153–168
- Yamashita T, Kanamori Y, Masuoka Y (2007) Relationship between demographic changes and environmental load generation. *Environ Syst Res* 35:315–325 (in Japanese)
- Yokoi T, Yamamoto Y, Tokai A, Morioka T (2010) Development of decision support system to integrate block renewal and energy planning towards low-carbon city. *J Infrastruct Plan Manag* G 66:17–34 (in Japanese)

Part V
Earth Observation Data Processing

Chapter 13

Support Vector Machines for Land Cover Mapping from Remote Sensor Imagery

Dee Shi and Xiaojun Yang

Abstract Land cover mapping is an important activity leading to the generation of various thematic products essential for numerous environmental monitoring and resources management applications at local, regional, and global levels. Over the years, various pattern recognition techniques have been developed to automate this process from remote sensor imagery. Support vector machines (SVM) as a group of relatively novel statistical learning algorithms have demonstrated their robustness in classifying homogeneous and heterogeneous land cover types. In this chapter, we review the status and potential challenges in the SVM implementation for land cover classification. The chapter is organized into two major parts. The first part reviews the research status of using SVM for land cover classification, focusing on some comparative studies that demonstrated the algorithm effectiveness over other conventional classifiers. We identify several areas for additional work, which are mostly related to appropriate treatments of some parametric and non-parametric factors in order to achieve improved mapping accuracies particularly for working over heterogeneous landscapes. Then, we implement the support vector machine technique to map various land cover types from a satellite image covering an urban area, and demonstrate the robustness of this pattern recognition technique for mapping heterogeneous landscapes.

Keywords Land cover • Image classification • Support vector machines • Heterogeneous landscapes • Thematic accuracy assessment

13.1 Introduction

Land cover is the pattern of ecological resources and human activities dominating different areas of Earth's surface (Turner and Meyer 1994). It is a critical type of data source essential for many environmental monitoring and natural resources management applications at local, regional, and global scales (Foley et al. 2005;

D. Shi (✉) • X. Yang

Department of Geography, Florida State University, Tallahassee, FL 32306, USA

e-mail: ds10f@my.fsu.edu; xyang@fsu.edu

© Springer Science+Business Media Dordrecht 2015

265

J. Li, X. Yang (eds.), *Monitoring and Modeling of Global Changes: A Geomatics Perspective*, Springer Remote Sensing/Photogrammetry, DOI 10.1007/978-94-017-9813-6_13

Alberti 2008). Land cover patterns are observable and therefore can be mapped by ground surveys or remote sensing. While ground surveys are largely limited by logistical constraints, remote sensing makes direct observations across large areas of the land surface, thus allowing land cover patterns to be mapped in a timely and cost-effective mode. Both visual interpretation and computer-based digital classification can be used to extract information on land cover from a variety of remotely sensed data varying in spatial, spectral, radiometric, and temporal resolutions. Digital pattern classification is generally preferred over visual interpretation for mapping land cover in large areas (Jensen 2005).

While conventional pattern classifiers (e.g., maximum likelihood) have been widely used, they generally work well with medium-resolution images and in relatively homogeneous areas rather than highly heterogeneous areas (Yang 2002). Over the years, substantial research efforts have been directed to improve the performance of land cover mapping in heterogeneous areas (e.g. Hoffer 1978; Richards et al. 1982; Skidmore et al. 1997; Duda et al. 2001; Yang and Lo 2002; Schmidt et al. 2004; Del Frate et al. 2007; Foody 2008; Heikkinen et al. 2010; Zhou and Yang 2011; Liu and Yang 2013).

This study targets support vector machines (SVM), a group of relatively novel machine learning algorithms based on statistical learning theory that have not been extensively exploited in the remote sensing community. They are found to outperform most of the conventional classifiers (Huang et al. 2002; Keuchel et al. 2003; Kavzoglu and Colkesen 2009; Su and Huang 2009). Moreover, SVM were found to even outperform some novel pattern recognition methods, such as neural networks (Huang et al. 2002; Foody and Mathur 2004a, b). Nevertheless, there are some parametric and non-parametric factors that can affect the performance of SVM, and there is a need to investigate them so that SVM could be used with improved performance (Yang 2011).

In this chapter, we examine the utilities of support vector machines (SVM) as a pattern recognition technique for landscape mapping particular for heterogeneous areas. It is organized into two major parts, beginning with a brief introduction of some basic knowledge on SVM and a review on the research status and possible challenges of using SVM for land cover mapping. The review focuses on some comparative studies that demonstrated the effectiveness of SVM over other conventional classifiers. Based on the review, we further discuss several areas that need additional research in order to improve SVM classification accuracies and reduce computational burdens, which are mostly related to appropriate treatments of some parametric and non-parametric factors. The second part of the paper discusses our implementation of SVM to map various land cover types from a remote sensor image covering an urban area, demonstrating the robustness of this type of pattern recognition technique for mapping heterogeneous landscapes.

13.2 Support Vector Machines

13.2.1 Basics

The basic idea behind the support vector machines (SVM) is to construct separating hyperplanes between classes in feature space through the use of support vectors which are lying at the edges of class domains; SVM seek the optimal hyperplane that can separate classes from each other with the maximum margin (Vapnik 1995).

SVM were originally designed as a binary linear classifier, which assumes two linearly separable classes to be partitioned. In most cases, the best separable hyperplane may not be located exactly between two classes. To account for this, an error item is introduced to manipulate the tradeoff between maximizing the separation margin and minimizing the count of training samples that locates on the wrong side. SVM are further extended to deal with non-linear classification by using a non-linear kernel function to replace the inner product of optimal hyperplane. Several commonly used kernel functions include linear kernel, polynomial kernel, radial basis function (RBF), and sigmoid kernel (Haykin 1999). Each of these kernel functions is constructed with multiple parameters, and the parameter settings can influence the performance of a specific support vector machine (Yang 2011).

Moreover, SVM have been used for multi-class mapping through reducing the multi-class problem into a set of binary problems so that the basic SVM principles can be still applied. Two commonly used strategies for this purpose include one-against-one and one-against-all (Foody and Mathur 2004b; Kavzoglu and Colkesen 2009). The former is generally preferred because of its less computational intensity and comparable accuracy to the later. The one-against-all method can result in unclassified instances (Huang et al. 2002; Hsu and Lin 2002; Pal and Mather 2005; Mountrakis et al. 2011), which is not suitable for land cover mapping.

13.2.2 SVM for Land Cover Classification

The performance of SVM has been examined through some comparative studies with other pattern classifiers for various land cover types (e.g., Huang et al. 2002; Foody and Mathur 2006; Keramitsoglou et al. 2006; Su and Huang 2009). Huang et al. (2002) found that SVM substantially outperformed maximum likelihood (MLC) or decision tree (DC) in terms of classification accuracy and even surpassed multilayer perceptron neural networks (MLP). Su and Huang (2009) implemented SVM and MLC on a Multi-angle Imaging SpectroRadiometer (MISR) image to differentiate eight semi-arid vegetation types, and found that SVM significantly outperformed MLC. Keramitsoglou et al. (2006) mapped various vegetation types using IKONOS data, and compared the performance of SVM with radial basis (RBF) neural networks. They found that SVM had strengths in terms of

classification accuracy and training time. Foody and Mathur (2006) also found that SVM can produce a more accurate classification of cultivated landscape types. Dixon and Candade (2008) compared SVM, MLC, and backpropagation neural networks (NN) for classifying a Landsat scene, and found that SVM and NN performed identically in the classification accuracy but SVM was more efficient in the training phase. They also noted that SVM can be quite attractive when working with high-dimensional data. This seems to be in line with an earlier work conducted by Huang et al. (2002) who found that SVM performed better for an image with seven bands than with three bands. The effectiveness of SVM for working with high-dimensional data classification was also confirmed by several other studies (e.g., Bazi and Melgani 2006; Camps-Valls et al. 2007), indicating that they could provide a solution to dealing with the problem of “curse-of-dimensionality” (Hughes 1968). Although SVM have demonstrated strengths when comparing with other classifiers, their performance can vary across different land cover types (Foody and Mathur 2004a, b; Keramitsoglou et al. 2006; Su and Huang 2009).

The performance of SVM can be affected by both parametric and non-parametric factors (Foody and Mathur 2006; Yang 2011). Existing studies on SVM classification have largely concentrated on either improving classification accuracy on specific land cover types or reducing computational burdens, both of which can be manipulated at the SVM configuration stage and at the training stage. The inner-product kernel between the support vectors in feature space and in input space largely determines the separability of optimal separable hyperplane (Haykin 1999). While introducing non-linear kernel functions could help deal with complex, non-linear classification, it can also lead to the difficulty in choosing the most appropriate kernel type and in the subsequent kernel parameterization (Huang et al. 2002; Kavzoglu and Colkesen 2009; Yang 2011). Yang (2011) conducted an empirical study assessing the performance of several most commonly used kernel types, along with their internal parameterization, and found that the kernel type and error penalty can substantially affect image classification accuracy. Some customized kernels, particularly those incorporating both spatial and spectral information, were found to be quite promising when comparing with spectral-based kernel types (Camps-Valls et al. 2006, 2007; Plaza et al. 2009).

Since the SVM is a supervised classifier by nature, both the size and quality of training sample can affect the classification accuracy (Foody and Mathur 2006). For land cover mapping from remote sensor imagery, training samples should consist of relatively pure pixels, and should be identified from homogeneous areas in large fields, which can be applicable for a variety of classifiers (Foody and Arora 1997). SVM performance can be sensitive to the noise in training samples due to the use of support vectors at the edges of class domains in feature space (Rodriguez-Galiano et al. 2012). A minimum of 10–30 pixels per class per waveband should be used to meet the assumption of normal distribution and be representative of the subclass (Foody and Mathur 2004a, b, 2006). Like other non-parametric classifiers, there is no need to maintain normal distributions in training samples for a SVM classification. Since only the support vectors are actually needed in constructing separate

hyperplanes for SVM, it may be highly possible to reduce training sample size to a small number of the most informative samples that are used to fit the decision hyperplanes. Several studies have been conducted to identify these critical samples. For example, Foody and Marthur (2004a, b, 2006) incorporated ancillary information of soil types and geographical boundary pixels of mixed spectral characteristics of two crop types in the selection of useful training samples, which dramatically reduced training samples before being applied to classification. They also examined the usefulness of applying other ancillary information (e.g., landform, moisture, and spatial texture) in targeting support vectors. Various techniques have been identified to automatically reduce the training sample size and hence help reduce the computational burden for SVM. For example, clustering-based algorithms are applied in training pattern selection to remove samples locating at the high density regions or to detect support vectors at the clustering centers (Demir and Ertürk 2009; Su 2009). With these support vectors obtained from clustering preprocessing, the computational load has been substantially reduced, while the classification accuracy was much higher than using the full training samples.

13.3 Implementation of SVM for Land Cover Mapping

In order to demonstrate the effectiveness of SVM for heterogeneous land cover mapping, we implemented SVM to map land cover types in an urban area. In this section, we will discuss the specific procedures, including the study site and data acquisition, classification scheme design, SVM configuration, and classification and accuracy assessment (Fig. 13.1).

13.3.1 Study Site and Data Acquisition

The study site covers the entire Gwinnett County, a suburban county located at northeastern Atlanta metropolitan area, Georgia, USA (Fig. 13.2). The county has an area of about 1,122 km² and its population was 805,321 according to the 2010 census survey. The majority of topography is relatively flat and has primarily a humid subtropical climate. Gwinnett has been one of America's fastest-growing counties and the second most populated county in Georgia. Its landscape is characterized by a mosaic of complex land use and land cover types, and therefore Gwinnett is an ideal site to examine the effectiveness of SVM for heterogeneous landscape mapping.

A cloud-free Landsat-5 Thematic Mapper (TM) image dated on 19 May 2007 was acquired from USGS EROS Data Center, and a subset of this scene covering the entire Gwinnett County was actually used in our study (Fig. 13.3). The image has been geometrically corrected at the EROS data center, and no further preprocessing was conducted. The spatial resolution of this image is 30 m for all

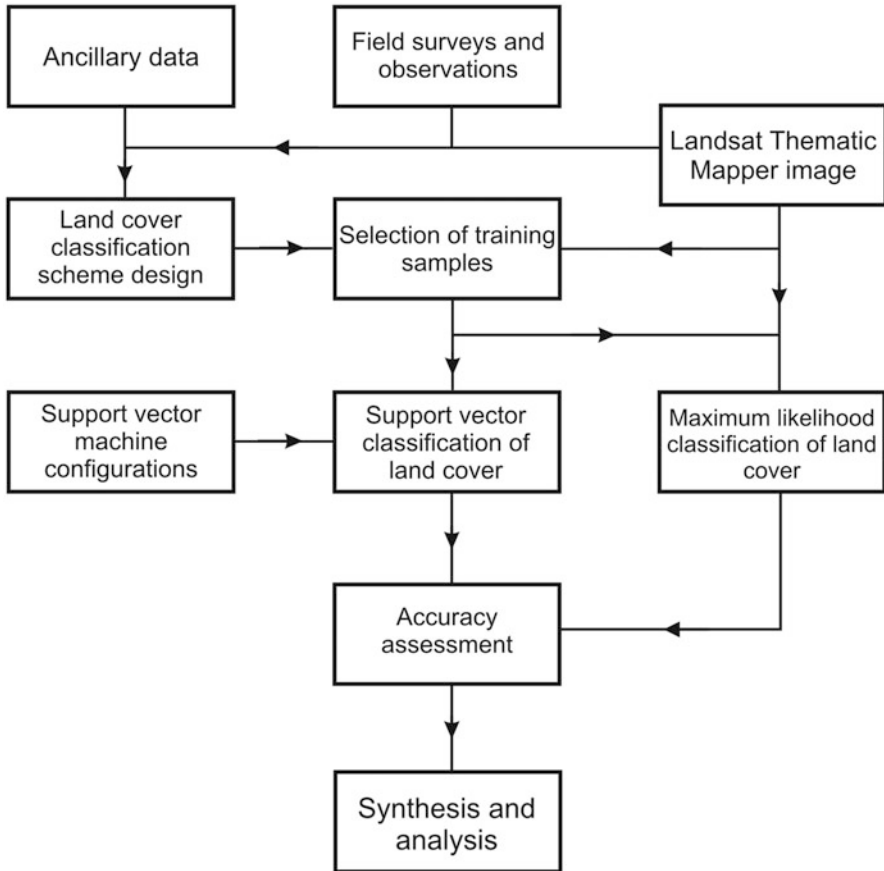


Fig. 13.1 Flowchart of the working procedural route used in this study

six non-thermal infrared bands, and 120 m for the thermal band. It was projected into the Universal Transverse Mercator Zone 16N with NAD 83 as the horizontal datum. Only six non-thermal infrared bands were used for land cover classification.

13.3.2 Classification Scheme and Training Samples

We designed a land use/cover classification scheme based on the Anderson scheme (Anderson et al. 1976) and our field surveys across the Atlanta metropolitan area. The study area covers a mosaic of different land use cover types, and our classification system includes ten major categories: high-density urban, low-density urban, barren or fallow land, pasture and cropland, grassland, shrub and scrub, evergreen forest, deciduous forest, mixed forest, and water (Table 13.1 and Fig. 13.4).

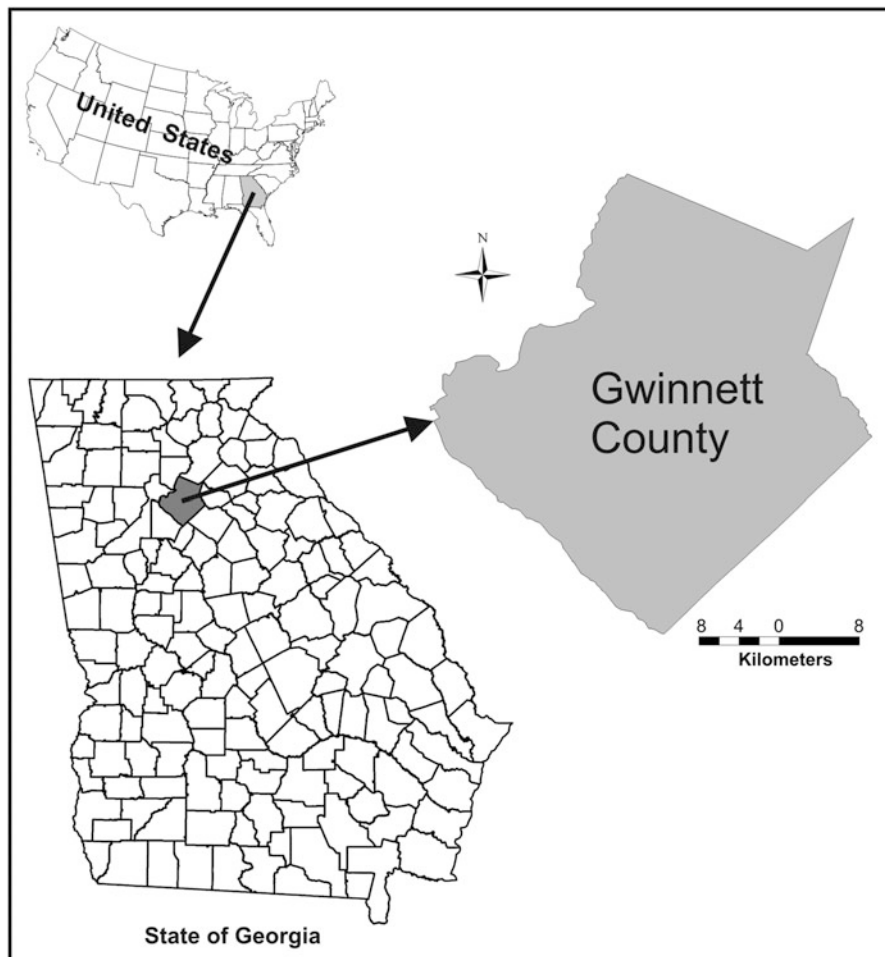


Fig. 13.2 Location of the study site. It covers the entire Gwinnet County in the State of Georgia, USA

After the classification scheme was adopted, we carefully selected training samples for each of the ten major categories by using several reference sources such as the high-resolution images from Google Earth and the 2006 National Land Cover Data (NLCD). Note that each information class listed in Table 13.1 may include multiple spectral classes. For the information classes with multiple spectral classes, we collected at least one training set with 25–35 pixels for each spectral class. Specifically, eight information classes, namely, high-density urban, low-density urban, barren or fallow land, pasture and cropland, grassland, evergreen forest, mixed forest, and water, are comprised of training data from multiple spectral classes. For the high density urban class, training samples were collected for three spectral classes with one for large roofs and the other two for parking lots

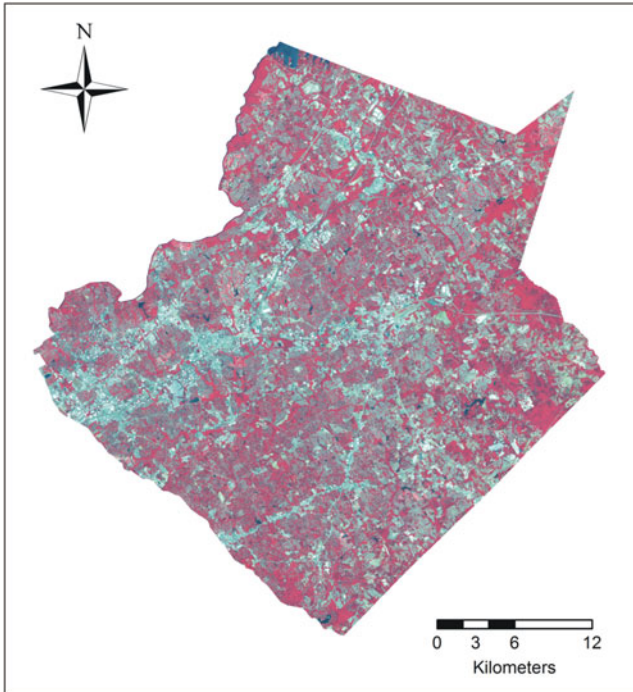


Fig. 13.3 The Landsat Thematic Mapper (TM) image used in this study. It was clipped to match the geographic coverage of Gwinnett County, Georgia. Note that the image is displayed in false color composite

with various pavement materials. For grassland, training samples were collected for two spectral classes with one for golf course with a bright color and the other for urban green spaces with low woody cover. Two spectral classes were defined for evergreen forest with one for highland evergreen forest and the other for wetland evergreen forest. For mixed forest, training samples were collected for two spectral classes that vary due to soil types. We calculated the spectral separability for each pair of the spectral classes, and finally selected 20 classes for use in the training phase of the SVM classification that will be discussed later.

13.3.3 SVM Configuration and Classification

As discussed before, SVM parameter settings can affect the classification performance (Huang et al. 2002; Kavzoglu and Colkesen 2009). Among them, the kernel type, error penalty, and Gamma term are the three most critical parameters (Yang 2011). We configured a support vector machine with radial basis function as the kernel type, a moderate error penalty value ($C = 100$), and a Gamma term equaling

Table 13.1 Land cover classification system, training sample size and reference data size

Class name	Description	Training sample size (# pixels)	Reference sample size (# pixels)
High-density urban	More than two-thirds impervious surfaces, mainly commercial, industrial, institutional facilities with large roofs, and public retail buildings, large transportation facilities	60	52
Low-density urban	Residential areas with impervious surfaces account for lower than two-thirds of total cover, including residential developments, smaller urban service buildings, such as detached stores and restaurants, state highways	54	84
Barren or fallow land	Urban areas with low percentages of constructed materials, vegetation, and low level of impervious surfaces, including bare soil lands, small amount fallow lands, exposed rock, mines and quarries	71	48
Grassland	Herbaceous cover, trees and shrub less than 10 %. Parks, lawns and golf courses	55	86
Pasture and cropland	Grazing area, field crops, horticulture, and vegetable	41	52
Shrub and scrub	Residential and agricultural shrub, scrub, orchards, groves, and transitional vegetation areas	27	47
Evergreen forest	Trees remain green throughout the year, wetland evergreen forests included, mainly cedar and pine trees	47	55
Deciduous forest	Trees lose their leaves when the dry or cold season, wetland deciduous forests included, mainly oak, maple, elm, and hickory	31	50
Mixed forest	Either evergreen or deciduous trees also mixed with shrub and scrub less than 10 %	49	114
Water	Rivers, streams, lakes, reservoirs	125	54

to 0.143 (Yang 2011). We used this SVM configuration to classify the Gwinnett subset of the 7-band TM image with the training samples described above. For comparison purpose, we also used the same training samples to classify the same image by using the maximum likelihood classifier (MLC) that has been widely used. After the implementation of SVM and MLC, we combined the 20 spectral classes into 10 information classes prior to the thematic accuracy assessment (Fig. 13.5).

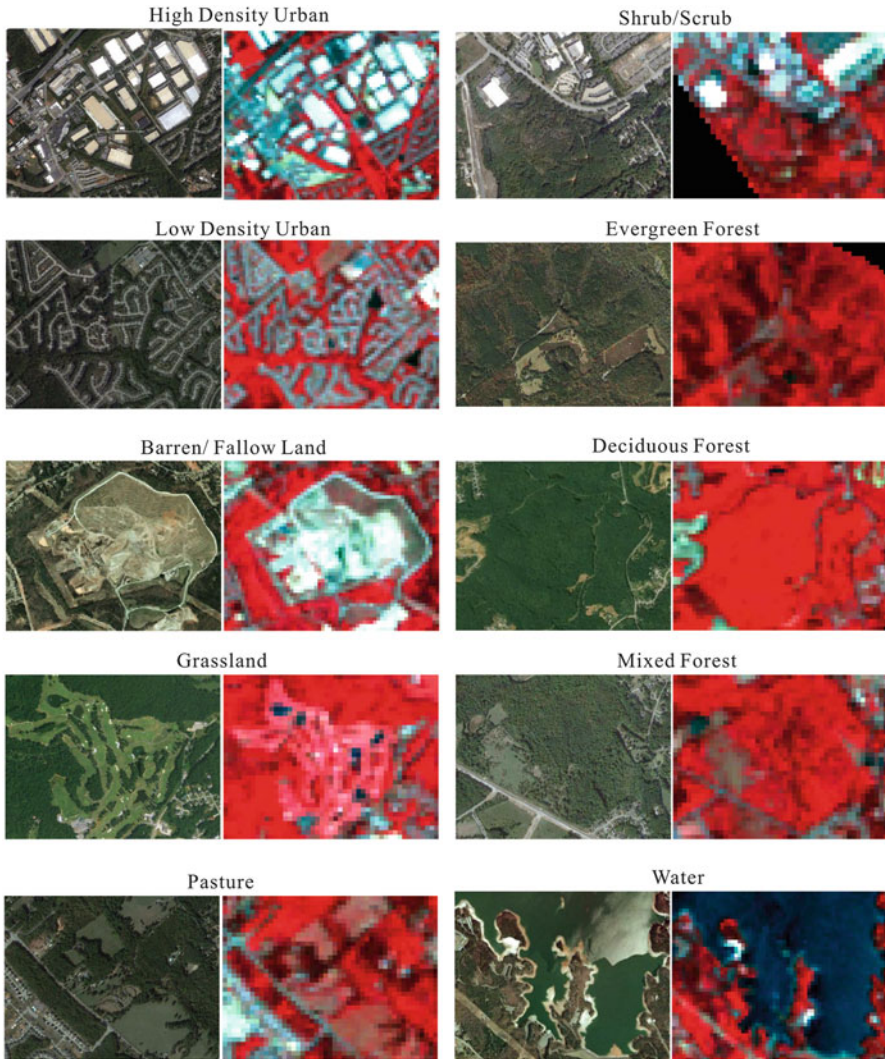


Fig. 13.4 Major land cover types shown in the very high resolution image (Source: Google Earth) and the corresponding Landsat Thematic Mapper (TM) image used in this study. For each image pair, the *left* is a very high resolution image displayed in natural color composite and the *right* is a TM image subset in false color composite

13.3.4 Accuracy Assessment

The accuracy assessment was conducted by using visual comparison and the error matrix approach. The visual comparison is qualitative by nature, while the error matrix approach is a quantitative method that compares the classification map with the ground reference information (Congalton 1991). A total of 498 reference

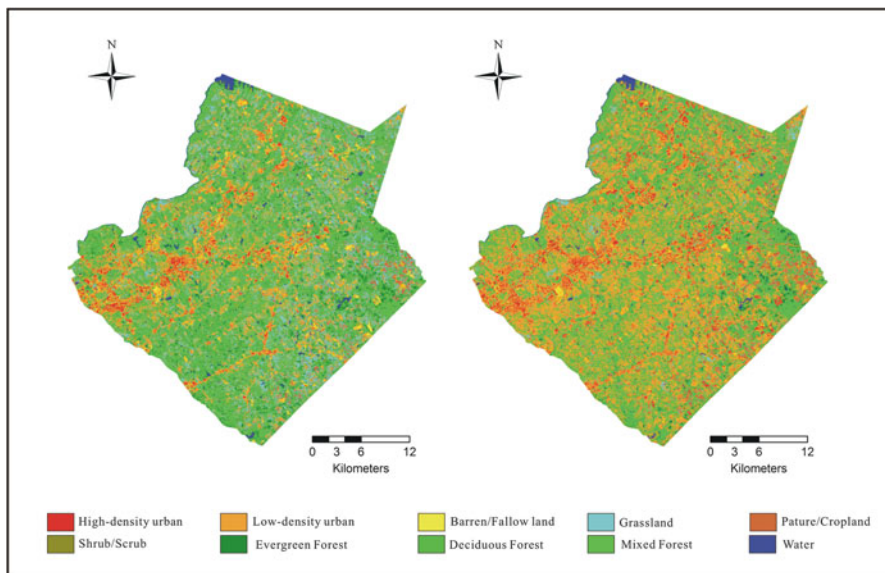


Fig. 13.5 Land cover maps produced by using support vector machines (SVM) (*Left*) and maximum likelihood classifier (*Right*)

samples were generated through the stratified random sampling method (Table 13.2). The identity of each sample was determined by the combined use of high spatial resolution data from Google Earth, USGS 2006 National Land Cover Data, and our field survey data. Kappa coefficients were calculated to quantify the overall and categorical accuracies (Congalton 1991).

13.3.5 Results and Analyses

The classification maps from SVM and MLC are displayed in Fig. 13.5. Both maps were geographically linked with the original remote sensor image, and specific land cover categories were further checked. In general, both maps show an overall correct land cover classification but misclassified areas or pixels can be clearly observed. While the two maps do not show much different large landscape patches, the one from SVM shows many scattered, isolated patches being correctly classified. In terms of specific classes, grassland and low density urban are classified differently, as shown on the two maps. Some grassland patches on the map from SVM were misclassified as low density urban class on the other map. And some mixed forest patches were classified as low density area, and some small patches of evergreen forests and shrubs were classified as mixed forest. Thus, if the spectral characteristics of a class are similar to other classes or if a class is dominated by mixed pixels, SVM clearly performed better than MLC.

Table 13.2 Summary of the thematic accuracy assessment for the two land cover maps produced by support vector machines (SVM) and maximum likelihood classifier (MLC), respectively

Class name	Conditional kappa coefficient (K)		100×(KSVM-KMLC)/KMLC
	Support vector machines (SVM)	Maximum likelihood classifier (MLC)	
High density urban	0.80	0.57	40 %
Low density urban	0.69	0.39	77 %
Barren/fallow land	0.71	0.80	-11 %
Grassland	0.70	0.55	27 %
Pasture	0.81	0.56	45 %
Shrub/scrub	0.76	0.69	10 %
Evergreen forest	0.94	0.94	0 %
Deciduous forest	0.95	0.88	8 %
Mixed forest	0.77	0.55	40 %
Water	1.00	1.00	0 %
Overall kappa coefficient	0.80	0.58	38 %

To further assess the performance of SVM when separating spectrally complex landscape categories, several sites were selected for a closer look. Figure 13.6 illustrates the original TM image, high resolution image from Google Earth, the two classified maps from SVM and MLC, for each of the three sites. For the two spectrally complex categories, namely, low density urban and mixed forest, MLC tended to include more neighboring pixels into these classes. MLC also misclassified some evergreen forest patches into water, barren land patches into high density urban, and grassland patches into low density urban and cropland. Contrastingly, SVM seemed to have done a better job in mapping spatially scattered patches. And SVM had correctly classified the residential patches on all the three sites and the pasture patches on Site 2.

For quantitative accuracy assessment, Kappa coefficient and conditional Kappa coefficients were calculated and summarized in Table 13.2. If judging by the overall Kappa coefficient, SVM significantly outperformed MLC. As for specific classes, SVM significantly surpassed MLC in terms of classification accuracy for most classes, except evergreen forest and water. And the largest improvements were with the categories of high density urban, low density urban, pasture, and mixed forest, of which the second and last classes are most spectrally complex. SVM also showed a moderate improvement for grassland. However, SVM and MLC had almost identical classification accuracies for several relatively homogeneous classes, such as evergreen forest and water.

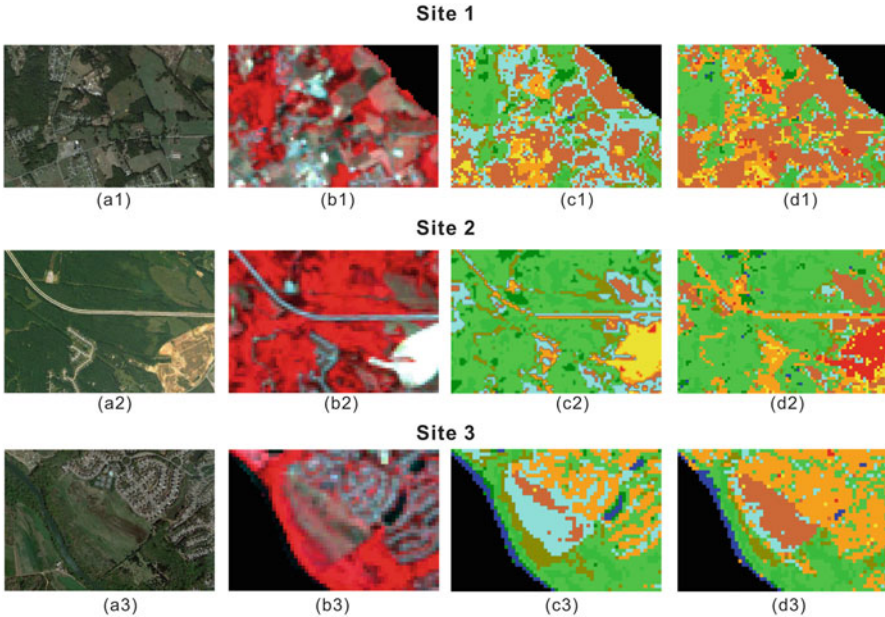


Fig. 13.6 Visual comparison of the land cover classification by support vector machines (SVM) and maximum likelihood classifier (MLC) at the three selected sites. Note that a1, a2, and a3 are natural color composites of very high resolution satellite images from Google Earth; b1, b2, and b3 are false color composites of the Landsat TM image used in this study; c1, c2, and c3 are subsets of the land cover classification by SVM; and d1, d2, and d3 are subsets of the classification by MLC. See Fig. 13.5 for specific legends for the land cover maps

13.4 Conclusion

In this chapter, we have reviewed the research status of using support vector machines (SVM) for land cover mapping with special attention on heterogeneous landscape types. Then, we have implemented this technique to map various land cover types in an urban area from a satellite remote sensor image. Our studies further confirm that SVM can significantly outperform the maximum likelihood classifier (MLC), the most widely used pattern recognition method in the remote sensing community. We found that SVM can significantly improve mapping accuracy, particularly for spectrally and spatially complex land cover categories.

Acknowledgements The authors like to thank the Florida State University for the time release in conducting this work. The research was partially supported by the Florida State University Council on Research and Creativity, CAS/SAFEA International Partnership Program for Creative Research Teams of “Ecosystem Processes and Services”, the Natural Science Foundation of China through the grant “A Study on Environmental Impacts of Urban Landscape Changes and Optimized Ecological Modeling” (ID 41230633).

References

- Alberti M (2008) *Advances in urban ecology: integrating humans and ecological processes in urban ecosystems*. Springer, New York
- Bazi Y, Melgani F (2006) Toward an optimal SVM classification system for hyperspectral remote sensing images. *Geosci Remote Sens IEEE Trans* 44(11):3374–3385
- Camps-Valls G, Gomez-Chova L, Muñoz-Mari J, Vila-Frances J, Calpe-Maravilla J (2006) Composite kernels for hyperspectral image classification. *IEEE Geosci Remote Sens Lett* 3(1):93–97
- Camps-Valls G, Bandos T, Zhou D (2007) Semi-supervised graph-based hyperspectral image classification. *IEEE Trans Geosci Remote Sens* 45(10):3044–3054
- Congalton RG (1991) A review of assessing the accuracy of classifications of remotely sensed data. *Remote Sens Environ* 37(1):35–46
- Del Frate F, Pacifici F, Schiavon G, Solimini C (2007) Use of neural networks for automatic classification from high-resolution images. *IEEE Trans Geosci Remote Sens* 45(4):800–809
- Demir B, Ertürk S (2009) Clustering based extraction of border training patterns for accurate SVM classification of hyperspectral images. *IEEE Geosci Remote Sens Lett* 6(4):840–844
- Dixon B, Candade N (2008) Multispectral landuse classification using neural networks and support vector machines: one or the other, or both? *Int J Remote Sens* 29(4):1185–1206
- Duda RO, Hart PE, Stork DG (2001) *Pattern classification*. Wiley, New York
- Foley JA, DeFries R, Asner GP, Barford C, Bonan G, Carpenter SR, Chapin FS, Coe MT, Daily GC, Gibbs HK, Helkowski JH, Holloway T, Howard TEA, Kucharik CJ, Monfreda C, Patz JA, Prentice IC, Ramankutty N, Snyder PK (2005) Global consequences of land use. *Science* 309:570–574
- Foody GM (2008) RVM-based multi-class classification of remotely sensed data. *Int J Remote Sens* 29(6):1817–1823
- Foody GM, Arora MK (1997) An evaluation of some factors affecting the accuracy of classification by an artificial neural network. *Int J Remote Sens* 18:799–810
- Foody GM, Mathur A (2004a) Toward intelligent training of supervised image classifications: directing training data acquisition for SVM classification. *Remote Sens Environ* 93(1–2):107–117
- Foody GM, Mathur A (2004b) A relative evaluation of multiclass image classification by support vector machines. *IEEE Trans Geosci Remote Sens* 42(6):1335–1343
- Foody GM, Mathur A (2006) The use of small training sets containing mixed pixels for accurate hard image classification: training on mixed spectral responses for classification by a SVM. *Remote Sens Environ* 103(2):179–189
- Haykin S (1999) *Neural networks: a comprehensive foundations*, 2nd edn. Prentice Hall, Upper Saddle River
- Heikkinen V, Tokola T, Parkkinen J, Korpela I, Jaaskelainen T (2010) Simulated multispectral imagery for tree species classification using support vector machines. *IEEE Trans Geosci Remote Sens* 48(3):1355–1364
- Hoffer RM (1978) Biological and physical considerations in applying computer aided analysis techniques to the remote sensor data. In: Swain PH, Davis SM (eds) *Remote sensing: the quantitative approach*. McGraw-Hill, New York, pp 227–289
- Hsu CW, Lin CJ (2002) A comparison of methods for multiclass support vector machines. *Neural Netw IEEE Trans* 13(2):415–425
- Huang C, Davis LS, Townshend JRG (2002) An assessment of support vector machines for land cover classification. *Int J Remote Sens* 23(4):725–749
- Hughes GF (1968) On the mean accuracy of statistical pattern recognizers. *IEEE Trans Inf Theory* 14:55–63
- Jensen JR (2005) *Introductory digital image processing: a remote sensing perspective*, 5th edn. Prentice Hall, Upper Saddle River
- Kavzoglu T, Colkesen I (2009) A kernel functions analysis for support vector machines for land cover classification. *Int J Appl Earth Obs Geoinfr* 11(5):352–359

- Keramitsoglou I, Sarimveis H, Kiranoudis CT, Kontoes C, Sifakis N, Fitoka E (2006) The performance of pixel window algorithms in the classification of habitats using VHSR imagery. *ISPRS J Photogramm Remote Sens* 60(4):225–238
- Keuchel J, Naumann S, Heiler M, Siegmund A (2003) Automatic land cover analysis for Tenerife by supervised classification using remotely sensed data. *Remote Sens Environ* 86(4):530–541
- Liu T, Yang X (2013) Mapping urban vegetation using layered classification and multiple endmember spectral mixture analysis. *Remote Sens Environ* 133:251–264
- Mountrakis G, Im J, Ogole C (2011) Support vector machines in remote sensing: a review. *ISPRS J Photogramm Remote Sens* 66(3):247–259
- Pal M, Mather PM (2005) Support vector machines for classification in remote sensing. *Int J Remote Sens* 26(5):1007–1011
- Plaza A, Benediktsson JA, Boardman JW, Brazile J, Bruzzone L, Camps-valls G, Chanussot J, Fauvel M, Gamba P, Gualtieri A, Marconcini M, Tilton JC, Trianni G (2009) Recent advances in techniques for hyperspectral image processing. *Remote Sens Environ* 113(1):110–122
- Richards JA, Landgrebe DA, Swain PH (1982) A means for utilizing ancillary information in multispectral classifications. *Remote Sens Environ* 12(6):463–477
- Rodriguez-Galiano VF, Ghimire B, Rogan J, Chica-Olmo M, Rigol-Sanchez JP (2012) An assessment of the effectiveness of a random forest classifier for land-cover classification. *ISPRS J Photogramm Remote Sens* 67:93–104
- Schmidt KS, Skidmore AK, Kloosterman EH, Van Oosten H, Kumar L, Janssen JAM (2004) Mapping coastal vegetation using an expert system and hyperspectral imagery. *Photogramm Eng Remote Sens* 70(7):703–715
- Skidmore AK, Turner BJ, Brinkhof W, Knowles E (1997) Performance of a neural network: mapping forests using GIS and remotely sensed data. *Photogramm Eng Remote Sens* 63(5):501–514
- Su L (2009) Optimizing support vector machine learning for semi-arid vegetation mapping by using clustering analysis. *ISPRS J Photogramm Remote Sens* 64(4):407–413
- Su L, Huang X (2009) Support vector machine (svm) classification: comparison of linkage techniques using a clustering-based method for training data selection. *GISci Remote Sens* 46(4):411–423
- Turner BL, Meyer WB (eds) (1994) *Changes in land use and land cover: a global perspective*. Cambridge University Press, Cambridge, UK
- Vapnik VN (1995) *The nature of statistical learning theory*. Springer, New York
- Yang X (2002) Satellite monitoring of urban spatial growth in the Atlanta metropolitan region. *Photogramm Eng Remote Sens* 68(7):725–734
- Yang X (2011) Parameterizing support vector machines for land cover classification. *Photogramm Eng Remote Sens* 77(1):27–37
- Yang X, Lo CP (2002) Using a time series of normalized satellite imagery to detect land use/cover change in the Atlanta, Georgia metropolitan area. *Int J Remote Sens* 23(9):1775–1798
- Zhou L, Yang X (2011) An assessment of internal neural network parameters affecting image classification accuracy. *Photogramm Eng Remote Sens* 77(12):1233–1240

Chapter 14

Digital Processing of SAR Data and Image Analysis Techniques

Saied Pirasteh, Hojjat O. Safari, and Somayeh Mollaei

Abstract Digital SAR processing is referred to the correlation process and computer vision approaches to utilize the outcome of the image to identify an object from the image. Thereby, the SAR signal from the image can be examined to extract the optimum Doppler returns. These are necessary for the successful reconstruction of the return signals into an acceptable image format. In addition to SAR signal processing of data, a number of computations may carry out from a digital SAR processor. Digital SAR processors allow the user to specify additional processing options which may include slant-range to ground-range conversion, range dependent gain correction, the number of independent looks in the azimuth dimension, or pixel spacing. These can also apply for the post-image generation phase. The general theory behind these methods is presented in this chapter. Then it follows the introduction and various digital radar image techniques that may use by an image analyst utilizing a digital image analysis system and suitable computer software packages.

14.1 Introduction

The applications of RADAR technology products particularly derived from space earth observation satellite and remote sensing integrated with GIS technology to various areas of earth sciences, geology, natural resources, agriculture, forest, oil spills pollution, geohazards, mapping, management, planning, early warning system and development has been highly rewarding. The use of RADAR remote sensing has opened the door for immense opportunities in large-scale investigation,

S. Pirasteh (✉) • S. Mollaei
Department of Geography and Environmental Management, University of Waterloo,
Waterloo, ON N2L 3G1, Canada
e-mail: s2pirast@uwaterloo.ca

H.O. Safari
Department of Geology, Golestan University, Gorgan, Iran

© Springer Science+Business Media Dordrecht 2015
J. Li, X. Yang (eds.), *Monitoring and Modeling of Global Changes:
A Geomatics Perspective*, Springer Remote Sensing/Photogrammetry,
DOI 10.1007/978-94-017-9813-6_14

281

updating of existing maps, projects planning and decision-making. This phenomenal growth in the field of RADAR remote sensing is due to the successful launching of series of satellites.

The digital SAR processing is referred to the correlation process whereby the SAR signal use to extract the optimum Doppler returns. Digital SAR processors allow the user to specify additional processing options which may include slant-range to ground-range conversion, range dependent gain correction, the number of independent looks in the azimuth dimension, or pixel spacing. These can also be applied in the post-image generation phase. The general theory behind these techniques is presented in this chapter, followed by an introduction of various digital enhancement techniques that may be applied by an image analyst using a digital image analysis system and suitable computer software packages.

14.1.1 Why Do We Use Radar Remote Sensing?

Nowadays, everyone is trying to work effectively on remote sensing and understanding of various applications of this technology. This is because, we can reduce the time and cost in a project. In addition, for the places that are inaccessible remote sensing can be implemented effectively to detect an object we are looking for.

Imaging radars are among the latest additions to a variety of remote sensing instrument available for analyzing Earth resources and for monitoring the environment. So far, the results obtained from many application oriented Research and Development (R&D) studies and from the operational use of airborne imaging radars are encouraging. But knowledge regarding the full extent of their capabilities and applications of radar remote sensing are still relatively limited compared to the experience with established techniques such as aerial photography and optical remote sensing techniques from space, e.g. LANDSAT TM, SPOT (Drury 1987; Ulaby 1989; Ali and Pirasteh 2004; Avery and Berlin 1992; Bürgmann et al. 2000; CCRS 2004, 2006; Pirasteh et al. 2009). So, why do we use radar?

The answer to this question is threefold. A very valid reason for using radar, from an operational point of view, is its *all-weather imaging capability*, since microwaves can penetrate cloud and any weather condition. Radars operating at wavelengths greater than 2 cm are not significantly affected by cloud cover, whereas rain does become a considerable factor for systems imaging at wavelengths below 4 cm. Furthermore, imaging radar operates independently of sun illumination, since it provides its own scene illumination as an active remote sensing system. The radar images have more potential to extract the information in haze climate conditions. This makes the advantages of using radar images (Goldstein 1997).

Microwaves also have the ability to penetrate a surface layer, for example, a vegetation canopy, more deeply than optical wavelengths can. However, there are a number of limiting factors (Goldstein 1997) to consider, since the extent of penetration is determined by the moisture content and the density of the vegetation on one hand, and by the wavelength of the radar and its viewing geometry on the other.

The penetration capability of longer radar wavelengths is much better than that of shorter wavelengths and thus potentially provides information on the vegetation volume. But shorter wavelengths provide more information about the top of the vegetation canopy. In the absence of any vegetation cover, microwaves can also penetrate soil, particularly when the soil is dry. The penetration is very much a function of wavelength. Longer wavelengths penetrate dry soil significantly, i.e. in magnitudes of centimeter, decimeter and even meter: the degree of penetration for shorter wavelengths is comparatively low, i.e. in the millimeter range, but nevertheless larger than the penetration of optical sensors.

The third reason for using radar systems from the fact that the information extracted from RADAR images is unique in its own right. The information content of radar imagery differs from the information content of optical imagery and may therefore be complementary. Consider the example of a vegetation canopy: the content of imagery taken in the visible or infrared regions of the spectrum is largely determined by the molecular resonance in the surface layer. However, the content of a radar image of the same object would be determined by the geometric properties, or structure and the moisture content of the surface as well as the volume of the vegetation canopy. The combined analysis of both data sets renders more useful information and results than the interpretation of one data set alone.

The following imaging characteristics set microwave remote sensing systems, particularly synthetic aperture radars (SARs), apart from the familiar sensor systems such as multispectral scanners:

- Radar is sensitive to surface roughness, moisture, electrical properties and motion within the illuminated scene;
- Radar instruments can be designed to record phase and polarization characteristics of the reflected microwave energy;
- Radar imagery shows relief displacement such as layover as a result of the slant range viewing geometry;
- SAR imagery displays speckle, or image ‘noise’ because of the coherent nature of the system.

These are important characteristics that will provide the radar with a different frame of reference for analyzing remote sensing data. A person familiar with aerial photography or multispectral image interpretation may find it relatively easy to identify objects on radar imagery by virtue of their size and shape alone, for example agricultural field patterns. However, the analysis of radar image tone and texture of these fields requires an understanding of the backscattering properties, of radar image formation and of the processing techniques available for radar data.

In addition, the recent technology of RADAR is *Interferometric synthetic aperture radar* (InSAR) remote sensing data. InSAR remote sensing data (Fig. 14.1) can be used in various applications of environment and earth sciences including natural hazards. For example: the Bam earthquake in Iran (Saraf et al. 2008; Fielding et al. 2009) occurred in December 26, 2003 with 6.6 magnitude has been studied (Amani et al. 2013) using InSAR data (Fig. 14.2).

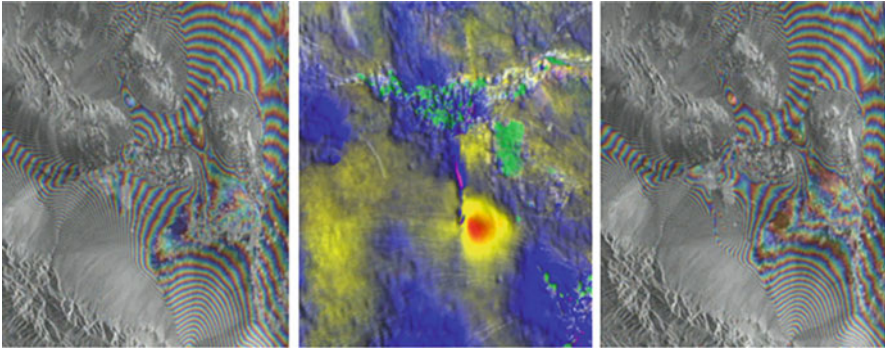


Fig. 14.1 Bam area’s topo-InSAR images and DEM (After Tarikhi 2011)

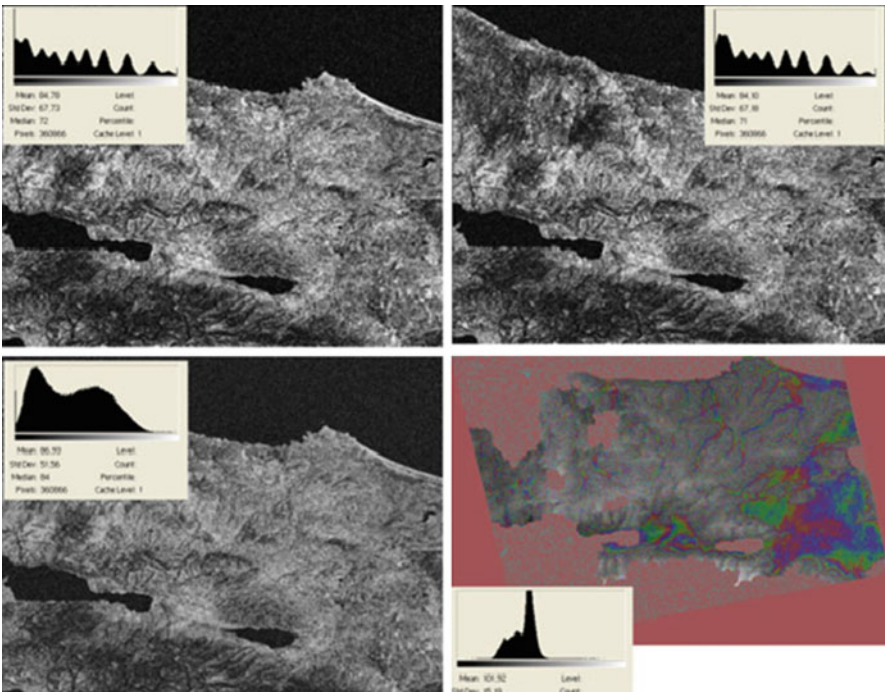


Fig. 14.2 InSAR products of Izmit area in western Turkey

14.2 Multiple-Look Processing

The appearance of speckle in a SAR scene, or multiplicative image noise, as described before, can be reduced using a technique known as multi-look processing. The concept of multi-look processing is SAR is a relatively simple one, whereby the along-track beam, Doppler bandwidth (Ren et al. 2002) is filtered into a number of

sub-beams. Each of these sub-beams, or sub-bands, provides an independent ‘look’ at the illuminated scene. This results in an enlarged resolution cell length and a number of independent images. The distribution of speckle levels within each ‘look’ will also be independent of each other. If the ‘looks’ are summed, resulting image intensity will have reduced speckle components. In the case where N independent images have been formed and systematically averaged the speckle variance is reduced by a factor of N .

The maximum number of “looks”, i.e. non-overlapped sub-apertures, over the full azimuth beam width is seldom processed. There are two reasons: to minimize signal ambiguities, and to maintain a reasonable image resolution. The latter point is of some consequence. The trade-off in Multi-look processing is that the available resolution of the image is also degraded by a factor of N , because in order to generate independent ‘looks’, different portions of the original signal must be used. Consider this example: the azimuth bandwidth of the SEASAT SAR data is sufficient to allow for a maximum azimuth resolution of approximately 6.5 m, if the signal is processed to full coherence; multi-look processing, and speckle reduction as a result, achieved 25 m image resolution by taking four independent “looks”.

The number of ‘looks’ one may desire depends very much on the SAR application field in mind and may vary accordingly. Those applications concerned with fine detailed structure or small area targets may place greater emphasis on high spatial resolution; other applications which require good radiometric resolution may choose a larger number of ‘looks’ when specifying SAR processing options. It is necessary to specify both the spatial resolution and associated number of look-requirements.

14.3 Radiometric Correction of Digital SAR Data

The radiometric fidelity of SAR imagery is affected by intensity variations resulting from surface scattering geometry and antenna pattern variations (Sabins 1987). The surface scattering geometry causes radiometric distortions, because at increasing incidence angle down-range less power is received. This causes less intense signal returns and less image brightness. Reference is made to the ‘radar equation’ (Eq. 14.1), which states that the power received is inversely proportional to the fourth power of the range. This relationship is known as the R^4 power loss. The antenna pattern causes radiometric distortion in the range dimension, because an antenna transmits more power from the centre of the antenna than from its edges. This results in more intense radar returns in the mid-range of the image swath relative to the near- and far-range edges where illumination is less intense.

Simple empirical techniques for correcting radiometric distortions in a SAR image (Richards and Jia 1999) may include the following steps. At various range locations, areas with the same surface state are identified. An average intensity value of the pixels is computed for each area and plotted versus range. Then a

smooth curve is fitted through these points. A multiplicative correction factor (C_i) is then obtained for each range sample by dividing the maximum value on this curve by the value at a given range sample:

$$C_i = S_{\max}/S_i \quad \text{for } i = 1 \dots N \quad (14.1)$$

Where S_i is the value on the smooth curve at a specific range sample i and S_{\max} is the maximum value encountered. Thus, a corrected data value V , for this range sample may be obtained by

$$V'_i = C_i V_i \quad \text{with } V_i \text{ being the uncorrected data value} \quad (14.2)$$

Sophisticated SAR systems use a Sensitivity Time Control (STC) function to accommodate large variations of range focused radar returns over a uniform surface. If the antenna pattern and the terrain type are well known, a STC function can be applied to incoming signals. The STC function has the effect that systematic variations in the processed image intensity (Pirasteh et al. 2010) in range is at a minimum. The new CCRS C- and X-band SARs, for example, offer five choices of STC functions: 'test', 'land', 'smooth water', 'rough water' and 'ice'. The 'test'--mode corresponds to an STC setting of 1, i.e. no modification of the range focused return signal. For the other modes nominal reflectance laws are modeled for each respective surface type. These models are then applied, together with the appropriate antenna pattern model, platform altitude and swath mode, to correct for systematic radiometric variations.

14.4 Geometric Correction of Digital SAR Imagery

In order to obtain a high degree of accuracy in the position of surface features in a SAR image, geometric correction algorithms are required to compensate for geometric distortions through image processing. Geometric distortions may be introduced internally by the SAR system itself. They are related to the inherent slant-range viewing geometry. External factors responsible for geometric distortions include changes in platform velocity, earth rotation, in the case of spaceborne SAR, and the map projection of the output imagery.

14.4.1 Internal Geometric Distortions

Recall that the natural coordinate system of the side-looking imaging radar is the slant-range plane along which the distance of an object relative to the SAR is defined. However, for image interpretation and reasons of geometric fidelity it is more desirable to measure the distance of objects from the ground- or nadir track of

the radar. The ground-range presentation has the advantage of being less distorted. The process to achieve this geometric correction is called slant-range to ground-range conversion. The relationship between slant-range and ground-range on a flat, horizontal surface is that of a simple but non-linear trigonometric function;

$$R_g = R_s / \sin \theta_i \quad (14.3)$$

Where θ_i is the incidence angle, R_s the slant-range, and R_g is the ground-range. The slant-range, which is always smaller than the ground-range, is highly dependent on the viewing geometry. Changes in incidence angle result in differential scale changes across the image swath. The relationship between the change in slant-range to ground-range is

$$DR_g = DR_s / \sin \theta_i \quad (14.4)$$

and differs at near-range and far-range. The scale of the slant-range presentation of an image is therefore not constant across the image swath. It results in maximum distortions when approaching the nadir, where the incidence angle equals zero, producing minimal scale change in slant-range and comparatively large discrepancy in ground-range. Because of the continuous change in range scale, there is only one range point where the slant-range scale is equal to a given map or ground-range scale; in the near-range the map scale would be smaller, and at far-range the map scale would be larger.

Assuming flat, horizontal terrain, this distortion may be removed by re-sampling the SAR data in the range dimension to ground-range using

$$R_g = R_s^2 - h^2 \quad (14.5)$$

where h represents the platform altitude. For high platform altitudes, i.e. spaceborne SARs, the curvature of the Earth surface must also be considered and factored into the equation.

14.4.2 External Geometric Distortions

External geometric distortions in SAR imagery are primarily induced by changes in terrain or target elevation and by changes in platform altitude, velocity and the effect of earth rotation. It has been demonstrated that any changes in elevation from a reference surface results in distortions known as foreshortening and, in extreme cases, layover. Although the internal system related distortions can be predicted by correcting the slant-range image plane to a ground-range image plane, the removal of external distortions due to elevation differences requires additional information. Two sources for this information are conceivable: topographic information (Pirasteh and Ali 2005) in form of digital elevation models (DEMs) (Mussakowski

et al. 1989; Wall et al. 1991), or from a second imaging angle, as available in radar stereo data or interferometry. Since radar stereo or interferometry data are not readily available in most cases, DEM information becomes an essential element for the determination of local distortions in radar imagery.

In general, two methods have been proposed for image rectification of terrain distortions. One relies mainly upon DEM information and has been used in conjunction with airborne and spaceborne SAR data. The other utilizes the platform trajectory information with a limited amount of DEM data and has been applied to correct spaceborne SAR data. The first method depends on the relative registration of a SAR image to a simulated image generated from the DEM. This technique employs a ‘rubber-sheeting’ process, after scan- and skew-distortions of the earth’s surface have been eliminated. A series of common reference points on both the actual and the simulated image are required in order to estimate the polynomial coefficients of the warping function. This function is then used to transform the radar image coordinates into the simulated image coordinates. Once the SAR scene is co-registered a re-sampling routine may be applied to provide a rectified format. The accuracy of this format is a function of the density of the selected reference points, or ground control points (GCPs). This method is often applied for small SAR sub-scenes.

The second method does not require the generation of a simulated radar image from a DEM, nor does it rely on a dense grid of GCPs to characterize the image-to-map distortions. Instead, an algorithm is employed which models the inherent geometric distortions based on the radar ephemeral data, such as platform altitude, the signal Doppler parameters, and the local terrain elevation. Using this algorithm an automated registration transformation may be performed. Only very few GCPs are required to remove residual translational errors between the predicted location and the actual geodetic location of a target area on a topographic map. In the case of severe terrain distortion, as in SAR images of mountain areas, DEMs are used in conjunction with the imaging geometry to generate a transformation ‘map’. This ‘map’ removes the local distortions, or foreshortening, when the slant-range pixels of an image are spatially mapped into their respective geo-coded pixel location. Using raw satellite SAR data it may generate an output product with an absolute location uncertainty of less than 50 m.

14.5 Enhancement of Digital SAR Data

Apart from radiometric and geometric corrections, a number of digital image processing techniques (Figs. 14.3, 14.4, and 14.5) may be applied to enhance the image content of a SAR scene. These enhancement techniques are useful, because they may provide a more suitable image product for subsequent manual interpretation (Trevett 1986). They can also be applied before or after performing digital classification. Enhancement techniques include filtering for (additional) speckle reduction, edge enhancement and contrast stretching. In addition the value of a SAR

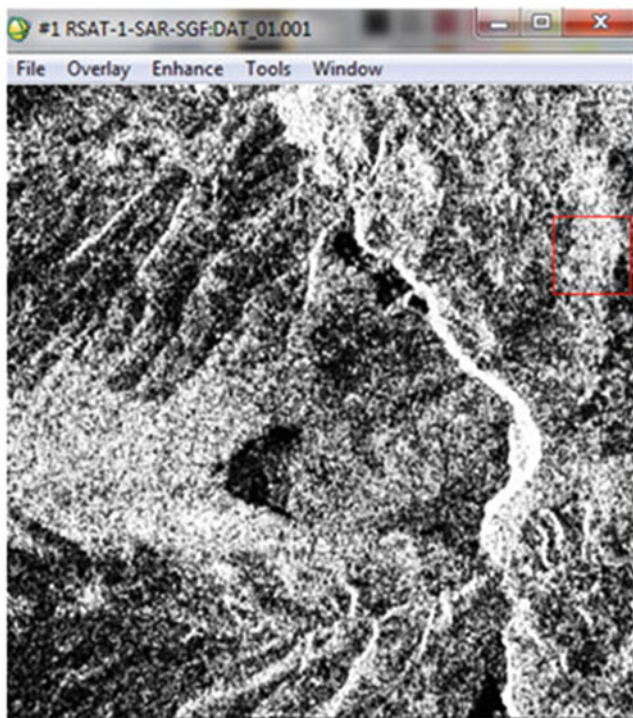


Fig. 14.3 Enhancement equalization

dataset can also be increased by co-registering the data with other remote sensing or GIS data available.

14.5.1 Speckle Reduction

The problem of speckle in SAR imagery has been addressed in previous chapter, and the multi-look concept to improve speckle reduction in the signal processing domain has been introduced in previous section in the image analysis domain, further speckle reduction may be achieved by using smoothing algorithms, or filters. Among the variety of filters available, four examples are introduced in the following discussion.

Average filtering is a very simple way of reducing the appearance of speckle. A window of x -number of rows and y -number of columns within the image matrix is selected. It is usually 3 by 3 or 5 by 5 pixels in size. The intensity of the centre pixel of the defined window is then replaced by the average value of all pixels around it. By sliding this filter window along the rows and columns of the image matrix, a

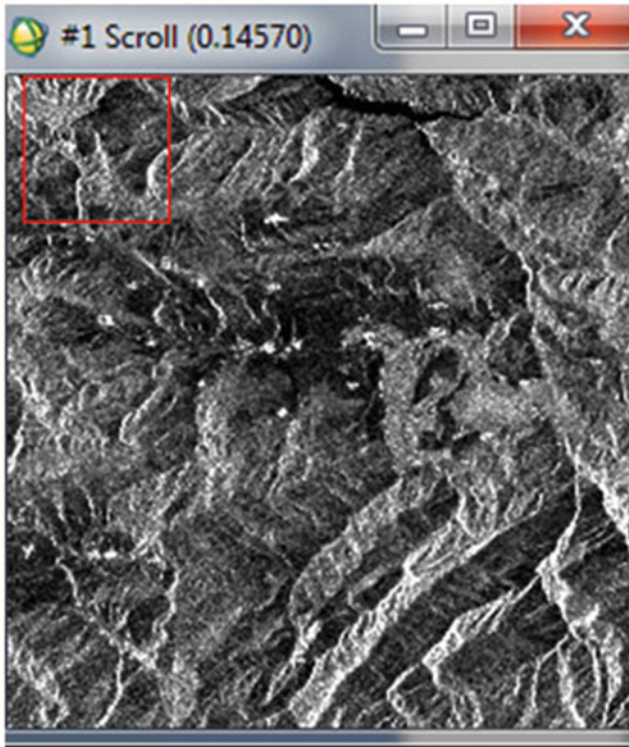


Fig. 14.4 Enhancement Lee

smoothing effect is achieved, because the intensity of the pixels within the window is now replaced by an average value.

Median filtering results in a similar effect. The filtering process works in the same way as average filtering. The difference lies in the fact that the centre pixel of the filtering window is replaced by the median or middle value of the surrounding pixels. The disadvantage of the average and median filters is their insensitivity to edges and their tendency to smooth out areas of interest. In order to avoid these shortcomings, other filters, such as the variance filter or the convex hull filter, may be applied.

The variance filter uses a process from which the intensity value of the centre pixel of the filter window is replaced by the statistical standard deviation of the surrounding pixel values. Variance filtering is therefore more sensitive to abrupt changes in image intensity values. It achieves a smoothing effect while still preserving most of the sharp changes.

The convex hull filter is a geometric filter. It evaluates the intensities of neighboring pixels within a filtering window in a three-dimensional space. The result of the smoothing operation is reduced small-scale intensity variation as it occurs in speckle, and it preserved intensity variation of large-scale image features.

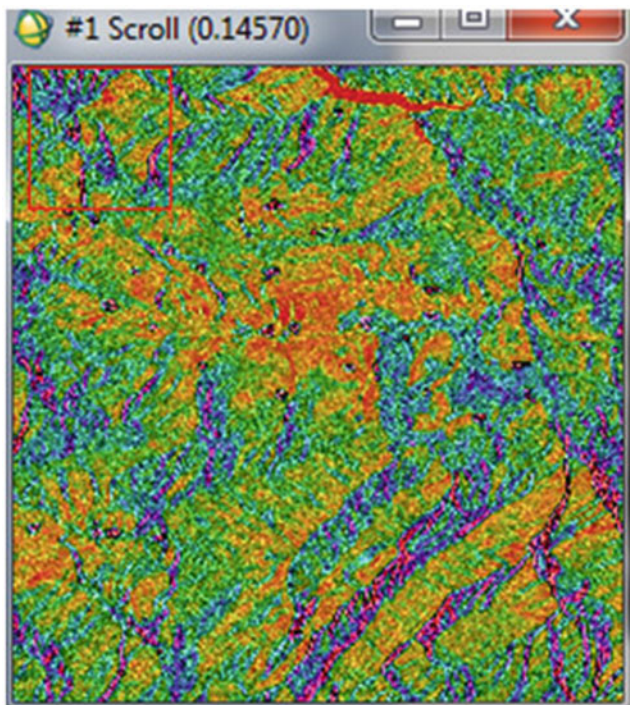


Fig. 14.5 Synthetic color image

14.5.2 Edge Enhancement

The brightness variations that define the edges and the text texture of objects in a SAR scene are an important element in image interpretation. Objects of interest may include those with a strong linear component, for instance geological fractures, ocean wave fronts, or the edges of pack ice. An increase in local contrast may be achieved by suppressing gradual brightness variations, which tend to obscure the object of interest. Edges and linear features are composed of rapid brightness variations, or high spatial frequencies, of a set of dark pixels next to a set of bright pixels in an image. There a number of edge enhance algorithm which have been designed to highlight these features. The examples presented below include the high pass filter, the K-averaging filter and Fast Fourier Transform (FFT). The variance and convex hull filters may be used for this purpose as well, but they are better suited for reducing the appearance of speckle.

In the high pass, or Laplacian filtering process the low frequency component of an image, as averaged over the filter window, is subtracted from the original image. In order to avoid the occurrence of negative pixel values, a constant is added to the intensity value of each pixel. An important consideration in the choice of the filtering window is not only the size of the window, but also its shape. Square

windows tend to enhance edges in all directions. A particular directional trend or orientation of edges and linear features may also be enhanced by using a rectangular filtering window.

In the K-averaging filter process (Ghandeharian et al. 2009), the filtering window is divided into sub-windows, thus creating a two-dimensional filter. A comparison of the average values and the standard deviation of the various sub-windows determine where in the window rapid brightness variations, e.g. 'edges', occur. This feature is then enhanced by averaging only those sub-windows along the features where rapid brightness variations were detected.

Linear features can also be analyzed through the fast Fourier transformed (FFT) of an image. The FFT can be used as an edge enhancement tool by smoothing the transformed image by means of an average filter, and then removing the very low and very high frequency components of the image by intensity level slicing. After the FFT, averaging and level slicing procedure the image is inverse Fourier transformed back into a residual image of the original scene.

14.5.3 Contrast Stretching

Synthetic aperture radar data potentially have a very wide dynamic range, encompassing intensity levels from 0 to more than 10^7 . Once processed and output on a CCT, the signal intensity is compressed to intensity levels which in the case of 8-bit data range from zero, for dark signatures, to 255, for very bright signatures. Yet, the full recording range of 256 intensity levels is rarely utilized. On average, SAR scene intensity occupies only half the digital levels available. This results in a greatly reduced image contrast, which may potentially cover the remaining intensity levels. The intention is to make optimal use of the limited dynamic range of the digital tape and avoid saturation of the intensity values.

Therefore, the idea behind contrast stretching is to redistribute the pixel values utilizing the full brightness range of the digital tape. A number of algorithms have been developed to enhance digital imagery in this fashion. Contrast stretching can also be applied to match image intensities to the characteristics of display and recording devices. The data manipulation process usually consists of two steps; First, the distribution, or histogram, of the pixel intensities in a given scene within the potential range, e.g. zero to 255, is evaluated. Then, the pixels are redistributed within the range of 0–255. Criteria for the redistribution can be selected by the image analyst and may include linear contrast stretch and non-linear contrast stretch. It is important to note that digital contrast enhancement should only be performed after other processing procedures have been completed, since contrast stretching results in some manipulation of the original pixel values.

The simplest form of contrast enhancement is called linear contrast stretching. It is based on the following procedure: Once the histogram of scene intensity values is generated, a digital number (DN) in the low range of this histogram is assigned to very dark, e.g. zero. Likewise, a high DN value in the upper range is assigned to

very bright, e.g. 255. In the example, digital number values of 49 and 106 are assigned to 0 and 255, respectively. In the following contrast stretch the remainders of the pixel values are distributed linearly between the assigned extreme values of zero and 255. This results in an improved contrast ratio of most brightness values in the original image. However, it should be noted that linear contrast stretch may also result in a loss of contrast at the extreme DN values. This implies saturation, or ‘clipping’ of very low and very high DN values.

Another form of contrast enhancement is the non-linear contrast stretch, whereby the intensity values of the original histogram are subject to a uniform distribution stretch, i.e. the original histogram is being redistributed to produce a uniform population density of pixels along the DN axis. This enhancement is most effective in providing better contrast for the most populated range of intensity values in the original scene. The drawback of the uniform distribution stretch is its compression of intensity values in the lower and upper ranges of the original histogram, similar to the one encountered in the linear contrast stretch procedure. However, a contrast stretch of the lower or upper ranges is required, and a non-linear Gaussian stretch may be applied in order to accommodate this. The Gaussian stretch fits the original components of the histogram to a normal distribution curve with zero and 255 as its lower and upper limit, respectively. The trade-off is a relative loss of contrast in the moderate intensity range.

14.6 Simulation of SAR Imagery

Many aspects in the design of a SAR system have very large cost impacts. Therefore, it is very important to fully understand the implications of specific design and system parameters on the resultant imagery prior to the implementation of a SAR. The question of how, for instance, a spaceborne SAR design can meet the requirements of the user must be addressed. Some parameters can be modeled by system engineers. However, the impact of other parameters, such as wavelength and incidence angle, on the reflectivity of targets needs to be explored and evaluated for a particular application by means of image simulation.

By examining simulated imagery with known characteristics the system designer and the user of SAR data alike obtain valuable information that helps to optimize the system design. Furthermore, systematic image simulation can also assist in the development of useful interpretation methodologies for spaceborne SARs appropriate filtering techniques (Sabins 1987) for image enhancement, the definition of SAR data compression and sampling techniques (Gibbins and Slaney 1991), as well as in the development of image and map registration techniques. Consider this example from an applications point of view. By simulating a spaceborne SAR with a 100 m 6-look resolution from a high resolution airborne SAR image of sea ice in the Beaufort Sea some important image characteristics could be derived. The simulations suggested that small hazards for shipping in these ice infested waters, for example multiyear ice floes, pressure ridges and icebergs

less than 100 m in size, were partly lost in the speckle pattern; otherwise, the scale and the resolution of the simulated imagery proved to be very valuable for large area strategic ice forecasting and operational planning.

The generation and evaluation of realistic image examples from hypothetical spaceborne SAR systems is of interest to those nations, which plan to implement such systems. In Canada, a methodology (Singhroy and Saint-Jean 1999) has been developed under contract by Intera Technologies Limited to simulate SAR imagery (CSA 2007; D'Iorio et al. 1997). The main purpose of the SRSIM software package is to simulate spaceborne SAR data of the ERS-1 and RADARSAT type, as they have been available since 1990s. The package provides a set of filters that resample fine resolution airborne SAR data, or those from synthetic test sites, and simulate the parameters of the spaceborne SAR under consideration. This can be accomplished by generating an idealized yet realistic source target reflectivity map and by generating speckle, thermal system noise and other system perturbations. Reflectivity map, speckle and thermal noise data are then combined to create the simulation. Speckle is simulated by generating a two-dimensional array of noise values. The user can specify the position, shape and weight for each sub-aperture ('look'). The usefulness of the resulting image can be determined from the means of standard digital image analysis techniques. Moreover, new image analysis, interpretation and classification techniques can be refined and tested using simulated imagery.

14.7 Visual Interpretation of SAR Imagery

The most common approach to visual SAR image interpretation is that of a modified air photo analysis procedure. The majority of airborne radar surveys conducted during the 1970s and early 1980s relied heavily on visual interpretation methods. Image analysts were familiar with both air photo and radar techniques. Major natural resource surveys, such as RADAM BRAZIL (Marcelo et al. 2011) or the Nigerian NIRAD Project, contributed to the development of manual analysis techniques. Likewise, airborne radar imagery of ice infected coastal waters of northern and eastern Canada have been interpreted manually by skilled ice observers for many years.

Visual image analysis procedures examine various important image elements, including tone, texture, size, shape and association. These image elements are equally applicable for the interpretation of SAR imagery. But in modifying the principles of visual air photo analysis for use in radar image interpretation, one should keep in mind that radar is a range measuring device. The analyst has to consider the radar parameters and the ground parameters when interpreting a radar image, since variations in the average backscatter cross-section (σ^0) result in different image characteristics, first and foremost. One must be familiar with interaction mechanism(s) of radar system parameters and ground parameters and what effect changes in these parameters might have on σ^0 . still, the analyst is left with two basic questions; first, are the parameters that the analysis of ground

features is concerned with of significance to the radar backscatter? Secondly, which ground parameter(s) determine(s) a ‘boundary’ or tonal change?

14.7.1 Tone

The visual interpretation of a radar image attempts to infer significant features in an area from observed tonal variation. Unlike aerial photography, where changes in tone are related to the reflection characteristics of an illuminated surface averaged over a relatively broad spectrum, radar image tone is the result of reflection at only one wavelength. The tonal expression in a SAR scene is generally a function of the strength of the radar backscatter from a corresponding ground area. The variations in the average backscatter cross-section σ^o for a given target has a profound influence on radar image tone, and therefore on the interpretability. σ^o is a function of many parameters:

$$\sigma^o = f(\kappa, \tau, P, \theta, \epsilon, \Gamma_1, \Gamma_2, \nu) \quad (14.6)$$

where the radar system parameters are given by:

κ = wavelength of the radar;

τ = depression angle;

P = polarization of the radar beam (both transmit and receive);

and where the ground parameters given by:

θ = aspect angle (local incidence);

ϵ = complex dielectric constant;

Γ_1 = micro-scale surface roughness of the air – solid boundary relative to the radar wavelength;

Γ_2 = subsurface of a discontinuity layer;

ν = complex volume scattering coefficient

To determine which parameter(s) cause(s) a particular change in grey tone (Fig. 14.6) requires ancillary information with regard to the terrain and surface properties; this may require the collection of ground data and/or the use of multi-parameter radar data, data from other sensors, or a combination of the above. The obvious approach is to select the controllable radar system parameters and strive to optimize the information that might be obtained from the terrain parameters. This selection requires knowledge of the backscatter mechanisms and the study of theoretical models and experimental data on the part of the interpreter.

The grey tone on the image is a relative index rather than an absolute one, because the exposure level of a particular SAR scene is controlled by a number of factors. These include, for example the gain setting of the radar system, chemical film processing of optically correlated data, or numerical corrections applied during digital processing. Imagery can therefore be as light or as dark as desired. For this

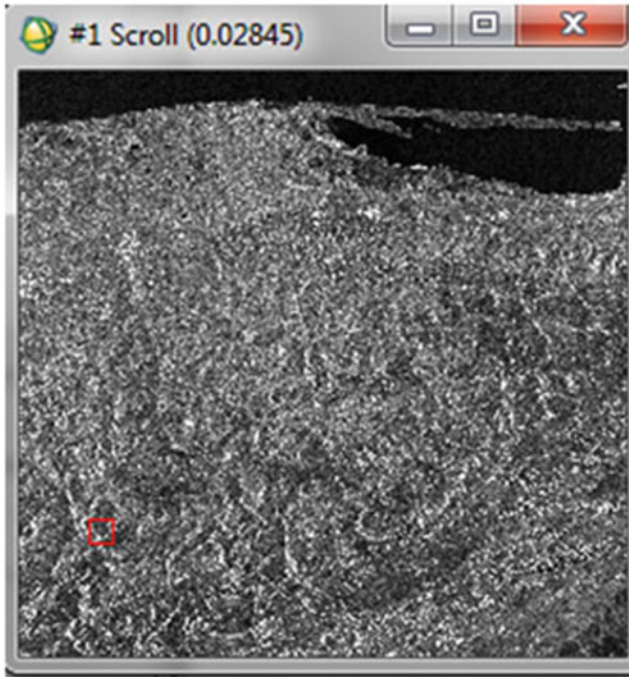


Fig. 14.6 Changes in tone

and other reasons, visual interpretation of (uncalibrated) radar imagery can only make a qualitative assessment of discrete tonal elements by detecting, identifying and recognizing light or dark levels of grey tones. Image tone, or density, may be described in a qualitative manner by means of grey tone scales, similar to those used for air photo interpretation. These can be combined with texture scales. An effective procedure may consist of three steps. First, the range of grey tones for a particular surface category must be assessed. Secondly, a number of individual features are identified by means of field check or other sources of information, using these features as a reference for the tonal classification; other features of the same category can then be interpreted.

14.7.2 Texture

Texture is of similar importance for the identification, mapping and classification process, particularly for geologic and vegetation mapping. Texture is defined as the spatial pattern or frequency of tonal variation within a particular area. It is produced by an assembly of features too small to be identified individually. Like contrast in grey tones, contrast in image texture, or speckle for that matter, allow for the

identification and delineation of homogeneous areas with particular surface properties.

The texture of a SAR scene may be classified as being smooth, fine, linear, gravity, speckled, flecked or checkered. Various degrees of coarseness can be applied in the different categories. Factors influencing the appearance of texture on a radar image include the dynamic range of the SAR system, processing and the amount of enlargement of the photographic product. These affect the coarseness of texture and must be considered in the interpretation. The texture on radar imagery is not as easily affected by the “gain setting” of the SAR system as tone and, therefore, remains relatively constant from one image to another.

Three components of texture, i.e. micro-texture, meso-texture and macro-texture, can be identified. Micro-scale texture, or speckle, is an inherent characteristics of SAR imagery, because of the sampling statistics of the fading signal, resolution, and independent sampling, i.e. single or multi-look processing. Even though a surface may be very smooth, it will still display a very fine, random texture at the micro-scale level. Meso-scale texture is produced by spatial in homogeneities, usually on the order of several resolution cells. It tends to be spatially and not randomly organized and relates, for example, to the distribution of vegetation associations; however, individual elements within a plant community may not be identified. Macro-scale texture allows the identification and delineation of unit areas that are located within boundaries of relative homogeneity. These may consist of an assembly of well-resolved terrain elements, but with different backscattering levels. In very general terms, macro-scale texture can also be conceived as a pattern, if it refers to an orderly spatial arrangement of features on an image. Patterns can be assessed and described using such categories as orientation, spacing, density or uniformity.

14.7.3 Size and Shape

The size of features in a radar image is essentially a function of the radar system parameters, the scaling ratio of the imagery and the amount of magnification. High resolution SAR imagery can be enlarged as much as ten times without suffering an appreciable loss of detail. Radar imagery are generally smaller in scale than aerial photographs. Therefore, the images of particular features are smaller than their equivalents on air photos obtained from similar platforms altitudes. However, SAR does have an advantage in that its resolution is independent of range, which makes its rendition of small sized features in far range superior to aerial photography.

Shape is defined as the spatial form of an object or area with respect to a relatively constant contour, or background. Regular geometric shapes, and the regular spatial arrangement of certain patterns for that matter, are valuable clues for distinguishing natural and cultural features. Even though natural features tend to have irregular outlines, many can be identified by their size and shape alone, for instance volcanic cones, glacial features or alluvial fans. The shape of natural

features and manmade objects is closely related to the oblique viewing geometry of the radar. The shape of radar shadows gives an indication of the terrain type, whereby the length of the shadow may provide an estimate of terrain height. Likewise, the shape of radar shadowing may be used to infer the spatial form, as in the shadow projection of the crest line of a mountain range.

14.7.4 Association

Many features or objects are so closely interrelated that one tends to indicate, or confirm, the other. An interpreter of a radar image can often derive additional information about a feature of interest by examining associated elements. Elements usually associated with it may provide valuable clues for the presence of this feature even if it is obscured. Take the example of a ship at sea. Imaging radar may detect the characteristic V-shape of the ship's bow wake, but the signature of the ship itself may be difficult to detect. Therefore, the term association refers to a situation where a feature is not recorded or only poorly displayed on the radar image, but where some of its attributes are recorded to allow the detection of the latent features.

References

- Ali SA, Pirasteh S (2004) Geological application of Landsat Etm for mapping structural geology and interpretation: aided by remote sensing and GIS. *Int J Remote Sens* 25(21):4715–4727
- Amani A, Mansor S, Biswajeet P, Lawal B, Pirasteh S (2013) Coupling effect of ozone column and atmospheric infrared sounder data reveal evidence of earthquake precursor phenomena of Bam earthquake. *Iran Arab J Geosci*. doi:10.1007/s12517-013-0877-6
- Avery TE, Berlin GL (1992) *Fundamentals of remote sensing and air photo interpretation*, 5th edn. Macmillan Publishing Company, New York, p 472
- Bürgmann R, Rosen PA, Fielding EJ (2000) Synthetic aperture radar interferometry to measure earth's surface topography and its deformation. *Annu Rev Earth Planet Sci* 28:169–209
- Canada Center for Remote Sensing (CCRS) (2006) *Fundamentals of remote sensing: teacher notes*, p. 258
- Canada Centre for Remote Sensing (CCRS) (2004) *Radar remote sensing training package (GlobeSAR-2)*, educational resources for radar remote sensing, p. 955
- Canadian Space Agency (CSA) (2007) *Radarsat 2: a new vision*, catalogue, p. 13
- D'Iorio MA, Budkewitsch P, Mahmood NN (1997) Practical considerations for geological investigations using RADARSAT-1 stereo image pairs in tropical environments, *geomatics in the era of RADARSAT*, proceedings, Ottawa, Canada, 27–30 May 1997, Paper #233, pp: 9
- Drury SA (1987) *Radar remote sensing*. In: *Image interpretation in geology*, London, Allen Unwin Pub., 165–174 (3rd Edition)
- Fawwaz T. Ulaby (1989) [Handbook of radar scattering statistics for terrain \(Artech house remote sensing library\)](#), Artech House (March 1, 1989), Library of Congress Cataloging, USA
- Fielding EJ, Lundgren PR, Bürgmann R, Funning GJ (2009) Shallow fault-zone dilatancy recovery after the 2003 Bam earthquake in Iran, *Nature*, 458:64–68. doi:10.1038/nature07817
- Ghandeharian B, Yazdi Hadi S, Homayouni F (2009) Modified adaptive center eighted median filter for suppressing impulsive noise in images. *Int J Res Rev Appl Sci* 1(3):218–227

- Gibbins WA, Slaney VR (1991) Preliminary geologic interpretation of SAR data, yellowknife-hearn lake area, N.W.T. *Antarct Inst N Am* 44:81–93
- Goldstein RH (1997) Atmospheric limitations to repeat-track radar interferometry. *Geophys Res Lett* 22:2517–2520
- Marcelo Muniz Benedetti, Nilton Curi, Gerd Sparovek (2011) Updated Brazilian's Georeferenced Soil Database – An Improvement for International Scientific Information Exchanging, Principles, Application and Assessment in Soil Science, pp 310–322. <http://www.intechopen.com/books/principles-application-and-assessment-in-soilscience/updated-brazilian-georeferenced-soil-database-an-improvement-for-international-scientific-informat>
- Mussakowski R, Trowell NF, Sage RP, Heather KB (1989) Digital integration of remote sensing and geoscience data for the Goudreau-Lochalsh study area, Michipicoten greenstone belt, Wawa, Ontario, Proceedings Seventh Thematic Conference on Remote Sensing for Exploration Geology, Calgary, Alberta, Canada, 2–6 October 1989, pp 1051–1065
- Pirasteh S, Woodbridge K, Rizvi SM (2009) Geo-information technology (GiT) and tectonic signatures: the River Karun & Dez, Zagros Orogen in south-west Iran. *Int J Remote Sens* 30(1–2):389–404
- Pirasteh S, Rizvi SMA, Ayazi MH, Mahmoodzadeh A (2010) Using microwave remote sensing for flood study in Bhuj Taluk, Kuchch district Gujarat, India. *Int Geoinformatics Res Dev J* 1(1):13–24
- Ren H, Brecke KM, Ding Z, Yonghua Z, Stuart Nelson J, Chen Z (2002) Imaging and quantifying transverse flow velocity with the Doppler bandwidth in a phase-resolved functional optical coherence tomography. *Opt Lett* 27(6):409–411
- Richards JA, Jia X (1999) Remote sensing digital image analysis – an introduction, 3rd edn. Springer, Berlin, p 356
- Sabins FF (1987) Radar images, In: Remote sensing – principles and interpretation. 2nd ed., New York, W.H. Truman & Co., pp 177–234
- Pirasteh S, Ali SA (2005) Lithostratigraphic study from Dezful to Brojerd-Dorood areas SW Iran using digital topography, remote sensing and GIS. *Indian Pet Geol J* 13(1):1–13
- Saraf AK, Rawat V, Banerjee P, Choudhury S, Panda SK, Sudipta D, Das JD (2008) Satellite detection of earthquake thermal infrared precursors in Iran. *Nat Hazards* 47:119–135
- Singhroy V, Saint-Jean R (1999) Effects of relief on the selection of RADARSAT-1 incidence angle for geological applications. *Can J Remote Sens* 25(3):211–217
- Tarikhi P (2011) [Early warning and earthquake monitoring using new earth observation radar techniques](#), the APSCO's third international symposium on earthquake monitoring and early warning by using space technology that was jointly organized by the Asia-Pacific Space Cooperation Organization (APSCO) and the Ministry of Industry and Information Technology of China (MIIT), held on 13–15 September 2011 in Beijing, China
- Trevett JW (1986) Geological interpretation, In: *Imaging radar for resources surveys*. Chapman and Hall, New York, pp 139–160
- Wall SD, Farr TG, Muller JP, Lewis P, Leberl FW (1991) Measurement of surface microtopography. *Photogramm Eng Remote Sens* 57(8):1075–1078

Chapter 15

Development of a New Wetness Index Based on RADARSAT-1 ScanSAR Data

Quazi K. Hassan and Charles P.-A. Bourque

Abstract A new wetness index (WI) was developed based on the temporal patterns in radar brightness (β^0) in a timeseries of RADARSAT-1 ScanSAR images collected over the July–September period of 2005. The WI proposed here provided an indirect measure of soil water content (SWC), as β^0 was documented to vary with land-surface water content. Hydrological factors affecting SWC, such as soil texture, topography, evapotranspiration, etc., were not considered in the current determination of WI. WI-values generated with the proposed method were subsequently compared against field measurements of SWC collected from three separate areas, including densely- and sparsely-forested and non-forested areas (i.e., bare fields), all located in southcentral New Brunswick (NB), Canada. The comparison revealed adequate agreement between WI and SWC for all three areas, including dense forests, yielding coefficients of determination (r^2 's) of 74–99 %. Reasonable agreement for dense forests ($r^2 = 74$ %) indicated the potential of the method in determining SWC under heavily-vegetated conditions. This correlation would arise because of the equilibrium established between foliage water content (picked up by the radar signal) and SWC under normal, non-stressed conditions. A second evaluation of the method was conducted by comparing WI-values with spatial calculations of SWC obtained with the Soil Water Assessment Tool (SWAT) for bare-field conditions common to the potato-growing area of northwestern NB. Again, suitable agreement was obtained, yielding r^2 -values ranging from 65 % to 81 %. However, further research is needed to evaluate the usefulness of the method for other forested and non-forested regions of the world. In principle, because the method relies mostly on β^0 , it is highly likely the method can be used to assess SWC in many different types of natural environments.

Q.K. Hassan (✉)

Department of Geomatics Engineering, Schulich School of Engineering, University of Calgary, 2500 University Drive NW, Calgary, AB, T2N 1N4, Canada
e-mail: qhassan@ucalgary.ca

C.P.-A. Bourque

Faculty of Forestry and Environmental Management, University of New Brunswick, 28 Dineen Drive, PO Box 4400, Fredericton, NB E3B 5A3, Canada
e-mail: cbourque@unb.ca

© Springer Science+Business Media Dordrecht 2015

J. Li, X. Yang (eds.), *Monitoring and Modeling of Global Changes: A Geomatics Perspective*, Springer Remote Sensing/Photogrammetry, DOI 10.1007/978-94-017-9813-6_15

301

Keywords Foliage and soil water equilibrium • Radar brightness • Soil water content • SWAT model • Synthetic aperture radar • Vegetation cover

15.1 Introduction

Soil water content (SWC) is a measure of the total amount of water, including water vapour, contained within a column of soil above the saturated zone above the groundwater table. The variable is one of the most critical regarding: (i) the duration and intensity of droughts; (ii) the production of crops; and (iii) the amount of soil erosion and runoff. The most standard protocol in estimating SWC is based on the “gravimetric” or “volumetric” method (Hassan et al. 2007). Both methods estimate SWC accurately, but only provide point measurements given the extent of work required to process a single field sample. Consequently, soil sampling fails to provide the spatial information needed for land-management applications. Remote sensing platforms, however, can provide greater detail of SWC at high spatial resolution, but small enough for implementation at the land-management unit (Hassan et al. 2007).

Radar remote sensing is an effective way of mapping SWC under adverse weather conditions, including under cloudy conditions. Since 1991, a number of microwave sensors have been launched (e.g., ERS, JERS, RADARSAT, and ENVISAT), creating opportunity to study and map SWC at a multitude of spatio-temporal resolutions. Radar-based methods of estimating SWC have been broadly classed into five main algorithm-types based on: i.e., (i) semi-empirical Synthetic Aperture Radar (SAR) formulations, (ii) multi-temporal SAR for SWC change detection, (iii) SAR data fusion of images from both passive and active microwave sensors, (iv) SAR-data fusion of images from microwave and optical sensors, and (v) SAR and microwave scattering properties (Moran et al. 2004). The method is based on processing multiple radar images from identical passes (i.e., same polarization and incident angles), but for different times. Due to the simplicity and ease with which the “*multi-temporal SAR for SWC change detection*” method can remove artifacts created by uneven terrain and changes in vegetation cover, enormous opportunity exists with using the method in an operational setting. Table 15.1 summarizes various “*multi-temporal SAR for SWC change detection*”-based methods developed over the past few years.

Here, we propose to (i) develop a new wetness index (WI) based on a chronological series of RADARSAT-1 ScanSAR images of the same area taken at different times over the July–September period of 2005, and (ii) evaluate its potential to estimate SWC in areas of diverse vegetation cover, including dense forests in humid, forest-dominated landscapes of southcentral New Brunswick (NB), Canada, and the potato-growing area of northwestern NB. In the latter evaluation, we use SWC calculated with the Soil Water Assessment Tool (SWAT) as field-measurements of SWC were not available to us.

Table 15.1 “Multi-temporal SAR for SWC change detection” approaches used in the past

Source	Approach ^a
Shoshany et al. (2000)	Introduced multi-temporal backscatter ratios, such as the simple ratio (SR) and normalized radar backscatter soil moisture index (NBMI); used ERS SAR images over humid to semi-arid regions of Israel. Obtained strong relations for both ratios ($r^2 > 85\%$). However, the NBMI produced a stronger relationship with SWC in the 20–40 % range.
Wagner and Scipal (2000)	Determined a relative measure of SWC from dry, wet, and instantaneous values of radar backscattering coefficient, σ^0 ; used ERS Scatterometer images over western Africa. Demonstrated promising qualitative results with soil water index (SWI) over wet-dry climatic zones.
Wickel et al. (2001)	Established relations between σ^0 with SWC; used RADARSAT SAR images over the Southern Great Plains 1997 Hydrology Experiment Sites in Oklahoma, USA. Observed strong correlation for wheat stubble fields ($r^2 = 89\%$) and no correlation for pasture fields. Demonstrated potential of using ScanSAR modes of RADARSAT for multi-temporal estimates of SWC (e.g., Boisvert et al. 1996).
Lu and Meyer (2002)	Used a correlation image computed from radar-image pairs for explaining observed changes in SAR intensity; used ERS SAR over southeast New Mexico, USA. Correlated SWC increments (within the 5–20 % range) with increments in SAR intensity.
Thoma et al. (2006)	Employed four approaches; i.e., empirical, physical, semi-empirical, and image difference-based (i.e., delta index; DI) approaches; used ERS SAR and RADARSAT SAR images over Southern Arizona, USA. DI produced strong correlations with SWC ($r^2 = 91\%$) and provided overall better results in comparison to the other methods considered.
Pathe et al. (2009)	Calculated a relative SWC as a function of dry, wet, and instantaneous σ^0 from ENVISAT ASAR acquired over Oklahoma, USA. ASAR-derived SWC were compared against ground-based measurements of SWC and found that in 75 % of the cases, the standard deviation fell within 13–27 % of field-based SWC.
Baghdadi et al. (2011)	Used a change-detection technique between data acquired during rainy and dry seasons (considered as the reference images) to retrieve SWC. Derived SWC-values were approximately 2.3 % (RMSE) from ground-based measurements.
Qin-Xue and You (2013)	Applied approaches similar to those of Wagner and Scipal (2000) and Pathe et al. (2009) to calculate relative SWC using ENVISAT ASAR-data over Hubei Province, China. Demonstrated reasonable correlation for cotton fields ($r^2 = 78\%$).

^aSR-ratio of σ^0 from two different dates; NBMI-a function of instantaneous σ^0 and σ^0 for dry soil; SWI-a function of actual SWC, wilting point and field capacity; DI-a function of instantaneous σ^0 (i.e., wet condition) and σ^0 for the same soil under dry conditions; ASAR-advanced Synthetic Aperture Radar

15.2 Study Area and Data

The study area extends over 70 % of the Province of New Brunswick (NB) in eastern Canada, from NB’s southern coast along the Bay of Fundy to northcentral NB (Fig. 15.1). The area is characterized by its temperate evergreen-deciduous mix,

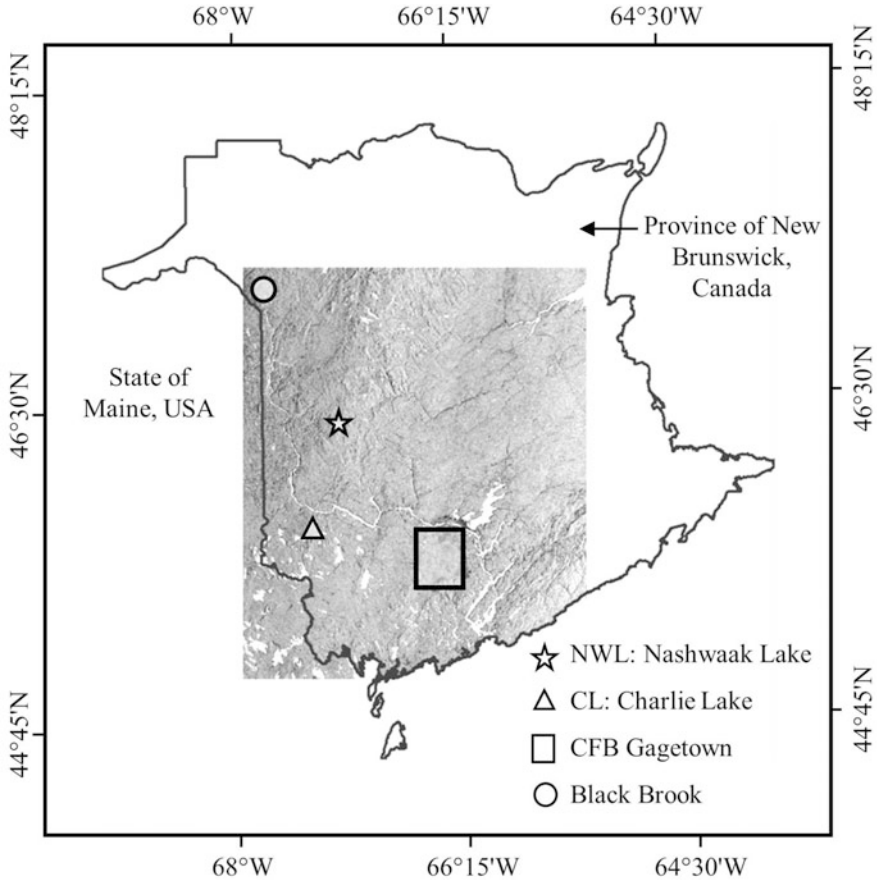


Fig. 15.1 New Brunswick study sites where observed and modeled volumetric soil water content were derived; sites are depicted as an overlay to the RADARSAT-1 ScanSAR image acquired on 01 September, 2005

transitional forest cover. The region experiences a cool-moist climate with mean annual temperature and precipitation ranges of 3.5–6.5 °C and 900–1500 mm, respectively. A generalized description of forest cover and geomorphology of NB can be found in Hassan et al. (2006).

The images used to generate WI include three descending RADARSAT-1 ScanSAR Narrow A (SNA) images, at a pixel spacing (resolution) of 25-m taken at incident angles of 20–40° in the C-band (i.e., 5.3 GHz). The images were acquired at approximately 6:00 a.m. local daylight time on 15 July, 08 August, and 01 September, 2005.

Field SWC conditions were measured at 10-cm depths at three representative areas having different vegetation cover. The areas include (i) two sites in dense forests (i.e., 100 % forested with a basal area in the range of 26–30 m² ha⁻¹; Xing

et al. 2005) in westcentral and southwest NB; i.e., Nashwaak Lake (NWL, 46° 28' 20" N, 67° 06' 00" W) and Charlie Lake sites (CL, 45° 53' 05" N, 67° 21' 25" W; Fig. 15.1), (ii) three locations in sparse forests at the Canadian Forces Base Gagetown, central NB (CFB Gagetown, 46° 40' N, 66° 22" W), and (iii) one location in a bare field at CFB Gagetown. A second evaluation of the method was conducted by comparing WI with SWC-values generated with a widely used hydrological model, the Soil Water Assessment Tool, SWAT (Arnold et al. 1998) for an area in the Black Brook Watershed in northwest NB (47° 07' N, 67° 46' W). Simulated SWC-values were descriptive of averaged soil water conditions within a 1-m soil block, in field conditions typical to the potato-growing area of northwest NB.

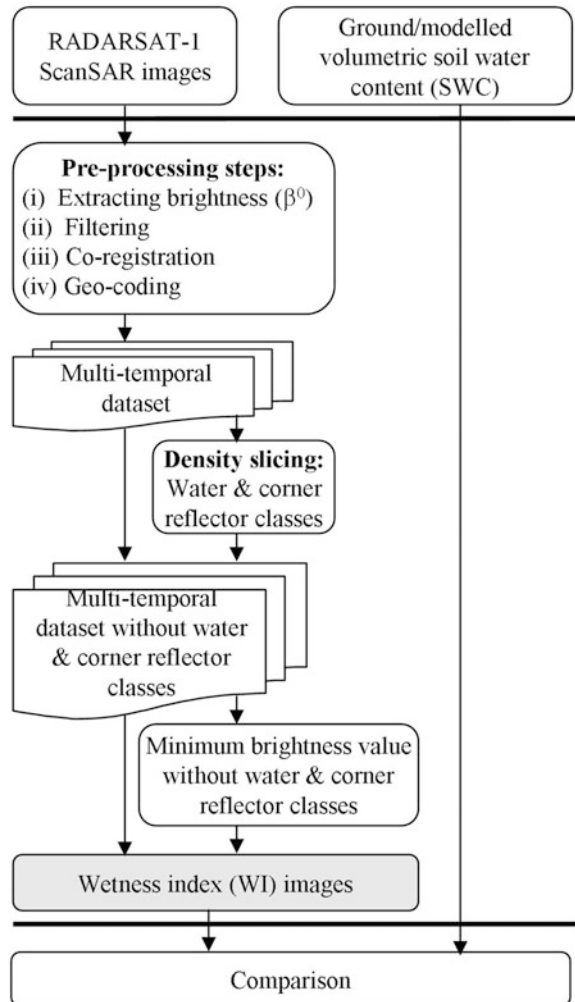
15.3 Methods

Figure 15.2 shows a schematic of workflow associated with deriving the new WI. The method is divided into three main procedural components, namely (i) the pre-processing of the RADARSAT-1 data, including extracting radar brightness values, filtering, co-registration, geo-coding, and creating a multi-temporal image sequence, (ii) deriving WI-values and associated images, and (iii) conducting comparisons between radar-based values of WI and estimates of SWC obtained in the field and with the ArcView™ GIS-version of the SWAT model (i.e., AVSWAT_2000; Luzio et al. 2002).

15.3.1 Image Pre-processing

Three calibrated, geo-referenced RADARSAT-1 ScanSAR images provided by the Canadian Space Agency (CSA) were used to extract radar brightness (β^0) in dB values following steps described in ALTRIX Systems (2000); β^0 is a measure of radar reflectivity in the slant range and independent of local incident angle. Instead of using the commonly-used radar backscattering coefficient (i.e., σ^0 ; a measure of radar reflectivity near ground range and dependent on local incident angle), we opted to use β^0 in this research. It is well recognized that β^0 is highly influenced by background features (Bamler 2000), such as surface roughness, local incidence angle, effective surface cover density and surface-scattering properties (e.g., biomass, leaf density), three-dimensional structure of the scattering surface (canopy layering, trunk placement, buildings), and dielectric constant of the scattering material. In general, background conditions vary with variations in SWC and the physiological status of the surface, particularly with respect to the vegetation cover. Since we intended to use images obtained during similar flight trajectories and signal polarization, the use of β^0 for estimating temporal changes in SWC by tracking changes in β^0 was possible. Note that the resolution of the β^0 images had

Fig. 15.2 Workflow in the generation of the Wetness Index (WI)-values and their comparison to soil water content (SWC), either measured in the field or modeled with the SWAT model



potential to be variable given that the incident angle of the ScanSAR Narrow beam varied from 20 to 40°. However, it was possible to proceed with a constant pixel spacing of 25 m for the β^0 images as these images were rectified (at 25-m resolution) by CSA (RADARSAT International 2004), prior to their implementation.

As speckles can hinder the interpretation of radar images, a Gamma-map filter (with a moving-window of 5×5 pixels) was employed to suppress speckles. Before filtering, the β^0 values (in dB) were converted to a power-scale, and then re-calculated into dB values as outlined in Wickel et al. (2001). The three images were co-registered by simply shifting the images using a stable high backscattering feature or corner reflector in both the x- and y-directions, as described in Hasan et al. (2003). Then, these images were geo-coded by using ground control points

(GCPs) to position and scale the images with respect to existing orthorectified LANDSAT-7 ETM+ images (from the 1999 to 2002 period) obtained from Geobase Canada website, <http://geobase.ca>, last accessed on 28 June 2008.

15.3.2 Deriving WI-Values and Associated Images

As an initial step, both low and high scattering land-surface features, such as water bodies and corner reflectors, were eliminated from the multi-temporal images. To do this, we used the density slicing approach of Lillesand et al. (2008) and delineation limits of β^0 (dB) < -12.22 and ≥ 0.00 to identify all water bodies and corner reflectors in the images.

For a given pixel and image, if a pixel was classified as either being water or a corner reflector in any one image, it was assumed that the same feature was also present in the other two images and excluded from all three images. Following elimination of water and high-scattering image features, we defined the minimum radar brightness value (i.e., β_{\min}^0) as -12.22 dB, coinciding with the driest brightness value. Wetness Index (non-dimensional) was then described as a function of β_{\min}^0 , i.e.,

$$WI = \frac{\beta_{\min}^0 - \beta_{\text{ins}}^0}{\beta_{\min}^0 + \beta_{\text{ins}}^0} \quad (15.1)$$

where β_{ins}^0 is the image-specific instantaneous radar brightness. WI-values from Eq. 15.1 vary from 0 to 1, with values = 0 representing dry conditions and values = 1, representing wet conditions, calibrated according to the wetness distribution in the current images. This new WI is founded on existing principles of another SWC-related index, namely that of Shoshany et al. (2000), the Normalized radar Backscatter soil Moisture Index (NBMI). The basic differences are: (i) usage of β^0 instead of σ^0 , (ii) determination of a β_{\min}^0 (dry-soil brightness value) is based on considering brightness values in the current radar images, whereas NBMI considers a dry-soil σ^0 -value as an average of like values reported in a series of separate articles, and (iii) re-formulation of NBMI to ensure that the values of WI remain in the range of [0–1], roughly to coincide with the natural range of SWC (i.e., 0–100 %, permanent wilting point to complete saturation).

15.3.3 Comparisons of WI with SWC-Values Determined in the Field and with the SWAT Model

Maps of WI-values (given in Sect. 15.4) were generated by applying Eq. 15.1 to the RADARSAT-1 images covering the same geographic area as all field

measurements and modeled SWC-values obtained. To directly relate WI-values at the field level, we determined point-location estimates of WI by (i) taking into account all WI-values, within a 500×500 m area (consisting of a 20×20 pixel window) centered on the measurement sites, and (ii) averaging their values (accounting for 400 pixel values). In the second comparison, as the SWAT model provides spatially-averaged estimates of SWC, we averaged WI-values to provide a mean value at spatial resolutions equivalent to those used in SWAT (i.e., 62–275 ha resolution). To compare WI-values with SWC-values directly, we used least squares regression (and the coefficient of determination, r^2) on WI-vs.-SWC data pairs to determine the degree of agreement between the two independent variables (i.e., WI and SWC).

15.4 Results and Discussion

Figure 15.3a provides a spatial distribution of WI-values over the study area based on the 08 August, 2005, RADARSAT-1 image. It revealed that the WI-values fell mostly in the wetness range of 20–45 % (~95 % of all values), with an average wetness of 31 % (Fig. 15.3b).

Figure 15.4 shows the variations of WI and SWC at the measurement sites (forests and bare field) for the radar-image acquisition dates (i.e., 15 July, 08 August, and 01 September, 2005). It revealed that both WI and SWC were the lowest on 08 August, 2005, except for the measurements at the CL site. Temporal variability in SWC is strongly coupled to episodes of rainfall within a 1–2 day period prior to image acquisition (Table 15.2). The unchanging SWC conditions on 08 August at the CL site despite a lack of rainfall during a significant period prior image acquisition, is most likely related to the site's position within a prominent landscape depression, ultimately leading to the site's elevated soil water conditions through lateral drainage from the surrounding landscape (Hassan et al. 2006).

Figure 15.5 shows a comparison between RADARSAT-1 ScanSAR-derived WI-values and field measurements of volumetric SWC at a 10-cm depth as a function of the three representative landcovers (i.e., dense forests, sparse forests, and bare field). We preferred to use the field measurements of SWC at 10-cm depth as it provided a better representation of available water to the vegetation. The comparisons revealed reasonable agreement between the two variables for the three areas, yielding r^2 -values of 74 % for the dense forests, 77 % for the sparsely-vegetated forests, and 99 % for the bare field.

The C-band SAR backscattering has been previously demonstrated to be highly influenced by vegetation water content in dense forests, opposed to SWC (Pulliainen et al. 2004). So it is quite possible that our WI-values produced for dense forests were affected similarly. However, since SWC is one of the most critical variables for forest-site productivity (Bourque et al. 2000; Wang and Klinka 1996) and since it has an important role in plant physiology (by means of photosynthesis and evapotranspiration), we could envision canopy foliage water content

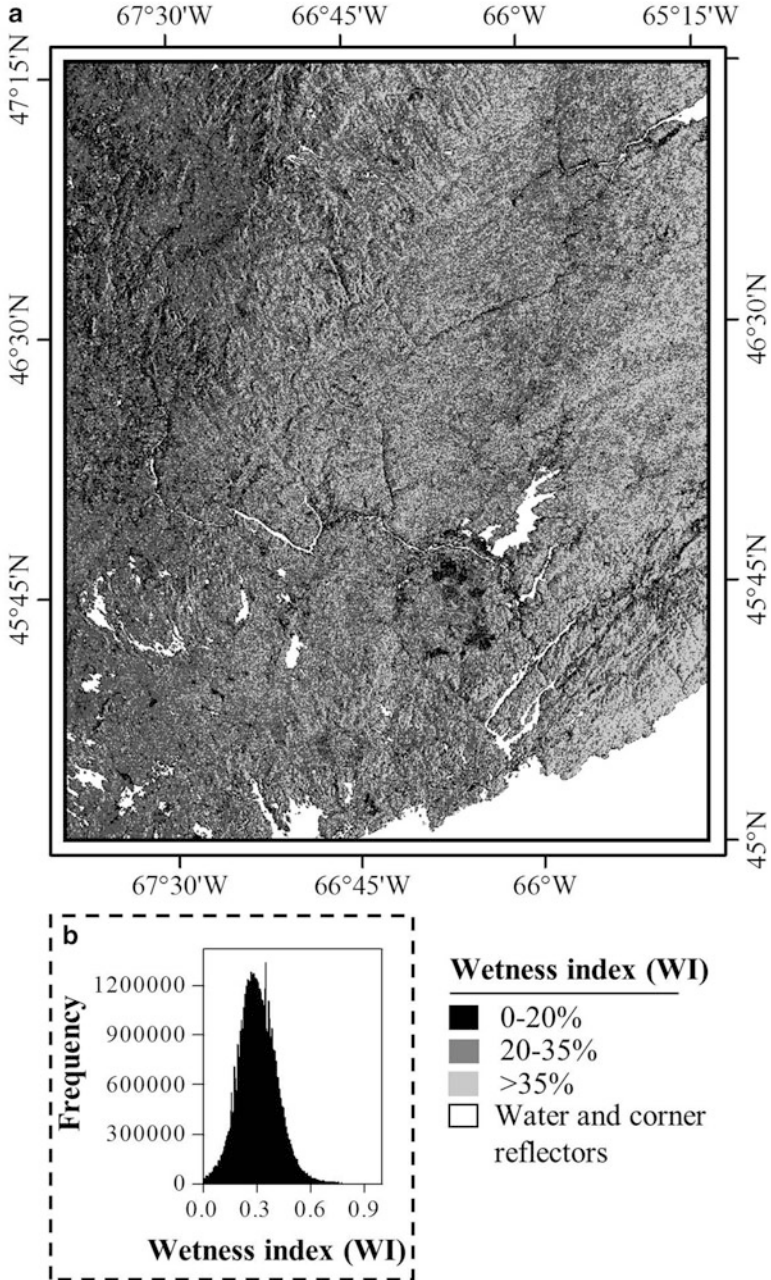


Fig. 15.3 Spatial (a) and frequency distribution of WI (b) over the entire study area (i.e., entire image) based on the RADARSAT-1 ScanSAR image acquired on 08 August, 2005

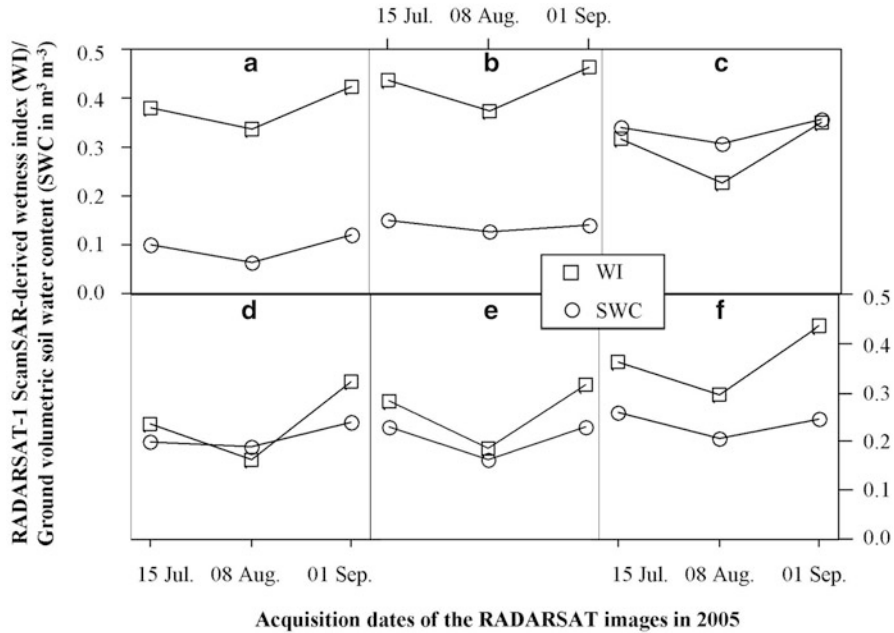


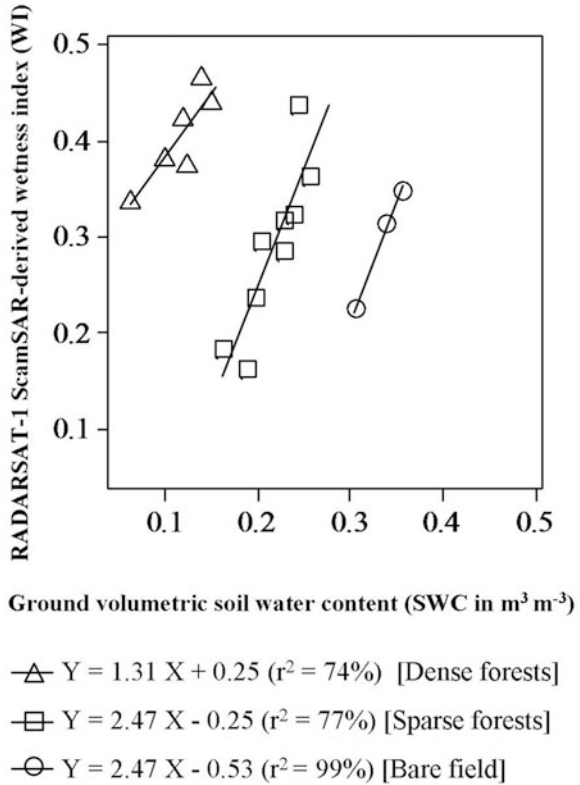
Fig. 15.4 Variations of WI and SWC at the measurement sites, i.e., two in dense forests at the NWL (a) and CL sites (b); one in a bare field at CFB Gagetown (c); and three in sparsely-vegetated forests at three different locations at CFB Gagetown (d–f), for the image-acquisition dates of 15 July, 08 August, and 01 September, 2005

Table 15.2 Rainfall conditions at the sites, where volumetric soil water content was either observed or modeled

Acquisition dates (2005)	Rainfall (in mm)			
	Dense forest	Dense forest	Sparse forests and bare field	Potato-production area
	NWL site	CL site	CFB gagetown sites	Black brook watershed site
14 July	14.1	12.2	20.6	11
15 July	2.1	8.0	0.0	0.0
07 August	0.0	0.0	0.0	0.0
08 August	0.0	0.0	0.0	0.0
31 August	34.9	22.0	29.2	52.4
01 September	17.0	12.2	7.6	10.2

of dense forests (overstory + understory) to be in equilibrium with SWC, due to the relationship between the local water balance and total leaf area index (Grier and Running 1977). A level of equilibrium should be maintained provided that plant growth is unaffected by disturbance agents such as disease, insect infestation, physiological drought caused by soil water-logging or disruption of root-to-shoot

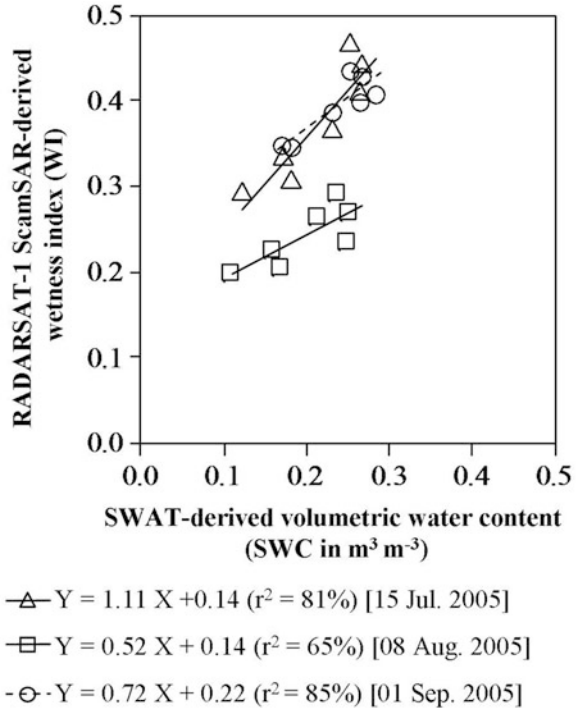
Fig. 15.5 Comparison of WI and field measurements of volumetric SWC at a 10-cm depth as a function of landcover type, i.e., dense forests, sparsely-vegetated forests, and a bare field



ratios by air pollutant deposition (e.g., Rennenberg et al. 1996; Persson and Majdi 1995) or winter conditions, such as prolonged winter thaws (Bourque et al. 2005). Soil water potential (an indirect measure of SWC) and plant water potential (a measure of in-canopy foliage water content) have been previously shown to be strongly correlated (Pabst et al. 1990; Fotelli et al. 2001). Given these conditions, the WI developed here can be viewed as an indirect measure of SWC and a basis for SWC-detection in forest-dominated landscapes.

Figure 15.6 provides a spatial comparison between RADARSAT-1 ScanSAR-derived WI and SWAT-derived, vertically-averaged estimates of volumetric SWC. Given the rapid growth rate of potato plants and changes in field-surface conditions during the growing season (3–4 months), emphasis of the second comparison was to substantiate spatial representation of derived values for a specific time period. Reasonably good agreement was obtained between estimates, yielding r²-values of 81 % for 15 July, 65 % for 08 August, and 79 % for 01 September, 2005 comparisons (Fig. 15.6). Both r² and the position of the regression lines were found to differ among the three images. Possible reasons for these differences could be related to differences in (i) rainfall (see Table 15.2 for the Black Brook Watershed site), (ii) leaf area index (LAI), (iii) misrepresentation of SWC by the

Fig. 15.6 Comparison of spatially-averaged WI-values and SWAT-derived estimates of mean volumetric SWC for a 1-m deep soil for field conditions in a potato-growing region of northwest NB



SWAT-model by averaging SWC within a 1-m block of soil, (iv) water content in the potato plant, and (v) surface roughness from July through September.

Despite demonstrating fairly strong relationships between WI and estimates of SWC (both observed and modeled), this study has a number of limitations, namely

- (i) As only three radar images and data from seven field sites were used in this study (i.e., two in dense forests, three in sparse forests, one in a bare field, and one in a potato-production area), we feel that a greater number of radar images and field measurements are required for a more comprehensive evaluation of the method.
- (ii) WI-vs.-SWC comparisons for the three landcover types (Fig. 15.5) revealed that WI is to some extent dependent on canopy density, and, therefore, LAI. As a result, refine mapping of SWC should consider landcover. At this moment, landcover effects on SWC are outside the scope of this work.
- (iii) For an improved comprehension of the temporal dynamics of WI, acquiring radar-images for the spring and fall periods would complement the current summer images.
- (iv) Question of applying the SWAT-model to the forest sites is a critical one, given that the SWAT model requires a number of inputs, which are not commonly available from forested sites.

15.5 Concluding Remarks

The method developed here has been shown to be viable for detecting SWC for specific landcover types (i.e., dense forests, sparse forests, bare field, and potato fields). Generally, good agreement was obtained between WI and field-measurement and modeled SWC, with r^2 -values ranging in between 65 % and 99 %. Our analysis has also shown the potential of using the method as an indirect measure of SWC in forest-dominated landscapes, where C-band radar signals have been shown to be most directly influenced by vegetation-cover water content. This is because radar-signal penetration into the forest is limited to a small fraction of the upper canopy. This indirect measurement of SWC is possible because of the equilibrium established between foliage water content and SWC under normal, non-stressed conditions. Further research is needed to evaluate the usefulness of the method in other areas of the world.

Acknowledgements The RADARSAT-1 ScanSAR images of this study were made available at subsidized rates from the Canadian Space Agency under the administration of the “Data Research Use Program”. We would like to thank Mr. Don Coleman, Meteorological Service of Canada, for providing the field measurements of SWC, and Dr. Yang Qi (University of Winnipeg) for conducting the SWAT-model runs and for making the results of her work available for incorporation in our paper.

References

- ALTRIX Systems (2000) Extraction of beta nought and sigma nought from RADARSAT. ALTRIX Systems, Rep. AS97-5001 Rev. 4
- Arnold JG, Srinivasan R, Muttiah RS, Williams JR (1998) Large area hydrologic modeling and assessment – part 1: model development. *J Am Water Resour Assoc* 34:73–89
- Baghdadi N, Camus P, Beaugendre N, Issa OM, Zribi M, Desprats JF, Rajot JL, Abdallah C, Sannier C (2011) Estimating surface soil moisture from TerraSAR-X data over two small catchments in the Sahelian Part of Western Niger. *Remote Sens* 3:1266–1283
- Bamler R (2000) Principles of synthetic aperture radar. *Surv Geophys* 21:147–157
- Boisvert JB, Pultz TJ, Brown RJ, Brisco B (1996) Potential of synthetic aperture radar for large-scale soil moisture monitoring: a review. *Can J Remote Sens* 22:2–13
- Bourque CP-A, Meng F-R, Gullison JJ, Bridgland J (2000) Biophysical and potential vegetation growth surfaces for a small watershed in northern Cape Breton Island, Nova Scotia, Canada. *Can J For Res* 30:1179–1195
- Bourque CP-A, Cox RM, Allen DJ, Arp PA, Meng F-R (2005) Spatial extent of winter thaw events in eastern North America: historical weather records in relation to yellow birch decline. *Glob Chang Biol* 11:1477–1492
- Fotelli MN, GeBler A, Peuke AD, Rennenberg H (2001) Drought affects the competitive interactions between *Fagus sylvatica* seedlings and an early successional species, *Rubus fruticosus*: responses of growth, water status and $\delta^{13}\text{C}$ composition. *New Phytol* 151:427–435
- Grier CC, Running SW (1977) Leaf area of mature northwestern coniferous forests: relation to site water balance. *Ecology* 58:893–899

- Hasan K, Hassan QK, Huque I (2003) Mapping the monsoon landuse/landcover in Bangladesh using RADARSAT-1 and ERS-2 images: a comparative study. Proceedings of ASPRS Annual Conference, 9p (on CDROM)
- Hassan QK, Bourque CP-A, Meng F-R (2006) Estimation of daytime net ecosystem CO₂ exchange over balsam fir forests in eastern Canada: combining averaged tower-based flux measurements with remotely sensed MODIS data. *Can J Remote Sens* 32:405–416
- Hassan QK, Bourque CP-A, Meng F-R, Cox RM (2007) A wetness index using terrain-corrected surface temperature and normalized difference vegetation index: an evaluation of its use in a humid forest-dominated region of eastern Canada. *Sensors* 7:2028–2048
- Lillesand TM, Kiefer RW, Chipman JW (2008) Remote sensing and image interpretation. Wiley, New York, 804 p
- Lu Z, Meyer DJ (2002) Study of high SAR backscattering caused by an increase of soil moisture over a sparsely vegetated area: implications for characteristics of backscatter. *Int J Remote Sens* 23:1063–1074
- Luzio D, Srinivasan MR, Arnold JG, Neitsch SL (2002) Soil and water assessment tool. ArcView GIS Interface Manual: Version 2000. GSWRL Report 02-03, BRC Report 02-07. Texas Water Resources Institute TR-193, College Station, 346p
- Moran MS, Peters-Lidard CD, Watts JM, McElroy S (2004) Estimating soil moisture at the watershed scale with satellite-based radar and land surface models. *Can J Remote Sens* 30:805–826
- Pabst RJ, Tappeiner JC II, Newton M (1990) Varying densities of Pacific madrone in a young stand in Oregon alter soil water-potential, plant moisture stress, and growth of Douglas fir. *For Ecol Manag* 37:267–283
- Pathe C, Wagner W, Sabel D, Doubkova M, Basara JB (2009) Using ENVISAT ASAR global mode data for surface soil moisture retrieval over Oklahoma, USA. *IEEE Trans Geosci Remote Sens* 47:468–480
- Persson H, Majdi H (1995) Effects of acid deposition on tree roots in Swedish forest stands. *Water Air Soil Pollut* 85:1287–1292
- Pulliaainen J, Hari P, Hallikainen M, Patrikainen N, Perämäki M, Kolari P (2004) Monitoring of soil moisture and vegetation water content variations in boreal forest from C-band SAR data. In: Proceedings of IEEE Geoscience and Remote Sensing Symposium, pp 1013–1016
- Qin-Xue X, You YY (2013) Retrieving surface soil moisture in cotton fields using ASAR and MODIS data without the auxiliary data in SIHU Region, Hubei Province, China. In: Proceedings of fifth international conference on measuring technology and mechatronics automation, pp 963–969
- RADARSAT International (2004) RADARSAT-1 data products specifications. gs.mdacorporation.com/includes/documents/R1_PROD_SPEC.pdf, last accessed on 16 July 2014
- Rennenberg H, Herschbach C, Polle A (1996) Consequences of air pollution on shoot-root interactions. *J Plant Physiol* 148:296–301
- Shoshany M, Svoray T, Curran PJ, Foody GM, Perevolotsky A (2000) The relationship between ERS-2 SAR backscatter and soil moisture: generalization from a humid to semi-arid transect. *Int J Remote Sens* 21:2337–2343
- Thoma DP, Moran MS, Bryant R, Rahman M, Holifield-Colins CD, Skirvin S (2006) Comparison of four models to determine surface soil moisture from C-band radar imagery in a sparsely vegetated semiarid landscape. *Water Resour Res* 42: W01418, 12 p
- Wagner W, Scipal K (2000) Large-scale soil moisture mapping in Western Africa using the ERS scatterometer. *IEEE Trans Geosci Remote Sens* 38:1777–1782
- Wang GG, Klinka K (1996) Use of synoptic variables in predicting white spruce site index. *For Ecol Manag* 80:95–105
- Wickel AJ, Jackson TJ, Wood EF (2001) Multi-temporal monitoring of soil moisture with RADARSAT SAR during the 1997 Southern Great Plains hydrology experiment. *Int J Remote Sens* 22:1571–1583
- Xing Z, Bourque CP-A, Swift DE, Clowater CW, Krasowski M, Meng F-R (2005) Carbon and biomass partitioning in balsam fir (*Abies balsamea*). *Tree Physiol* 25:1207–1217

Index

A

Aerial imagery, 44, 50, 53, 56, 58, 59, 65
Aerial orthophotos, 92
Aerial survey, 177–178, 195
Aerotriangulation, 178, 179
Agent-based models (ABM), 5, 9, 11, 13
Airborne laser survey, 138–140, 142, 146, 147, 153
Alps, 174
Al-Qala Citadel, 41–43, 45, 49–54, 56–57, 59, 60
Anderson classification scheme, 270–272
Arase Station, 232, 233, 238
ArcGIS, 22, 182, 222–225
Artificial neural networks (ANNs), 5, 6, 13
Aso Mountain, 234, 237
Associated area, 91
Association, 294, 297, 298
Atlanta, 70, 269, 270
Austria, 173–195
Automated landform classification, 142–144, 148–151
Automated Meteorological Data Acquisition System (AmeDAS), 223–226, 231

B

Bayesian statistics, 5
Biodiversity, 13, 137–153

C

Calibration, 22–23, 25–27, 29, 58, 226, 232, 234

Carbon dioxide (CO₂) emissions, 241–260
Categorical accuracy, 275
Cellular automata model (CA), 7–8, 11, 13
Change detection, 64–71, 77–80, 302, 303
Chikugo River, 232, 238
City development, 56, 59
City growth, 37–60
City map, 93–95, 108
Climate change, 12, 17–32, 64, 114, 222, 242–245, 255, 259
 adaptation, 242, 243, 255
 mitigation, 242–245, 254, 255, 259
Cluster analysis, 205–206, 212–214, 217
Coastal Dynamics Index (CDI), 204, 208, 210–213
Coastal erosion, 199–219
Co-benefit, 243, 245
Coefficient of determination, 102, 308
Comma-separated values (CSV), 224
Compact city, 243–245, 254–256, 259
Compatible climate change adaptation and mitigation measures, 244
Complex adaptive system (CAS), 7
Complexity, 4, 5, 9, 11, 13, 52, 222
Contrast stretching, 292–293
Conversion of Land Use and its Effects at Small regional extent (CLUE-S) model, 5, 12
Convex, 143, 144, 148, 149
Cophenetic correlation coefficient (COPCC), 211, 212, 214
Core area, 91, 92, 96, 97
Corine Land Cover, 39, 40, 48

Correlation coefficient, 27, 103–105, 181, 211, 212, 214
 Coupled human-environmental systems, 5, 9, 10, 12
 Crown thickness, 15
 Cultural heritage, 43, 49

D

Dac Lac, 202
 Daily commodity consumption-based CO₂ emissions, 244, 246
 Dam, 202
 Da River, 201
 Day River, 201, 202, 207, 210
 Dead ice, 193–195
 Debris cover, 174, 175, 180, 182–185, 188–191, 193, 195
 Deciduous forest, 273, 276
 Decision support system, 252, 259
 Deforestation, 4, 5, 12, 19
 Deglaciation, 174, 177, 190
 Delta, 199–219
 Dependent variable, 5–6, 100–101, 103, 106, 107, 308
 Deposition, 191, 192, 202, 207, 210, 211, 213, 238, 311
 Digital elevation model (DEM), 20, 140, 175, 179–180, 226, 231, 287
 Digital image processing (DIP), 282, 288, 292, 294
 Digital number (DN), 292–293
 Digital orthophotos, 179, 180
 Digital surface model (DSM), 179, 180
 Direct emissions, 244, 246, 252, 259
 Dissimilarity, 127, 206
 Distributed hydro-geotechnical model, 221–238

E

Earthquake, 243, 244, 250, 260, 283
 Economical change, 106
 Economic models, 5, 8, 13
 Edge enhancement, 288, 291–292
 Electricity supply source, 250
 Electric vehicle (EV), 245, 250, 252, 254, 256, 258, 259
 Embodied Energy and Emission Intensity Data (3EID), 246, 247
 Emission factor, 246, 250
 Energy risk, 243, 259
 Energy use, 244–246
 Enhancement, 242, 282, 288–293

Erbil, 41–44, 46, 47, 49, 51, 53, 55–57, 59–60
 Error penalty, 268, 272
 Evaporation, 27, 28, 30–32, 156
 Evergreen forest, 3, 272, 273, 275, 276
 Explanatory variable, 5, 99, 101, 102
 Extreme weather event, 242, 243

F

Factor of safety (FS), 228
 Fast Fourier transform (FFT), 291, 292
 Flood, 25, 28, 30, 32, 201–202, 241–260
 Flood-hazard area, 243, 244, 255
 Flood risk prevention, 254–255
 Flow velocity, 180–181, 193, 194
 Foliage and soil water equilibrium, 302, 304, 306, 308, 310, 311, 313

G

General circulation models (GCM), 12
 Generalized additive models, 5
 Generalized linear models, 5
 Geodetic survey, 50–52, 54
 Geographic information systems (GIS), 17–32, 39, 83, 94, 96, 108, 221–238, 245, 281, 289
 Geohazards, 281
 Geometric correction, 286–288
 Geometric distortions, 286–288
 Geomorphology, 304
 Glacial, 176, 179, 184, 193, 195, 297
 Glacier recession, 174, 180
 Glacier tongue, 174, 176–178, 182–190, 194, 195
 Global environmental change, 4, 12, 14
 Google Earth, 271, 274, 276, 277
 Grassland ecosystems, 8
 Greenhouse gases (GHGS), 242–244, 246
 Grid-Cell Distributed Rainfall Runoff Model Version 3 (CDRMV3), 222, 226, 227
 Ground control points (GCPs), 178, 179, 204, 288, 307
 Ground-range, 282, 287
 Gulf of Tonkin, 200, 202
 Gwinnett County, 269, 272

H

Hai Hau, 202, 205, 210, 211, 213
 Hai Phong, 201
 Hanoi, 201
 Heterogeneous landscapes, 266

High-density urban, 71, 75, 79, 81, 270, 271, 273
 Hoa Binh reservoir, 201
 Hokkaido Island, 139, 140
 Household consumption, 246–248
 Household Expenditure Survey (HES), 247, 250
 Household type, 246, 248, 249, 253, 259
 Hufeisenbruch, 174, 177, 191
 Hydrological Predictions for the Environment (HYPE) model, 20, 22, 23, 25–27, 29, 32
 Hydrological Response Units (HRU), 20–22
 Hydrologic modeling, 22, 232
 Hydrology, 19, 20, 28, 29, 32, 223, 224, 303
 Hypothetical Taxonomic Unit (HTU), 206

I

Ice, 113–134, 174–177, 181, 182, 184, 185, 187–190, 193–195, 286, 291, 293, 294
 Image classification, 74–76, 83, 268
 Image matching, 179–181
 Independent variable, 100, 101, 103, 107, 308
 Indicator, 88, 91, 94–103, 106, 107
 Indirect emissions, 244, 246, 252, 256, 258, 259
 Information system of historical object, 59
 Input-output table (I-O table), 246
 InSAR. *See* Interferometric synthetic aperture radar (InSAR)
 Integrated evaluation system for CO₂ emissions, 245, 251, 259
 Interferometric synthetic aperture radar (InSAR), 283, 284
 Internal parameterization, 268
 Inverse distance weighted (IDW), 224

J

Japanese Geodetic Datum 2000 (JGD 2000), 224
 Japan Meteorology Agency (JMA), 224, 231
 Japan Society for the Promotion of Science (JSPS), 238
 JERS-1/SAR, 204, 210, 218

K

Kamo River basin (KRB), 18–22, 25–32
 Kappa coefficient, 275, 276
 Kernels, 119, 122–126, 267, 268, 272
 Kurdistan, 41, 43, 44
 Kyushu Island, 223, 225, 230–232, 234, 235, 237, 238

L

Land change modeling/land change models (LCM), 3–14
 Land change science, 4, 13
 Land cover, 4, 5, 13, 39, 40, 48, 65, 70, 71, 76, 83, 157, 227, 265–278
 Land cover classification, 74, 267–270, 273, 275, 277
 Landsat Thematic Mapper (TM), 39, 45, 65–67, 73, 269, 272–274, 276, 277
 Landscape ecological map, 137–153
 Landscape ecology, 138
 Land use
 change, 5, 7, 12, 13, 17–32, 38, 63, 70, 243, 245, 249, 255, 256
 and land cover change, 4, 5, 13
 Land-use regulation, 243
 Land-use scenario, 13, 244, 245, 248, 254–256, 259
 Laplacian filtering process, 291
 Large scale, 107, 194, 223, 225, 238, 245, 256, 281, 290
 L-band, 204
 LCM. *See* Land change modeling/land change models (LCM)
 Lifecycle CO₂ (LC-CO₂), 248
 Light detection and ranging (LIDAR/Lidar), 138–151, 153
 Liquefaction risk, 254, 255
 Local town scale, 245
 Logistic regression, 5
 Lo River, 201
 Low-density urban, 71, 75, 79–81, 270, 271, 273, 275, 276

M

Mangrove, 202, 203, 207, 208
 Mann Kendall test (MKT), 23, 25
 Mapping, 37–60, 70, 94, 113–134, 137–153, 158, 160, 179–181, 183, 185, 195, 199–219, 222, 225, 234, 265–277, 281, 296, 302, 312
 Markov chain models, 6–7, 13
 Mass loss, 181, 193
 MAUP. *See* Modifiable Areal Unit Problem (MAUP)
 Maximum likelihood classifier (MLC), 70, 74, 267, 268, 273, 275–277
 Megacity, 58, 88, 243–245
 Melt, 20, 116, 174, 176, 177, 185, 188
 Meltwater, 182–185, 188, 189
 Microwave, 115, 116, 156, 204, 282, 283, 302
 Ministry of Land, Infrastructure, Transport and Tourism (MLIT), 21, 224, 231, 252

Mittlerer Burgstall, 177, 190, 192
 MKT. *See* Mann Kendall test (MKT)
 MLC. *See* Maximum likelihood classifier (MLC)
 MLIT. *See* Ministry of Land, Infrastructure, Transport and Tourism (MLIT)
 Model uncertainty, 29–30
 Modifiable Areal Unit Problem (MAUP), 10, 11, 14
 MODIS Derived C:N ratio map, 167
 Monitoring, 4, 22, 38–40, 59, 64–67, 70, 114–116, 175, 185, 193, 195, 265, 282
 Monte Carlo simulation, 22, 23
 Morphology, 65, 175, 304
 Mountain, 41, 42, 139, 140, 145–147, 150, 151, 153, 175–179, 190, 193, 223, 230, 234, 237, 288, 298
 Mt. Rausu, 140–144, 153
 Multi-market static economic equilibrium model, 249
 Multiple layers, 142, 147, 153
 Multiple linear regression, 96, 99, 101–103, 107
 Multiple-Look processing, 284–285
 Multispectral, 38, 46, 48, 54, 58, 66, 182, 283
 Multi-temporal analysis, 64, 77

N

Nam Dinh, 202
 Nash-Sutcliffe (NS) coefficient, 233, 234
 Nash-Sutcliffe efficiency (NSE), 22, 27, 238
 National Research Institute for Earth Science and Disaster Prevention (NIED), 226, 231, 236
 National Space Development Agency of Japan (NASDA), 204
 Natural disaster risk, 243
 Net primary productivity (NPP), 156–158, 160–167
 Neural networks, 5, 6, 13, 266, 267
 Ninh Binh, 201
 Ninh Co River, 200, 207, 210
 Normalized cross-correlation coefficient (NCC), 181

O

Off-grid power source, 245
 Operational Taxonomic Unit (OUT), 206
 Optimal hyperplane, 267
 Orthoimages, 74–76
 Other area, 89, 92, 94–97, 101, 102, 104, 105, 207, 313

P

Paraglacial, 175, 195
 Pasterze, 173–195
 Peripheral area, 91
 Permafrost, 175, 177
 Permutation distribution, 216, 217
 Photogrammetry, 38, 40, 44, 48–50, 52, 59, 179
 PhotoModeler, 50, 54–57, 59
 Photovoltaic (PV), 245, 256, 258, 259
 Political change, 88, 91, 97, 106, 107
 Population density, 200, 250, 251, 259, 293
 Potential occurrences level, 234–235
 Precipitation, 18, 19, 23, 25, 28, 31, 175, 200, 201, 210, 211, 304
 Production area, 94–97, 101–107
 Productivity modelling, 155–167
 P-value, 101–103

Q

QuickBird, 47, 50, 54–56, 65

R

Radar brightness, 305, 307
 Radarsat, 114–117, 128–134, 294, 301–313
 Radial basis function, 267, 272
 Radiometric correction, 285–286
 Recreational area, 94, 96, 97, 101, 102, 104–106
 Red river, 199–219
 Remote sensing, 4, 10, 38, 64–66, 74, 83, 94, 95, 108, 116, 155–167, 181, 182, 219, 266, 281–284, 289, 302
 Renewable energy, 244, 245
 Research Institute for Humanity and Nature (RIHN), 238
 Reservoir, 71, 201–202, 273
 Residential area, 71, 94–96, 101–107, 273
 Residential block scale, 245
 Resilient city, 243, 259
 Retreat and cohesion area, 259
 Risk map, 204–206, 211–213, 217, 218, 222, 230, 237, 238
 Road traffic intensity, 88, 91, 96, 97, 99, 100, 103–107
 Rock fall, 175–177, 190, 192

S

Satellite data, 38, 39, 45, 47, 49, 54–56, 59, 64–71, 94, 199, 211
 Sea level rise, 202, 243
 Sea-wall, 202

- Sector-based models, 8
- Sediment delivery model (SEDEM), 12, 13
- Senoshita Station, 233, 234, 238
- Shallow landslide risk, 221–238
- Shape, 40, 75, 224, 283, 291, 294, 297–298
- The Shiretoko Peninsula, 139–145, 151, 153
- Shuttle Rader Topography Mission (SRTM), 203, 208
- Significance level, 102
- Simulation, 8, 9, 11–14, 18, 19, 22–25, 27, 29, 155–167, 223, 226, 230, 234, 236, 238, 293–294
- Single layer, 141, 142, 144, 147, 153, 228
- Size, 12, 13, 49, 50, 54, 71, 76, 89, 91, 94, 97, 98, 114, 115, 128, 131, 139, 142, 157, 174, 179, 181, 215, 224, 234, 268, 269, 273, 283, 289, 291, 294, 297–298
- Slant-range, 286–288
- Sliver, 94
- Slope degree, 143, 148, 153
- Slope, Land use, Exclusion, Urban extent, Transportation, Hillshade model (SLEUTH), 7
- Slope stable model, 228
- Smart grid, 245
- Snow, 20, 177, 178, 180, 181, 185, 187, 193
- Soil degradation, 12
- Soil Water Assessment Tool (SWAT), 20, 115–117, 222, 285–287, 301, 302, 305–308, 311–313
- Soil water content (SWC), 302–308, 310–313
- Son La Reservoir, 202
- Spaceborne SAR data, 288, 294
- Spatial distribution of CO₂ emissions, 256, 257, 259
- Spatially disaggregate models, 8
- Spatially explicit land-use model, 249–250, 259
- Spatial randomization test, 214–217
- Speckle reduction, 289–291
- Spot, 39, 45, 65, 161–165, 282
- SRTM. *See* Shuttle Rader Topography Mission (SRTM)
- Statistical regression models, 5–6, 11, 13
- Stream flow, 17–32, 226
- Sub-basins, 20, 22, 234
- Supply-demand balance, 250
- Support vector machines, 74, 265–277
- Supraglacial, 174, 175, 181–185, 188–191, 193–195
- Surface, 4, 13, 20, 31, 38, 39, 42, 65, 66, 70, 74, 82, 114–116, 118, 138, 140, 141, 156, 174, 175, 178–183, 187, 188, 190–195, 204, 222, 225, 227–230, 238, 265, 266, 273, 282, 283, 285–287, 295–297, 305, 312
- elevation, 175, 181–182, 184–187, 190–194
- runoff, 19, 28, 29, 31, 32, 227
- SWAT. *See* Soil Water Assessment Tool (SWAT)
- T**
- Temperature, 18, 19, 23, 25, 28, 31, 174, 175, 177, 191, 243, 252, 304
- Temporal analysis, 77
- Terminus, 176, 185, 188, 191, 193
- Texture, 55, 59, 75, 118, 120, 122–126, 134, 149–151, 153, 179, 181, 193, 269, 283, 291, 294, 296–297
- Texturing, 52
- Thac Ba reservoir, 201
- Thanh Hoa, 201, 202, 205
- Thao River, 201
- Thematic accuracy assessment, 273, 276
- Three dimensional vegetation structure, 140, 141, 145, 153
- Time series, 7, 23, 56, 57, 60, 82, 94, 107, 175, 178
- TM. *See* Landsat Thematic Mapper (TM)
- Tokyo metropolitan area, 244, 245, 252–257
- Tone, 75, 118, 127, 163, 283, 294–297
- Topology, 94, 206, 212, 214
- Trade-off, 243, 245, 259, 285
- Training sample quality, 82, 83, 268
- Training sample size, 269, 273
- Transport area, 101, 102
- Trend analysis, 19, 24, 25
- T-statistical, 102
- Tsunami, 243, 244, 255, 260
- Tuyen Quang reservoir, 202
- Typhoon, 200–203, 208, 210, 211, 222, 237, 243
- U**
- Uncertainty, 10, 29–30, 157, 166, 167, 226, 288
- United Nations University Institute for the Advanced Study of Sustainability (UNU-IAS), 238
- Unweighted pair-group method using arithmetic averages (UPGMA), 206, 212–214, 217

- Urban area, 18, 25, 30–32, 38, 40, 49, 53, 56, 58, 63, 64, 70, 71, 79, 81–83, 87–108, 242, 243, 259, 266, 269, 273, 277
- Urban dynamics mapping, 59
- Urbanization, 4, 5, 7, 28, 29, 31, 38, 63, 70, 71, 80, 88, 91
- V**
- Validation, 22, 25–27, 29
- Van Ly, 203, 208, 217
- Variations, 18, 19, 24–25, 30, 32, 118, 120, 125, 134, 160, 162, 201, 228, 259, 285, 286, 290–292, 294–296, 305, 308, 310
- Vectorisation, 48, 54
- Vector map, 50, 60
- Vegetation classification, 140–142, 145, 147
- Vegetation height, 141, 147, 153
- Vermin damage of deer, 151
- Very high resolution imagery, 274, 277
- Vietnam, 199–219
- Virtual 3D Model, 49
- Visual comparison, 161, 274, 277
- Vulnerability, 206–207, 212–218, 242, 243, 260
- W**
- Water balance, 20, 310
- Water level, 201, 202
- Wind speed, 203, 209
- World Geodetic System 1984 (WGS 1984), 72, 224
- World Natural Heritage Area, 153